# Modelling, analysis and control of linear feed axes in precision machine tools

Jeffrey W. Moscrop
University of Wollongong

# MODELLING, ANALYSIS AND CONTROL OF LINEAR FEED AXES IN PRECISION MACHINE TOOLS

A thesis submitted in fulfilment of the
requirements for the award of the degree

**DOCTOR OF PHILOSOPHY**

from

**UNIVERSITY OF WOLLONGONG**

by

**JEFFREY WILLIAM MOSCROP, BE (HONS.)**

**SCHOOL OF ELECTRICAL, COMPUTER AND TELECOMMUNICATIONS ENGINEERING**

**2008**

# CERTIFICATION

I, Jeffrey W. Moscrop, declare that this thesis, submitted in fulfilment of the requirements for the award of Doctor of Philosophy, in the School of Electrical, Computer and Telecommunications Engineering, University of Wollongong, is wholly my own work unless otherwise referenced or acknowledged. The document has not been submitted for qualifications at any other academic institution.

Jeffrey W. Moscrop

19th June 2008

# Acknowledgements

There are many people who have assisted me throughout my candidature and I would like to thank them for the support that made this thesis possible. In particular, I would like to give special thanks to my supervisor Professor Chris Cook for his guidance, patience and understanding of the dual pressures associated with combining a PhD with full time employment. The unwavering support provided by Professor Cook has been an invaluable asset throughout this project.

Thanks to the wonderful staff of the University of Wollongong who have assisted and/or supported my work at various times throughout my candidature. I would especially like to thank John Norrish, Joe Chicharo, Fazel Naghdy, Sarath Perera and Maree Burnett. Thanks also to the workshop staff of the Faculty of Informatics and especially to Mr Brian Webb for his work in machining various components of the test-beds used in this thesis. To my fellow engineers and colleagues John Simpson, Steve Gower, Stephen van Duin, Dominic Cuiuri, David McLean, Alexander Nicholson and Anders Jørgensen, thanks for always listening and supporting an environment where ideas could be discussed openly.

Finally, and most importantly, I would like to thank my family. To my parents, brother and sister and all of their families – thank you for the strength you provide through encouragement and love. To my darling wife Natalie and beautiful son Nathan – thank you for everything, you are my inspirations!

# Contents

# List of Figures

# List of Tables

# Abstract

The precision control of linear feed axes in machine tools is examined in this thesis. Although high precision in machining has been a focal point for engineers for over 200 years, the traditional solutions have often been based on complex mechanical designs. In this thesis, two aspects of feed axis controller design are examined: i) the use of appropriate mathematical models and ii) the significance of three of the most common performance limiting factors that have traditionally affected precision in linear feed axes. The three particular performance limiting factors considered are: i) dynamic stiffness, ii) torsional vibrations and iii) backlash.

The most effective way of obtaining knowledge about a control system is through appropriate mathematical modelling. A new two-body model for a simple motor-transmission-load system is presented in this thesis. This new model is shown to provide a more accurate representation of both the total inertia and lowest natural frequency of a system, when compared with the two-body model that is traditionally used by researchers and system designers. A new model to represent backlash in a two-body system is also presented. These new models are then extended to provide accurate mathematical models of four common linear feed axis drive configurations: i) a rotary motor driving a rack and pinion transmission, ii) a rotary motor directly driving a ballscrew transmission, iii) a rotary motor driving a ballscrew transmission via a synchronous belt, and iv) a linear motor directly driving the axis.

Different control solutions to the problems of dynamic stiffness, torsional vibrations and backlash are examined in this thesis, with each controller implemented on specially constructed test-beds. An approach using Quantitative Feedback Theory (QFT) is presented

for systems with inherently low dynamic stiffness. This QFT approach is shown to provide a transparent design process, which results in high dynamic stiffness. Different controllers for torsional vibrations are compared both theoretically and experimentally, with many previously published solutions shown to be theoretically equivalent. A new backlash controller is also presented, which is shown experimentally to provide dynamic stability and good tracking performance at both high and low velocities.

The importance of treating these performance limiting factors simultaneously is also addressed in this thesis, with the control solutions developed to address some factors shown to also affect the other factors. The QFT approach is shown to provide a suitable integrated design process, where the implications of any compromises, on the control of each factor, are clearly visible.

# Published Papers Arising From This Thesis

1. Jeffrey Moscrop, Chris Cook and John Turner, "Modelling and Control of Motor/Load Inertia Mismatch in Servo Systems," in Proceedings of the Fifth International Conference on Control, Automation, Robotics and Vision, Singapore, 1998, pp. 429-433.

2. Jeffrey Moscrop, Chris Cook and Fazel Naghdy, "Comparative Study of Feedback Sensor Locations for Servo Systems with Motor/Load Inertia Mismatch," in Proceedings of the Australian Conference on Robotics and Automation, Brisbane, 1999, pp. 202-207.

3. Jeff Moscrop, Chris Cook and Fazel Naghdy, “An Analysis of Motor/Load Inertia Mismatch in Machine Tool Servo Systems,” in Proceedings of the 1st IFAC Conference on Mechatronic Systems, Darmstadt - Germany, 2000, pp. 235-240.

4. J. Moscrop, C. Cook and F. Naghdy, “Development and Performance Analysis of a Single Axis Linear Motor Test-Bed,” in Proceedings of the Australasian Universities Power Engineering Conference, Perth, 2001, pp. 607-612.

5. Jeff Moscrop, Chris Cook and Peter Moll, “Control of Servo Systems in the Presence of Motor-Load Inertia Mismatch,” in Proceedings of the 27th Annual Conference of the IEEE Industrial Electronics Society, Denver – USA, 2001, pp. 351-356.

6. Chris Cook, Fazel Naghdy, Zheng Li, Jeff Moscrop and John Simpson, “Industrial Automation Research at the University of Wollongong,” in Proceedings of the International Manufacturing Leaders Forum, Adelaide, 2002, pp. 113-118.

7. Jeff Moscrop, Phil Commins and Chris Cook, “Torque Perturbations and Dynamic Stiffness of Linear Motors for Grinding Machines,” in Proceedings of the 6th International Symposium on Linear Drives for Industrial Applications, Lille France, 2007

Chapter 1

# Introduction

## 1.1 Background

The research presented in this thesis is concerned with precision in machine tools. In particular, the research focuses on the control of linear feed axes in machine tools. Two specific aspects of controller design for linear feed axes are studied: i) the use of appropriate mathematical models to improve performance and ii) the significance of three of the most common performance limiting factors that have traditionally affected precision in linear feed axes. The three performance limiting factors considered are: i) dynamic stiffness, ii) torsional vibrations and iii) backlash. Four different drive train configurations, which are commonly used in linear feed axes, are also considered in the research. The first three configurations all consist of a rotary electric motor coupled with a mechanical transmission mechanism. The three mechanical transmission mechanisms considered are the rack and pinion, the direct driven ballscrew and the belt driven ballscrew. The fourth drive train configuration consists of a linear motor directly driving the axis.

High precision in machining has been a focal point for engineers ever since the industrial revolution of the 18th century. For instance, James Watt's steam engine design of 1765 (with patent granted in 1769 [1]) was dependent on a steam-tight piston and hence, on the accuracy of the cylinder bore. Since that period there has been a great deal of research undertaken in many areas relating to both productivity and precision in machining. Such

research has directly led to the machine tool becoming the most important industrial tool in existence. While it is difficult to think of any product that does not depend in some way upon the use of machine tools [2], there are a number of well known inventions, such as the automobile, which would simply never have existed without them [3]. Modern Computer Numerical Control (CNC) machine tools offer far greater productivity and precision than would be possible with any human operated machine. However, tolerances on machined products continue to be tightened, resulting in constant pressure on machine tool manufacturers to improve machine precision without increasing costs or lowering productivity.

The ever-increasing demands placed on precision in machining have ensured that machine tool design has maintained the interest of researchers. In particular, the ongoing computer revolution along with the development of improved sensor and actuator technologies has introduced the potential of economically meeting these increasing demands through new approaches in machine tool design. Some notable areas of machine tool design that currently attract research attention are:

- Machine Structure — From the perspective of precision it is essential that the machine structure has high rigidity. Modern computer processing power has enabled researchers to use advanced analysis methods, such as Finite Element Methods (FEM), to study rigidity in machine structures. This research has directly led to newer machine structures, such as Parallel Link Manipulators (PLM), gaining favour in some multi-degree of freedom machine designs.

- Spindles — With the increasing demands of precision often coupled with increasing demands on productivity, high speed machining has become an active research area. In particular, various chatter suppression techniques along with improved actuator and bearing technologies have been examined to reduce the effects of high spindle speeds on work-piece quality. Also, since optimal spindle speeds can vary between machining operations and work piece materials, research into various high power variable-speed spindle alternatives has become quite active.

- Feed Axes — Since machine tool feed axes often include complex mechanical transmission mechanisms, there are a number of linear and nonlinear performance limiting factors that can adversely affect the precision of these axes. As such, there has been substantial research attention given to both the make-up and control of feed axes. In particular, alternative drive train configurations have been examined, along with advanced control techniques designed to compensate for the various performance limiting factors.

- CNC Axes Control — When considering any machine tool, it is desirable to achieve a constant material removal rate. In most machining operations, a constant material removal rate is achieved when the spindle and feed axes of the machine are co-ordinated such that the spindle has constant power and the feed has constant torque (or linear force). Over recent years there has been considerable research attention given to the overall Computer Numerical Control and co-ordination of machine tool axes. This research has focused particularly on software packages for the simulation and optimisation of tool paths, along with overall co-ordinated control to implement optimised trajectories at machine level.

- Measuring Systems — In order to achieve precise axis control and optimisation of tool paths, accurate measuring systems are required. Along with the development of improved position sensors for axis control, there has been significant research undertaken in the area of machine tool error measurement. Measuring equipment such as ball-bars, probe-balls and laser interferometers have been extensively used for studying machine tool thermal errors, deformations and vibrations. Such research has helped in improving overall axes control and in the development of error compensation techniques.

- Process and Materials Research — In addition to the extensive research attention given to various aspects of machine design, there have been significant recent studies performed on individual machining processes and the machining of specific materials. This research has focused on process and material dependent requirements

and has directly influenced many of the aforementioned areas of machine design research.

While it is acknowledged that each of these research areas are vital to the continued development of precision machine tools, the research presented in this thesis focuses directly on one particular area – linear feed axes. This chapter provides an introduction to the research undertaken, along with an outline of the remainder of the thesis. Section 1.2 presents a brief account of the history of machine tools and precision in machining. Although there have been numerous significant contributions made throughout the long history of machine tools, the focus of this account is on the major events that have directly led to the high precision CNC machine tools that both dominate the modern industrial world and are the subject of interest to this thesis.

Section 1.3 presents an introduction to linear feed axes. In particular, an overview of the common make-up of a linear feed axis is given, with a major focus on how the drive train design is dependent upon the particular machining operation.

The motivation behind this research is presented in Section 1.4. Included is a brief discussion on appropriate modelling and control techniques, along with a description of the associated control problems inherent in the particular mechanical drive trains considered.

Section 1.5 provides an outline to the remainder of the thesis.

## 1.2 Machine Tools and Precision in Machining

It can be said that a tool is any device a human may use to extend the power of his or her hands and aid in doing work [4]. If such a device requires the user to provide the power, hand-skills and intelligence in order to do the work, the device is usually referred to as a ‘hand tool’. If a tool device still requires hand-skills and intelligence to do the work but is driven by an external power source, it is usually referred to as a ‘power tool’. In contrast,

the term ‘machine tool’ is applied to an elite class of tool devices that incorporate the power, skills and intelligence required to do the work in the tool itself.

The Encyclopedia of Britannica [5] defines a machine tool as a stationary power-driven machine that either shapes or forms parts made of metal or some other material. Although the definition of a machine tool has undoubtedly evolved with time, it is generally accepted that the modern term describes a tool consisting of a heavy and rigid support structure, a source of power, devices for both work-holding and tool-holding and a means for accurately controlling the desired process [4, 5]. While a large number of machines would satisfy this description, the term ‘machine tool’ is predominately used with reference to precision metal-cutting machines.

It appears that the earliest advancements in machining came through the work of clock-makers in the 15th century [3]; most notably, it is from their work that the first recorded mechanical means of producing screw threads is found. Some of the earliest references to many more modern machine tool features come from the famous Italian Renaissance artist, Leonardo Da Vinci (1452-1519). Da Vinci’s illustrations show a number of screw-cutting lathes, boring mills and grinding machines. As well as displaying improvements to the machines of his era, Da Vinci’s illustrations reveal the earliest recorded ideas of such things as the self-centering chuck, the fabricated grinding wheel and the internal grinding machine [3].

In both Europe and America it was the production of war weapons that became the major influence in the early development of machine tools and machining. In Europe the first machine tools to undertake the defining role of heavy metal-cutting were the machines used for cannon boring [3]. It was also these boring machines that influenced the production of the first steam engines, which (as mentioned in Section 1.1) became the first great catalyst in the development of precision in metal-cutting machines. The success of the steam engine resulted in the formation of a number of engine building businesses in the early 19th century and it is through these businesses that the respective works of Maudslay, Clement, Roberts, Nasmyth and Whitworth became recognised as the first ma-

jor advancements in machine precision [3, 5]. During this period there were three main areas identified as being important to machine precision: i) accurate screw threads (resulting in the development of the lead-screw), ii) true plane surfaces in machine construction (resulting in the development of the planing machine) and iii) rigidity. Other notable developments during the 19th century include the birth of the milling machine in America (a result of the requirement for part uniformity in arms manufacture), and although alluded to many years earlier by Leonardo Da Vinci, the production of fabricated abrasives and grinding machines [3, 5].

A major milestone in the history of precision machining occurred in 1906 when Frederick Taylor published the results of an extensive study into metal cutting: "On the Art of Cutting Metals" [6]. Metal cutting had now become a science, as Taylor's work marked the beginning of machine tool research. The research attention that followed, in the early 20th century, focused on increasing the machining capacity of machine tools. The major results of this early research were improvements in cutting materials, cutting techniques, machine rigidity and consequently, machine output [3]. What followed throughout the mid to late 20th century was increased research into both productivity and precision in machining, with the most important results being the development of powered control systems and machine automation.

Although some early engineers employed feedback control mechanisms (one example being Watt's flyball governor of 1788), Hazen's 1934 paper "Theory of Servomechanisms" was possibly the first major milestone in automatic control for machine tools. It is from this paper that the term 'servomechanism' originated (*servant mechanism*) [7]. Servomechanisms have since become an essential component in all modern machine tool axes. While the inherently variable-speed DC motor was at the heart of many early machine tool servomechanisms, brushless servomotors have since become widespread in most modern machines. Brushless servomotors are based on permanent magnet synchronous motors and are characterised by their very high torque to inertia ratios [8].

The first numerically controlled machine tool was developed at the Massachusetts Insti-

tute of Technology in 1952 [9]. Numerical Control (NC) can be defined as a means for sequencing machine tool operation (ie cutting rates, tool positioning, coolant control etc.) by coded numeric information. The earliest numerically controlled machines usually had this coded information recorded on perforated cards, paper tapes or magnetic tapes [9, 10]. However, as advancements began to take place in mini and micro computer technologies throughout the early 1970s, numerical control of machine tools was replaced with Computer Numerical Control (CNC). On a CNC machine tool the numeric information for machine sequencing is programmed directly into the controlling computer. Although CNC systems were originally considered during the initial 1950s development of numerical control, it was not until the cost of computers reduced that this option became viable in industry [9, 10]. In the 21st century, CNC machine tools dominate the industrial world.

## 1.3 Linear Feed Axes

In general, there are two basic types of axes found in modern machine tools: spindles and feed axes. For most machining operations the spindle axis provides high-speed rotation of the machining tool, while the feed axes are used to 'feed' the machining process. As mentioned in Section 1.1, it is desirable for any machine tool to achieve a constant material removal rate. In general, this equates to a desire for the spindle to provide constant power and for the feed axes to provide constant 'feed'. Since feed axes can be either rotational or linear, a constant 'feed' is usually achieved through constant torque on rotational axes and constant force on linear axes.

In Section 1.2, it was stated that accurate screw threads were identified by the early 19th century engineers as being one of the three main areas of importance in machine precision. In identifying the importance of accurate screw threads, these 19th century engineers showed an early understanding of the importance of constant linear feed in machine precision. This understanding directly led to the development of machines with lead-screws [5]. Since this period there has been extensive research undertaken to continually improve

the performance of lead-screws. Some of the major research attention has been focused on performance limitations caused by friction and backlash, with mechanical solutions such as the use of recirculating ball bearings (to reduce friction) and preloaded double nuts (to eliminate backlash) resulting.

In the modern machine tool there are a number of drive train configurations that are commonly used to provide linear feed. The most common configurations consist of a rotary servomotor coupled with some type of mechanical transmission mechanism, which converts the motor torque into a linear force. Ballscrews, the modern derivative of the early lead-screws, remain the most commonly used mechanical transmission mechanism. However, the drive train configuration largely depends on the machining operation being undertaken. For instance, while all linear feed axes would require a constant feed capability, accurate positioning capability (typically linear accuracy down to 1 or 2$\mu$m is required) and high acceleration rates (for quick transient responses and contour accuracy), there are other considerations that depend on the particular machining operation (such as length of travel, speed requirements and magnitude of machining forces) that can influence the make-up of a machine tool drive train.

While there are hundreds of varieties of metal-cutting machines used in modern industry, there are only six basic operations by which machines are generally classified [5]:

- *Drilling* – the operation where the tool (usually a twist drill) cuts holes in solid metal,
- *Turning* – the operation of cutting or removing metal from a spinning workpiece. The most common turning machines are lathes and boring mills,
- *Milling* – the operation of cutting metal through the workpiece being fed against a rotating multiple-edge cutting tool, called a milling cutter,
- *Grinding* – the operation of removing metal through the workpiece being brought into contact with a rotating abrasive (grinding) wheel,
- *Shaping and Planing* – involve the machining of flat surfaces, grooves or slots using a single-point cutting tool. The tool in a shaper moves back and forth over the

work-piece, cutting on the forward stroke while the workpiece is fed against the cutting tool on the return stroke. A planer performs the same operation; however, the motions of the cutting-tool and work-piece are reversed,

- *Power Sawing* – the operation of cutting shapes in metal plate.

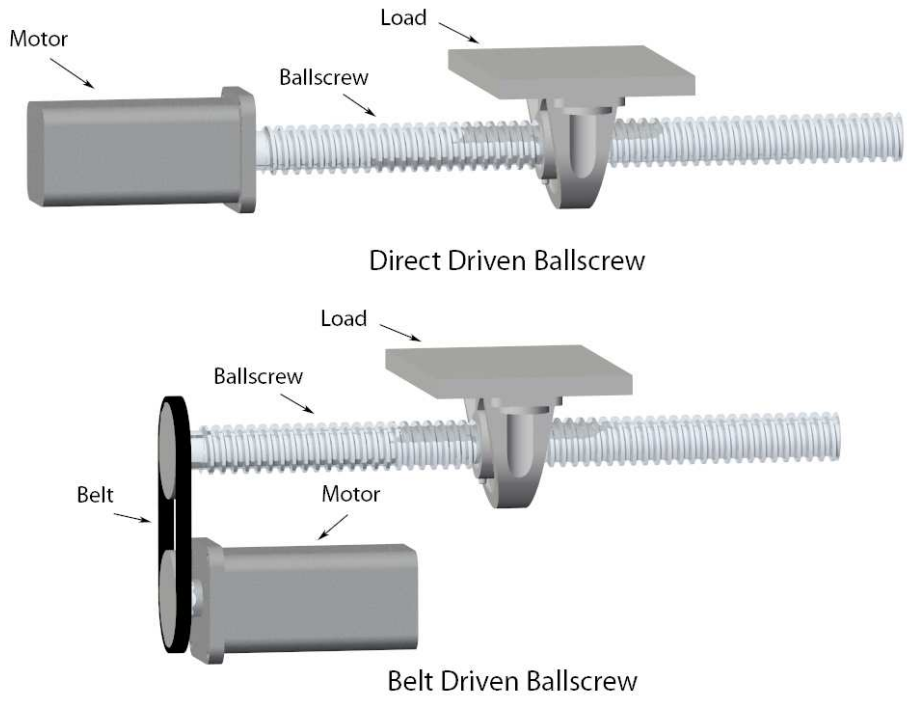


Figure 1.1: Ball Screw Configurations

The common ballscrew configurations consist of a ballscrew coupled to a rotary servo-motor either directly or via a belt (as a space-saving measure). Figure 1.1 illustrates the two common ballscrew configurations. The inherent gearing of a ballscrew provides very good dynamic stiffness, which makes ballscrew configurations particularly suited to machining operations with high machining forces, such as grinding, milling and turning. However, although the rotary servomotors are capable of providing constant torque and high accelerations rates, when coupled to a ballscrew the drive can suffer from high friction, torsional flexing and speed limitations.

The flexing and speed limitations of ballscrew configurations make them unsuitable for machining operations where high speed and/or long travels are required, such as many

power sawing operations. Modern sawing machines include plasma and laser cutters, which are characterised by very low (or even zero) machining forces and long travels. In these machines the mechanical transmission mechanism is usually a rack and pinion (as illustrated in Figure 1.2). In a rack and pinion drive the servomotor is normally mounted very close to the pinion, to limit any torsional flexing. Although this drive configuration can provide much higher speeds and reduced flexing when compared to a ballscrew drive, rack and pinions suffer from poor dynamic stiffness and increased backlash. Hence, rack and pinions are normally only used on machines with long travels.

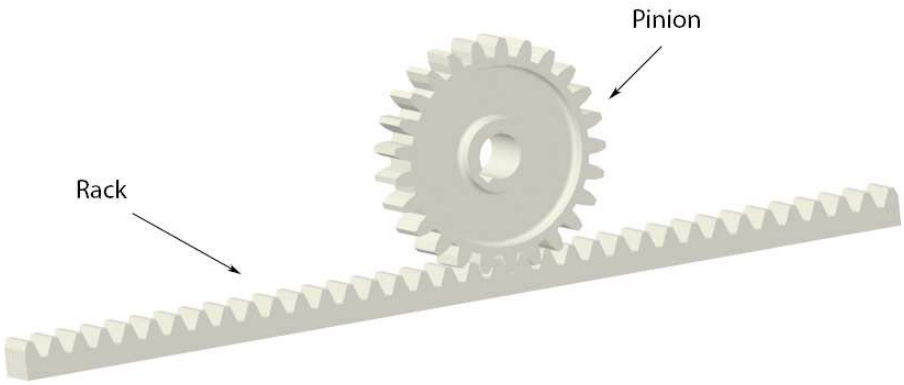


Figure 1.2: Rack and Pinion Mechanism

As an alternative to the common rotary driven linear feed axes, linear motors offer a mechanically simpler solution that eliminates the mechanical transmission mechanism along with any associated flexing, backlash, friction and component wear. Although the very first linear motor was built in the early 1840s (by Wheatstone) [11], the use of linear motors in precision machine tools has only come under study relatively recently [12, 13, 14]. The attraction of linear motors is not limited to the elimination of the mechanical transmission mechanism, as linear motors also offer a linear feed solution capable of extremely high speeds and long travel. However, elimination of the mechanical transmission mechanism reduces the friction and dynamic stiffness of the system and as such, linear motor driven axes are often the most sensitive to load variations and external disturbances (such as machining forces).

With the linear brushless servomotor ‘inheriting’ many of the desirable attributes of its

rotary counterpart it has become the most popular linear motor for precision applications. A typical linear brushless servomotor is illustrated in Figure 1.3 and consists of a motor block (containing the motor windings) that travels linearly along a stationary permanent-magnet track. At this stage linear motors have become most popular in replacing rack and pinions in machines with low machining forces, such as laser cutters, due to their inherent advantages in eliminating the mechanical transmission mechanism while providing improved high speed performance. For machining operations with high machining forces, such as grinding machines, linear motors are less suitable due to their low dynamic stiffness and the fact that the most common linear motors have magnetic material along their entire length of travel (thus attracting metallic waste, such as grinding swarf). However, the fact that linear motor driven axes have less wearing components has meant that there remains a potential advantage in the use of linear motors in any machining operation.

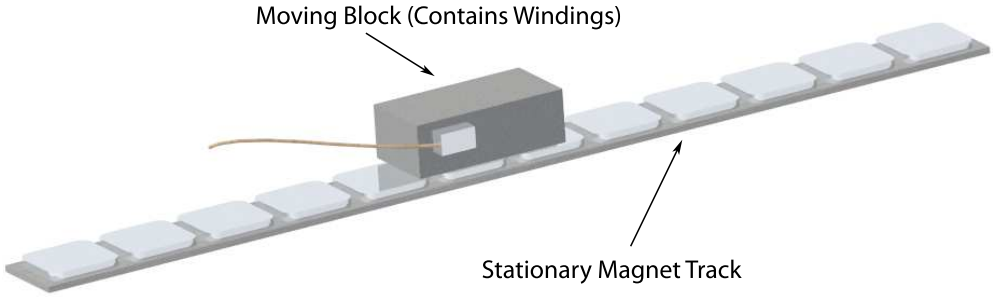


Figure 1.3: Linear Motor

## 1.4 Research Motivation

The main focus of the research presented in this thesis is precision control of linear feed axes in machine tools. Some of the factors that are known to affect the precision of linear feed axes include friction, torsional vibrations, bearing vibration, motor cogging, backlash and dynamic stiffness. Although engineers have been examining these performance limitations for many years, the traditional solutions have often been attained through improved mechanical designs. One of the results of such mechanical solutions is the variety

of different drive configurations that are now available to modern machine tool designers. As mentioned in Section 1.3, the actual choice of drive configuration is usually dependent on the particular requirements of the machining operation. However, complex mechanical solutions are often very expensive.

This thesis explores the hypothesis that improved precision in linear feed axes can be achieved through the use of fast computer control algorithms, alternative actuator technologies and non-ideal mechanical components. Thus, the thesis proposes that the choice of actuator and mechanical drive components need not be so dependent on the machining operation and can be made from an economical perspective. The work that is presented studies the development of precise control algorithms and in particular covers two specific aspects of controller design: i) the use of appropriate mathematical models and ii) the significance of three of the most common performance limiting factors that have traditionally affected linear feed axes in machine tools.

### 1.4.1 Appropriate Mathematical Modelling

It can be said that feedback in control systems is only necessary when there is plant parameter uncertainty and/or disturbances acting on the system [15]. In other words: if a perfect mathematical model of a plant could be developed, the control system would only need to be open-loop as it would be possible to achieve a desired output through careful construction of the input signal. The use of feedback has allowed engineers to develop reliable control systems without developing particularly accurate mathematical models. However, the design of a precise feedback control system benefits from sound knowledge of the parameter variation likely to occur and the disturbances likely to act on the system. The most effective way of obtaining this knowledge is through appropriate mathematical modelling.

Since the major elements of machine tool feed axes are non-rigid (flexible or elastic) they are most accurately described by continuous models, where both mass and stiffness

are distributed continuously over the entire system. It can however be very difficult to derive continuous models and even more difficult to analyse and design control systems for them. Hence, approximate discrete models are usually preferred by control system designers. Discrete models consist of a discrete number of rigid masses connected by springs that are assumed to be flexible but massless. When very precise position and velocity control are required though, there remains a question as to what discrete model offers the 'best approximation' of a machine tool feed axis. This thesis looks into the appropriate level of mathematical modelling required for precise control of linear feed axes in machine tools. A number of different models are developed from simple 'single degree of freedom' models to continuous models, with comparisons made between the models under a wide range of motor, transmission and load conditions.

### 1.4.2 Significance of Performance Limiting Factors

Although there are a large number of performance limiting factors that can affect linear feed axes, this thesis concentrates on three particular factors: i) dynamic stiffness, ii) torsional vibrations and iii) backlash. With increased use of linear motors and other direct drive actuators, dynamic stiffness has become a major issue in precision machine tools relatively recently [16]. In contrast, torsional vibrations and backlash have concerned machine tool designers for decades [17]. What is common between all three of these factors is that the degree of performance limitation associated with each factor is very dependent on the drive configuration and consequently, each of these factors continues to challenge control system designers. While it is acknowledged that other factors, such as friction and motor cogging, are also very significant, such factors form large independent areas of academic study and are not the main focus of this thesis.

As discussed in Section 1.3, linear motors and other direct drive actuators offer many advantages in machine tool drives due to reduced friction and a reduction in wearing components. However, the reduced mechanical transmission also results in a system that is more sensitive to load variations and external disturbances. Dynamic stiffness is a

measure of the sensitivity of a system to disturbances at all frequencies and has only become of major interest to researchers since the mid 1990s. Although there has been some effort by control system researchers to improve the dynamic stiffness of direct drive actuators, the issue of dynamic stiffness has become more important with the increasingly widespread use of linear motors in machine tools.

Torsional vibrations in machine tool axes are introduced through an interaction between the motor to load inertia ratio, flexing of the motor-load coupling and positioning of the feedback elements. These vibrations can result in visible scoring of the machined material and in extreme cases even result in absolute stability problems. The precise reasons behind these stability problems often remain unclear to many system designers, with (for example) a commonly used “rule of thumb” resulting in the costly recommendation of re-sizing the motor to maintain a 1:1 motor-load inertia ratio. Unfortunately, such recommendations fail to take into account the other drive train components and promote a poor understanding of the interacting factors behind the stability problems. While the stabilising of torsional vibrations has received a lot of attention from control systems researchers, this research has not yet resulted in a single “standard” approach to the problem.

Backlash is present in all mechanical systems where the driving member is not directly coupled to the load. The inherent difficulties in controlling a system in the presence of backlash are clear, especially when very high precision is required. For instance, if the driving member in a high precision control system reverses direction, the backlash gap becomes open and two separate systems exist. During this period the transmission members on the motor side of the backlash are the only members under direct control. This often results in lost motion on the load side and impact oscillations when the driving member and load come back into contact. Since the control of systems with backlash has been a subject of study since the 1940s, there have been a great number of solutions proposed. However, as with the torsional vibration problem, the research undertaken in controlling systems with backlash has not yet resulted in a single “standard” approach to the problem.

In this thesis, precise control algorithms are developed for each of the three limiting factors discussed in this section. The mathematical modelling presented in this thesis is used as a basis for controller development and the controllers are tested over a wide range of motor, transmission and load conditions. The impact of the drive configuration, on the overall control strategy, is also discussed.

## 1.5 Thesis Outline

This first chapter of the thesis presents an introduction to the research undertaken, including the historical background of the research area and impetus for the particular work undertaken.

Chapter 2 presents a review of key literature published in the area of interest to this thesis. The chapter is divided into sections that individually review literature relevant to dynamic stiffness, torsional vibrations and backlash. Appropriate mathematical modelling and the overall control of linear feed axes, in light of these performance limiting factors, are also covered.

Chapter 3 presents details of the mathematical modelling developed throughout this work. The chapter looks at modelling from a control perspective, with each of the performance limiting factors considered. Detailed mathematical models are then developed for each of the four drive configurations introduced in Section 1.1. Some basic rules for appropriate levels of modelling are also presented.

Chapter 4 details the experimental equipment used throughout the research presented in this thesis. There are three individual test-beds that have been considered in the research: i) a simple rotary motor-transmission-load system, ii) a single linear feed axis that can be driven by either a ballscrew or a rack and pinion and iii) a high precision linear motor driven single axis test-bed.

Chapter 5 presents a study on dynamic stiffness in linear feed axes. The inherent dynamic stiffness and periodic disturbances of each of the four drive configurations, introduced in Section 1.1, are discussed in this chapter. A robust control solution that includes dynamic stiffness in the design process is also presented and tested on the single axis linear motor driven test-bed.

Chapter 6 presents the results of the work undertaken in drive train flexing and torsional vibration suppression. Each of the four drive configurations are considered in this study. The work presented in Chapter 6 highlights the interacting factors that influence torsional vibrations and also examines various control solutions for vibration suppression. The most effective vibration suppression techniques are highlighted in this chapter.

In Chapter 7 a new approach to the non-linear control of machine tool servo systems with backlash is presented. This control approach takes both backlash and torsional vibrations into account during the design stage, and addresses both dynamic stability and the tracking performance of systems with backlash. The control approach also includes a new method for identifying whether a system is in the backlash phase or contact phase.

Chapter 8 is a summary of the relevant conclusions from each of the research areas presented in this thesis. Comments are made regarding the overall (drive dependent) control strategy for linear feed axes. The original hypothesis that ‘improved precision in linear feed axes can be achieved through the use of fast computer control algorithms, alternative actuator technologies and non-ideal mechanical components’ is examined in light of the research presented throughout this thesis. Suggestions for future work in this area are also identified.

Chapter 2

# Literature Review

## 2.1 Introduction

As discussed in Chapter 1, the concept of precision in machine tools is not new. Further, the general concept of precise control of electrically driven mechanical systems is not new. For example, it was as early as 1896 when Harry Ward Leonard first discussed the fundamental desire to operate electric motors, used in applications such as elevators and printing presses, 'under perfect and economical control' [8]. Such a statement is still valid some 100 years or so later and, for the machining industry in particular, the tightening of tolerances on machined products continues to apply pressure on manufacturers to improve the control and accuracy of machine tool feed axes. Just like the notion of precise control, the study of factors known to limit the performance of machine axes is not by any means new. In 1969, Carter [17] noted that the more significant characteristics of a driven mechanical system are torsional vibrations, cyclic rotational disturbances (ie bent shafts, mechanical misalignment etc.) and backlash. The true significance of these factors remains evident in that they all continue to limit the performance of modern machine axes.

In this thesis, three of the major performance limiting factors that are known to affect linear feed axes are studied: i) dynamic stiffness, ii) torsional vibrations and iii) backlash. This chapter critically reviews the prominent literature relating to each of these three

factors, identifying key advancements in the study of each factor along with the most significant methods that have been used to improve control and overall system performance in the presence of each factor. Issues relating to appropriate modelling for controller development are discussed for each individual factor and presented in the relevant sections.

Section 2.2 discusses dynamic stiffness in servo systems and covers material that has been published on improving dynamic stiffness through control methods. Section 2.3 discusses research relevant to torsional vibrations and techniques used for vibration suppression. Section 2.4 discusses backlash and in particular, the material that has been published in the areas of backlash avoidance, backlash modelling and the control of systems with backlash. Finally, Section 2.5 summarises the key points and conclusions that can be drawn from this literature review.

## 2.2 Dynamic Stiffness

### 2.2.1 General Background

Dynamic stiffness is a measure of the sensitivity of a system to disturbances at all frequencies. Systems with low dynamic stiffness are hence characterised by poor disturbance rejection and can be unsuitable in operations with high machining forces. Due to the elimination of any gearing and additional friction associated with mechanical transmission mechanisms, linear motors and other direct drive actuators are the most common sources of low dynamic stiffness in machine tools.

In the early 1990s there were only two manufacturers who had successfully used linear motors for precision positioning of machine tools; namely, the Ingersoll Milling Machine Company in the U.S.A. and the Ex-Cell-O Company in Germany [18]. Less than a decade later, at the 20th Japan International Machine Tool Fair in 2000, there were some 17 exhibitors of machine tools using linear motor technologies [19]. The advantages of linear motors in eliminating mechanical transmission mechanisms are seen as very attractive by

many machine tool manufacturers, especially in machines where high linear speeds and accelerations are required.

The major disadvantage that is often associated with linear motor driven axes is high cost [20, 21]. However, as the demand for linear motors has been increasing the capital costs have reduced. Also, with less wearing components, the overall life cycle cost of a linear motor driven system can actually be less when the high maintenance costs of other options are taken into account. As an example, a linear motor used in a vehicle crash test facility at the UK Motor Industry Research Association was described in 1993 by Aston [22] as providing 25 years of completely trouble-free operation.

In terms of performance, it is the inherently low dynamic stiffness of linear motor driven axes that is seen as the main disadvantage. In 1994 Alter and Tsao [16] examined the stability of linear brushless servomotor feed drives in precision turning applications, concluding that stability was not a problem and that attention should be focused on the important performance issues of disturbance rejection and trajectory tracking. Since that time the issue of dynamic stiffness has become a major area of interest to researchers with the increasingly widespread use of linear motors in precision machine tools.

Consider the response of a general positioning axis to a disturbance force. For a sinusoidal response at a particular frequency ($f$), the position displacement ($x$) can be described by:

$$x(t) = \mathrm{E}_f \sin(2\pi f t) \tag{2.1}$$

where $\mathrm{E}_f$ is the maximum position displacement at $f$. It follows that:

$$\dot{x}(t) = 2\pi f \mathrm{E}_f \cos(2\pi f t) \tag{2.2}$$

$$\text{and } \ddot{x}(t) = -(2\pi f)^2 \mathrm{E}_f \sin(2\pi f t) \tag{2.3}$$

For a general linear axis with negligible friction and no motor or mechanical transmission connected, the disturbance force required to produce the response of Equation (2.1) is

governed by Newton's second law of motion:

$$\mathrm{F}_d = \mathrm{M}\left(-(2\pi f)^2 \mathrm{E}_f \sin(2\pi f t)\right) \tag{2.4}$$

Hence, the magnitude of this disturbance force is:

$$|\mathrm{F}_d| = \mathrm{M}(2\pi f)^2 \mathrm{E}_f \tag{2.5}$$

Defining $\mathrm{E}_m$ as the maximum allowable position error at any frequency, it can be seen that the magnitude of the force required to exceed $\mathrm{E}_m$ increases with frequency ($|\mathrm{F}_d|$ is proportional to frequency squared). The magnitude of dynamic stiffness (DS) for the general case is thus defined by Equation (2.6). Dynamic stiffness in a practical machine tool axis varies with the mechanical transmission parameters, bearing friction and the control system. However, it is clear that with the elimination of mechanical transmission, the inherent dynamic stiffness of a linear motor driven axis can be approximated by Equation (2.6).

$$\mathrm{DS} = \frac{|\mathrm{F}_d|}{\mathrm{E}_m} = \mathrm{M}(2\pi f)^2 \tag{2.6}$$

### 2.2.2 Control of Dynamic Stiffness

With the absence of a mechanical transmission mechanism, the control system of a linear motor (or any direct drive axis) is the primary means of disturbance rejection (particularly in applications with high machining forces). However, with the reduced mechanical system, the overall controller bandwidth of a linear motor is essentially only limited by the peak force of the motor, the resolution of the feedback mechanism and the servo drive electronics [20, 23, 24]. As a result, the research effort in improving dynamic stiffness has been applied at all levels of the overall control system, including the current, flux linkage, velocity, position and overall path-planning levels.

Weigel and Mutschler [25, 26] studied deadbeat control of dynamic stiffness in a linear brushless servomotor at both the current and flux linkage levels. It was found that

deadbeat flux linkage control met the demand for a high bandwidth low level controller; however, the flux linkage feedback required an observer and a very accurate model of the system to avoid nonlinear oscillations. Finite element methods coupled with direct system measurements were recommended to produce a detailed system model. Cui et al [27] also studied the use of finite element methods to develop an accurate model for direct thrust control of a linear brushless servomotor. It was concluded, through simulation, that direct thrust control could be effective for low level control of linear motors. In a related piece of work, Zhao et al [28] studied the use of wavelet analysis to identify the primary resistance of a brushless linear motor system. It was concluded, again through simulation, that wavelet analysis produced a higher resolution for the primary resistance identification and could be used to improve the flux linkage observation in a direct thrust controller. Interestingly, in [26] Weigel and Mutschler concluded that although a standard PI current loop had inferior dynamic performance it was more robust and easier to implement than the thrust control methods.

Alter and Tsao [29] examined the effects of an optimal $H_\infty$ controller, in the position loop, on the dynamic stiffness of a practical linear motor. It was found from experimental analysis that the $H_\infty$ controller provided a 27-46% improvement in dynamic stiffness when compared with a conventional Proportional plus Derivative (PD) position controller. With the addition of machining force feedback, the optimal $H_\infty$ method was found to provide a further 70-100% improvement in dynamic stiffness when compared with position feedback alone. In a further work [12], Alter and Tsao investigated the use of optimal $l_1$ and $H_\infty$ feedforward control to enhance the tracking performance of a linear motor system. Although parameter uncertainty limited the practical effectiveness of the feedforward control, a 50% reduction in the rms tracking error was still achieved. Alter and Tsao concluded that the combination of $l_1$ and $H_\infty$ optimal feedforward and feedback control represented a viable control approach for linear motor systems, resulting in both high dynamic stiffness and optimal tracking performance.

Shen and Tsai [30] also investigated the use of $H_\infty$ to enhance the dynamic stiffness of a

linear motor controlled via a pseudo derivative feedback with feedforward (PDFF) control scheme. It was found that with the addition of $H_\infty$ the dynamic stiffness of an experimental linear motor system showed an 85% improvement when compared with standard PDFF control.

As an alternative to $H_\infty$, sliding mode control was examined by Van Brussel and Van den Braembussche [31] for robust tracking performance of linear motors. It was found that sliding mode control achieved the desired robust performance, as long as the control law contained no discontinuous terms (which were said to lead to possible high frequency errors). Sliding mode techniques were also combined with adaptive control techniques by Xu and Yao [32, 33, 34] to improve both dynamic stiffness and tracking performance of linear motors. The combined control scheme, termed Adaptive Robust Control (ARC), was tested for both velocity feedback [32, 33] and position only feedback (using a velocity observer) [34]. For both the velocity and position feedback cases, it was concluded that the ARC control scheme showed good transient performance and final tracking accuracy in the presence of parametric uncertainties and bounded disturbances. In a related piece of work, Hong and Yao [35] added actuator saturation information to the ARC design process to improve the experimental realisation of theoretically guaranteed tracking and dynamic stiffness performance.

Other control approaches that have used a nonlinear actuator model to improve dynamic stiffness in linear motor systems include the Auto-Disturbance Rejection Controller (ADRC) and the input-output linearisation technique. Yang et al [36] claim, through simulation, that the ADRC approach (which uses a nonlinear state error feedback control law) when applied to both the current and velocity loops of a linear motor system can provide improved dynamic stiffness and tracking performance. Dolinar and Štumberger [37] used the input-output linearisation technique (which involved the exact cancellation of system nonlinearities in an overall position feedback loop) on a linear synchronous reluctance motor model. Simulation and experimental results demonstrated good tracking performance; however, no disturbance rejection results were given.

One of the most comprehensive approaches to the control of dynamic stiffness was presented by Renton and Elbestawi [38] and involves improved control effort at both the low servo and high path-planning levels of a linear motor feed drive. The approach uses Minimum-Time Path Optimisation (MTPO) to address feed-rate scheduling at the path-planning level and Minimum-Time Tracking Control (MTTC) to address the primary sources of path error at the servo level. The focus of this approach is on the actual capabilities of an axis and all primary sources of path error are included in the overall design. Renton and Elbestawi found that the disturbance rejection properties of this approach were superior to both standard PD and $H_\infty$. They also found that the dynamic stiffness could be further improved through the use of a periodic disturbance observer that is synchronised to the spindle axis.

In this thesis the control of dynamic stiffness is examined from the perspective of practical implementation. In many cases a linear motor can only be incorporated into a multiple axis machine tool if it is compatible with the drive system used on the other axes. Although there are clear advantages in addressing dynamic stiffness at the lower current or flux levels [25, 26, 27, 28, 38], access to these lower servo-level control loops is often limited in standard servo drives. However, it is sometimes possible to take advantage of the information contained in lower level feedback (current or torque/force) in higher level control algorithms. Another important practical issue is computational efficiency of the control algorithms. Although processor speeds are continually increasing, many standard servo drives still only have a small window (within the sampling interval) for the implementation of control algorithms. For this reason artificial intelligence methods, such as Fuzzy Logic [39], are often not a practical solution.

When considering the control approaches that have been examined for the velocity and position loops of direct drive systems, the various robust techniques, such as $H_\infty$ and sliding mode control, were shown throughout the literature to provide improved dynamic stiffness [12, 29, 32, 33, 34]. One robust control technique that was absent from the available literature is Quantitative Feedback Theory (QFT). QFT offers a general design

approach based on stability bounds, loop shaping and uncertainty in the system. In the benchmark control session of the 1995 European Control Conference, both the winning entry and the runner up used QFT. Further, the winning QFT design was the only entry that fulfilled all of the design specifications [40]. For these reasons, a QFT design approach to the control of dynamic stiffness is presented in this thesis.

## 2.3 Drive Train Flexing and Vibration Suppression

### 2.3.1 General Background

The most basic elements of any drive train are the motor, the load and any devices used to couple the motor to the load. It is therefore no surprise that the three most significant performance limiting factors, as discussed by Carter [17], are related to the interaction between these basic drive elements. Consider the very simple drive train shown in Figure 2.1. This system consists only of a motor and load coupled through a single transmission element. As there is no 'free-play' in the system, backlash has been avoided. Also, it is assumed that the transmission element is perfectly straight and perfectly aligned, thus avoiding any alignment related cyclic disturbances. Transmission flexing and torsional vibrations cannot be considered negligible however, as all real transmission devices (used to form the motor-load coupling) are non-rigid by nature.

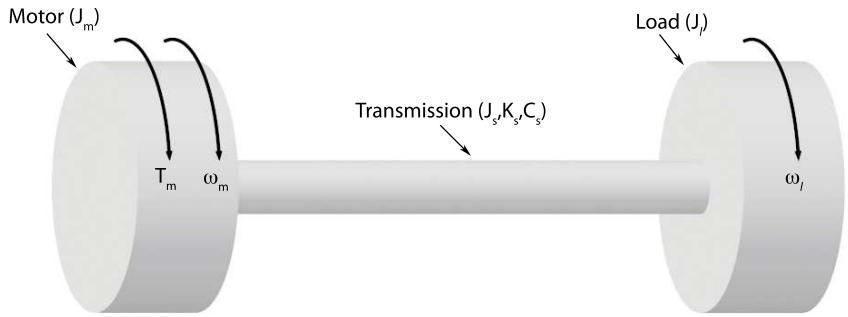


Figure 2.1: Simple Motor-Transmission-Load System

As discussed in Section 1.4.2, torsional vibrations are introduced through an interaction between the motor and load inertias, flexing of the motor-load coupling and positioning of the feedback elements. However, Industry has traditionally only concentrated on the relative sizes of the motor and load inertias. From the control systems perspective, a low total inertia is particularly desirable as the resulting high torque to inertia ratio results in faster accelerations and faster transient responses. The claims from many servo motor manufacturers though, are that motor-load inertia ratios close to 1:1 should always be maintained in order to avoid vibrations and related stability problems. As a result, manufacturer "rules of thumb" are often used to define acceptable inertia ratios. For instance, Baldor (a servo motor manufacturer) state in their product catalogues that inertia matching is a critical motor selection criteria and although motor-load inertia ratios of higher than 1:5 may be possible, they are not recommended because of possible stability problems [41]. Such recommendations neglect the impact of other drive train components and these "rules of thumb" can also often vary between manufacturers [42]. This thesis provides an analysis that overcomes these shortcomings.

One of the most important issues overlooked by such widely used "rules of thumb" is the fact that practical devices used to form motor-load couplings are non-rigid by nature. Designers tend to traditionally treat motor and load inertias as a single 'lumped' inertia. Along with this, the feedback element is usually attached to the motor. In treating a system in this manner there is an inherent assumption that the coupling device connecting motor and load is infinitely stiff. In reality, all coupling devices have finite stiffness and the load response is not identical to that of the motor [43]. This becomes a particularly critical issue when attempting to design controllers for highly 'flexible' systems, where feedback is only available from the motor and the variables of interest are load velocity and position. Such highly 'flexible' systems often arise in industry when designers choose low inertia coupling devices in order to improve system transient responses. When reducing the inertia of the coupling devices, the rigidity of the transmission is also often reduced. While there is some advantage to matching motor and load inertias as a solution, the practice of re-sizing motors in order to maintain unity motor-load inertia ratios can be a

far more costly solution when compared with choosing a more rigid transmission.

The importance of high rigidity in motor-load couplings is not new knowledge, as Carter [17] described torsional vibrations as occurring due to springiness of shafts and couplings interacting with load inertias. Despite this, infinitely stiff couplings are still often assumed in the analysis and design of servo systems. For example, Armstrong [42] (from Kollmorgen Motion Technologies) even used an infinitely stiff coupling while discussing why motor and load inertias should be 'matched'. It should be clear that an infinitely stiff coupling results in one single inertia and as such, an inertia mismatch cannot exist. One of the major points in [42], is that inertias should be matched for maximum power transfer. While the notion of maximum power transfer is valid, any attempts to analyse the stability problems associated with motor-load inertia ratios cannot be undertaken using an infinitely stiff coupling.

### 2.3.2 Modelling and Analysis of Torsional Vibrations

The analysis and control of torsional vibrations has received considerable research attention. However, while most published material has acknowledged the importance of treating motor-load couplings as non-rigid, the standard model used by researchers is an approximate two-body model based on the system shown in Figure 2.1 [40, 43, 44, 45, 46, 47, 48]. With this system, backlash, friction and other factors that would normally affect servo system performance are generally regarded as negligible. It is also assumed that the relationship between the flexing of the transmission element and the resulting 'spring' force can be completely described by Hooke's Law and as such, any nonlinear spring characteristics are negligible.

With reference to Figure 2.1:

- $J_m$ is the motor inertia,
- $J_l$ is the load inertia,
- $J_s$ is the inertia of the transmission element,

- $T_m$ is the torque produced by the driving motor,
- $K_s$ is the torsional stiffness of the transmission element,
- $C_s$ is the coefficient of internal damping that is inherent in the transmission element, and
- $\omega_m$ and $\omega_l$ are the radial velocities ($\dot{\theta_m}$ and $\dot{\theta_l}$) at the motor and load ends of the transmission element respectively.

In the two-body model of the system shown in Figure 2.1 the inertia of the transmission element is assumed to be zero. Hence, the system is completely described by two equations of motion, with two generalised coordinates $\theta_m$ and $\theta_l$:

$$J_m\ddot{\theta}_m = T_m - K_s(\theta_m - \theta_l) - C_s\left(\dot{\theta}_m - \dot{\theta}_l\right) \tag{2.7}$$

$$J_l\ddot{\theta}_l = K_s(\theta_m - \theta_l) + C_s\left(\dot{\theta}_m - \dot{\theta}_l\right) \tag{2.8}$$

Through further analysis of Equations (2.7) and (2.8), expressions can also be obtained for the undamped natural frequencies of this system. Equation (2.9) represents the undamped natural frequency due to the zeros in the frequency response of the system, while Equation (2.10) represents the undamped natural frequency due to the poles in the frequency response of the system.

$$\omega_z = \sqrt{\frac{K_s}{J_l}} \tag{2.9}$$

$$\omega_p = \sqrt{\frac{K_s(J_m + J_l)}{J_m J_l}} \tag{2.10}$$

Many papers focus predominately on the control of vibrations rather than on how the various factors interact to introduce these vibrations. This fact has resulted in the publication of many apparently different control solutions, which turn out to be mathematically based on the same approach. While the undamped natural frequency equations (Equations (2.9) and (2.10)) are derived in many of the reviewed articles [40, 43, 44, 48, 49], only Welch

[43] and Vukosavić et al [44] go on to discuss the importance of considering all of the interacting factors (including the positioning of feedback elements).

Apart from the limited analyses performed in many of the above articles, there are also problems with the standard use of the 'traditional' two-body model, represented by Equations (2.7) and (2.8). The major problem is that any inertia associated with the motor-load coupling device is considered negligible, whereas in many drive trains the mass or inertia of the coupling device can be quite significant and often larger than the inertia of the load itself (as seen by the motor). Some examples of this are in many of the power sawing operations where feed axes transmissions can be over 10m in length. Also, in general ballscrew axes the load inertia is reflected to the motor side through the inherent gearing of the ballscrew, which can reduce it to a value less than the inertia of the ballscrew itself. Another important aspect when considering ballscrew driven axes is the fact that torsional stiffness and the transmission inertia both vary with the load position.

Nordin [40] deals with the issues discussed in the preceding paragraph by claiming that the realism of the two-body model can be increased through treating some parameters as uncertain. While this is a good approach for ensuring a robust control solution, designing a controller at all can be difficult if the bounds of uncertainty are unknown. For all of these reasons the 'traditional' two-body model can be greatly improved upon when modelling motor-transmission-load systems.

### 2.3.3 Control Solutions

Traditionally, the velocity control of servo systems has been based on some form of simple Proportional (P), Proportional plus Integral (PI) or Proportional plus Integral plus Derivative (PID) regulator, with PI being the most common. The early methods used to improve system performance, in the presence of torsional vibrations, focused on reducing the gains of such regulators to ensure any resonant frequencies occurred outside the system bandwidth. Of course such remedies also resulted in sluggish transient responses.

Some alternatives suggested in 1969 by Carter [17], included the introduction of low-pass or notch filtering to suppress resonances and allow an increase in system bandwidth. Carter also suggested that improvements could be achieved by moving the feedback element to a nodal point (a point along the transmission where oscillations do not occur), or at least as close as possible to a nodal point. However, in many machine tool feed axes the only practical position for a feedback sensor is at the motor. It is also worth noting that caution is required when using a single feedback device placed at (or near) the load as the system can quickly become unstable.

The early methods of using simple P, PI or PID regulators, coupled with vibration suppression filtering, have remained among the most common control approaches used in modern servo systems. In fact, with the ongoing computer revolution and increasing preference towards digital control, software tunable filters have become a standard feature in many industrial servo controllers. The continual advancement of digital controllers has also allowed for much more flexibility in the control of servo systems, leading to an increase in the research of higher order control schemes and complex filtering techniques.

A number of different approaches for controlling torsional vibrations in servo systems have been published since the mid 1980s. In general though, these solutions can all be classified as belonging to one of three fundamental groups:

1. Conventional control, with vibration suppression filtering and a single feedback device (usually attached to the motor),
2. Higher order control, with multiple feedback devices (attached to both the motor and load) and
3. Higher order control, with a single feedback device (usually attached to the motor).

The first of these groups represents all variations of the traditional approach, which consists of a simple regulator and vibration suppression filtering. However, significant work in digital signal processing and filtering has recently been applied to servo systems. In particular, both Finite Impulse Response (FIR) filtering and Infinite Impulse Response

(IIR) filtering have been successfully used for the suppression of various types of mechanical vibrations in machine axes [44, 50].

The second and third groups both focus on using higher order controllers. The most common approaches in both of these groups are based on using state feedback with either pole placement or linear quadratic design techniques [46, 47, 48, 49, 51, 52]. In [51] the author of this thesis used state feedback sensors at the motor and load to stabilise a two-mass experimental system; the same controller was successfully adjusted to use a single motor sensor and full order state observation in [52]. Similarly, [46, 47, 48, 49] all report success using state feedback with a single motor sensor and estimation techniques (such as state observers) to provide feedback of the other states. Due to practical concerns in most mechatronic systems (such as mounting constraints, expense and noise) a single feedback device at the motor is generally preferred over the inclusion of a load sensor.

While most high order servo controllers are based on general state feedback, some authors have also reported success with controller designs based around specific flex-related feedback quantities. In [52], the author of this thesis used a 'shaft-flex' inner feedback loop in conjunction with a standard PI controller to successfully stabilise oscillations in a simple two-mass system. Brandenburg et al [45], reported similar success with the use of a 'shaft-torque' inner feedback loop. Other feedback quantities that have also reportedly delivered success in stabilising such systems include load torque (Ji et al [46]), load acceleration (Hori et al [49]) and motor acceleration (Welch [43]). Of particular interest among these solutions is the motor acceleration feedback system proposed by Welch [43], as it does not require any load feedback (either direct or estimated).

Almost all of the higher order control approaches that use a single feedback device (Group 3), require some form of feedback estimation. There are however some notable exceptions to this generalisation including the aforementioned approach by Welch [43] (using motor acceleration feedback), along with single feedback designs based on QFT. Although estimation techniques can be used with QFT, they are in conflict with the fundamental basis of the theory [15]. As mentioned in Section 2.2.2, both the winning entry and the runner

up in the benchmark control session of the 1995 European Control Conference used QFT. It is interesting to note that this benchmark control session involved competing designs for control of a three mass flexible system [40].

The choice between vibration suppression filtering and the use of higher order controllers has become very subjective; however, previous results have generally shown that simple PI regulators tend to only achieve comparable performance when the current loop has a low bandwidth. If the current loop is fast enough to damp the resonance, higher order control schemes generally offer superior performance [40, 53, 54].

The most interesting of the higher order control approaches are the various solutions that use specific flex-related feedback quantities. All of these solutions claim to successfully stabilise torsional vibrations and each one of them can be used in conjunction with a standard PI velocity loop, an outer state feedback loop or incorporated into QFT designs. However, while each of these solutions appears to offer a unique approach to the problem, a quick analysis of system flexing (under such feedback) reveals many of them to be fundamentally equivalent. Although some articles have compared various control approaches [40, 47], these comparisons have not been comprehensive, have not been performed over a wide range of motor-transmission-load conditions and have not recognised the equivalence of many of the feedback solutions. Hence, a standard approach to the problem has yet to be adopted.

In this thesis a comprehensive comparison of the various approaches to controlling torsional vibrations is presented. This comparison is performed over a wide range of motor-transmission-load conditions and uses an experimental test-bed that was specifically designed to analyse torsional flexing and vibrations. The comparison also includes control approaches that were developed as part of this thesis. The importance of using an accurate system model in the controller design process is studied and a two-body model with improved accuracy (when compared with the ‘traditional’ two-body model) is developed.

## 2.4 Backlash

### 2.4.1 General Background

According to the Oxford English Dictionary, the term backlash was originally used to describe the ‘jarring reaction or striking back of a wheel or set of connected wheels in a piece of mechanism, when the motion is not uniform or when sudden pressure is applied’ [55]. The same term was later used to describe ‘the play between adjacent movable parts (as in a series of gears)’, along with ‘the jar caused by this when the parts are put into action’ [56]. Some other simple definitions of backlash include: ‘the lost motion in a gear train’ [57] and ‘the amount by which a tooth space exceeds the thickness of an engaging tooth’ (again with reference to a gear train) [58]. For the purposes of this thesis, backlash can be thought of as the whole phenomenon resulting from play between movable mechanical parts. This includes both lost motion (when the parts are not in contact) and the system reaction when such parts come back into contact. The term “backlash gap” is used to describe the actual play itself.

As discussed in Section 1.4.2, the inherent difficulties of controlling a system with backlash are clear. During any period when the backlash gap is open two separate systems exist with only the transmission members on the motor side of the backlash gap being driven, while the load is in a sense ‘uncontrolled’. When the backlash gap closes, the resulting collision can cause severe system oscillation. Control systems can often exhibit steady state errors in the presence of backlash. Further, limit cycles with irregular oscillation and peak-peak amplitudes greater than the total backlash gap can be experienced [40]. For these reasons, backlash has historically been considered as one of the most serious problems associated with precision control of machine tool drive trains [40, 59].

Since the precise control of systems with backlash has been an enduring engineering problem for over 60 years, the traditional (and still the most common) approach to overcoming the effects of backlash is to minimise it through improved mechanical design and

manufacture [17, 60]. Precise manufacturing techniques and accurate assembly allow for a reduction in the clearance between gearbox teeth and hence, a reduction in the width of any backlash gap. However, there are limitations with this method in that a certain amount of space between gearbox teeth is necessary for lubrication and assembly. The most common mechanical approach used in modern precision machine tools is to provide a preload to ensure persistent contact of gear teeth. There are a number of preload methods commonly used, including the use of a second inverse motor and the use of spring loaded gearboxes to ensure there is always gear contact in both directions. One example of a preloaded anti-backlash configuration, which is often found in modern precision machine tools, is the double nut ballscrew system.

In general, the mechanical techniques for reducing the effects of backlash are expensive and can also result in higher friction and increased energy consumption. These disadvantages have traditionally been compared with the projected costs of allowing a mechanism to function in the presence of backlash (ie the cost of reduced dynamic performance, increased wear, service failures, noise etc.) [60]. For these reasons, the research of more cost-effective control solutions to backlash has remained of interest to engineers.

### 2.4.2 Backlash Modelling

Like the torsional vibration problem, all analyses on the effects of backlash, along with any associated controller development, require an accurate mathematical description of backlash in the system. The appropriate representation of backlash in a system model is very dependent on the actual configuration of the mechanical transmission elements surrounding the backlash. However, the common approaches to backlash modelling are generally defined in terms of a two-body system. Figure 2.2 illustrates the motor-transmission-load system of Figure 2.1, with the addition of a backlash element in the transmission shaft. If this is treated as a 'traditional' two-body system, the transmission shaft is considered to have an inertia of zero, along with torsional stiffness $K_s$ and an inherent internal damping coefficient of $C_s$.

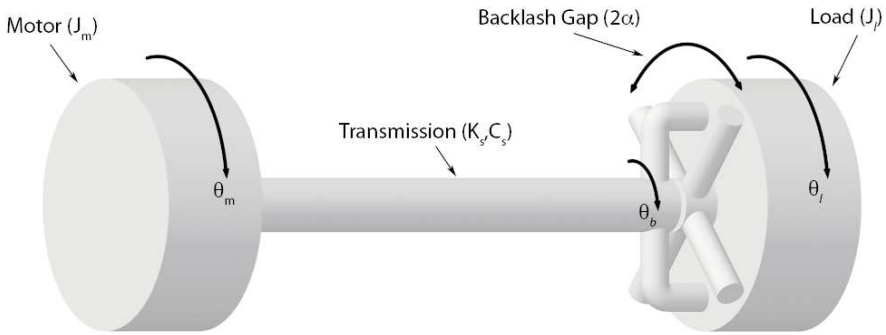


Figure 2.2: Transmission Backlash

With reference to Figure 2.2:

- $\theta_m$ is the absolute position of the motor inertia ($J_m$),
- $\theta_l$ is the absolute position of the load inertia ($J_l$) and
- $\theta_b$ is the absolute position of the transmission shaft at the backlash.

Defining $\theta_{BL}$ as the backlash angle: $\theta_{BL}(t) = \theta_b(t) - \theta_l(t)$. Also, since the backlash angle is usually defined symmetrically within the backlash gap, a total backlash gap of $2\alpha$ results in: $|\theta_{BL}| \leq \alpha$. If the shaft flex is then defined as $\theta_s(t) = \theta_m(t) - \theta_b(t)$, the overall displacement between motor and load ($\theta_d(t) = \theta_m(t) - \theta_l(t)$) is equivalent to the addition of the shaft flex ($\theta_s$) and the backlash angle ($\theta_{BL}$).

Recall that Equations (2.7) and (2.8) are the equations of motion for the two-body model of the system shown in Figure 2.1. In these equations, the transmission torque (the torque delivered to the load) is given by $K_s(\theta_m - \theta_l) + C_s(\dot{\theta}_m - \dot{\theta}_l)$. If backlash is included in this system (as shown in Figure 2.2), the transmission torque becomes:

$$T_{trans} = K_s(\theta_s) + C_s(\dot{\theta}_s) = K_s(\theta_d - \theta_{BL}) + C_s(\dot{\theta}_d - \dot{\theta}_{BL}) \tag{2.11}$$

Equation (2.11) is the exact expression for the transmission torque of the two-body system with backlash, shown in Figure 2.2. The difficulty with Equation (2.11) is that it contains a third degree of freedom, represented by $\theta_b$. The relationship between $\theta_b$ and the load position ($\theta_l$) is expressed by the backlash angle ($\theta_{BL}$), which saturates at $\pm\alpha$. Due to

obvious difficulties in dealing with a third degree of freedom in a two-body model, the most common backlash models are approximate models that do not include the coordinate $\theta_b$.

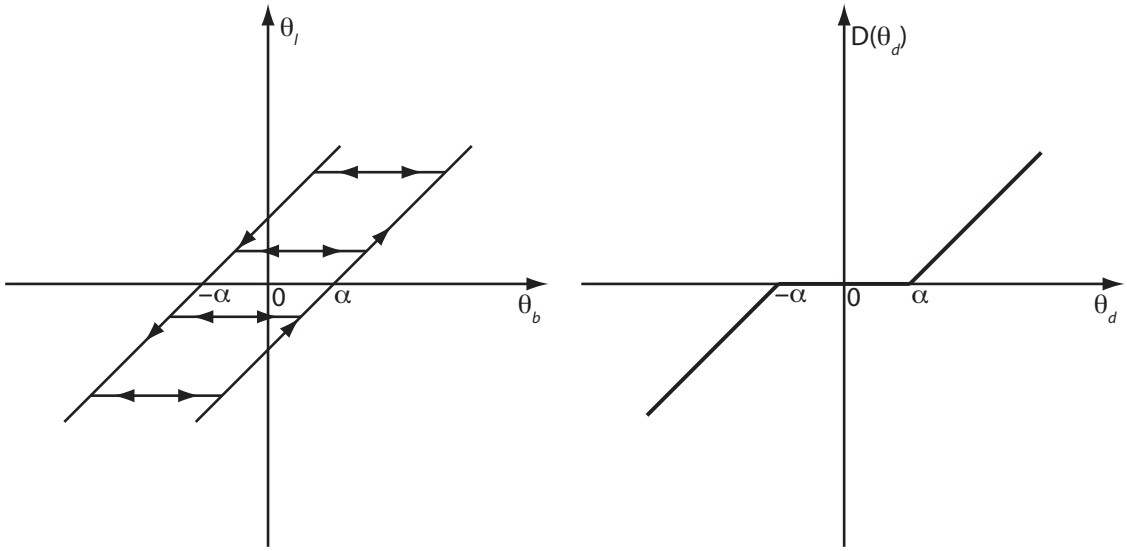


(a) Hysteresis Model (b) Dead Zone Model

Figure 2.3: Common Backlash Models

In introductory control texts, a hysteresis model is often used as the basic method for describing the effects of backlash [61, 62, 63]. This modelling approach can be described with reference to Figure 2.3 (a). Consider initially that the input and output positions at the backlash are zero ($\theta_b$ is the input position at the backlash and $\theta_l$ is the output position). If the transmission shaft begins to move in a positive direction, contact is not established with the load until $\theta_b = \alpha$. While there is continual positive contact, the load position is $\theta_l = \theta_b - \alpha$. If contact is lost (through a reversal of direction) the output is no longer driven by the input and output position is no longer a function of the input. If the reversal of direction continues, contact is not established again until the backlash gap is traversed. If continual contact is established in the negative direction, the load position becomes $\theta_l = \theta_b + \alpha$. The two diagonal lines of Figure 2.3 (a), describe the relationships between input and output positions during the two contact phases. The horizontal lines of Figure 2.3 (a), illustrate the uncontrolled state of output position during the non-contact phase.

The problem with the hysteresis model is that it only describes the relationship between the input and output positions of a backlash element. It is clear, from the fundamental

laws of dynamics, that the effect of backlash on transmission torque is the most important element when modelling backlash. Unfortunately, the hysteresis model does not account for the fact that the transmission torque is zero during the non-contact phase. For this reason, the hysteresis model can only be applied to either the input or output positions of a system (depending on the location of the backlash) and cannot be included in an expression for transmission torque. Although the hysteresis model has been used by some researchers [64, 65, 66, 67, 68], it is clear that this model does not effectively represent the complete dynamics of backlash.

A common and more accurate alternative to the hysteresis model is to use a dead zone in the expression for transmission torque. The input to this dead zone is the overall displacement between motor and load ($\theta_d$) and the output ($D(\theta_d)$) represents the actual shaft flex ($\theta_s$). An example of this common dead zone model can be seen in Figure 2.3 (b), where the output of the dead zone is:

$$D(\theta_d) = \begin{cases} \theta_d - \alpha & \theta_d > \alpha \\ 0 & |\theta_d| < \alpha \\ \theta_d + \alpha & \theta_d < -\alpha \end{cases} \tag{2.12}$$

The transmission torque for the dead zone model is:

$$T_{trans} = K_s D(\theta_d) \tag{2.13}$$

When comparing Equations (2.12) and (2.13) with Equation (2.11), it can be seen that the dead zone model accurately describes the torque component due to transmission flexing; however, the torque component due to damping in the transmission is neglected. Hence, this dead zone model is only valid when the internal damping coefficient ($C_s$) of the transmission is zero. A slight modification of the dead zone model is shown in Equation (2.14), where internal damping is taken into account. Together, the standard and modified dead zone models represent the most common modelling approach found in the literature

on backlash control [45, 54, 69, 70, 71, 72, 73, 74].

$$T_{trans} = \begin{cases} K_s(\theta_d - \alpha) + C_s\dot{\theta}_d & \theta_d > \alpha \\ 0 & |\theta_d| < \alpha \\ K_s(\theta_d + \alpha) + C_s\dot{\theta}_d & \theta_d < -\alpha \end{cases} \tag{2.14}$$

Although the modified dead zone model of Equation (2.14) does take internal damping into account, Nordin [40] has shown (through a phase plane analysis) that this model does not accurately predict when contact is lost. Hence, the modified dead zone model remains inaccurate if the internal damping of the transmission is significant and can actually predict a sign change in the transmission torque without the backlash gap being traversed. As an alternative, Nordin presents a phase plane backlash model that is intended to provide a much more accurate prediction of when contact is established and lost. The Nordin phase plane model is represented by Equations (2.15) to (2.18) [40]. When the internal damping of the transmission is zero, this model reduces to the form of the standard dead zone model.

$$T_{trans} = \begin{cases} K_s(\theta_d - \alpha) + C_s\dot{\theta}_d & (\theta_d, \dot{\theta}_d) \in A^+ \\ 0 & (\theta_d, \dot{\theta}_d) \in A^0 \\ K_s(\theta_d + \alpha) + C_s\dot{\theta}_d & (\theta_d, \dot{\theta}_d) \in A^- \end{cases} \tag{2.15}$$

where:

$$A^+ = (\theta_d, \dot{\theta}_d) : \begin{cases} (\theta_d + \alpha) + (\frac{C_s\dot{\theta}_d}{K_s})e^{\left(-\frac{K_s(\theta_d+\alpha)}{C_s\dot{\theta}_d}-1\right)} \geq 2\alpha & \dot{\theta}_d > 0 \\ K_s(\theta_d - \alpha) + C_s\dot{\theta}_d \geq 0 & \forall\dot{\theta}_d \end{cases} \tag{2.16}$$

$$A^- = (\theta_d, \dot{\theta}_d) : \begin{cases} (\theta_d - \alpha) + (\frac{C_s\dot{\theta}_d}{K_s})e^{\left(-\frac{K_s(\theta_d-\alpha)}{C_s\dot{\theta}_d}-1\right)} \leq -2\alpha & \dot{\theta}_d < 0 \\ K_s(\theta_d + \alpha) + C_s\dot{\theta}_d \leq 0 & \forall\dot{\theta}_d \end{cases} \tag{2.17}$$

$$A^0 = (\theta_d, \dot{\theta}_d) \backslash (A^+ \cup A^-) \tag{2.18}$$

In this thesis, the physical implications of the phase plane analysis presented in [40] are investigated. As a result, a new backlash model is presented that is shown to appropriately address the shortcomings of the common dead zone model through a very clear and simple

extension of the dead zone model.

### 2.4.3 Control of Backlash

Since researchers have been studying backlash for over 60 years, many different approaches to controlling servo systems in the presence of backlash have been investigated and published. With a very high number of publications, it is difficult to provide an exhaustive literature survey on this topic. For this reason, the literature survey presented in this thesis is specifically aimed at identifying all of the major, and essentially unique, contributions to the advancement of backlash control. The fundamental differences between the large number of published approaches are highlighted, with the approaches classified according to these differences. Since many of the published control approaches are both theoretically and mathematically complex, this survey also addresses the practical issues of implementing backlash controllers in real servo systems.

The traditional methods for reducing limit cycles and associated vibrations in systems with backlash involve reducing the bandwidth of standard linear controllers. Generally, a linear approximation of the backlash non-linearity is determined and then used in the linear design process to avoid limit cycles. The most common technique used to find a linear approximation of a non-linearity is the describing function technique, which was developed independently in England, Russia, Germany, France and the United States during the late 1940s and early 1950s [75]. Describing functions that specifically represent the backlash non-linearity were developed by Tustin [76], Chestnut [77] and Thomas [78]. Some examples of using describing functions in the design of linear controllers for systems with backlash can be found in [57, 58, 61, 65, 79]. Although the describing function technique is by far the most common, other more rigorous methods based on absolute stability criteria have also been used to describe backlash in linear controller designs [68, 80].

Linear approximation methods, such as describing functions, have also been used in the

design of more complex backlash controllers. Brandenburg et al [81] used describing functions to show that the limit cycle amplitude in systems with backlash can depend on the size of the load disturbance torque. Hence, a linear controller that incorporated a load torque observer was shown to reduce limit cycles in such systems. Brandenburg also claimed further improvements in limit cycle avoidance through the application of adaptive control on the disturbance model gains [45]. Nordin [40, 82] used dual-input describing functions and the QFT design technique to develop a switched non-linear controller for systems with backlash. Nordin's controller switched between two linear controllers, one tuned optimally for the contact phase and another with reduced gains for the backlash phase. Boneh and Yaniv [70] also used the concept of a switched non-linear controller, with the backlash phase controller designed via the QFT technique with an upper bound placed on the limit cycle amplitude.

All of the approaches discussed so far, whether linear or non-linear, are based upon the concept of reducing the speed at which the system traverses the backlash gap. The main reason for doing this is to limit the severity of any collisions that may result when the backlash gap closes. This group of approaches is sometimes referred to as having 'weak' action in the backlash gap [40]. An alternative group of approaches use 'strong' action in the backlash gap. These approaches are based upon the concept of increasing the speed at which the system traverses the backlash gap, so that regular contact between the motor and load is resumed as quickly as possible. While the weak action control approaches are predominately concerned with the dynamic stability of the system, the strong action approaches are more concerned with lost motion at the load.

The work of Tao et al [62, 67, 69, 83, 84, 85, 86, 87] is the most prominent in the area of strong action backlash controllers. Tao's early publications in this area [62, 67, 83, 84] focused on backlash at either the input or output of a system, and involved the use of an adaptive inverse controller to effectively cancel the backlash. The adaptive approach theoretically allows for the control of systems with unknown backlash gap and unknown plant parameters. Although adaptive inverse controllers were successfully simulated by

Tao, there are serious practical issues in implementing these controllers. Firstly, backlash is rarely located at the input or output of practical dynamic systems, with the transmission between the motor and load the most common source of backlash. Secondly, inverse compensation at the input of a system implies that the backlash gap will be traversed instantaneously, which is not possible. In [88], Dean et al implemented an inverse controller on a practical system and actually found that the inverse controller degraded the system performance when compared with a traditional linear controller.

In more recent publications by Tao [69, 85, 86, 87] switched non-linear controllers are proposed, which use traditional linear controllers during the contact phase and controllers based on optimal open-loop compensation laws during the backlash phase. Each of these controllers could again be classified as using a strong action during the backlash phase. Although the switched controllers address some of the drawbacks of the inverse control approach, the control laws applied during the backlash phase are mathematically complex and only simulation results could be found in the available publications.

Other approaches that can be classified as using a strong action during the backlash phase include controllers proposed by Yang et al. [89], Mata-Jiménez et al. [90] and Schöling et al. [91]. Yang used an adaptive switched nonlinear controller. The control objective in Yang's approach was to traverse the backlash gap as quickly as possible, although the importance of "unacceptable collisions" was noted. Good tracking performance was claimed by Yang through simulation; however, no practical results were given. Mata-Jiménez proposed a constant-impulsive hybrid control structure, where appropriately timed impulses were used during the backlash phase. The work by Mata-Jiménez was essentially theoretical and the controller required position and velocity feedback from both sides of the backlash, which limits the practical value of this approach. Schöling used a state feedback approach with input-output linearisation. The controller proposed by Schöling showed good dynamic behaviour and steady-state accuracy for a particular experimental set-up. However, feedback from all of the states, or alternative estimation methods, are required with this approach, which may also limit its practical application on many machine tools.

A lot of the more recent research in controlling backlash has concentrated on artificial intelligence methods such as fuzzy logic and neural networks. The use of fuzzy logic has generally been in the area of controlling systems with input or output backlash [92, 93]. With the fuzzy logic approach, an inverse controller is not required; however, the problem that backlash is rarely located at the input or output of a dynamic system still remains. The neural network approaches generally complement traditional linear control structures, with the neural networks used in the application of strong action during the backlash phase [94, 95]; however, neural networks have also been used to complement inverse controllers [66]. As noted in Section 2.2.2, one of the major difficulties with both neural networks and fuzzy logic is the additional computational power required by these methods. Although there is potential in these approaches, the additional computational requirements would still be excessive for many practical servo systems.

The many different approaches to controlling backlash can be classified in a number of different ways. Some of the important classifications include linear or non-linear, weak or strong action in the backlash phase, classical/modern or artificially intelligent based, feedback sensed from motor or load (or both) and velocity or position controlled. However, the most important classification is whether the controller is designed to provide good tracking performance or to guarantee dynamic stability (or both). In [40] Nordin claims that strong action in the backlash phase does not work very well and that weak action is more advantageous. However, Nordin was looking at the problem from the perspective of dynamic stability, where weak action is indeed advantageous. In most of the papers where strong action is proposed, good tracking performance is the main design specification. One of the claimed advantages in implementing weak action approaches is that the width of the backlash gap does not need to be known. However, if feedback from the load is not available and the design specifications require good position tracking, it is essential that the backlash gap is known. The main issue with many of the strong action approaches is that they are not practical to implement on real servo systems, either because of unrealistic system modelling or a requirement for excessive computational power.

A new approach to controlling backlash that combines both weak and strong action is proposed in this thesis. Through this approach both dynamic stability and tracking performance is addressed. Further, the proposed controller is designed for practical implementation on standard servo drives, requiring feedback from the motor side only and minimal computational power.

## 2.5 Conclusions

The literature review presented in this chapter has covered three performance limiting factors that are known to affect linear feed axes in machine tools: i) dynamic stiffness, ii) torsional vibrations and iii) backlash. Although some of these factors have attracted research attention for more than 50 years, areas for further study were clearly identified throughout the literature review.

Dynamic stiffness was described in Section 2.2 as a measure of the sensitivity of a system to disturbances at all frequencies. In machine tool feed axes, low dynamic stiffness has become a more prominent issue with the increasingly widespread use of linear motors. The literature review indicated that research effort in improving dynamic stiffness has been applied at all levels of the overall machine tool control system, including the current, flux linkage, velocity, position and path-planning levels. However, with access to the lower current and flux levels limited in standard servo drives, the velocity and position loop levels were identified as the most practical for implementing control strategies designed to improve dynamic stiffness.

Various robust techniques applied at the velocity and position loop levels, such as $H_\infty$ and sliding mode control, were found throughout the review to provide improved dynamic stiffness. One robust technique that was absent from the available literature was Quantitative Feedback Theory. In this thesis the theoretical aspects of dynamic stiffness are studied, with a method for including dynamic stiffness in a QFT design process pre-

sented. The advantages of using a QFT approach to designing velocity and position loops for improved dynamic stiffness are also examined.

Literature relevant to the analysis and control of torsional vibrations was reviewed in Section 2.3. It was found that this particular performance limitation had received considerable research attention over the past 50 years. Although most of the reviewed literature acknowledged the importance of treating motor-load couplings as non-rigid, the impact of other drive train components was often neglected in the analyses presented. Also, the standard model used by researchers was found to be an approximate two-body model. It was shown that this 'traditional' two-body model had a major limitation in that the inertia of the motor-load coupling device is considered negligible. In contrast, the coupling inertia in practical machine tool drive trains can actually be quite significant and, for some drive configurations, can also vary with the load position.

Although many different approaches to controlling torsional vibrations have been published, particularly since the 1980s, these approaches were found to fall into three fundamental categories: 1. Conventional Control, 2. Higher order control with feedback from both the motor and load, and 3. Higher order control with a single feedback device (usually attached to the motor). It was also found that existing comparisons between these control approaches were very limited and had not been performed over a wide range of motor-transmission-load conditions. In this thesis a thorough analysis of torsional vibrations in machine tool feed drives is presented, along with a comprehensive comparison of the various approaches to controlling torsional vibrations. This comparison includes control approaches that were developed as a part of this thesis. Limitations in the modelling of machine tool drive trains are also addressed in this thesis, with a new two-body model that takes the inertia of the motor-load coupling device into account developed.

In Section 2.4, improved mechanical design was identified as the most common technique for reducing the effects of backlash. However, it was also found that a large amount of research into more cost-effective control solutions had taken place over the past 60 years. The different control solutions identified throughout the literature review can be classified

as providing either ‘weak’ or ‘strong’ action during the backlash phase. It was generally found that the control solutions with a strong action were difficult to implement practically, due to either requiring excessive computational power or being based on unrealistic system modelling. One important issue that was also identified as being overlooked by many researchers, is the fact that weak and strong control actions address different system design specifications. While weak control action can only address the problem of dynamic stability, strong control action is used to improve the tracking performance of systems with backlash.

The most common models for representing backlash in a system were found to be the hysteresis model and the dead zone model. It was shown that both of these models had significant shortcomings in accurately describing backlash in real systems. The hysteresis model can only describe the relationship between the input and output positions of a backlash element and not the transmission torque. While the dead zone model does describe the transmission torque, it is only accurate when the inherent damping of the transmission is zero. In this thesis a very clear and simple extension to the dead zone model is presented and shown to appropriately address the shortcomings of these common backlash models. Further to this modelling contribution, a new approach to controlling backlash that combines both weak and strong action is presented. This control approach is shown, through both simulation and experimental application, to effectively address both the dynamic stability problems and the tracking performance of systems with backlash.

The interaction between dynamic stiffness, torsional vibrations and backlash is also addressed in this thesis, with the final control solutions for each of these factors shown to be affected by the others.

Chapter 3

# Modelling of Machine Tool Drive Trains

## 3.1 Introduction

In general, there are two classes of mathematical model that can be used to describe a non-rigid machine tool drive train: lumped parameter (discrete) and distributed-parameter (continuous) models. Discrete models consist of a discrete number of masses and springs, where the masses are assumed to be rigid and the springs assumed to be flexible but massless. The number of masses in a system coincides with the number of degrees of freedom of the system. In a continuous model there is both mass and stiffness at each point and these are distributed over the entire system. The interior points of such a system define a domain (D), while the points on the exterior of D define the boundary (S). Since there are an infinite number of points in D, a continuous system can be regarded as having an infinite number of degrees of freedom [96].

One commonly used approach for the modelling of dynamical systems is the Lagrangian approach. The Lagrangian approach holds true across different coordinate systems and provides a systematic method for handling a broad class of physical systems, regardless of their complexity [97]. Lagrange's equations can be derived from any one of a number of formulations of the fundamental laws of dynamics and although they are most commonly used for discrete system modelling, Lagrange's equations can also be extended to

continuous systems [96, 98].

$$\begin{aligned} \frac{d}{dt}\left[\frac{\partial \mathrm{L}}{\partial \dot{q}_r}\right] - \frac{\partial \mathrm{L}}{\partial q_r} &= \mathrm{F}q_r \\ \text{where: } \mathrm{L} &= \mathrm{T}-\mathrm{V} \end{aligned} \tag{3.1}$$

Equation (3.1) is the standard form of Lagrange's equation for discrete systems. In Equation (3.1), $q_r$ represents a generalised coordinate and L represents the Lagrangian. The Lagrangian is a function of all the generalised coordinates and generalised velocities of the system and is equivalent to the difference between the total kinetic energy (T) and the total potential energy (V) of the system. An *n*-degree-of-freedom discrete system contains *n* generalised coordinates. Lagrange's equation must be applied for each of these coordinates, resulting in *n* ordinary differential equations of motion that completely describe the system.

As would be expected, the mathematical formalism for continuous systems is different from that of discrete systems. Where the motion of an *n*-degree-of-freedom discrete system is described by *n* ordinary differential equations, the motion of continuous systems is governed by boundary-value problems consisting of partial differential equations to be satisfied over D and appropriate boundary conditions to be satisfied at every point of S [96]. When using the Lagrangian approach for continuous systems, the partial differential equations to be satisfied over D are formulated through application of Lagrange's differential equation of motion (Equation (3.2)).

$$\frac{\partial \hat{\mathrm{L}}}{\partial q} - \frac{\partial}{\partial x}\left(\frac{\partial \hat{\mathrm{L}}}{\partial q'}\right) + \frac{\partial^2}{\partial x^2}\left(\frac{\partial \hat{\mathrm{L}}}{\partial q''}\right) - \frac{\partial}{\partial t}\left(\frac{\partial \hat{\mathrm{L}}}{\partial \dot{q}}\right) + \frac{\partial^2}{\partial x \partial t}\left(\frac{\partial \hat{\mathrm{L}}}{\partial \dot{q}'}\right) + \mathrm{F}_q = 0 \tag{3.2}$$

In Equation (3.2), $q$ represents a generalised coordinate and $\hat{\mathrm{L}}$ represents the Lagrangian Density. The generalised coordinate $(q)$ in a distributed system is a function of both the spatial variable $(x)$ and time $(t)$. As such, the equations of motion for a continuous system consist of partial-derivatives with respect to both $x$ and $t$. In Equation (3.2), derivatives with respect to $x$ are denoted by primes ($q'$) and derivatives with respect to $t$ by over-

dots ($\dot{q}$). As with the discrete case, the Lagrangian in a continuous system is equivalent to the difference between the total kinetic energy and total potential energy. However, the Lagrangian for distributed systems consists of both boundary Lagrangians and the Lagrangian density.

As discussed in Section 1.4.1, the major elements of machine tool feed axes are most accurately described by continuous models. However, while there has been a great deal of recent research on the topics of simulation and controller design for continuous systems, these solutions are still regarded as complex and would not be the most appropriate for the systems considered in this thesis. In fact, in terms of accurately predicting the performance of most machine tool feed axes, it is generally only the total system inertia and the lower natural frequencies that are of practical concern (along with any nonlinearities such as friction and backlash). For this reason, a two-body model would generally be an acceptable approximation for many systems, as long as the model accounted for all significant inertias and provided an accurate estimate of the lowest natural frequency of the system. The problem with the traditional models used by servo system designers is that they often do not meet either of these criteria.

In this chapter, the Lagrangian approach has been used to develop models for linear feed axes based on each of the four mechanical transmission mechanisms introduced in Chapter 1. Using the basic motor-transmission-load system as a starting point (Figure 2.1), various discrete models have been derived and then compared with the continuous model of the system. As a result of these comparisons, a new approximate two-body model has been defined, which provides far greater accuracy over a wide range of realistic motor-transmission-load conditions than the 'traditional' two-body model. In addition to the development of the new approximate two-body model, this chapter also discusses the impact of friction and damping in machine tool feed axes along with addressing the non-linear modelling of backlash. The modelling approaches presented have also been extended to provide accurate models for each of the four mechanical transmission mechanisms under consideration. The final models take into account all significant system inertias and

lowest natural frequencies, along with friction, damping and backlash.

In Section 3.2 the continuous model and various discrete models for a simple motor-transmission-load system are derived. The discrete models are then compared with the continuous model, with the most accurate approximate models identified and the most appropriate model for controller design defined.

Section 3.3 discusses the impact of damping, friction and other torque disturbances on the system and the best ways of taking these factors into account in any system modelling and simulation.

A new backlash model is defined in Section 3.4. This new backlash model addresses the shortcomings of the common dead zone model and is shown to be easily incorporated into the approximate two-body models discussed in Section 3.2.

In Section 3.5 the basic approximate model, including any backlash, damping, friction and disturbance considerations, is extended to provide accurate approximate models of the four most common mechanical transmissions currently used in linear machine tool feed axes. Sections 3.5.1, 3.5.2, 3.5.3 and 3.5.4 detail the extended models for direct driven ballscrew, belt driven ballscrew, rack and pinion and linear motor driven systems respectively.

Finally, Section 3.6 summarises the key points and conclusions that can be drawn from this chapter.

## 3.2 Basic Motor-Transmission-Load Models

### 3.2.1 Initial System Models

Recall the simple motor-transmission-load system illustrated in Figure 2.1 and described in Section 2.3. This simple system is used to develop the basic system models and forms

the basis for all of the extended modelling presented in this chapter. The equations of motion for the 'traditional' two-body model of this system are given in Section 2.3 (Equations (2.7) and (2.8)). If damping is considered negligible, these equations become:

$$\mathrm{J}_m\ddot{\theta}_m = \mathrm{T}_m - \mathrm{K}_s(\theta_m - \theta_l) \tag{3.3}$$

$$\mathrm{J}_l\ddot{\theta}_l = \mathrm{K}_s(\theta_m - \theta_l) \tag{3.4}$$

Figure 3.1 illustrates the system of Figure 2.1, with the transmission shaft split into 4 equal sections. If the transmission shaft is uniform, each of the 4 sections have identical inertia ($J_{s1} = J_{s2} = J_{s3} = J_{s4} = \frac{J_s}{4}$).

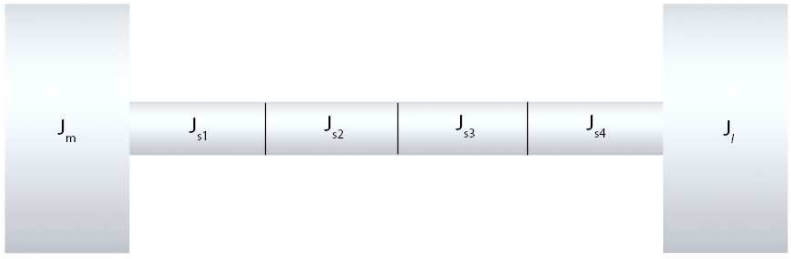


Figure 3.1: Motor-Load System with a Multi-Inertia Transmission Shaft

For analysis, consider the shaft inertias to be lumped at the centre of each section (as indicated in Figure 3.1) and that all of the inertias in the system are coupled by inertia-less flexible elements. This system is described by six generalised coordinates, $\theta_m$, $\theta_{s1}$, $\theta_{s2}$, $\theta_{s3}$, $\theta_{s4}$ and $\theta_l$, where $\theta_{sn}$ is the absolute angular position of shaft inertia $\mathrm{J}_{sn}$. The Lagrangian of this system is formulated as follows:

$$\begin{aligned}
\mathrm{L} &= \mathrm{T} - \mathrm{V} \\
&= \frac{1}{2}\mathrm{J}_m\dot{\theta}_m^2 + \frac{1}{2}\frac{\mathrm{J}_s}{4}\dot{\theta}_{s1}^2 + \frac{1}{2}\frac{\mathrm{J}_s}{4}\dot{\theta}_{s2}^2 + \frac{1}{2}\frac{\mathrm{J}_s}{4}\dot{\theta}_{s3}^2 + \frac{1}{2}\frac{\mathrm{J}_s}{4}\dot{\theta}_{s4}^2 + \frac{1}{2}\mathrm{J}_l\dot{\theta}_l^2 \\
&\quad -4\mathrm{K}_s(\theta_m - \theta_{s1})^2 - 2\mathrm{K}_s(\theta_{s1} - \theta_{s2})^2 - 2\mathrm{K}_s(\theta_{s2} - \theta_{s3})^2 \\
&\quad -2\mathrm{K}_s(\theta_{s3} - \theta_{s4})^2 - 4\mathrm{K}_s(\theta_{s4} - \theta_l)^2
\end{aligned}$$

Applying Lagrange's Equation (Equation (3.1)), with $q_r = \theta_{s1}$:

$$\begin{aligned}
\frac{\partial \mathrm{L}}{\partial \dot{\theta}_{s1}} &= \frac{\mathrm{J}_s}{4}\dot{\theta}_{s1} \\
\frac{d}{dt}\left[\frac{\partial \mathrm{L}}{\partial \dot{\theta}_{s1}}\right] &= \frac{\mathrm{J}_s}{4}\ddot{\theta}_{s1} \\
\frac{\partial \mathrm{L}}{\partial \theta_{s1}} &= 8\mathrm{K}_s(\theta_m - \theta_{s1}) - 4\mathrm{K}_s(\theta_{s1} - \theta_{s2}) \\
\mathrm{F}_{\theta_{s1}} &= 0
\end{aligned}$$

thus:

$$\begin{aligned}
\frac{\mathrm{J}_s}{4}\ddot{\theta}_{s1} - 8\mathrm{K}_s(\theta_m - \theta_{s1}) + 4\mathrm{K}_s(\theta_{s1} - \theta_{s2}) &= 0 \\
\Rightarrow \mathrm{J}_s\ddot{\theta}_{s1} &= 32\mathrm{K}_s(\theta_m - \theta_{s1}) - 16\mathrm{K}_s(\theta_{s1} - \theta_{s2})
\end{aligned}$$

Through a similar application of Lagrange's Equation to the other 5 generalised coordinates, the dynamics of this 'multi-body' system can be completely described by six equations of motion:

$$\mathrm{J}_m\ddot{\theta}_m = \mathrm{T}_m - 8\mathrm{K}_s(\theta_m - \theta_{s1}) \tag{3.5}$$

$$\mathrm{J}_s\ddot{\theta}_{s1} = 32\mathrm{K}_s(\theta_m - \theta_{s1}) - 16\mathrm{K}_s(\theta_{s1} - \theta_{s2}) \tag{3.6}$$

$$\mathrm{J}_s\ddot{\theta}_{s2} = 16\mathrm{K}_s(\theta_{s1} - \theta_{s2}) - 16\mathrm{K}_s(\theta_{s2} - \theta_{s3}) \tag{3.7}$$

$$\mathrm{J}_s\ddot{\theta}_{s3} = 16\mathrm{K}_s(\theta_{s2} - \theta_{s3}) - 16\mathrm{K}_s(\theta_{s3} - \theta_{s4}) \tag{3.8}$$

$$\mathrm{J}_s\ddot{\theta}_{s4} = 16\mathrm{K}_s(\theta_{s3} - \theta_{s4}) - 32\mathrm{K}_s(\theta_{s4} - \theta_l) \tag{3.9}$$

$$\mathrm{J}_l\ddot{\theta}_l = 8\mathrm{K}_s(\theta_{s4} - \theta_l) \tag{3.10}$$

The equations of motion represented by Equations (3.5) to (3.10) can be generalised for similar systems with the transmission shaft split into *n* sections:

$$\begin{aligned}
\mathrm{J}_m\ddot{\theta}_m &= \mathrm{T}_m - 2n\mathrm{K}_s(\theta_m - \theta_{s1}) \\
\mathrm{J}_s\ddot{\theta}_{s1} &= 2n^2\mathrm{K}_s(\theta_m - \theta_{s1}) - n^2\mathrm{K}_s(\theta_{s1} - \theta_{s2}) \\
\mathrm{J}_s\ddot{\theta}_{s2} &= n^2\mathrm{K}(\theta_{s1} - \theta_{s2}) - n^2\mathrm{K}_s(\theta_{s2} - \theta_{s3}) \\
&\vdots \\
J_s\ddot{\theta}_{sn} &= n^2\mathrm{K}_s(\theta_{s(n-1)} - \theta_{sn}) - 2n^2\mathrm{K}_s(\theta_{sn} - \theta_l) \\
\mathrm{J}_l\ddot{\theta}_l &= 2n\mathrm{K}_s(\theta_{sn} - \theta_l)
\end{aligned}$$

For an $n$-sectioned transmission shaft, there are $n+2$ equations of motion and the inertia of each section is $\frac{J_s}{n}$. A more detailed derivation of the six equations of motion for the 4-sectioned transmission shaft of Figure 3.1 is given in Appendix B.

---

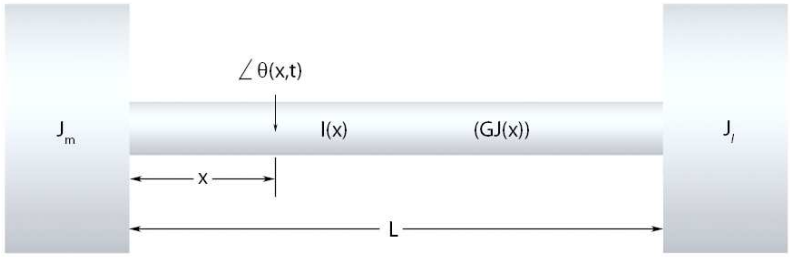


Figure 3.2: Motor-Load System with a Distributed Inertia Transmission Shaft

Consider once more the simple motor-transmission-load system of Figure 2.1. In order to derive a continuous model of this system, the transmission shaft must be treated with distributed inertia (as shown in Figure 3.2). In Figure 3.2, the shaft flex ($\theta$) is a function of both the position ($x$) along the length of the shaft and time ($t$). The inertia and torsional stiffness of the shaft are also functions of $x$, with I($x$) being the mass moment of inertia density and GJ($x$) the product of the shear modulus (G) and the area polar moment of inertia of the cross section J($x$). It should also be noted that L in Figure 3.2 is the overall length of the transmission shaft.

If $L_0$ and $L_L$ are the boundary Lagrangians at $x$=0 and $x$=L respectively, the Lagrangian of the continuous system is:

$$\begin{aligned} L &= L_0 + L_L + \int_0^L \hat{L}\,dx \\ &\text{where} \\ L_0 &= T_0 - V_0 \\ &= \frac{1}{2} J_m \dot{\theta}^2(0,t) \\ L_L &= T_L - V_L \\ &= \frac{1}{2} J_l \dot{\theta}^2(L,t) \\ \hat{L} &= \hat{T} - \hat{V} \end{aligned}$$

$$= \quad \frac{1}{2}\mathrm{I}(x)\dot{\theta}^2(x,t) - \frac{1}{2}\mathrm{GJ}(x)\theta'^2(x,t)$$

thus

$$\mathrm{L} \quad = \quad \frac{1}{2}\mathrm{J}_m\dot{\theta}^2(0,t) + \frac{1}{2}\mathrm{J}_l\dot{\theta}^2(\mathrm{L},t) + \frac{1}{2}\int_0^{\mathrm{L}} \left(\mathrm{I}(x)\dot{\theta}^2(x,t) - \mathrm{GJ}(x)\theta'^2(x,t)\right) dx$$

Applying Lagrange's equation for distributed systems (Equation (3.2)), with $q = \theta$:

$$\begin{aligned}
\frac{\partial \hat{\mathrm{L}}}{\partial \theta} &= 0 \\
\frac{\partial \hat{\mathrm{L}}}{\partial \theta'} &= -\mathrm{GJ}(x)\theta'(x,t) \\
\frac{\partial}{\partial x}\left(\frac{\partial \hat{\mathrm{L}}}{\partial \theta'}\right) &= -\frac{\partial}{\partial x}\left(\mathrm{GJ}(x)\theta'(x,t)\right) \\
\frac{\partial \hat{\mathrm{L}}}{\partial \theta''} &= 0 \\
\frac{\partial^2}{\partial x^2}\left(\frac{\partial \hat{\mathrm{L}}}{\partial \theta''}\right) &= 0 \\
\frac{\partial \hat{\mathrm{L}}}{\partial \dot{\theta}} &= \mathrm{I}(x)\dot{\theta}(x,t) \\
\frac{\partial}{\partial t}\left(\frac{\partial \hat{\mathrm{L}}}{\partial \dot{\theta}}\right) &= \mathrm{I}(x)\ddot{\theta}(x,t) \\
\frac{\partial \hat{\mathrm{L}}}{\partial \dot{\theta}'} &= 0 \\
\frac{\partial^2}{\partial x \partial t}\left(\frac{\partial \hat{\mathrm{L}}}{\partial \dot{\theta}'}\right) &= 0
\end{aligned}$$

thus:

$$\frac{\partial}{\partial x}\left(\mathrm{GJ}(x)\theta'(x,t)\right) - \mathrm{I}(x)\ddot{\theta}(x,t) + \mathrm{F}_\theta = 0 \tag{3.11}$$

(where $\mathrm{F}_\theta$ is a distributed Torque)

The Boundary Conditions at *x*=0 and *x*=L are:

$$\mathrm{GJ}(x)\theta'(0,t) = \mathrm{J}_m\ddot{\theta}(0,t) \tag{3.12}$$

$$\mathrm{GJ}(x)\theta'(\mathrm{L},t) = -\mathrm{J}_l\ddot{\theta}(\mathrm{L},t) \tag{3.13}$$

Equation (3.11) is the partial differential equation of motion for the continuous model of the system shown in Figure 2.1. Equations (3.12) and (3.13) are the boundary conditions at x=0 and x=L respectively. Equations (3.11), (3.12) and (3.13) together represent the

boundary value problem for the continuous model of the system shown in Figure 2.1.

### 3.2.2 Natural Frequencies of Oscillation

When considering a simple motor-transmission-load system, the total system inertia and lowest natural frequencies are two of the highest practical concerns for control system designers. Hence, any approximate model should take into account all significant system inertias and give an accurate prediction of the lowest natural frequency of the system. Although the 'traditional' two-body model does not take the transmission inertia into account, it is a fairly trivial task to slightly modify the model and include any significant transmission inertia. Such modifications however, will affect the natural frequency of the model. For this reason, the accuracy of the natural frequency of any approximate model can be considered to be one of the most important qualities of the model.

The first step in analysing the accuracy of any approximate model is to compare the natural frequencies of the approximate model with that of the continuous model. In order to determine the natural frequencies of the continuous model, the boundary-value problem represented by Equations (3.11), (3.12) and (3.13) must be solved. The solution of such a boundary-value problem requires the solution of an associated differential eigenvalue problem consisting of an infinite set of eigenvalues and eigenfunctions. However, the eigenvalue problem of the continuous model must first be derived before it can be solved.

To derive the eigenvalue problem, first let the distributed torque $F_\theta$ in Equation (3.11) equal zero – so that the transmission shaft is in free vibration:

$$\frac{\partial}{\partial x}\left(\mathrm{GJ}(x)\theta'(x,t)\right) = \mathrm{I}(x)\ddot{\theta}(x,t),\ 0 < x < \mathrm{L} \tag{3.14}$$

Hence, the free vibration of the transmission shaft is described by Equation (3.14) and the boundary conditions of Equations (3.12) and (3.13). If a solution in the form of Equation (3.15) is assumed, Equations (3.15), (3.16) and (3.17) can be substituted into Equations

(3.11), (3.12) and (3.13) to determine the characteristic equation of the continuous model.

$$\theta(x,t) = \Theta(x)\mathrm{F}(t) \tag{3.15}$$

where $\mathrm{F}(t)$ satisfies:

$$\ddot{\mathrm{F}}(t) = -\lambda \mathrm{F}(t) \tag{3.16}$$

$$\text{and: } \lambda = \omega^2 \ (\omega \text{ is the frequency of oscillation})$$

$$= \beta^2 \frac{\mathrm{GJ}}{\mathrm{I}} \tag{3.17}$$

Equation (3.18) is the resulting characteristic equation of the continuous model and must be solved numerically for $\beta$. A complete mathematical description of the boundary value problem and the derived solution is given in Appendix B.

$$\tan\beta\mathrm{L} + \frac{\beta\,(\mathrm{J}_m + \mathrm{J}_l)}{\mathrm{I} - \frac{\beta^2 \mathrm{J}_m \mathrm{J}_l}{\mathrm{I}}} = 0 \tag{3.18}$$

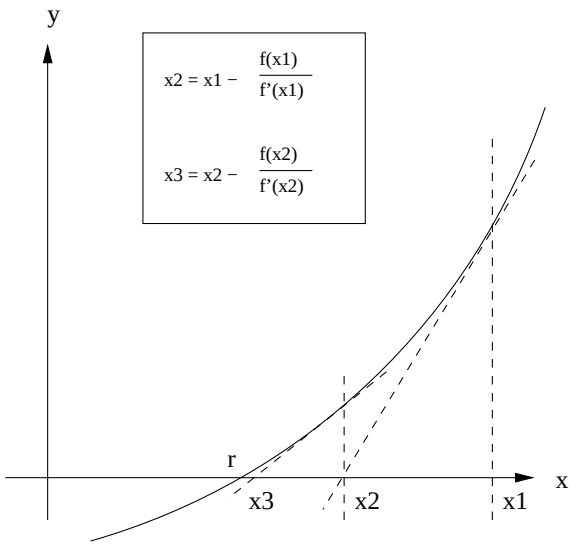


Figure 3.3: Illustration of the Newton-Raphson Numerical Method

One common numerical method that can be used to find values of $\beta$ is the 'Newton-Raphson' method. The underlying principle of the 'Newton-Raphson' method is that tangent lines can be used to approximate the graph of a function f($x$). For instance, if $r$ is a root of $\mathrm{f}(x) = 0$ and $x_1$ is an initial approximation of $r$, the x-intercept ($x_2$) of the tangent line $\mathrm{f}'(x_1)$ is a closer approximation of $r$ (as shown in Figure 3.3). Similarly, the x-

intercept of the tangent line $f'(x_2)$ is an even closer approximation of $r$. The continuation of this process generates successive approximations, which converge at $r$ itself.

As there are an infinite number of roots to Equation (3.18), an initial approximation of the root corresponding to the lowest natural frequency ($\beta_1$) can best be chosen through an inspection of the graph of Equation (3.18). Once an accurate approximation of $\beta_1$ is determined, the lowest natural frequency of the continuous model can be calculated using Equation (3.17).

For approximate models, the number of natural frequencies is dependent on the number of bodies in the system. One of the most common methods used to determine the natural frequencies of such discrete systems is an approximate method due to Holzer. This method is based on the fact that an undamped vibrational system requires no external torque to vibrate at a natural frequency. For a multiple-body system, such as the 4 body system of Figure 3.1, an approximate two-body model can be used to make an initial estimate of the lowest natural frequency. Holzer's method would then involve an assumption that the system is oscillating at the estimated frequency and that the load end of the system has an angular amplitude of 1 radian. Since the torque necessary to vibrate the load has to come from the inertial body that is immediately to the left of the load (referring to Figure 3.1), the value of the torque and the angular amplitude of this inertial body can be calculated. This process would then be repeated for each body of the system, until the input torque of the motor is determined. If the input torque of the motor is zero, the estimated frequency is a natural frequency. If the torque is non-zero, the value of the torque can be used to make a more refined estimate of the natural frequency and the process repeated until an acceptably accurate estimation is determined. For a more thorough description of Holzer's method the reader is referred to [99].

A particular case of discrete model is the simple two-body model, which has two degrees of freedom and only one natural frequency. Although Holzer's method is still valid for the two-body model, the simplicity of the model allows for an exact determination of the natural frequency. One way of determining the exact natural frequency of a two-body

model is to determine the transfer function of the system with transmission flex ($\theta_s$) as output and equate this with the standard form of a second order transfer function. This method of equating the system flex transfer function with the standard second order form was used when determining the natural frequencies of all of the two-body approximate models presented in Section 3.2.3, while Holzer's method was used for all of the higher order multiple-body models.

### 3.2.3 A Comparison of Approximate Models

As the continuous model is considered to be the 'benchmark' in terms of accuracy, the lowest natural frequencies of various approximate models (of the simple motor-transmission-load system of Figure 2.1) have been compared in terms of their percentage error from that of the lowest natural frequency of the continuous model. This comparison has been performed over a wide range of realistic motor-transmission-load conditions, with a total of 11 approximate models considered. Of these 11 approximate models, 4 are multiple-body models, while the remaining 7 represent different possible variations of distributing the transmission shaft inertia between the motor and load sides of a two-body model. The natural frequencies for the continuous model and all of the approximate models were determined using the methods outlined in Section 3.2.2. The mathematics package 'Matlab' was used to automate the numerical methods and calculate the various natural frequencies. The Matlab functions developed for this task are given in Appendix C.

The first four models considered are multiple-body models (as described in Section 3.2.1):

1. A 'multiple body' model with the transmission shaft split into 4 equal sections.
2. A 'multiple body' model with the transmission shaft split into 8 equal sections.
3. A 'multiple body' model with the transmission shaft split into 16 equal sections.
4. A multiple-body model with the transmission shaft split into 100 equal sections.

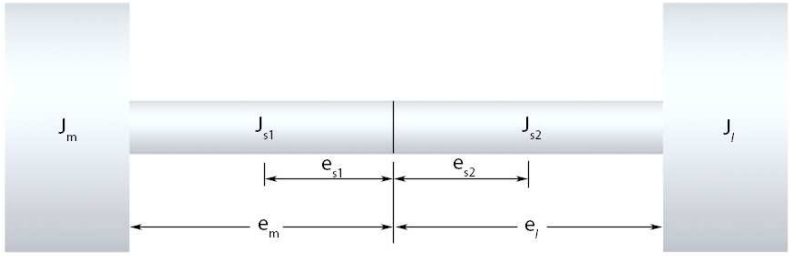


Figure 3.4: Inertias and Compliance of Simple Motor-Transmission-Load System

Each of the seven two-body models considered can be described in terms of Figure 3.4. In this figure the simple motor-transmission-load system is shown with a line indicating the centre of the transmission shaft. The transmission shaft has been split into two equal sections with half of the shaft inertia 'lumped' mid-way between the centre of the transmission shaft and the motor. The other half of the shaft inertia is 'lumped' mid-way between the centre of the transmission shaft and the load. For each of the four inertias shown in Figure 3.4, $e_x$ represents the compliance between the particular inertia and the centre of the transmission shaft.

The two-body models considered are:

1. The 'traditional' two-body model. The inertia on the motor side is $J_m$ and the inertia on the load side is $J_l$. The transmission shaft is considered to have zero inertia ($J_{s1} = J_{s2} = 0$). The compliance between motor and load inertias is $e_m + e_l$.

2. Two-body model with transmission inertia equally distributed between the motor and load. The inertia on the motor side is $J_M = J_m + J_{s1}$, while the inertia on the load side is $J_L = J_l + J_{s2}$ and the compliance between the motor and load side inertias is $e_m + e_l$.

3. Two-body model with transmission inertia lumped at the motor. The inertia on the motor side is $J_M = J_m + J_{s1} + J_{s2}$, the inertia on the load side is $J_l$ and the compliance between the motor and load side inertias is $e_m + e_l$.

4. Two-body model with transmission inertia lumped at the load. The inertia on the motor side is $J_m$, the inertia on the load side is $J_L = J_l + J_{s1} + J_{s2}$ and the compliance between the motor and load side inertias is $e_m + e_l$.

5. Two-body model with transmission inertia lumped at both the motor and load, but distributed so that original motor-load inertia ratio is retained. The inertias on the motor and load sides respectively are:

$$J_M = J_m \left(1 + \frac{J_{s1} + J_{s2}}{J_m + J_l}\right) \text{ and } J_L = J_l \left(1 + \frac{J_{s1} + J_{s2}}{J_m + J_l}\right)$$

   The compliance between motor and load side inertias is $e_m + e_l$.

6. Two-body model with transmission inertia equally distributed between the motor and load sides. In this model however, the total inertia of the motor side is lumped at an effective position along the transmission shaft based on the relative sizes of the motor and motor-side transmission inertias. The compliance between the new position of the motor-side inertia and the centre of the transmission shaft is described by:

$$e_M = \frac{e_m J_m + e_{s1} J_{s1}}{J_m + J_{s1}}.$$

   Similarly, the total inertia of the load side is lumped at an effective position along the transmission shaft based on the relative sizes of the load and load-side transmission inertias. The compliance between the new position of the load-side inertia and the centre of the transmission shaft is described by:

$$e_L = \frac{e_l J_l + e_{s2} J_{s2}}{J_l + J_{s2}}.$$

   Thus, the resulting inertia on the motor side is $J_M = J_m + J_{s1}$, the resulting inertia on the load side is $J_L = J_l + J_{s2}$ and the compliance between the motor and load side inertias is $e_M + e_L$.

7. Two-body model with transmission inertia distributed so that original motor-load

inertia ratio is retained. However, like model 6, the total motor and load side inertias are lumped at effective positions along the transmission shaft based on the relative sizes of the inertias involved. The compliance between the new position of the motor-side inertia and the centre of the transmission shaft is described by:

$$e_M = \frac{e_m J_m + e_{S1} J_{S1}}{J_m + J_{S1}} \text{ where, } J_{S1} = \frac{J_m (J_{s1} + J_{s2})}{J_m + J_l}$$

The compliance between the new position of the load-side inertia and the centre of the transmission shaft is described by:

$$e_L = \frac{e_l J_l + e_{S2} J_{S2}}{J_l + J_2} \text{ where, } J_{S2} = \frac{J_l (J_{s1} + J_{s2})}{J_m + J_l}$$

The resulting inertias on the motor and load sides respectively are:

$$J_M = J_m \left(1 + \frac{J_{s1} + J_{s2}}{J_m + J_l}\right) \text{ and } J_L = J_l \left(1 + \frac{J_{s1} + J_{s2}}{J_m + J_l}\right)$$

The compliance between motor and load side inertias is $e_M + e_L$.

A total of 6 different transmission elements have been included in this comparison, with the load:motor inertia ratio varied between 3 different values (0.05,1,12) for each transmission element. The particular transmission elements included in this comparison were chosen to illustrate extremes in possible drive-train configurations. The first 2 were chosen to represent both a very flexible transmission and a quite stiff transmission. The last 4 were chosen to represent realistic ballscrew configurations that are commonly used in machine tool feed drives. It is important to realise that low load:motor inertia ratios are often likely in ballscrew configurations due to the inherent gearing of the ballscrew. It should also be noted that with torsional stiffness of ballscrews being variable, the cases considered in this comparison are the most demanding as they all assume the lowest possible torsional stiffness for each individual configuration (ie these comparisons are valid for cases where the position of the load along each ballscrew is furthest away from the motor).

The chosen transmissions are:

- A long thin transmission shaft (6mm diameter, 0.5m length),
- A shorter and thicker transmission shaft (20mm diameter, 0.1m length),
- A 16mm diameter ballscrew, 1m in length,
- A 25mm diameter ballscrew, 1m in length,
- A 25mm diameter ballscrew, 3m in length and
- A 50mm diameter ballscrew, 3m in length.

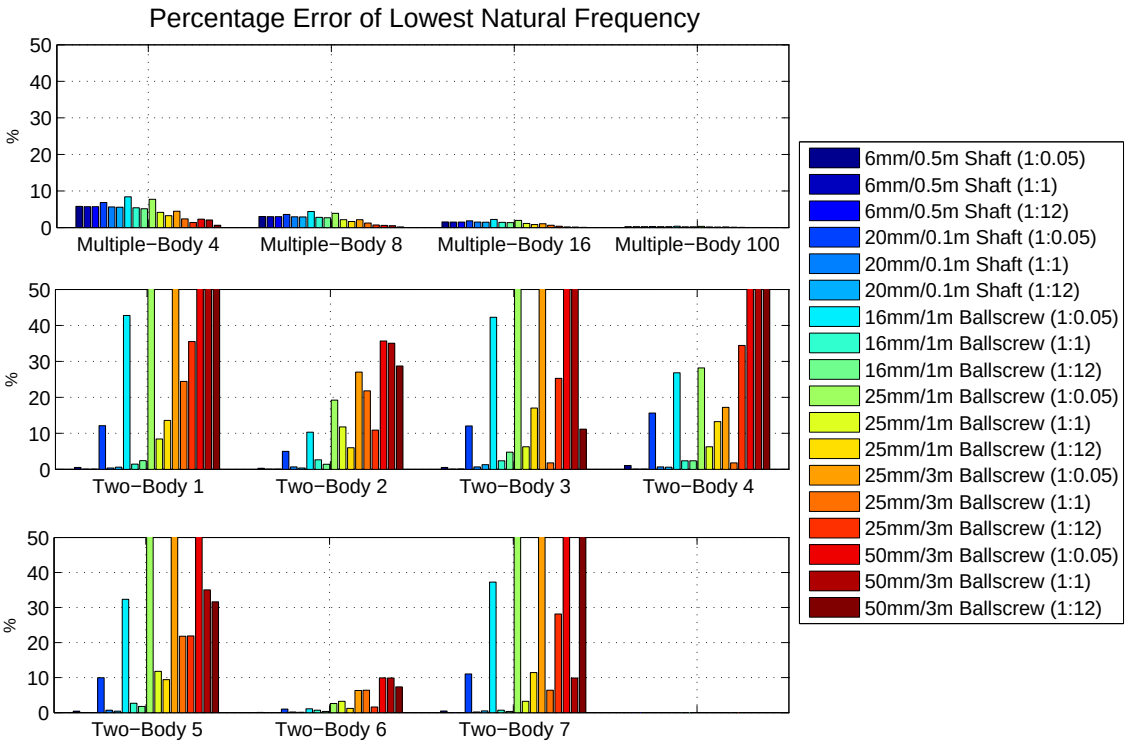


Figure 3.5: Model Comparison

The results of the approximate model comparison are shown in Figure 3.5. In this figure the percentage error of the lowest natural frequency, for each motor-transmission-load condition, has been graphed for each of the approximate models. The continuous model has been used as the benchmark when calculating the percentage errors. Although the percentage errors for some cases were much greater than 50%, the vertical (y) axis in Figure 3.5 was limited to 50% to allow for an easy comparison between the models.

From the results shown in Figure 3.5, it can be seen that the multiple-body models show a consistent improvement in accuracy with the increased number of sections used (as expected). However, it was not until the number of sections was increased to 100 that a percentage error of less than 1% was achieved under all motor-transmission-load conditions. Of course, an approximate model with over 100 sections can be as difficult for control system designers as the continuous model itself.

The 'traditional' two-body model (Two-Body 1) showed high accuracy when the inertia of the transmission element was very small, while the accuracy reduced as the inertia of the transmission element became more significant. In fact, each of the two-body models showed reduced accuracy as the inertia of the transmission element became more significant, particularly in the important ballscrew cases where the load inertia was relatively small. In some cases the percentage errors were much more than the axis limit of 50%, with errors of up to an order of magnitude higher recorded.

In general, it can be seen that 'Two-Body 2' and 'Two-Body 6' were the most accurate two-body models over the entire range of motor-transmission-load conditions. In particular, 'Two-Body 6' was the only two-body model that had a percentage error of less than 10% under all motor-transmission-load conditions. Also, 'Two-Body 6' was the only model that had percentage errors less than that of the 'traditional' two-body model under all conditions (including all of the multiple-body models). When further comparing 'Two-Body 6' with the multiple-body models, it was found that under some conditions 'Two-Body 6' was more accurate than all of the multiple-body models. However, like the other two-body models, this accuracy reduced as the inertia of the transmission element became more significant.

For control system designers, the overall modelling goal is to minimise complexity while still accurately accounting for any significant inertias and resonances in the system. From the results presented in Figure 3.5, it can be seen that a well constructed two-body model is the most appropriate choice in meeting this goal. If the transmission element has a very low inertia (such as a belt), the traditional 'two-body' model with an inertia-less

transmission is a simple and appropriate choice. However, if the transmission element has significant inertia (such as many ballscrew cases), an alternative two-body model that takes the inertia of the transmission element into account will always provide a better representation of the total system inertia. The choice of where to 'lump' the transmission inertia though, has a very significant influence on the accuracy of the natural frequency estimates. The most accurate two-body model in terms of accounting for both significant inertias and resonances in the system, was found to be 'Two-Body 6'. This model equally distributes the transmission inertia between the motor and load sides and uses an adjusted system compliance based on the relative sizes of all inertial bodies. This model is a much more accurate standard for modelling than the 'traditional' two-body model and can be used for developing more complicated system models. Throughout the remainder of this thesis, 'Two-Body 6' is referred to as the 'adjusted' two-body model. The equations of motion for the 'adjusted' two-body model are given by Equations (3.19) and (3.20).

$$\begin{aligned} \ddot{\theta}_m &= \frac{2\mathrm{T}_m}{2\mathrm{J}_m + \mathrm{J}_s} \\ &\quad - \left[\frac{4\mathrm{K}_s(2\mathrm{J}_l + \mathrm{J}_s)}{8\mathrm{J}_m\mathrm{J}_l + 3\mathrm{J}_s(\mathrm{J}_m + \mathrm{J}_l) + \mathrm{J}_s^2}\right](\theta_m - \theta_l) \end{aligned} \tag{3.19}$$

$$\ddot{\theta}_l = \left[\frac{4\mathrm{K}_s(2\mathrm{J}_m + \mathrm{J}_s)}{8\mathrm{J}_m\mathrm{J}_l + 3\mathrm{J}_s(\mathrm{J}_m + \mathrm{J}_l) + \mathrm{J}_s^2}\right](\theta_m - \theta_l) \tag{3.20}$$

## 3.3 Damping, Friction and General Torque Variations

The modelling presented in Section 3.2 assumed any friction and internal damping inherent in the transmission element to be negligible. In reality, all machine tool drive trains have internal damping in the transmission elements and quite significant friction. In general, the friction in a drive train is much more significant than any internal damping associated with the drive train materials. However, accurate friction models are very non-linear and make up a large independent area of academic study.

Since non-linear friction models are not the main topic of this thesis, only coulomb and

viscous frictions are considered as specific frictional terms in the standard system models. Internal damping of the transmission elements is also considered as a specific term in the standard models; however, all other losses are treated as general torque disturbances. If coulomb friction, viscous friction and internal damping of the transmission are included in the 'adjusted' two-body model, the equations of motion become:

$$\begin{aligned}\ddot{\theta}_m &= \frac{2T_m}{2J_m+J_s} \\ &\quad -\left[\frac{4K_s(2J_l+J_s)}{8J_mJ_l+3J_s(J_m+J_l)+J_s^2}\right](\theta_m-\theta_l) \\ &\quad -\frac{2C_s}{2J_m+J_s}\left(\dot{\theta}_m-\dot{\theta}_l\right)-\frac{2B_m}{2J_m+J_s}\dot{\theta}_m-\frac{2T_{fcm}}{2J_m+J_s} \end{aligned} \tag{3.21}$$

$$\begin{aligned}\ddot{\theta}_l &= \left[\frac{4K_s(2J_m+J_s)}{8J_mJ_l+3J_s(J_m+J_l)+J_s^2}\right](\theta_m-\theta_l) \\ &\quad +\frac{2C_s}{2J_l+J_s}\left(\dot{\theta}_m-\dot{\theta}_l\right)-\frac{2B_l}{2J_l+J_s}\dot{\theta}_l-\frac{2T_{fcl}}{2J_l+J_s} \end{aligned} \tag{3.22}$$

In Equations (3.21) and (3.22), $C_s$ is the internal damping coefficient of the transmission element, while $B_m$ and $B_l$ are the viscous friction coefficients and $T_{fcm}$ and $T_{fcl}$ are coulomb friction constants at the motor and load ends of the transmission respectively. Since friction, other than coulomb and viscous, and other torque (or force) disturbances are also very significant in most machine tool feed axes, a complete model should take these disturbances into account. Of particular significance are the cyclic rotational disturbances discussed in Section 2.1. It has been shown that many of these disturbances can be quantified through a study of periodic torque/force variations on a machine tool axis [100]. This useful information about a mechanical system can be obtained by recording drive torque (or force) as a function of position (not time). A Fast Fourier Transform (FFT) can be taken for torque/force values recorded at equally spaced position intervals, transforming the signal from the position domain to the 'position frequency domain'. The resulting 'position frequency' spectrum will normally have a relationship to various components in the machine tool drive train.

If $T_{pos}(\theta)$ is a general function for system torque disturbances and $\Omega_0$ is the fundamental angular position frequency (in cycles/revolution), the Fourier series describing $T_{pos}(\theta)$ is:

$$T_{pos}(\theta) = \frac{a_0}{2} + \sum_{n=1}^{\infty} a_n \cos(n\Omega_0\theta) + \sum_{n=1}^{\infty} b_n \sin(n\Omega_0\theta) = \sum_{n=-\infty}^{\infty} c_n e^{jn\Omega_0\theta} \tag{3.23}$$

Normally, the periodic torque/force data for an axis is recorded while the axis is running at a constant velocity. Hence, the DC component of the FFT is equivalent to the combination of coulomb and viscous frictions, while the remaining spectrum is associated with cyclic torque disturbances. Through the recording of periodic torque/force data at a number of different velocities, the viscous friction component can be determined and extracted from the combined DC friction value. This process of determining the position frequency spectrum of a machine tool axis is known as the study of Position Dependent Torque (or Force) Variations (PDTV and PDFV). For a complete treatment of PDTV and PDFV the reader is referred to [101].

Equations (3.24) and (3.25) represent the new equations of motion when the 'adjusted' two-body model is extended to include general periodic torque disturbances (as described by Equation (3.23)) at both the motor and load ends of the transmission.

$$\begin{aligned}
\ddot{\theta}_m &= \frac{2T_m}{2J_m + J_s} \\
&\quad - \left[\frac{4K_s(2J_l + J_s)}{8J_mJ_l + 3J_s(J_m + J_l) + J_s^2}\right](\theta_m - \theta_l) \\
&\quad - \frac{2C_s}{2J_m + J_s}\left(\dot{\theta}_m - \dot{\theta}_l\right) - \frac{2B_m}{2J_m + J_s}\dot{\theta}_m - \frac{2T_{fcm}}{2J_m + J_s} \\
&\quad - \frac{2}{2J_m + J_s}\sum_{n=-\infty}^{\infty} c_{nm} e^{jn\Omega_0\theta_m}
\end{aligned} \tag{3.24}$$

$$\begin{aligned}
\ddot{\theta}_l &= \left[\frac{4K_s(2J_m + J_s)}{8J_mJ_l + 3J_s(J_m + J_l) + J_s^2}\right](\theta_m - \theta_l) \\
&\quad + \frac{2C_s}{2J_l + J_s}\left(\dot{\theta}_m - \dot{\theta}_l\right) - \frac{2B_l}{2J_l + J_s}\dot{\theta}_l - \frac{2T_{fcl}}{2J_l + J_s} \\
&\quad - \frac{2}{2J_l + J_s}\sum_{n=-\infty}^{\infty} c_{nl} e^{jn\Omega_0\theta_l}
\end{aligned} \tag{3.25}$$

## 3.4 Backlash

In Section 2.4.2, several different methods for modelling backlash in a two-body system (as depicted by Figure 2.2) were discussed. Of these methods, the standard dead zone model was shown to provide an accurate representation of backlash when internal damping of the transmission element is negligible. However, when internal damping of the transmission element is significant, the dead zone model does not accurately predict loss of contact at the backlash element.

An alternative backlash model, for the two-body system depicted by Figure 2.2, was suggested by Nordin [40] to address the shortcomings of the dead zone model. The Nordin model is represented by Equations (2.15) to (2.18) and was developed using a phase plane analysis based on the exact expression for transmission torque in a two-body system with backlash (Equation 2.11). Nordin defines the case of '*right contact*' as being when $\theta_{BL} = \alpha$ and $\dot{\theta}_{BL} = 0$. Similarly, the case of '*left contact*' is defined as being when $\theta_{BL} = -\alpha$ and $\dot{\theta}_{BL} = 0$. These definitions, together with Equation (2.11) give:

$$\text{For } \textit{right contact}\text{: } \mathrm{T}_{trans} > 0 \Rightarrow \mathrm{T}_{trans} = \mathrm{K}_s(\theta_d - \alpha) + \mathrm{C}_s\dot{\theta}_d > 0 \tag{3.26}$$

$$\text{For } \textit{left contact}\text{: } \mathrm{T}_{trans} < 0 \Rightarrow \mathrm{T}_{trans} = \mathrm{K}_s(\theta_d + \alpha) + \mathrm{C}_s\dot{\theta}_d < 0 \tag{3.27}$$

The phase plane plot shown in Figure 3.6 (a) is claimed by Nordin to be an exact representation of the physical model of the system and is based on Equations (3.26) and (3.27). The areas in the phase plane plot of Figure 3.6 (a) are defined by Equations (3.28), (3.29) and (3.30) [40]. The borders separating each area of Figure 3.6 (a) have a gradient of -$K_s$/$C_s$. Hence, for the case where $C_s$ is zero, the phase plane plot of the physical model is equivalent to the phase plane plot of the dead zone model (shown in Figure 3.6 (b)).

$$A_+ = \{(\theta_d, \dot{\theta}_d) : \mathrm{K}_s\theta_d + \mathrm{C}_s\dot{\theta}_d \geq \mathrm{K}_s\alpha \tag{3.28}$$

$$A_r = \{(\theta_d, \dot{\theta}_d) : \left|\mathrm{K}_s\theta_d + \mathrm{C}_s\dot{\theta}_d\right| < \mathrm{K}_s\alpha \tag{3.29}$$

$$A_- = \{(\theta_d, \dot{\theta}_d) : \mathrm{K}_s\theta_d + \mathrm{C}_s\dot{\theta}_d \leq -\mathrm{K}_s\alpha \tag{3.30}$$

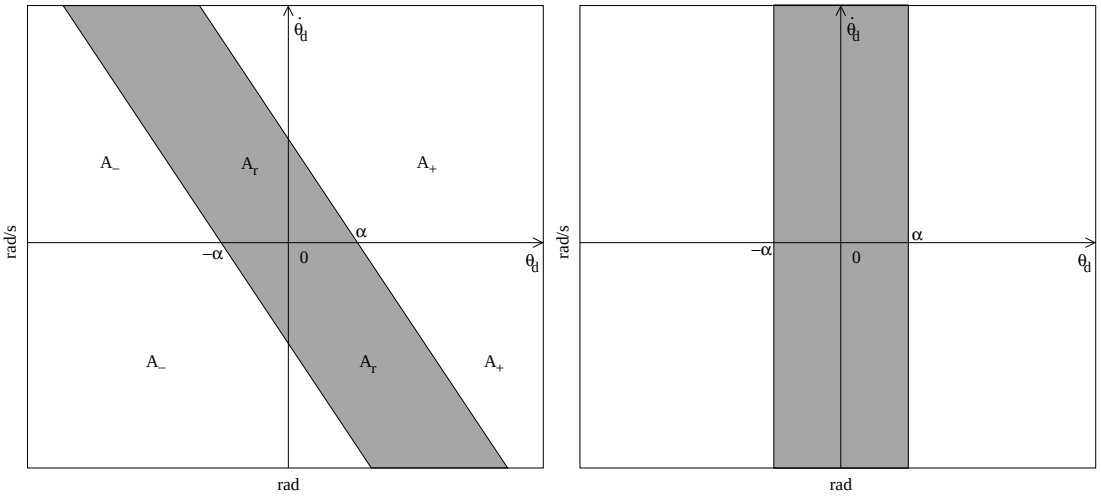


(a) Physical Model (b) Dead Zone Model

Figure 3.6: Phase Plane Plots [40]

With reference to the phase plane plot shown in Figure 3.6 (a), Nordin states that there can be persistent right contact only in $A_+$ and persistent left contact only in $A_-$. Also, when an initial state $(\theta_d, \dot{\theta}_d)$ lies within $A_+$ right contact will remain until the state $(\theta_d(t), \dot{\theta}_d(t))$ leaves $A_+$. Similarly, if an initial state $(\theta_d, \dot{\theta}_d)$ lies within $A_-$ left contact will remain until the state $(\theta_d(t), \dot{\theta}_d(t))$ leaves $A_-$. Hence, contact (either left or right) is only released when the state reaches the 'release set' $A_r$ [40].

One important issue relating to the phase plane plot of Figure 3.6 (a) is that it appears to be possible for a state to lie within the $A_+$ area when $\theta_d < \alpha$. Similarly, it appears to be possible for a state to lie within the $A_-$ area when $\theta_d > -\alpha$. The problem with these two situations relates to Equations (3.26) and (3.27), which this phase plane plot is based on. Recall from Section 2.4.2 that $\theta_d$ is equivalent to the addition of the shaft flex ($\theta_s$) and the backlash angle ($\theta_{BL}$). Equation (3.26) is only valid when $\theta_{BL} = \alpha$ and $\dot{\theta}_{BL} = 0$, so if a state lies within the $A_+$ area when $\theta_d < \alpha$: Equation (3.26) implies that $\theta_s$ has to be less than 0. However, it is not physically possible for the system to be in right contact when $\theta_s < 0$. Similarly, Equation (3.27) is only valid when $\theta_{BL} = -\alpha$ and $\dot{\theta}_{BL} = 0$, so if a state lies within the $A_-$ area when $\theta_d > -\alpha$: Equation (3.27) implies that $\theta_s$ has to be greater than 0. Again, it is not physically possible for the system to be in left contact when $\theta_s > 0$. The reality in both of these situations is that $\theta_{BL} \neq \pm\alpha$ and hence, Equations (3.26) and

(3.27) are not valid. For this reason the phase plane plot shown in Figure 3.6 (a) is not actually an exact representation of the physical model of the system.

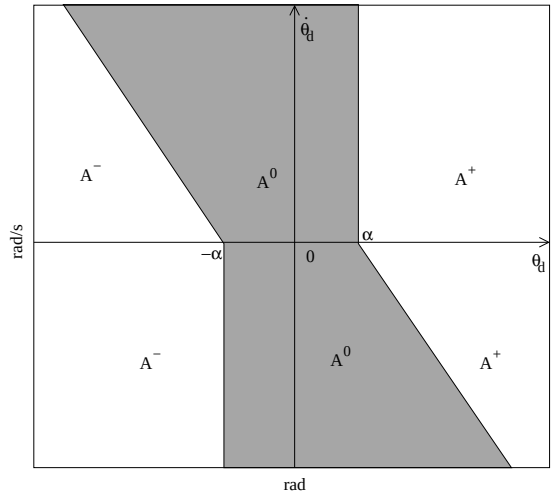


(a) Adjusted Backlash Model

Figure 3.7: Adjusted Phase Plane Plot

An adjusted phase plane plot that accounts for the physical limitations of Figure 3.6 (a) is shown in Figure 3.7. In this plot, the backlash element is defined to be in *right contact* whenever a state $(\theta_d, \dot{\theta}_d)$ lies within the $A^+$ area. Similarly, the backlash element is defined to be in *left contact* whenever a state $(\theta_d, \dot{\theta}_d)$ lies within the $A^-$ area. Hence, the backlash element is in non-contact whenever a state $(\theta_d, \dot{\theta}_d)$ lies within the $A^0$ area. This adjusted phase plane plot can also be used to describe a new backlash model that addresses the shortcomings of previous models, yet is a simple extension to the common dead zone model. The new backlash model is represented by Equations (3.31) to (3.34) and like the Nordin phase plane model, the new model reduces to the standard dead zone model when internal damping of the transmission is zero.

$$T_{trans} = \begin{cases} K_s(\theta_d - \alpha) + C_s\dot{\theta}_d & (\theta_d, \dot{\theta}_d) \in A^+ \\ 0 & (\theta_d, \dot{\theta}_d) \in A^0 \\ K_s(\theta_d + \alpha) + C_s\dot{\theta}_d & (\theta_d, \dot{\theta}_d) \in A^- \end{cases} \tag{3.31}$$

where:

$$A^+ \;=\; (\theta_d, \dot{\theta}_d) : \begin{cases} \theta_d > \alpha & \dot{\theta}_d \geq 0 \\ K_s(\theta_d - \alpha) + C_s\dot{\theta}_d \geq 0 & \dot{\theta}_d < 0 \end{cases} \tag{3.32}$$

$$A^- = (\theta_d, \dot{\theta}_d) : \begin{cases} \theta_d < -\alpha & \dot{\theta}_d \leq 0 \\ \mathrm{K}_s(\theta_d + \alpha) + \mathrm{C}_s\dot{\theta}_d \leq 0 & \dot{\theta}_d > 0 \end{cases} \tag{3.33}$$

$$A^0 = (\theta_d, \dot{\theta}_d) \backslash (A^+ \cup A^-) \tag{3.34}$$

Since Equations (3.31) to (3.34) represent backlash in a two-body system, this new backlash model can easily be included in an extension to the 'adjusted' two-body model (developed in Section 3.2). Equations (3.35) to (3.41) represent the new equations of motion when the 'adjusted' two-body model is extended to include both general periodic torque disturbances and backlash.

$$\ddot{\theta}_m = \frac{2}{2\mathrm{J}_m + \mathrm{J}_s}\left[\mathrm{T}_m - \mathrm{T}_{trans} - \mathrm{B}_m\dot{\theta}_m - \mathrm{T}_{fcm} - \sum_{n=-\infty}^{\infty} c_{nm} e^{jn\Omega_0\theta_m}\right] \tag{3.35}$$

$$\ddot{\theta}_l = \frac{2}{2\mathrm{J}_l + \mathrm{J}_s}\left[\mathrm{T}_{trans} - \mathrm{B}_l\dot{\theta}_l - \mathrm{T}_{fcl} - \sum_{n=-\infty}^{\infty} c_{nl} e^{jn\Omega_0\theta_l}\right] \tag{3.36}$$

where:

$$\mathrm{T}_{trans} = \begin{cases} \mathrm{K}_{Sadj}(\theta_d - \alpha) + \mathrm{C}_s\dot{\theta}_d & (\theta_d, \dot{\theta}_d) \in A^+ \\ 0 & (\theta_d, \dot{\theta}_d) \in A^0 \\ \mathrm{K}_{Sadj}(\theta_d + \alpha) + \mathrm{C}_s\dot{\theta}_d & (\theta_d, \dot{\theta}_d) \in A^- \end{cases} \tag{3.37}$$

and:

$$A^+ = (\theta_d, \dot{\theta}_d) : \begin{cases} \theta_d > \alpha & \dot{\theta}_d \geq 0 \\ \mathrm{K}_{Sadj}(\theta_d - \alpha) + \mathrm{C}_s\dot{\theta}_d \geq 0 & \dot{\theta}_d < 0 \end{cases} \tag{3.38}$$

$$A^- = (\theta_d, \dot{\theta}_d) : \begin{cases} \theta_d < -\alpha & \dot{\theta}_d \leq 0 \\ \mathrm{K}_{Sadj}(\theta_d + \alpha) + \mathrm{C}_s\dot{\theta}_d \leq 0 & \dot{\theta}_d > 0 \end{cases} \tag{3.39}$$

$$A^0 = (\theta_d, \dot{\theta}_d) \backslash (A^+ \cup A^-) \tag{3.40}$$

$$\mathrm{K}_{Sadj} = \frac{2\mathrm{K}_s(2\mathrm{J}_m + \mathrm{J}_s)(2\mathrm{J}_l + \mathrm{J}_s)}{8\mathrm{J}_m\mathrm{J}_l + 3\mathrm{J}_s(\mathrm{J}_m + \mathrm{J}_l) + \mathrm{J}_s^2} \tag{3.41}$$

## 3.5 Models for Common Drive Train Configurations

The simple motor-transmission-load systems shown in Figures 2.1 and 2.2, allow for concentrated analyses on the individual factors that are known to limit the performance of a machine tool axis. Although these systems are simplified, they do form the basis of many common drive train configurations. Similarly, the 'adjusted' two-body model, in both its standard and extended forms, can be used as a basic building block in developing accurate models for many drive configurations. In this section, accurate approximate models of the four most common drive train configurations currently used in linear machine tool feed axes are developed.

### 3.5.1 Direct Drive Ballscrew Axes

Consider a directly driven ballscrew as shown in Figure 3.8. This configuration consists of a rotary motor directly coupled to the ballscrew, producing linear motion at the load end. It is clear to see that this configuration is almost identical to the simple motor-transmission-load system with backlash (as shown in Figure 2.2). The ballscrew forms the transmission element and there is a source for possible backlash between the ballscrew and the ballscrew nut (attached to the load). With this system the load inertia is dependent on both the mass of the load and the gearing ratio of the ballscrew. Also, the torsional stiffness of the transmission ($K_s$) is now a function of the load position ($x$).

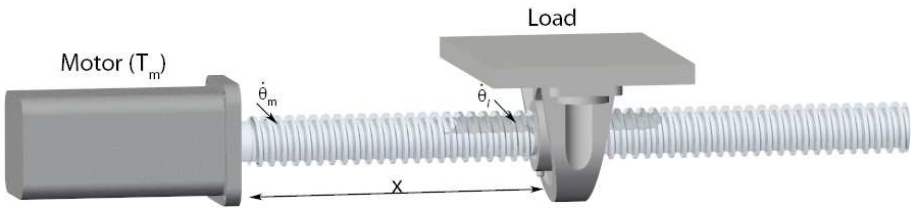


Figure 3.8: Dynamics of a Directly Driven Ballscrew

For the directly driven ballscrew system of Figure 3.8, let $L_{BS}$ be the overall length of the ballscrew, $J_{BS}$ the total inertia of the ballscrew, $K_{sBS}$ the torsional stiffness of the entire

ballscrew, $P_{BS}$ the pitch of the ballscrew and $M_L$ the mass of the load. If it is assumed that flexing of the ballscrew only occurs between the motor and load, the remaining ballscrew inertia can be lumped with the load. For the case where friction, general torque disturbances and backlash are considered negligible, the 'adjusted' two-body model represented by Equations (3.19) and (3.20) are valid with the following substitutions:

$$K_s = \frac{K_{sBS} L_{BS}}{x} \tag{3.42}$$

$$J_s = \frac{J_{BS} x}{L_{BS}} \tag{3.43}$$

$$\theta_l = \frac{2\pi}{P_{BS}} x \tag{3.44}$$

$$J_l = \left(\frac{P_{BS}}{2\pi}\right)^2 M_L + \left(\frac{J_{BS}(L_{BS} - x)}{L_{BS}}\right) \tag{3.45}$$

Since the torsional stiffness ($K_s$), the transmission inertia ($J_s$) and load inertia ($J_l$) are now functions of the load position, it is clear to see that, even with backlash considered negligible, this system is non-linear and the resonant frequencies will vary with the load position. This extended model, although non-linear, can be used to accurately simulate the system and the given substitutions provide all necessary information to predict the parameter variations likely to occur. Hence, this extended system model provides accurate information for developing a robust control solution.

Similarly, if friction, internal damping, general torque disturbances and backlash are considered to be significant, Equations (3.35) to (3.41) for the complete two-body model are valid with the same substitutions given by Equations (3.42) to (3.45). In this complete model any linear friction at the load needs to be translated into rotary terms and lumped with $B_l$ and $T_{fcl}$. The defined backlash gap of $\pm\alpha$ remains valid and refers to the angular displacement that is traversed by the ballscrew (in each direction) before coming into contact with the ballscrew nut.

### 3.5.2 Belt Driven Ballscrew Axes

The belt driven ballscrew is a slightly modified ballscrew configuration that consists of a rotary motor coupled to the ballscrew via a belt, as shown in Figure 3.9. This configuration is commonly used in machine tools as a space saving measure. While the characteristics of the ballscrew are the same as the directly driven model, flexing of the coupling between motor and ballscrew is now significant.

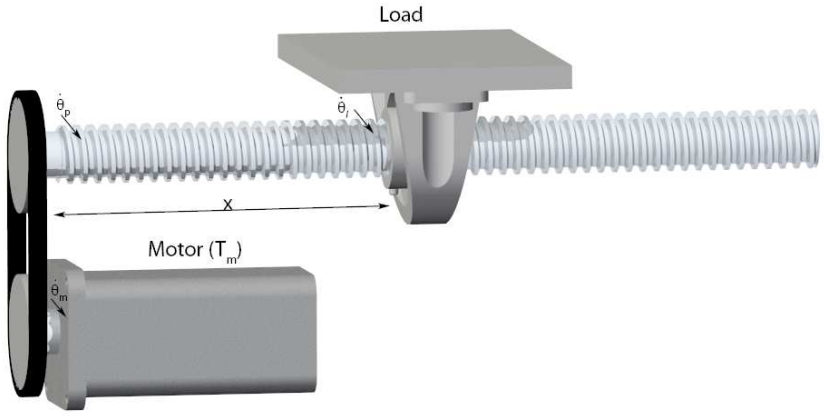


Figure 3.9: Dynamics of a Belt Driven Ballscrew

Since there are two non-rigid transmission elements in the system of Figure 3.9, three equations of motion are required. Although the flexing and internal damping of the belt are significant, the inertia of the belt can be considered negligible. Also, along with any backlash associated with the ballscrew, there are extra sources of possible backlash at both the motor and ballscrew ends of the belt. However, these two backlash sources (at each end of the belt) can be treated as a single backlash element and described by a single backlash gap. The complete equations of motion for the belt driven ballscrew system, including friction, internal damping, general torque disturbances and backlash, are:

$$\ddot{\theta}_m = \frac{1}{J_m}\left[T_m - R_m F_{blt} - B_m\dot{\theta}_m - T_{fcm} - \sum_{n=-\infty}^{\infty} c_{nm} e^{jn\Omega_0\theta_m}\right] \tag{3.46}$$

$$\ddot{\theta}_p = \frac{2}{2J_p + J_s}\left[R_p F_{blt} - T_{bs} - B_p\dot{\theta}_p - T_{fcp} - \sum_{n=-\infty}^{\infty} c_{np} e^{jn\Omega_0\theta_p}\right] \tag{3.47}$$

$$\ddot{\theta}_l = \frac{2}{2J_l + J_s}\left[T_{bs} - B_l\dot{\theta}_l - T_{fcl} - \sum_{n=-\infty}^{\infty} c_{nl} e^{jn\Omega_0\theta_l}\right] \tag{3.48}$$

where:

- $J_m$ is the combined inertia of the motor and the motor pulley,
- $J_p$ is the inertia of the pulley driving the ballscrew,
- $R_m$ is the radius of the motor pulley,
- $R_p$ is the radius of the pulley driving the ballscrew,
- $\theta_p$ is the absolute angular position of the pulley driving the ballscrew,
- $F_{blt}$ is the linear force transmitted through the belt and
- $T_{bs}$ is the torque transmitted through the ballscrew.

In Equations (3.46), (3.47) and (3.48), the values $J_s$, $\theta_l$ and $J_l$ are subject to the same substitutions as in the directly driven ballscrew case (described by Equations (3.43) to (3.45)). Also, the torque transmitted through the ballscrew ($T_{bs}$) is defined by Equations (3.37) to (3.41), where $T_{trans} = T_{bs}$, $\alpha = \alpha_{bs}$, $J_m = J_p$ and $K_s$ is subject to the substitution described by Equation (3.42). Power is transmitted linearly through the belt, with the belt stiffness coefficient ($K_{sblt}$) and internal damping coefficient ($C_{sblt}$) both defined in terms of linear force. Hence, if the backlash gap in the belt transmission ($\pm\alpha_{blt}$) refers to the angular displacement that is traversed by the motor (in each direction) before the belt comes into contact with the pulleys, the linear force transmitted through the belt can be described by:

$$F_{blt} = \begin{cases} K_{sblt}(x_d - x_\alpha) + C_{sblt}\dot{x}_d & (x_d, \dot{x}_d) \in A^+ \\ 0 & (x_d, \dot{x}_d) \in A^0 \\ K_{sblt}(x_d + x_\alpha) + C_{sblt}\dot{x}_d & (x_d, \dot{x}_d) \in A^- \end{cases} \tag{3.49}$$

and:

$$A^+ = (x_d, \dot{x}_d) : \begin{cases} x_d > x_\alpha & \dot{x}_d \geq 0 \\ K_{sblt}(x_d - x_\alpha) + C_{sblt}\dot{x}_d \geq 0 & \dot{x}_d < 0 \end{cases} \tag{3.50}$$

$$A^- = (x_d, \dot{x}_d) : \begin{cases} x_d < -x_\alpha & \dot{x}_d \leq 0 \\ K_{sblt}(x_d + x_\alpha) + C_{sblt}\dot{x}_d \leq 0 & \dot{x}_d > 0 \end{cases} \tag{3.51}$$

$$A^0 = (x_d, \dot{x}_d) \backslash (A^+ \cup A^-) \tag{3.52}$$

$$x_d = \mathrm{R}_m \theta_m - \mathrm{R}_p \theta_p \tag{3.53}$$

$$x_\alpha = \mathrm{R}_m \alpha_{blt} \tag{3.54}$$

### 3.5.3 Rack and Pinion Driven Axes

Consider the rack and pinion drive configuration shown in Figure 3.10. This configuration usually consists of a rotary motor directly coupled to the pinion, producing linear motion along the length of the rack. In this configuration torsional stiffness of the motor/pinion coupling is a constant. As such, it can easily be described in terms of Equations (3.35) to (3.41).

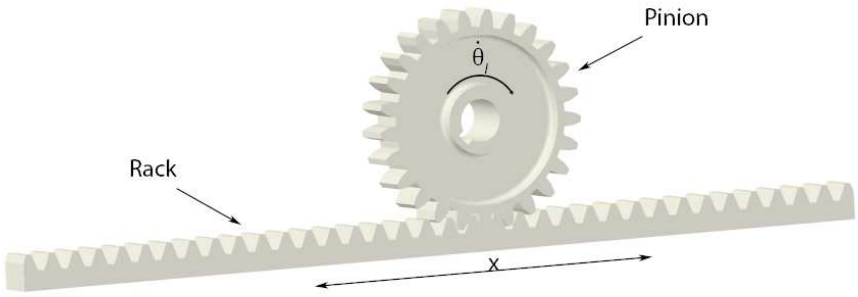


Figure 3.10: Dynamics of a Rack and Pinion

The most important point to note about this configuration is that the load inertia is dependent on both the load mass and the gearing ratio of the rack and pinion. For the system shown in Figure 3.10, let $x$ be the absolute linear position of the pinion on the rack, $r$ be the radius of the pinion, $\mathrm{J}_{PIN}$ be the inertia of the pinion and $\mathrm{M}_L$ be the mass of the load. Further, let the backlash gap ($\pm\alpha$) refer to the angular displacement that is traversed by the motor (in each direction) before the pinion comes into contact with the rack. Hence,

for this system Equations (3.35) to (3.41) are valid with the following substitutions:

$$\theta_l = \frac{x}{r} \tag{3.55}$$

$$\mathrm{J}_l = \mathrm{J}_{PIN} + \mathrm{M}_L r^2 \tag{3.56}$$

Unlike the two ballscrew configurations, it can be seen that the flexing of the rack and pinion can be described linearly if backlash is considered negligible. However, backlash is often very significant in rack and pinion drives.

### 3.5.4 Linear Motor Driven Axes

Finally, consider the linear motor configuration shown in Figure 3.11. Unlike all of the rotary motor driven configurations, the linear motor directly drives a linear machine tool feed axis and does not require a mechanical transmission mechanism. The moving part of the linear motor is always attached directly to the load and as such, the system can be appropriately described as having only one degree of freedom. This direct drive approach also eliminates any backlash in the system. For these reasons, the 'adjusted' two-body model and new backlash model developed throughout this chapter are not required to accurately describe the motion of a linear motor axis. However, friction and linear force variations are still significant.

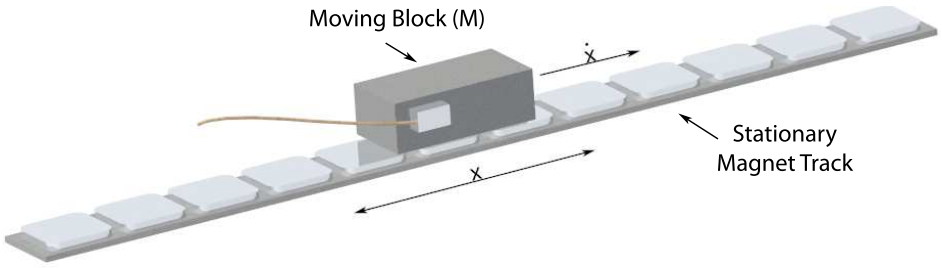


Figure 3.11: Dynamics of a Linear Motor Driven Axis

For the linear motor system of Figure 3.11, let $x$ be the absolute linear position of the motor and M be the combined mass of the motor and load. Hence, the equation of motion

for this system including friction and general periodic force variations is:

$$\ddot{x} = \frac{1}{\mathrm{M}}\left[\mathrm{F}_m - \mathrm{B}\dot{x} - \mathrm{F}_{fc} - \sum_{n=-\infty}^{\infty} c_n e^{jn\Omega_0 x}\right] \tag{3.57}$$

In Equation (3.57), $\mathrm{F}_{fc}$ represents the constant coulomb frictional force and $\Omega_0$ represents the fundamental position frequency. As with the rotary motor cases, the fundamental position frequency is expressed in cycles per revolution. However, for the linear motor one revolution is defined as the linear distance travelled during one electrical cycle of the motor.

## 3.6 Conclusions

Mathematical models for linear feed axes of machine tools were developed in this chapter. Initially, a model for a simple motor-transmission-load system was developed, with descriptions for friction, damping and backlash subsequently added to improve the accuracy of the model. The complete motor-transmission-load model was then extended to accurately describe the direct driven ballscrew, belt driven ballscrew, rack and pinion, and linear motor driven axis configurations.

In Section 3.2 the Lagrangian approach to modelling was used to determine both discrete and continuous models of a simple motor-transmission-load system. The lowest natural frequencies of 11 approximate discrete models were then compared with that of the continuous model of this system, over a wide range of motor-transmission-load conditions. It was found that the lowest natural frequency of the traditional two-body model, used by most researchers, had a percentage error (with reference to the continuous model) of greater than 50% under some common motor-transmission-load conditions. Although models with increased degrees of freedom were shown to improve the accuracy, it was found that approximately 100 degrees of freedom were required to achieve a percentage error of less than 1% over the entire range of motor-transmission-load conditions considered.

A total of 7 different two-body model configurations were included in the comparison presented in Section 3.2. In one of the two-body model configurations the inertia of the transmission element was equally distributed between the motor and load sides, with the system compliance adjusted with respect to the relative sizes of all inertial bodies. This particular configuration was found to achieve a percentage error of less than 10% over the entire range of motor-transmission-load conditions considered. The same configuration was also found to be more accurate than the traditional two-body model under all of the conditions considered, and even more accurate than all of the higher degree of freedom models under some of the conditions. Since the modelling goal from a control perspective is to minimise the complexity of the model, while accurately accounting for significant inertias and resonances in the system, this 'adjusted' two-body model was identified as the most appropriate choice for modelling a simple motor-transmission-load system.

The 'adjusted' two-body model was extended in Section 3.3 to include simple expressions for damping, coulomb friction, viscous friction and general torque disturbances. A Fourier series was used to describe the general torque disturbances in this extended model. Practical values for this Fourier series can be determined using the PDTV method, with the resulting position frequency spectrum representing torque variations in the system.

In Section 3.4 a new model for accurately representing backlash in a two-body system was developed. This new model was shown to provide a simple description of backlash, while addressing the shortcomings of previous backlash models. It was also shown that the 'adjusted' two-body model from Section 3.2 could be easily extended to include this improved description of backlash. This complete two-body model provides dual advantages over previous descriptions of systems with backlash, with an improved representation of the backlash element itself and a more accurate prediction of the resonant frequencies of the system. This dual advantage is quite significant as the changes in inertia experienced in a system with backlash can be a source of excitation for system resonances.

In Section 3.5, the complete approximate model for a simple motor-transmission-load system was used to develop new models for common machine tool drive configurations.

The drive configurations modelled in this section were the direct driven ballscrew, belt driven ballscrew, rack and pinion, and linear motor configurations. These complete drive train models take into account each of the factors described in this chapter, and are used throughout the remainder of this thesis to accurately model actual linear and rotary drive axes.

Chapter 4

# Experimental Equipment

## 4.1 Introduction

The control schemes developed and analysed in this thesis were tested on specially constructed experimental test-beds. In total there were three test-beds used throughout the research: i) a simple rotary motor-transmission-load test-bed, ii) a single linear axis test-bed driven by a rotary motor that can be coupled with either a ballscrew or rack and pinion, and iii) a high precision linear motor driven single axis test-bed. The combination of these four test-beds allowed for comprehensive testing of all four of the common drive train configurations, along with the effects of each of the three performance limiting factors considered in the research.

The overall automated control of each of the four test-beds was handled by a typical industry CNC system. The CNC system consists of a servo power supply, two digital servo drives, an input output unit and safety stop unit. These components are all mounted on a light steel frame, with castors for mobility. The CNC software is run on a standard personal desktop computer. Communication between the digital servo drives, the input output unit and the desktop computer is handled by SERCOS (SErial Real time COmmunications System). SERCOS is based on the international standard IEC 1491 and exchanges data via a fibre optic ring. This CNC system is easily configured and tuned

for different test-beds via a database system, providing a flexible solution for testing the same control schemes on the four different test-beds.

The specific details of each of the four test-beds and the drive-level control scheme of the CNC system are discussed in this chapter. System parameters are determined in order to describe each of the test-beds in terms of the drive train models developed in Chapter 3. Since the drive-level control scheme of the CNC system is common for all four test-beds, an analysis of this control scheme is presented first in Section 4.2. In Section 4.3 the details of the simple rotary motor-transmission-load system (Motor-Transmission-Load Test-Bed) are discussed, with the mechanical parameters of this test-bed presented. Section 4.4 presents the details of the single linear axis that can be driven by either a ballscrew or rack and pinion (Drive Comparison Test-Bed), while Section 4.5 describes the single axis linear motor driven test-bed (Linear Motor Test-Bed). Finally, Section 4.6 summarises the key points and conclusions that can be drawn from the details presented in this chapter.

## 4.2 CNC Control Scheme

As mentioned in Section 4.1, the control of each of the three test-beds used throughout this research was handled by the same CNC system. Although individual gains and settings need to be adjusted for each of the test-beds (easily handled via a database system on the CNC), the overall drive-level control strategy is common. With brushless servomotors used to drive each of the different mechanical configurations, the digital servo drives of the CNC system were configured to control the output torque (or force in the case of the linear motor) of these servomotors. It is this motor torque (or force) that is the driving input in all of the system equations developed in Chapter 3.

Although brushless servomotors are often labelled as ‘Brushless DC’ motors or ‘Brushless AC’ motors, the standard construction of these motors is based on that of a permanent magnet synchronous motor with continuous rotation obtained by controlling three-phase

current flow in the stator coils. For a rotary brushless servomotor, maximum torque is maintained by monitoring the rotor position and controlling the three-phase stator currents to produce a resultant MagnetoMotive Force (MMF) that is always at a 90 degree angle to the permanent magnet rotor MMF [8]. If $\beta$ is defined as the angle between the stator and rotor MMFs, the three phase stator currents can be described by a stator current phasor referred to the rotor:

$$\tilde{i}e^{-j\beta} = i_d + ji_q \tag{4.1}$$

In Equation (4.1), $i_d$ (direct axis current) is the component of the resulting stator current phasor that is parallel to the rotor frame of reference and $i_q$ (quadrature axis current) is the component of the resulting stator phasor current that is perpendicular to the rotor frame of reference. It follows that $i_d$ must equal zero for maximum torque to be maintained ($\beta = 90^o$). In the case where $i_d$ does equal zero, the torque of a rotary brushless servomotor is described by [8]:

$$\mathrm{T}_m = \left(\frac{Z}{\pi}\right)\phi\frac{i_q}{2} \tag{4.2}$$

In Equation (4.2), $Z$ is the total number of stator conductors, $\phi$ is the magnetic flux and $i_q$ is the quadrature axis current. Since $Z$ never changes in a finished motor and the magnetic flux is determined by the motor dimensions and the state of magnetisation, a torque constant can be defined for brushless servomotors:

$$\begin{aligned} K_t &= \left(\frac{Z}{2\pi}\right)\phi \\ \text{and hence: } \mathrm{T}_m &= K_t i_q \end{aligned} \tag{4.3}$$

From Equations (4.1) and (4.3) it can be seen that, as long as the direct axis current is controlled with a set point of zero, the torque developed in a rotary brushless servomotor is proportional to the quadrature axis current. For a brushless linear motor the linear force is developed in the same manner; however, in a linear motor it is the permanent magnets that are often stationary while the motor coils move linearly along the axis. In this case, it is the position of the moving coils that must be monitored to ensure that the two MMFs

are always at 90 degrees. The overall drive-level control scheme of the CNC system is illustrated in Figure 4.1.

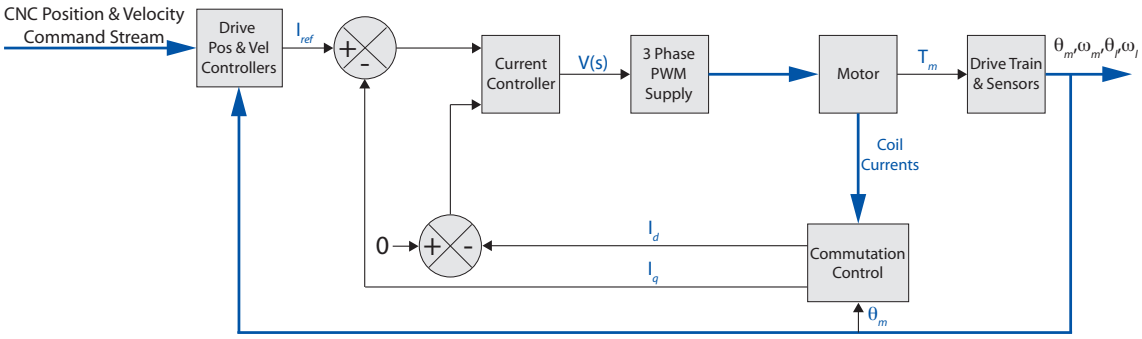


Figure 4.1: CNC Digital Servo Drive – Control Diagram

In Figure 4.1, the input is a stream of position and velocity commands from the CNC motion control software and the output is the actual position and velocity of the overall drive-train system sensed at the motor and/or load. The thicker blue arrows in Figure 4.1 represent the flow of multiple system signals, while the black arrows represent the flow of individual system signals. The drive position and velocity controllers are embedded in the CNC drive code and output a reference control current ($I_{ref}$) representing the desired motor torque. The current controller is a PI regulator with the output described (in Laplace Transform notation) by Equation 4.4.

$$V(s) = K_p \left(1 + \frac{1}{T_i s}\right) \left(I_{ref}(s) - I_{fb}(s)\right) \tag{4.4}$$

In Equation 4.4, $I_{fb}$ is a function of both $I_q$ and $I_d$. However, since the set-point for $I_d$ is zero (as shown in Figure 4.1), $I_{fb}$ is approximately equivalent to $I_q$. The output of the current controller is a voltage command that is applied to the three-phase Pulse Width Modulated (PWM) supply, which feeds the servomotor. The resulting coil currents in the motor are sensed, with the actual motor position and a commutation routine used to determine the $I_q$ and $I_d$ components. The output from the motor is a torque ($T_m$) used to drive the mechanical transmission and load (drive train).

From Equation (4.3) it can be seen that the feedback system of Figure 4.1 reduces to the

simplified system illustrated in Figure 4.2, where $G_c(s) = \frac{I_q(s)}{I_{ref}(s)}$. Hence, if the closed loop transfer function with $I_{ref}$ as input and $I_q$ as output is known, the entire current control system including the PI regulator, drive electronics and internal motor components can be represented by the single block $K_t G_c(s)$.

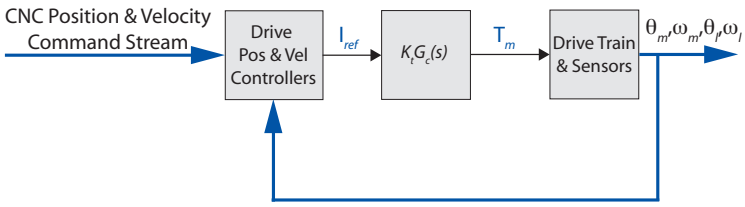


Figure 4.2: CNC Digital Servo Drive – Reduced Control Diagram

In both of the rotary motor driven test-beds, which are discussed further in Sections 4.3 and 4.4, the same brushless servomotors (Siemens 1FK6042-6AF71) were used. For this reason, the overall CNC drive/servomotor current response is the same for both of these test-beds. In order to model the current control system, a closed loop frequency response of this system was measured on the CNC and is shown in Figure 4.3.

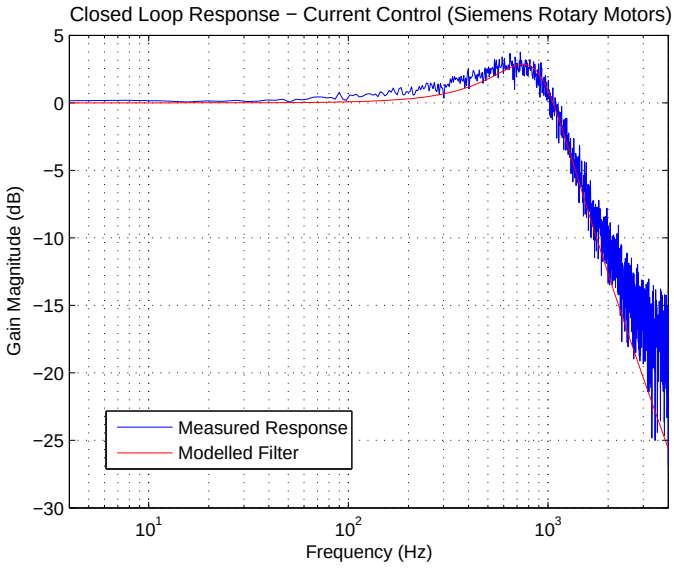


Figure 4.3: Rotary CNC drive/servomotor Current Response

The solid blue line in Figure 4.3 is the measured response of $G_c(s)$ when the CNC is coupled to the rotary servomotors. The solid red line is the response of a simple second-order filter that was used in this thesis to model $G_c(s)$. It can be seen from Figure 4.3 that

this simple filter provides a very close approximation of the actual system response. The transfer function of the simple filter model is given by Equation (4.5).

$$G_c(s) = \frac{5654^2}{s^2 + 4410s + 5654^2} \tag{4.5}$$

Given that the Siemens rotary brushless servomotors have a torque constant $K_t = 1.18$, the overall current control system can be described by Equation (4.6).

$$\frac{\mathrm{T}_m}{I_{ref}} = K_t G_c(s) = \frac{1.18\left(5654^2\right)}{s^2 + 4410s + 5654^2} \tag{4.6}$$

The linear motor test-bed was driven by a linear brushless servomotor (Linear Drives LD3806). In order to model the linear CNC drive/servomotor current control system, a closed loop frequency response of the system was again measured on the CNC and is shown in Figure 4.4.

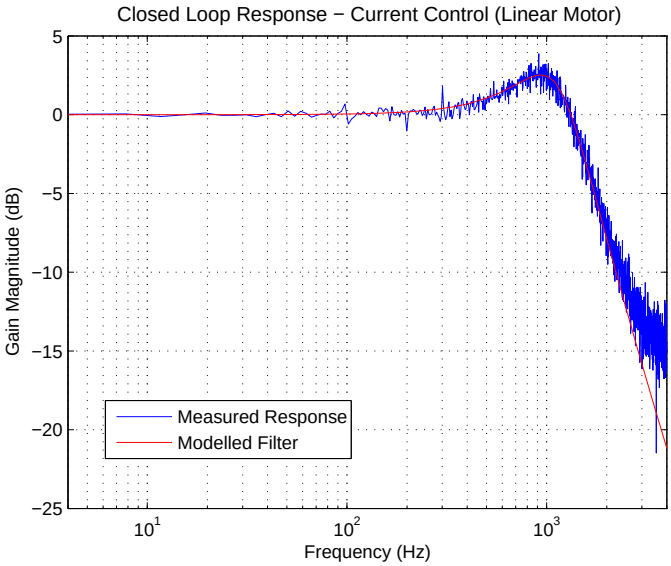


Figure 4.4: Linear CNC drive/servomotor Current Response

The solid blue line in Figure 4.4 is the measured response of $G_c(s)$ when the CNC is coupled to the linear motor. The solid red line is the response of another simple second-order filter that was used to model $G_c(s)$ for the linear motor case. It can be seen from Figure 4.4 that once again the simple filter provides a very close approximation of the

actual system response. The transfer function of the simple filter model used for the linear motor case is given by Equation (4.7).

$$G_c(s) = \frac{7225^2}{s^2 + 5925s + 7225^2} \tag{4.7}$$

Given that the Linear Drives motor has a force constant $K_f = 75$, the overall current control system can be described by Equation (4.8).

$$\frac{\mathrm{F}_m}{I_{ref}} = K_f G_c(s) = \frac{75\left(7225^2\right)}{s^2 + 5925s + 7225^2} \tag{4.8}$$

## 4.3 Motor-Transmission-Load Test-Bed

### 4.3.1 General Description

The Motor-Transmission-Load Test-Bed was constructed to resemble the basic two-body model introduced in Section 2.3. The test-bed consists of two of the Siemens rotary servomotors mounted on fabricated right angle brackets. The mounting brackets rest on a sturdy base constructed from 16mm thick steel plate, and were machined such that they were able to slide back and forth along the base while maintaining correct alignment. Special couplings allow the two motors to be connected by a variety of shafts of varying lengths and diameters. The couplings also act as a carrier for removable discs, which allow the load inertia to be varied in steps. The motor at the load end was used only for applying load disturbance torques. Figure 4.5 (a) shows the test bed with motor mounts and test shaft in their assembled positions. Figure 4.5 (b) shows a closer view of the directly connected load coupling with removable inertia disc.

As can be seen, the constructed test-bed is consistent with the basic two-body system illustrated in Figure 2.1. This simple test-bed allowed for a concentrated analysis of drive-train flexing and torsional vibrations, while other important factors such as friction

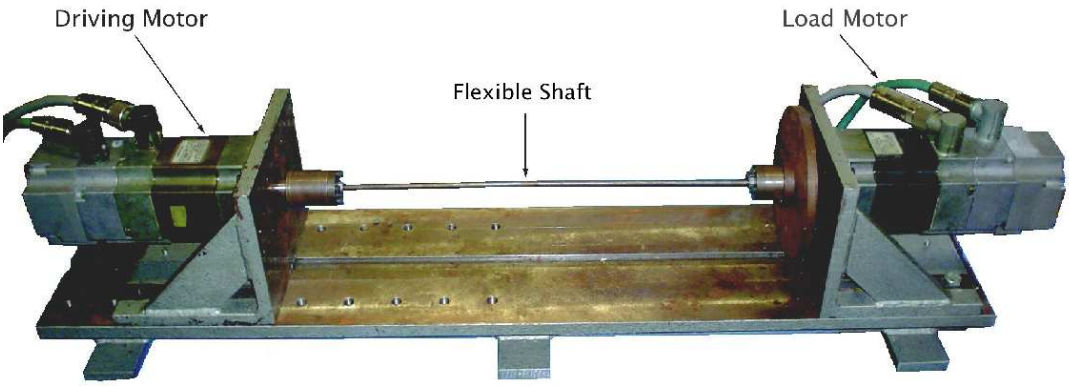


(a) Motor, Transmission and Load

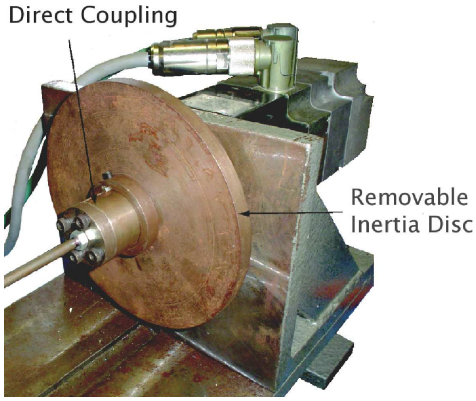


(b) Load Inertia

Figure 4.5: Experimental Motor-Transmission-Load System

and backlash were minimised. The major difference between the experimental system of Figure 4.5 and the ideal system of Figure 2.1 is that the difficulties in perfectly aligning a practical transmission element result in alignment related cyclic disturbances being present in the experimental system.

Through the addition of backlash couplings between the transmission element and the load, this simple test-bed can be varied to resemble the basic two-body model with backlash (as illustrated in Figure 2.2). To achieve this a number of extra couplings were machined with known backlash gaps, allowing for an analysis that concentrated on the effects of backlash and the inter-relating effects of backlash and torsional vibrations. A selection of these backlash couplings is shown in Figure 4.6 (a), with Figure 4.6 (b) showing how the couplings are mounted on the test-bed. Detailed drawings of the basic test-bed and couplings are given in Appendix D.

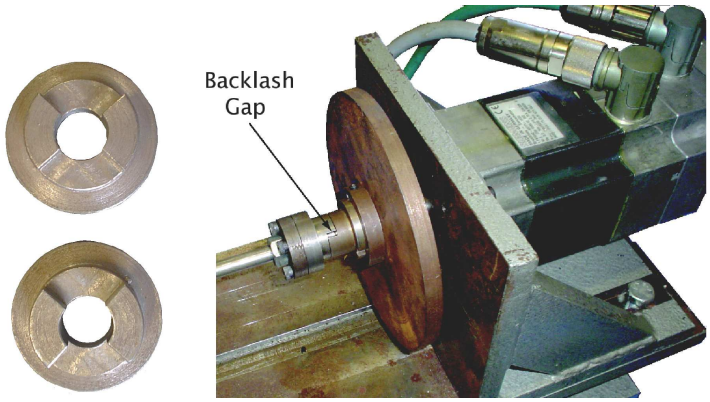


(a) Couplings (b) Couplings Mounted on Test-Bed

Figure 4.6: Backlash Couplings

Position feedback at both the motor and load ends of the test-bed is achieved through rotary encoders embedded in the Siemens motors. These incremental optical encoders produce two channels of differential sinusoids in quadrature, thus providing both position and directional information. The CNC system interpolates using the basic period of the encoders (3.068 mrad) along with instantaneous sine and cosine information to improve the resolution of the position feedback. For additional acceleration feedback, a Hübner rotary accelerometer (based on the Ferraris Principle) was also used during some of the experimentation undertaken on the test-bed. The accelerometer can be attached to either the motor or load end of the system. Additional data on these feedback elements is included in Appendix D.

### 4.3.2 Mechanical System Parameters

In the control diagrams shown in Figures 4.1 and 4.2, the 'Drive Train & Sensors' block represents the overall mechanical drive system including all relevant inertias, friction, flexing and backlash etc.. The input to this block is a torque ($T_m$), while the output represents all available motor and load feedback signals. All of the system equations developed in Chapter 3 are in the appropriate form to describe the various mechanical systems that can be represented by the 'Drive Train & Sensors' block.

Since the Motor-Transmission-Load Test-Bed was designed to be consistent with a basic

two-body system, Equations (3.24) and (3.25) were used to describe the mechanical drive train of this test-bed when backlash was zero. For the cases where backlash was non-zero, Equations (3.35) to (3.41) were used. The set of mechanical parameters used in these system equations are given in Tables 4.1 to 4.4.

Table 4.1: System Parameters – Motor and Load

| Parameter | Symbol | Value |
|---|---|---|
| Motor Inertia (kgm$^2$) | $J_m$ | 4.108x10$^{-4}$ |
| Load Inertia (kgm$^2$) | $J_l$ | 4.108x10$^{-4}$ |
| Viscous Friction at Motor (Nms/rad) | $B_m$ | 2.62x10$^{-3}$ |
| Viscous Friction at Load (Nms/rad) | $B_l$ | 3.65x10$^{-3}$ |
| Coulomb Friction at Motor (Nm) | $T_{fcm}$ | 0.08 |
| Coulomb Friction at Load (Nm) | $T_{fcl}$ | 0.06 |

Table 4.1 lists the inertia and friction parameters for both the motor and load ends of the test-bed. The total inertia at each end consists of the rotor inertia and the inertia of the transmission coupling. The rotor inertia of the motors was specified by the manufacturer (3.47x10$^{-4}$ kgm$^2$), while the inertias of the transmission couplings were calculated using Equation (4.9).

$$J = \frac{M\left(R_2^2 + R_1^2\right)}{2} \tag{4.9}$$

Equation (4.9) describes the moment of inertia of a uniform hollow cylinder (which is a good approximation of the transmission couplings), where $M$ is the total mass of the cylinder and $R_2$ & $R_1$ are the outer and inner radii of the cylinder respectively. For the inertia values given in Table 4.1, the masses and radii of the couplings were directly measured. The viscous and coulomb friction values given in Table 4.1 were obtained using the PDTV method described in Section 3.3. Since the DC component of the PDTV spectrum represents the combination of viscous and coulomb frictions, these two friction components can be separated by measuring the DC component of the PDTV spectrum at several different velocities.

Table 4.2 lists the inertia and torsional stiffness parameters of the interchangeable trans-

Table 4.2: System Parameters – Transmission Shafts

| Parameter | Symbol | Shaft 1 | Shaft 2 | Shaft 3 |
|---|---|---|---|---|
| Transmission Inertia (kgm$^2$) | $J_s$ | 2.08x10$^{-6}$ | 1.55x10$^{-6}$ | 5.25x10$^{-7}$ |
| Torsional Stiffness (Nm/rad) | $K_s$ | 402 | 70.35 | 23.6 |

mission shafts. There were three shafts that were used with this test-bed, one short and reasonably stiff shaft ('Shaft 1') and two longer shafts that were machined to be deliberately flexible ('Shaft 2' and 'Shaft 3'). The values of inertia for each of these shafts were again calculated using Equation (4.9) and directly measured values of mass and radii. The torsional stiffness of each shaft was calculated using Equation (4.10).

$$K_s = \frac{G\pi d^4}{32l} \tag{4.10}$$

Equation (4.10) describes the torsional stiffness constant of a uniform shaft, where $G$ is the shear modulus (80x10$^9$ Pa for steel), $d$ is the diameter of the shaft and $l$ is the length of the shaft. For the torsional stiffness values given in Table 4.2, the diameters and lengths of the shafts were directly measured. The internal damping coefficient ($C_s$) for each shaft is not listed in Table 4.2. The reason for this is that $C_s$ is very approximate and also dependent on the total motor and load side inertias (which can be varied on this test-bed). In this thesis $C_s$ was determined individually for each experimental set-up using Equation (4.11), where $\eta$ is the material loss factor (estimated at 0.05 for steel). The derivation of Equation (4.11) is given in Appendix B.

$$C_s = \eta\sqrt{\frac{J_m J_l K_s}{(J_m + J_l)}} \tag{4.11}$$

Table 4.3: System Parameters – Additive Components

| Parameter | Disc 1 | Disc 2 | Disc 3 | Accelerometer |
|---|---|---|---|---|
| Inertia (kgm$^2$) | 1.544x10$^{-3}$ | 5.02x10$^{-3}$ | 1.417x10$^{-3}$ | 2.98x10$^{-4}$ |
| Viscous Friction (Nms/rad) | 0 | 0 | 0 | 2.71x10$^{-3}$ |

There were three different additive discs used with the test-bed to vary the inertia at either

the motor or load end. Table 4.3 lists the inertia of each of these discs, along with both the inertia and added viscous friction of the rotary accelerometer (which could also be mounted at either end of the test-bed). The inertias of these additive components were again calculated using Equation (4.9) and directly measured values for the masses and radii. The added viscous friction of the accelerometer was determined using the PDTV method.

Table 4.4: System Parameters – Coupling Backlash Gaps

| Coupling | Backlash Gap ($\alpha$) |
|---|---|
| Coupling 1 | 0.0873 rad |
| Coupling 2 | 0.1745 rad |

Table 4.4 lists the backlash gaps of the additional couplings that were machined for the test-bed. These gaps were directly measured.

## 4.4 Drive Comparison Test-Bed

### 4.4.1 General Description

The Drive Comparison Test-Bed is a single axis positioning system designed for testing the relative performance of three common drive-train configurations under similar test conditions. The three drive-train configurations incorporated into the test-bed are: 1. a rotary motor directly coupled to a ballscrew, 2. a rotary motor coupled to a ballscrew via a synchronous timing belt and 3. a rotary motor directly coupled to a rack and pinion transmission. The main structure of the test-bed consists of a 1m length of 150mm universal column, supported at each end by 16mm steel plate. The top surface of the universal column is machined to accurately support a rack and two linear guides in parallel. A 10mm thick steel plate is mounted on the linear guides as a load carrying table. The overall test-bed is shown in Figure 4.7.

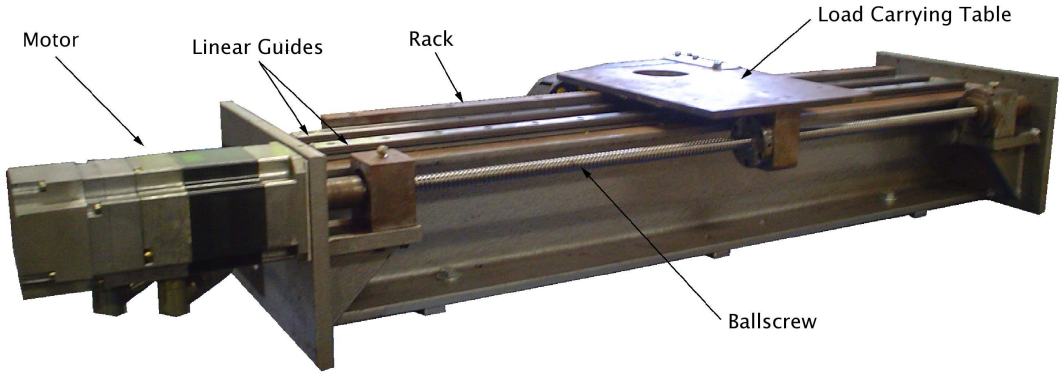


Figure 4.7: Drive Comparison Test-Bed in Direct Driven Ballscrew Configuration

It can be seen in Figure 4.7 that a rotary servomotor is mounted at one end of the main test-bed structure and directly coupled to a ballscrew. The ballscrew itself is mounted to one side of the universal column. Figure 4.8 shows how the alternative drive configurations are achieved with the test-bed. In Figure 4.8 (a), the servomotor has been moved to the other side of the steel end plate and coupled to the ballscrew via a belt and pulley system. Figure 4.8 (a) also clearly illustrates the space saving that is achieved through the belt driven ballscrew configuration (when compared with the direct driven ballscrew of Figure 4.7). In Figure 4.8 (b), the rack and pinion configuration is illustrated. When using the rack and pinion system, the ballscrew is detached from the load table and the pinion is directly coupled to the servomotor, which is mounted on the load table.

In general, the mechanical components used in the drive trains of this test-bed were chosen to emphasise the effects being studied. For instance, the ballscrew was deliberately chosen to have a small diameter and only a single nut system so that torsional flexing and backlash would be significant. Similarly, a coarse rack and pinion transmission with no inherent anti-backlash mechanisms was chosen. The application of precision control algorithms on this test-bed allowed for the testing to be undertaken under worst-case conditions.

Position feedback for each of the drive configurations on this test-bed is achieved through the rotary encoders embedded in the Siemens servomotors. Additional load position feedback can be achieved by placing a rotary encoder at the other end of the ballscrew (when the system is being driven by one of the ballscrew configurations). Detailed drawings of

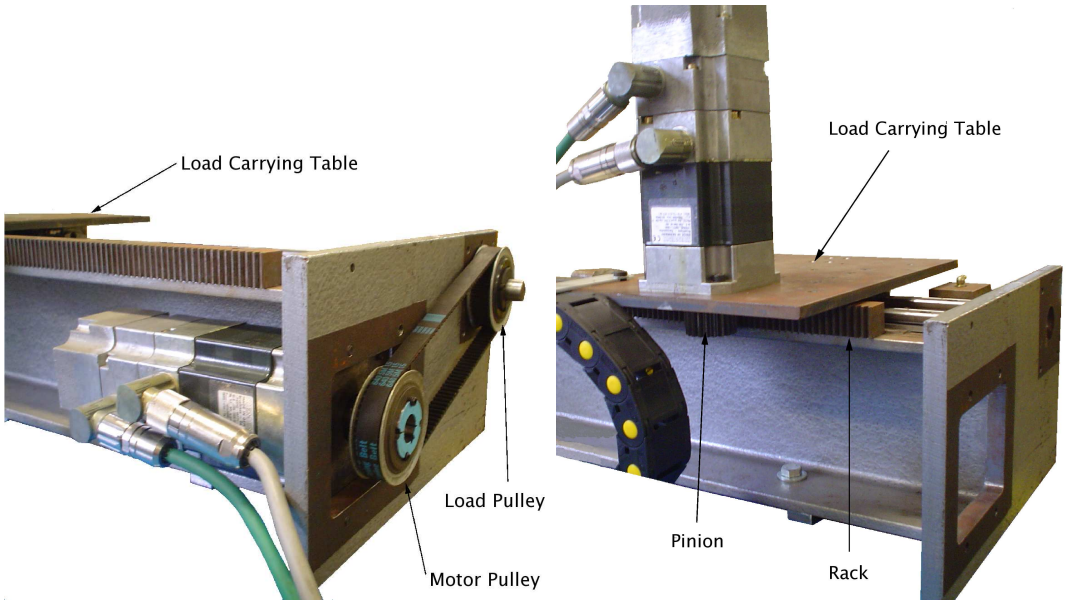


(a) Belt Driven Ballscrew (b) Rack and Pinion

Figure 4.8: Drive Comparison Test-Bed in Alternative Configurations

the drive comparison test-bed are given in Appendix D.

### 4.4.2 Mechanical System Parameters

Since the Drive Comparison Test-Bed can be varied between three different drive configurations, there are three different sets of system equations that were used to describe the mechanical drive train:

1. Direct Driven Ballscrew Configuration — the substitutions specified in Equations (3.42) to (3.45) were applied to the non-zero backlash system equations (Equations (3.35) to (3.41)).
2. Belt Driven Ballscrew Configuration — the substitutions specified in Equations (3.42) to (3.45) were applied to Equations (3.46) to (3.48). In this case, the ballscrew torque is described by Equations (3.37) to (3.41) and the belt force is described by Equations (3.49) to (3.54).
3. Rack and Pinion Configuration — the substitutions specified in Equations (3.55) and (3.56) were applied to the non-zero backlash system equations (Equations (3.35) to (3.41)).

A complete description of how each of these system equations apply to the different configurations is given in Chapter 3. The set of mechanical parameters used in all of the system equations for the Drive Comparison Test-Bed is given in Tables 4.5 to 4.7.

Table 4.5: Drive Comparison Test-Bed Parameters – Direct Driven Ballscrew

| Parameter | Symbol | Value |
|---|---|---|
| Motor Inertia (kgm$^2$) | $J_m$ | 3.716x10$^{-4}$ |
| Ballscrew Inertia (kgm$^2$) | $J_{BS}$ | 3.22x10$^{-5}$ |
| Load Mass (kg) | $M_L$ | 8.8 |
| Length of Ballscrew (m) | L | 1 |
| Pitch of Ballscrew (m) | $P_{BS}$ | 5x10$^{-3}$ |
| Viscous Friction at Motor (Nms/rad) | $B_m$ | 3.05x10$^{-3}$ |
| Viscous Friction at Load (Nms/rad) | $B_l$ | 1.75x10$^{-3}$ |
| Coulomb Friction at Motor (Nm) | $T_{fcm}$ | 0.175 |
| Coulomb Friction at Load (Nm) | $T_{fcl}$ | 0.205 |
| Torsional Stiffness of Overall Ballscrew (Nm/rad) | $K_{sBS}$ | 225 |
| Internal Damping Coefficient of Ballscrew (Nms/rad) | $C_s$ | $\frac{1.75\times10^{-3}}{\sqrt{x}}$ |
| Ballscrew Backlash Gap (rad) | $\alpha$ | 0.03 |

Table 4.5 lists the set of mechanical parameters for this test-bed when configured in direct driven ballscrew mode. The total motor inertia in Table 4.5 is a combination of the rotor inertia and the inertia of the motor/ballscrew coupling. The inertia of the ballscrew and the inertia of the motor/ballscrew coupling were calculated using Equation (4.9), with the masses and radii of each component directly measured. The total load mass is a combination of the mass of the load carrying table, the mass of the linear bearings and the mass of the ballscrew nut. The masses for each of these individual components were directly measured.

The viscous and coulomb friction values given in Table 4.5 were obtained using the PDTV method. The PDTV study was performed with and without the total load connected, so that the motor and load friction components could be accurately separated from the total system friction.

The torsional stiffness of the overall ballscrew ($K_{sBS}$) was calculated using Equation (4.10) and directly measured values of ballscrew diameter and length. As mentioned in Section 3.5.1, the actual torsional stiffness of the transmission is a function of both $K_{sBS}$ and the load position ($x$). Likewise, the internal damping coefficient is dependent on the load position. Equation (4.12) was used to determine the internal damping coefficient and is a modified version of Equation (4.11) taking the variable torsional stiffness of the transmission into account.

$$C_s = \eta \sqrt{\frac{J_m P_{BS}^2 M_L K_{sBS} L}{x\left(4\pi^2 J_m + P_{BS}^2 M_L\right)}} \tag{4.12}$$

The ballscrew backlash gap was measured by locking the ballscrew in place and measuring the linear free-play of the table with a dial indicator. The linear free-play was then translated into a rotary backlash gap (in radians).

Table 4.6 lists the set of mechanical parameters for this test-bed when configured in belt driven ballscrew mode. The total motor inertia in this case is a combination of the rotor inertia and the inertia of the motor pulley. The inertias of the motor and load pulleys were both calculated using Equation (4.9), with the masses and radii of the pulleys directly measured. The ballscrew inertia and total load mass are identical to the direct driven ballscrew case.

The viscous and coulomb friction values given in Table 4.6 were again obtained using the PDTV method. The PDTV study for this system was performed for three different cases: 1. with the motor and motor pulley disconnected, 2. with the motor and motor pulley connected to the load pulley, but with no load connected and 3. with the load connected. This approach allowed for the friction components at the motor, load pulley and load to be accurately separated from the total system friction.

The torsional stiffness of the ballscrew is identical to the direct driven ballscrew case. However, the internal damping coefficient of the ballscrew is slightly different due to the fact that the ballscrew is now driven by the load pulley rather than the motor. The stiffness

Table 4.6: Drive Comparison Test-Bed Parameters – Belt Driven Ballscrew

| Parameter | Symbol | Value |
|---|---|---|
| Motor Inertia (kgm$^2$) | $J_m$ | 6.67x10$^{-4}$ |
| Load Pulley Inertia (kgm$^2$) | $J_p$ | 3.53x10$^{-4}$ |
| Ballscrew Inertia (kgm$^2$) | $J_{BS}$ | 3.22x10$^{-5}$ |
| Load Mass (kg) | $M_L$ | 8.8 |
| Length of Ballscrew (m) | L | 1 |
| Pitch of Ballscrew (m) | $P_{BS}$ | 5x10$^{-3}$ |
| Radius of Motor Pulley (m) | $R_m$ | 34.5x10$^{-3}$ |
| Radius of Load Pulley (m) | $R_p$ | 34.5x10$^{-3}$ |
| Viscous Friction at Motor (Nms/rad) | $B_m$ | 1.6x10$^{-3}$ |
| Viscous Friction at Load Pulley (Nms/rad) | $B_p$ | 1.45x10$^{-3}$ |
| Viscous Friction at Load (Nms/rad) | $B_l$ | 1.75x10$^{-3}$ |
| Coulomb Friction at Motor (Nm) | $T_{fcm}$ | 0.08 |
| Coulomb Friction at Load Pulley (Nm) | $T_{fcp}$ | 0.145 |
| Coulomb Friction at Load (Nm) | $T_{fcl}$ | 0.205 |
| Stiffness of Belt (N/m) | $K_{sblt}$ | 997 |
| Torsional Stiffness of Overall Ballscrew (Nm/rad) | $K_{sBS}$ | 225 |
| Internal Damping Coefficient of Belt (Ns/m) | $C_{sblt}$ | 0.048 |
| Internal Damping Coefficient of Ballscrew (Nms/rad) | $C_s$ | $\frac{1.75\times10^{-3}}{\sqrt{x}}$ |
| Belt Backlash Gap (rad) | $\alpha_{blt}$ | $\approx 0$ |
| Ballscrew Backlash Gap (rad) | $\alpha_{BS}$ | 0.03 |

of the belt was calculated using Equation (4.13).

$$K_{sblt} = 4K_{sp}\frac{b}{L} \tag{4.13}$$

In Equation (4.13), $K_{sp}$ is the belt specific stiffness (i.e. the stiffness of a unit long, unit wide belt – from manufacturer testing this is estimated at 10,635 N/m for a 5mm pitch synchronous timing belt), $b$ is the belt width and $L$ is the overall length of the belt. The internal damping coefficient of the belt was calculated using Equation (4.11), with the loss factor ($\eta$) estimated at 0.1 for a Neoprene based synchronous belt. The ballscrew backlash gap is identical to the direct driven ballscrew case, while the belt backlash gap

is approximately zero (as long as the belt is tensioned correctly).

Table 4.7: Drive Comparison Test-Bed Parameters – Rack and Pinion

| Parameter | Symbol | Value |
|---|---|---|
| Motor Inertia (kgm$^2$) | $J_m$ | 3.43x10$^{-4}$ |
| Transmission Shaft Inertia (kgm$^2$) | $J_s$ | 4x10$^{-6}$ |
| Pinion Inertia (kgm$^2$) | $J_{PIN}$ | 4.4x10$^{-5}$ |
| Load Mass (kg) | $M_L$ | 13.2 |
| Radius of Pinion (m) | r | 20x10$^{-3}$ |
| Viscous friction at Motor (Nms/rad) | $B_m$ | 1.6x10$^{-3}$ |
| Viscous friction at Load (Nms/rad) | $B_l$ | 32.8x10$^{-3}$ |
| Coulomb Friction at Motor (Nm) | $T_{fcm}$ | 0.08 |
| Coulomb Friction at Load (Nm) | $T_{fcl}$ | 0.35 |
| Torsional Stiffness of Transmission Shaft (Nm/rad) | $K_s$ | 25,588 |
| Internal Damping Coefficient of Transmission Shaft (Nms/rad) | $C_s$ | 0.0499 |
| Backlash Gap (rad) | $\alpha$ | 0.014 |

Table 4.7 lists the set of mechanical parameters for when the test-bed is configured in rack and pinion mode. The motor inertia in this case is simply the rotor inertia. The pinion inertia and transmission shaft inertia were calculated using Equation (4.9), with the masses and radii of each component directly measured. The total load mass is a combination of the mass of the load carrying table, the mass of the linear bearings and the mass of the motor itself. All of these masses were directly measured.

The viscous and coulomb friction values given in Table 4.7 were once again obtained using the PDTV method. The PDTV study was performed with the motor/pinion mounted on the table and again with the motor/pinion unmounted, so that the motor and load friction components could be accurately separated from the total system friction. The torsional stiffness of the transmission shaft was calculated using Equation (4.10) and directly measured values of shaft diameter and length. The internal damping coefficient of the transmission shaft was calculated using Equation (4.11). The backlash gap in the rack and pinion transmission was measured by locking the table in place and directly measuring the angle of free-play of the pinion.

## 4.5 Linear Motor Test-Bed

### 4.5.1 General Description

The ‘Linear Motor Test-Bed’ is a single axis positioning system designed to replicate one axis of a laser cutting machine. The long travels, high speeds and zero machining forces associated with the laser cutting process are commonly thought to be ideal for a linear motor. The particular linear motor used in this test-bed (Linear Drives – LD3806) is a ‘tubular’ style linear motor. This type of linear motor consists of a thrust block containing three phase armature windings and a tube that houses the permanent magnets for field excitation (the complete excitation rod passes through the centre of the thrust block). Through a balancing of the forces, the tubular style linear motor eliminates the magnetic attraction that exists between the separate armature and field components of more common ‘flat’ style linear motors. This magnetic attraction can often be up to an order of magnitude higher than the actual payload (affecting supporting rail requirements, peak force requirements, cooling and cost), and is a particular problem in high force iron-core motors. The overall test-bed is shown in Figure 4.9.

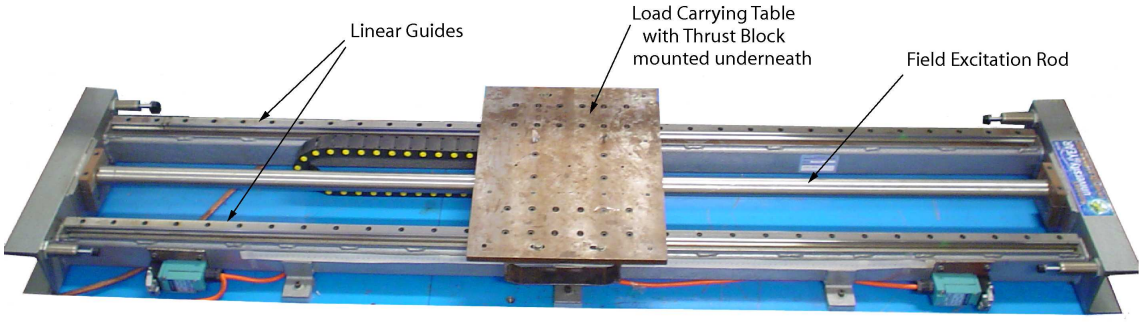


Figure 4.9: Linear Motor Test-Bed

As can be seen in Figure 4.9, the main test-bed structure consists of a rectangular welded steel frame made from Rectangular Hollow Section (RHS – 4mm wall thickness) on the axial sides and parallel flange channel at the ends. The linear guides are mounted on machined 10mm flat bar, which is welded to the RHS along the axial sides of the frame. A 15mm steel plate is mounted on the linear guides as a load carrying table. The field

excitation rod is mounted in the centre of the test-bed and passes through the thrust block, which is attached to the underside of the moving table. The complete test-bed structure is mounted on a separate rigid support table. The Linear Motor Test-Bed represents a state of the art machine tool positioning system and was used throughout this thesis for performance comparisons with the other drive configurations studied. Detailed drawings of the test-bed are given in Appendix D.

Position feedback on this test-bed is achieved through an incremental linear encoder (Renishaw – RGS-S/RGH22B) mounted on one side of the frame structure. The linear encoder is an optical encoder and produces two channels of differential sinusoids in quadrature (similar to the output of the rotary encoder embedded in the Siemens motors). The CNC system interpolates using the basic period of the linear encoder (20$\mu$m) along with instantaneous sine and cosine information for improved resolution of position feedback. The CNC system also uses this position feedback for commutation purposes. Additional data on the linear encoder is included in Appendix D.

### 4.5.2 Mechanical System Parameters

Since the Linear Motor Test-Bed has the simplest mechanical drive train of all of the test-beds considered in this chapter, a single system equation (Equation (3.57)) was used to describe the test-bed. The set of mechanical parameters used in Equation (3.57) for the Linear Motor Test-Bed are given in Table 4.8.

Table 4.8: Linear Motor Test-Bed Parameters

| Parameter | Symbol | Value |
|---|---|---|
| Load Mass (kg) | M | 23 |
| Viscous Friction (Ns/m) | B | 1.56 |
| Coulomb Friction (N) | $F_{fc}$ | 0.41 |

In Table 4.8, the load mass is a combination of the mass of the load carrying table, the masses of the linear bearings and the mass of the thrust block. Like the other test-beds,

the viscous and coulomb friction values of the Linear Motor Test-Bed were determined using the PDTV method.

## 4.6 Conclusions

The experimental equipment used throughout this research project has been described in this chapter. In particular, three different test-beds were described: 1. Motor-Transmission-Load Test-Bed, 2. Drive Comparison Test-Bed and 3. Linear Motor Test-Bed.

The drive-level control scheme of the CNC system (used on all of the test-beds) was discussed, along with the basic construction details and specific features of each of the three individual test-beds. The response of the CNC system's closed loop current controller was analysed when driving both a rotary servomotor and the linear servomotor. It was shown that simple second order filters provided a close approximation of the CNC system's closed loop current response for both types of motor and hence, simple transfer functions that represent the drive-level control system were presented for both cases. The output of the rotary servomotor transfer function is torque, while the output of the linear servomotor transfer function is force. These torque and force outputs are equivalent to the inputs of the system equations developed in Chapter 3.

For each test-bed axis configuration, the relevant system equations (as developed in Chapter 3) were identified and the mechanical system parameters required by the equations presented. The methods used for determining each mechanical parameter were described for all of the test-beds and generally consisted of a combination of experimental measurement, appropriate calculations and known component data. The resulting system models are used in both simulation and controller design throughout Chapters 5, 6 and 7 of this thesis.

Chapter 5

# Dynamic Stiffness

## 5.1 Introduction

A study of the dynamic stiffness of linear feed axes in precision machine tools is presented in this chapter. The term ‘dynamic stiffness’ can best be described as the frequency response of a system’s sensitivity to force disturbances at the load. In precision machining operations, the machining forces resulting from contact between the tool and workpiece are often the major source of load disturbance. In some machining processes, such as laser cutting, there is no direct contact between the tool and workpiece, which results in very low (or even zero) machining forces. However, in most machining processes these machining forces can be quite high.

The study presented in this chapter focuses particularly on the dynamic stiffness of linear motor driven axes. One of the advantages of a linear motor over a rotary driven linear axis is a reduction in periodic torque/force disturbances, which is inherent through elimination of the mechanical transmission mechanism. However, this also results in a system that is more sensitive to load variations and external disturbances. Inherently low dynamic stiffness is regarded as one of the major performance limitations of linear motor driven axes. In this chapter the inherent dynamic stiffness and periodic disturbances of both

linear motor and rotary driven axes are compared. A QFT approach that includes dynamic stiffness in the design process is also examined.

In Section 5.2 measurements of the position dependent torque/force variations for a linear motor driven axis, along with those for the common rotary motor driven configurations, are presented. The Linear Motor Test-Bed (described in Section 4.5) and the Drive Comparison Test-Bed (described in Section 4.4) were used for the experimental measurements presented in this section. The inherent periodic torque/force disturbances of the linear motor system and the rotary motor driven configurations are then quantitatively compared.

In Section 5.3 the inherent dynamic stiffness of a linear motor driven axis is compared with that of the common rotary motor driven configurations. Initially, mathematical expressions for dynamic stiffness (based on Equation 2.6) are developed for each axis configuration. The system parameters for both the Linear Motor Test-Bed and the Drive Comparison Test-Bed (presented in Chapter 4) are then used to quantify the inherent dynamic stiffness of each of the test-bed configurations.

In Section 5.4 experimental responses to an applied load disturbance are compared for the Linear Motor Test-Bed and each configuration of the Drive Comparison Test-Bed. The initial responses were recorded using the standard PI velocity and P position loops of the existing servo drives, tuned using the manufacturer's recommended method. A robust QFT approach, that includes both dynamic stiffness and transient performance specifications, is then described and implemented on the Linear Motor Test-Bed, using the same servo drives. As a comparison, experimental responses to the applied load disturbance are also presented for the QFT designed controller.

Finally, Section 5.5 summaries all of the key points and conclusions that can be drawn from this chapter.

## 5.2 Torque/Force Variations in Feed Axes

Some of the performance limiting factors associated with machine tool feed axes can be quantified through a study of periodic torque/force variations. As described in Section 3.3, a position frequency spectrum of torque or force can be constructed for machine tool axes. As an example, consider a linear motor system represented by Equation (3.57). If the system is moving at a constant velocity, the motor force can be described by:

$$F_m = B\dot{x} + F_{fc} + \sum_{n=-\infty}^{\infty} c_n e^{jn\Omega_0 x} \tag{5.1}$$

It can be seen from Equation (5.1) that the resulting motor force (at any position) is equivalent to the addition of the constant frictional forces ($B\dot{x} + F_{fc}$) and the sum of the forces required to overcome periodic disturbances. Hence, the frictional forces make up the DC component of the position frequency spectrum, while the remaining spectrum is associated with the position dependent force variations.

In order to compare the torque/force disturbances inherent to the common feed axis configurations, position frequency spectra were determined for the Linear Motor Test-Bed and all of the Drive Comparison Test-Bed configurations. The position frequency spectrum of the Linear Motor Test-Bed is shown in Figure 5.1.

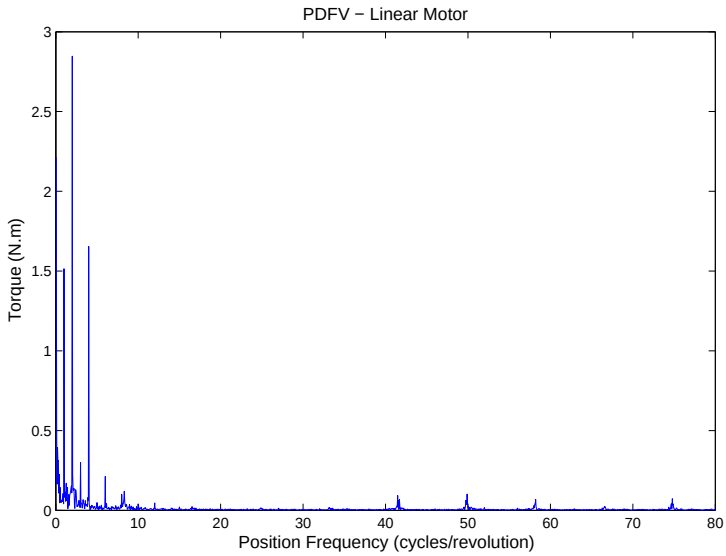


Figure 5.1: Position Frequency Spectrum - Linear Motor

The position frequency spectrum of the Drive Comparison Test-Bed in the direct drive ballscrew configuration is shown in Figure 5.2. Similarly, the position frequency spectra of the Drive Comparison Test-Bed in the belt driven ballscrew and rack and pinion configurations are shown in Figures 5.3 and 5.4 respectively. While collecting data for the frequency spectra, each test-bed configuration was run at a constant linear velocity of 200mm/min.

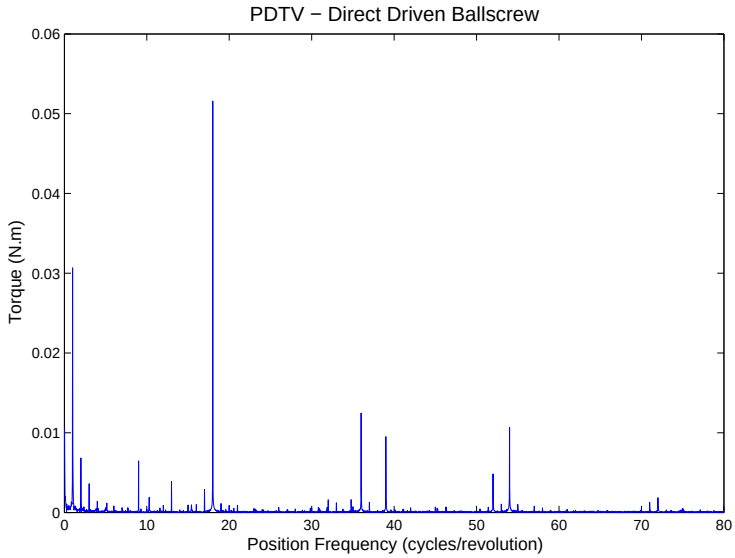


Figure 5.2: Position Frequency Spectrum - Direct Driven Ballscrew

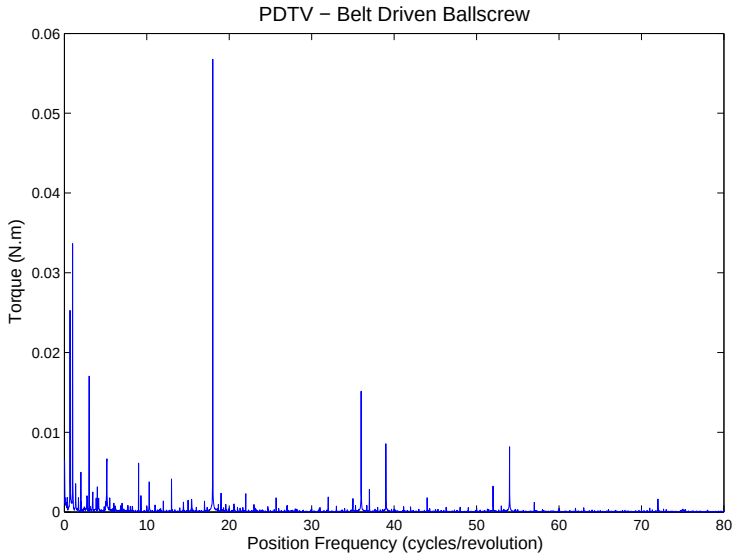


Figure 5.3: Position Frequency Spectrum - Belt Driven Ballscrew

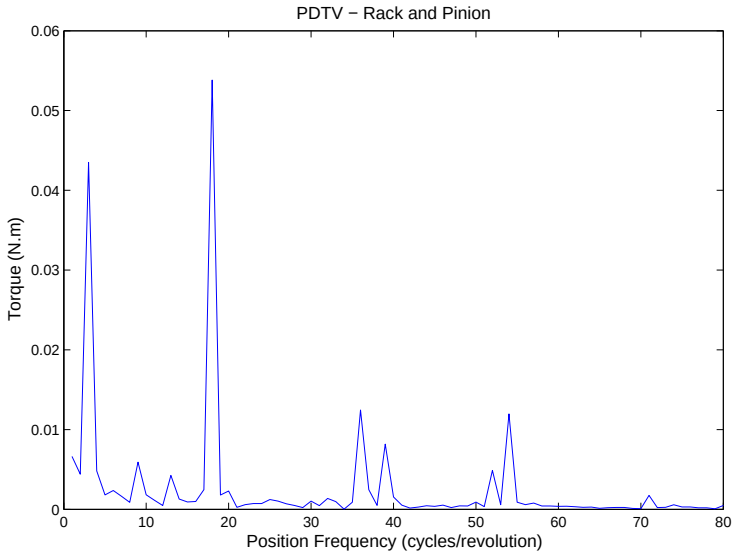


Figure 5.4: Position Frequency Spectrum - Rack and Pinion

The position frequency in Figures 5.1, 5.2, 5.3 and 5.4 is expressed in cycles per revolution. For the Linear Motor Test-Bed, one revolution is the linear distance traversed during one electrical cycle of the linear motor. For the Drive Comparison Test-Bed, one revolution refers to one mechanical revolution of the rotary motor. The DC component in each spectrum has been set to zero, in order to concentrate on the periodic disturbances.

The fundamental frequency in each spectrum corresponds to the actual length of travel used during the testing procedure. There is a 25:1 ratio between the linear lengths traversed by the rack and pinion and ballscrew configurations during one revolution of the rotary motor. Hence, there is also a 25:1 ratio between the fundamental frequencies of the rack and pinion and ballscrew spectra (as the same linear length of travel was used during the testing procedure). As a result, the rack and pinion has a much coarser spectrum than the other cases.

A summary of the PDFV/PDTV results is given in Table 5.1, where both the DC component and the most significant frequency components from Figures 5.1, 5.2, 5.3 and 5.4 are listed. The most likely causes of the frequency components are also included in Table 5.1.

Table 5.1: Significant Components of Experimental PDFV/PDTV

| | Frequency (Cyc/Rev) | Magnitude | Cause |
|---|---|---|---|
| Linear Motor | DC | 20N | Friction |
| | 2 | 2.85N | Motor Poling |
| | 0.05 | 1.9N | Fundamental |
| | 4 | 1.67N | Motor Poling |
| | 1 | 1.52N | Electrical Cycle |
| Direct Driven Ballscrew | DC | 0.311Nm | Friction |
| | 18 | 0.052Nm | Stator Teeth |
| | 1 | 0.031Nm | Rotor Shaft Cycle |
| | 36 | 0.012Nm | Stator Teeth |
| | 54 | 0.011Nm | Stator Teeth |
| | 0.03 | 0.011Nm | Fundamental |
| | 39 | 0.009Nm | Ballscrew Bearing Cycle |
| Belt Driven Ballscrew | DC | 0.319Nm | Friction |
| | 18 | 0.057Nm | Stator Teeth |
| | 1 | 0.034Nm | Rotor Shaft Cycle |
| | 0.68 | 0.025Nm | Belt Cycle |
| | 3 | 0.017Nm | Motor Poling |
| | 36 | 0.015Nm | Stator Teeth |
| | 39 | 0.009Nm | Ballscrew Bearing Cycle |
| | 54 | 0.008Nm | Stator Teeth |
| Rack and Pinion | DC | 0.238Nm | Friction |
| | 18 | 0.053Nm | Stator Teeth |
| | 3 | 0.045Nm | Motor Poling |
| | 54 | 0.015Nm | Stator Teeth |
| | 36 | 0.013Nm | Stator Teeth |
| | 39 | 0.010Nm | Pinion Teeth |

As can be seen in Figure 5.1 and Table 5.1, the largest component in the linear motor spectrum was found at 2 cycles/revolution. This component, along with the components at 1 and 4 cycles/revolution, can be attributed to the motor's electrical cycle and associated cogging forces. The only other significant component in the linear motor spectrum is the fundamental at 0.05 cycles/revolution, which does not represent a performance limitation.

In comparison to the linear motor, the spectra of the Drive Comparison Test-Bed configurations have more significant components. From Table 5.1 and Figures 5.2, 5.3 and 5.4, it can be seen that components at 18, 36 and 54 cycles/revolution are significant in all three configurations of the Drive Comparison Test-Bed. These frequency components have been attributed to the stator teeth of the rotary motor. The most signif-

icant transmission-related frequency component in the ballscrew configurations is at 1 cycle/revolution, which is the shaft cycle and is related to the alignment of the ballscrew itself. Another significant transmission-related component is at 39 cycles/revolution in the ballscrew configurations and has been attributed to the bearings of the ballscrew. The rack and pinion configuration also has a significant component at 39 cycles/revolution; however, this is related to the pinion teeth. The number of teeth of the pinion is identical to the number of balls cycled through one revolution of the ballscrew. There is an additional component at 0.68 cycles/revolution on the belt driven ballscrew configuration, which is due to the belt cycle (the belt in this system has 128 teeth and the two pulleys have 44 teeth – 88/128 = 0.68).

The DC components listed in Table 5.1 were used to determine the mechanical power required by the motors to overcome friction at 200mm/min. It was found that 0.068W of mechanical power was required from the linear motor to overcome friction. In comparison, the rotary motor supplied 1.3W, 1.34W and 0.04W to overcome friction in the direct driven ballscrew, belt driven ballscrew and rack and pinion configurations respectively. As expected, the mechanical power required to overcome friction was much more on the ballscrew configurations. With reduced power required to overcome friction and the elimination of all transmission-related periodic torque/force disturbances, linear motors offer clear advantages when used in precision linear machine axes.

## 5.3 Inherent Dynamic Stiffness in Feed Axes

A mathematical expression for the dynamic stiffness of a general linear feed axis was derived in Section 2.2.1 (Equation (2.6)). Using the same process, detailed expressions for the inherent dynamic stiffness of individual axis configurations are presented in this section. It should be noted that the transmission elements of each configuration have been assumed to be infinitely stiff, in order to reduce the complexity of each expression and allow for a concentrated comparison of dynamic stiffness. Also, since both the disturbance

force and the maximum position error are expressed linearly, all rotary system parameters have been referred to the linear load side.

Consider first the equation of motion for a linear motor driven axis (Equation (3.57)). For inherent dynamic stiffness the system is considered to be uncontrolled (ie $F_m$ = 0). If coulomb friction and the general periodic force variations are assumed to be negligible, the disturbance force required to produce the response of Equation (2.1) is described by:

$$F_d = M\left(-(2\pi f)^2 E_f \sin(2\pi f t)\right) + B\left(2\pi f E_f \cos(2\pi f t)\right) \tag{5.2}$$

It can be seen that Equation (5.2) is identical to the general disturbance force expression (Equation (2.4)) with the addition of a viscous friction term. The resulting dynamic stiffness expression for a linear motor driven axis is:

$$DS = \frac{|F_d|}{E} = 2\pi f\sqrt{M^2(2\pi f)^2 + B^2} \tag{5.3}$$

As a comparison, consider the dynamics of a direct driven ballscrew system (described in Section 3.5.1). If the ballscrew in this system is considered to be infinitely stiff, with coulomb friction and general periodic force variations considered negligible, the disturbance force required to produce the response of Equation (2.1) is described by:

$$\begin{aligned} F_d &= \left(M_L + \left(\frac{2\pi}{P_{BS}}\right)^2 (J_m + J_{BS})\right)\left(-(2\pi f)^2 E_f \sin(2\pi f t)\right) \\ &\quad + \left(\frac{2\pi}{P_{BS}}\right)^2 (B_m + B_l)\left(2\pi f E_f \cos(2\pi f t)\right) \end{aligned} \tag{5.4}$$

It is clear that Equation (5.4) has the same form as Equation (5.2), with the total mass (M) described by Equation (5.5) and the viscous friction co-efficient described by Equation (5.6). Hence, the dynamic stiffness expression of Equation (5.3) is also valid using the

substitutions given in Equations (5.5) and (5.6).

$$\mathrm{M} = \mathrm{M}_L + \left(\frac{2\pi}{\mathrm{P}_{BS}}\right)^2 (\mathrm{J}_m + \mathrm{J}_{BS}) \tag{5.5}$$

$$\mathrm{B} = \left(\frac{2\pi}{\mathrm{P}_{BS}}\right)^2 (\mathrm{B}_m + \mathrm{B}_l) \tag{5.6}$$

The disturbance force expressions for the belt driven ballscrew and rack and pinion configurations (when the transmission elements are considered to be infinitely stiff and both coulomb friction and general periodic force variations are considered negligible) also have the same form as Equation (5.2). Further, with the appropriate substitutions for mass and viscous friction co-efficients, the dynamic stiffness expression of Equation (5.3) is again valid for both of these configurations. For a belt driven ballscrew system (as described in Section 3.5.2), the total mass is described by Equation (5.7) and the viscous friction co-efficient is described by Equation (5.8).

$$\mathrm{M} = \mathrm{M}_L + \left(\frac{2\pi}{\mathrm{P}_{BS}}\right)^2 \left(\mathrm{J}_{BS} + \mathrm{J}_p + \left(\frac{\mathrm{R}_p}{\mathrm{R}_m}\right)^2 \mathrm{J}_m\right) \tag{5.7}$$

$$\mathrm{B} = \left(\frac{2\pi}{\mathrm{P}_{BS}}\right)^2 \left(\mathrm{B}_l + \mathrm{B}_p + \left(\frac{\mathrm{R}_p}{\mathrm{R}_m}\right)^2 \mathrm{B}_m\right) \tag{5.8}$$

For a rack and pinion system (as described in Section 3.5.3), the total mass is described by Equation (5.9) and the viscous friction co-efficient is described by Equation (5.10).

$$\mathrm{M} = \mathrm{M}_L + \frac{1}{\mathrm{r}^2} (\mathrm{J}_m + \mathrm{J}_s + \mathrm{J}_{PIN}) \tag{5.9}$$

$$\mathrm{B} = \frac{1}{\mathrm{r}^2} (\mathrm{B}_m + \mathrm{B}_l) \tag{5.10}$$

For each of the rotary motor configurations, the total mass and viscous friction seen by the load are very dependent on the gearing of the transmission system. In both of the ballscrew configurations (Equations (5.5) to (5.8)), the total mass and viscous friction increase as the pitch of the ballscrew becomes finer. Consequently, the inherent dynamic stiffness of these configurations also increases as the ballscrew pitch becomes finer. For

the belt driven ballscrew configuration (Equations (5.7) and (5.8)), the total mass and viscous friction increase further as the ballscrew side pulley becomes larger than the motor side pulley. In a rack and pinion configuration (Equations (5.9) and (5.10)), the mass and viscous friction increase as the radius of the pinion decreases. Since the pitch of most ballscrews (used in machine tool feed axes) is in the low mm range, the inherent dynamic stiffness is generally much higher in ballscrew driven axes when compared with linear motor or rack and pinion driven axes (although the stiffness of rack and pinion driven axes is often improved through the use of gearboxes).

To further compare the inherent dynamic stiffness of the common drive configurations, the disturbance forces required to exceed position error tolerances of $10\mu m$, $5\mu m$ and $1\mu m$ were calculated for the Linear Motor Test-Bed and all three configurations of the Drive Comparison Test-Bed. For an accurate comparison of the required disturbance forces, actual system parameters (as detailed in Chapter 4) and detailed models of each test-bed configuration (that included both stiffness and damping of the transmission elements) were used in these calculations. Due to the added complexity of including stiffness and damping, Matlab was used to calculate all of the disturbance forces (the Matlab functions used for these calculations are given in Appendix C).

Figure 5.5 shows the required disturbance forces (plotted against frequency) for the Linear Motor Test-Bed. Similarly, Figures 5.6, 5.7 and 5.8 show the required disturbance forces (plotted against frequency) for the Drive Comparison Test-Bed in direct driven ballscrew, belt driven ballscrew and rack and pinion configurations respectively. The disturbance forces required to exceed the given position error tolerances when the load mass of each configuration was increased to 200kg are also shown in Figures 5.5, 5.6, 5.7 and 5.8.

Consider the Linear Motor Test-Bed subject to a typical machining force of 60N. With the standard load mass of 23kg and a position error tolerance of $10\mu m$, Figure 5.5 shows that the system will inherently provide the required stiffness for frequencies above 510rad/s (approx.). When the position error tolerance is tightened to $1\mu m$, the required stiffness is only provided at frequencies much higher than the 1000rad/s limit of Figure 5.5. If

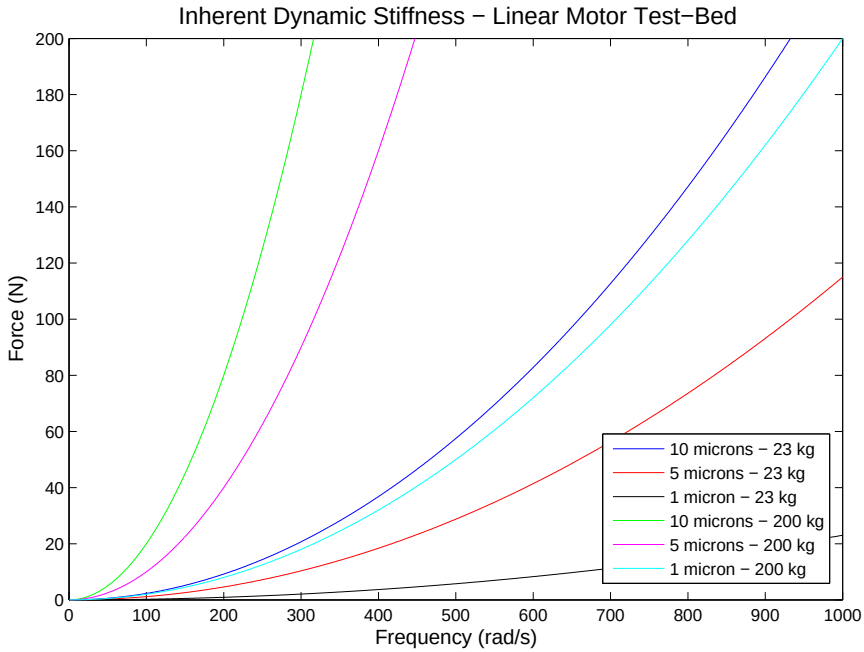


Figure 5.5: Disturbance Forces vs Frequency - Linear Motor

the load mass is increased to 200kg though, the $10\mu m$ tolerance is inherently satisfied at frequencies above 175 rad/s and the $1\mu m$ tolerance is inherently satisfied at frequencies above 550rad/s.

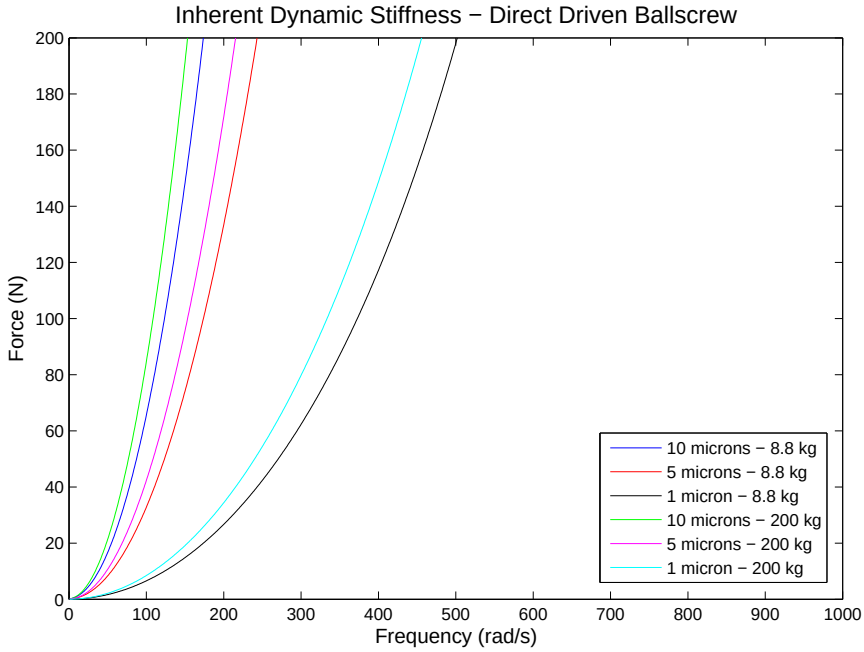


Figure 5.6: Disturbance Forces vs Frequency - Direct Driven Ballscrew

Consider the same 60N machining force applied to the three Drive Comparison Test-Bed configurations. Figure 5.6 shows that for the standard load mass of 8.8kg and a position error tolerance of $10\mu m$, the direct driven ballscrew configuration will inherently provide the required stiffness for frequencies above 95rad/s (approx.). When the position error tolerance is tightened to $1\mu m$, the required stiffness is still provided for frequencies above 295rad/s. As expected, the ballscrew driven system inherently provides the required stiffness at much lower frequencies than the linear motor driven system, even though the Drive Comparison Test-Bed has a lower standard load mass. In further contrast to the Linear Motor Test-Bed, increasing the load mass to 200kg on the directly driven ballscrew configuration only results in a marginal improvement to the dynamic stiffness of the system.

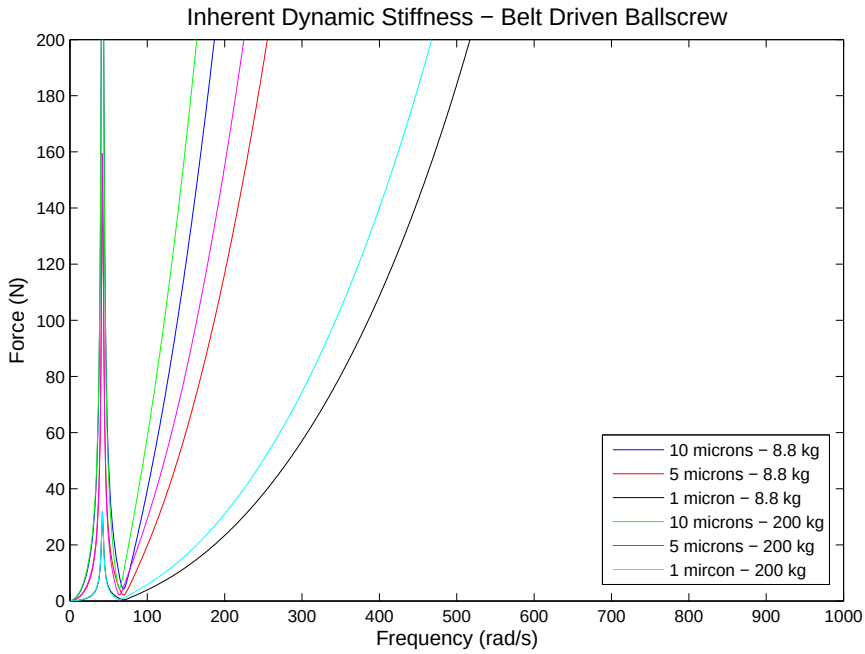


Figure 5.7: Disturbance Forces vs Frequency - Belt Driven Ballscrew

In Figure 5.7 it can be seen that the belt driven ballscrew configuration has low frequency peaks in the required disturbance forces, for all position error tolerances. These peaks are due to the low stiffness of the belt. When comparing Figure 5.7 with Figure 5.6 though, it can also be seen that the belt driven ballscrew configuration still provides the required stiffness at very similar frequencies to the direct driven ballscrew configuration (again for all position error tolerances). This is expected as the ballscrew and motor side pulleys are

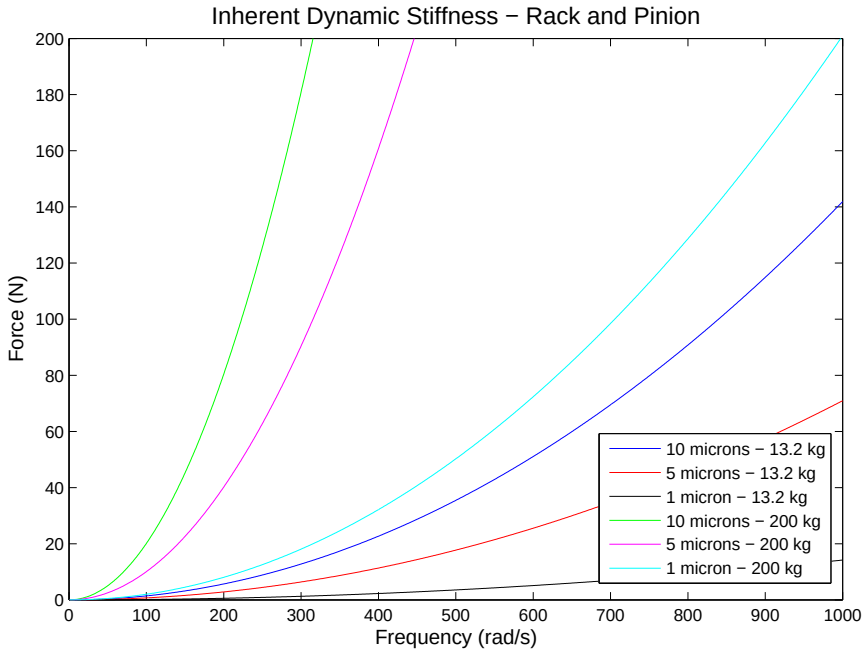


Figure 5.8: Disturbance Forces vs Frequency - Rack and Pinion

the same size on the Drive Comparison Test-Bed.

When comparing Figure 5.8 with Figure 5.5, it can be seen that the inherent dynamic stiffness of the rack and pinion configuration is almost identical to that of the Linear Motor Test-Bed, particularly when the load masses are identical (as in the 200kg cases). Although the inherent dynamic stiffness of the rack and pinion configuration can be improved through the use of an additional gearbox, this also introduces more sources of backlash and component wear. In contrast, the inherent dynamic stiffness of the ballscrew driven configurations was shown to be much higher than that of the Linear Motor Test-Bed. The dynamic stiffness of the ballscrew configurations was also less affected by changes in load mass.

## 5.4 Controller Design for High Dynamic Stiffness

Control systems are the primary means of increasing low dynamic stiffness in feed axes. For this reason, research effort in increasing dynamic stiffness (of linear motor feed axes

in particular) has been applied at many different levels of the overall machine tool control system. However, as discussed in Section 2.2.2, the velocity and position control loops are often the most practical levels at which dynamic stiffness can be addressed in standard servo drives. In this section, the important aspects of designing velocity and position control loops for high dynamic stiffness are studied.

The most common control schemes used for velocity and position loops in standard servo drives consist of P, PI or PID regulators. Although it is possible to achieve quite high dynamic stiffness with these control schemes, the common design approaches often concentrate solely on transient performance with respect to the velocity and position reference commands. Hence, the degree of dynamic stiffness in such systems can become arbitrary. In Section 5.4.1, the dynamic stiffness of the Linear Motor Test-Bed and all three configurations of the Drive Comparison Test-Bed are compared using the standard control schemes of the CNC system and the manufacturer's tuning guidelines. In Section 5.4.2, a QFT design approach that includes dynamic stiffness as one of the design specifications is described, with an example design shown for the Linear Motor Test-Bed. The QFT based design for the Linear Motor Test-Bed is then experimentally tested in Section 5.4.3.

### 5.4.1 Standard Control of the Experimental Systems

For the digital servo drives (of the CNC system) used in this thesis, the standard velocity and position control consisted of cascaded PI velocity and P position loops. The manufacturer's recommendations for machine tool feed axes are for the velocity and position control loops to have the highest possible closed-loop bandwidth, whilst not exceeding maximum closed-loop gains of 5dB for the velocity loop and 0dB for the position loop. The recommended tuning method involves iteratively increasing the proportional gain of the velocity loop until the maximum closed-loop gain is around 3dB. The integral action of the velocity loop is then increased until the 5dB closed-loop limit is reached. The position loop is subsequently tuned by iteratively increasing the proportional gain to the highest possible value without exceeding 0dB. Although there are a number of other well

recognised methods for tuning P and PI regulators, methods that involve increasing the gains until sustained oscillation is achieved (such as Ziegler-Nichols second method) are generally avoided on machine tool feed axes for safety reasons. Hence, the manufacturers recommended tuning method was used in this section.

In order to compare the dynamic stiffness of different linear feed axis configurations under the standard control structure (PI velocity, P position) and the manufacturer's recommended tuning, a 125N step disturbance force was applied to the load side of the Linear Motor Test-Bed and all three configurations of the Drive Comparison Test-Bed. During each of these tests the CNC system was in steady-state position control, with a reference position of zero. The response of the Linear Motor Test-Bed is shown in Figure 5.9.

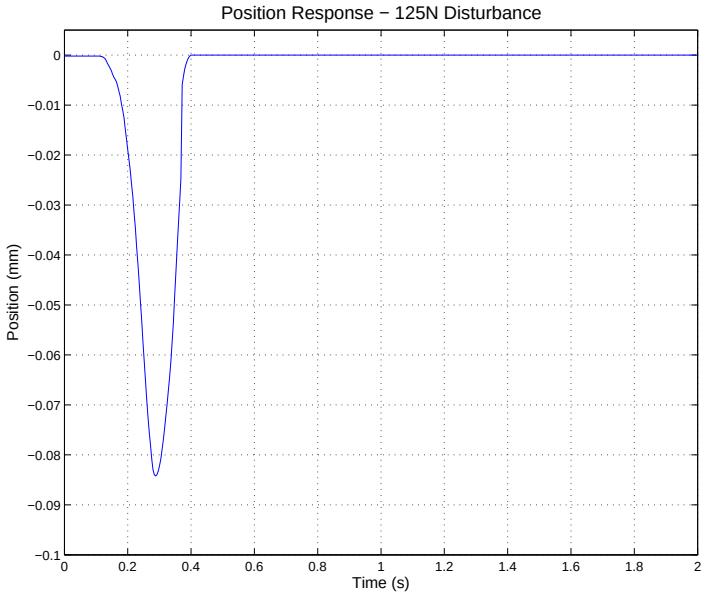


Figure 5.9: Linear Motor Position (125N Disturbance)

A maximum position error of approximately $85\mu m$ can be seen in the linear motor response of Figure 5.9. In an actual machine tool, a position error of this magnitude could result in poor surface finish on the work piece. The responses of the Drive Comparison Test-Bed in the direct driven ballscrew and belt driven ballscrew configurations are shown in Figures 5.10 and 5.11 respectively.

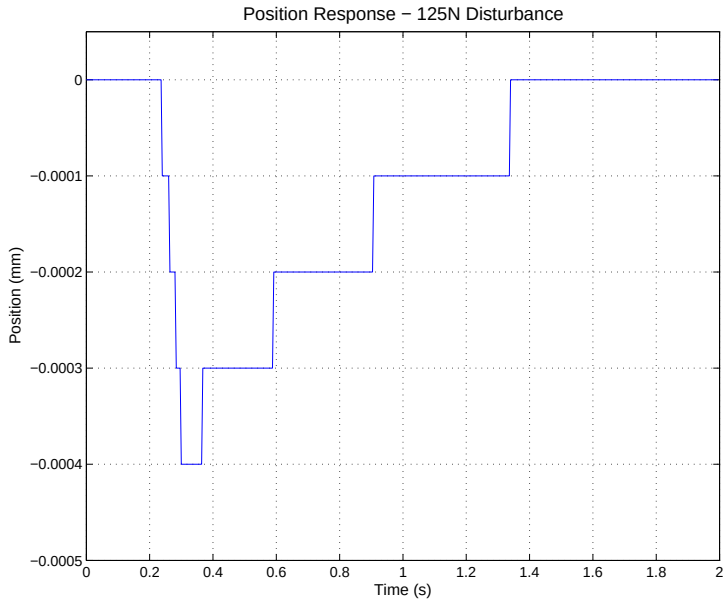


Figure 5.10: Direct Driven Ballscrew Position (125N Disturbance)

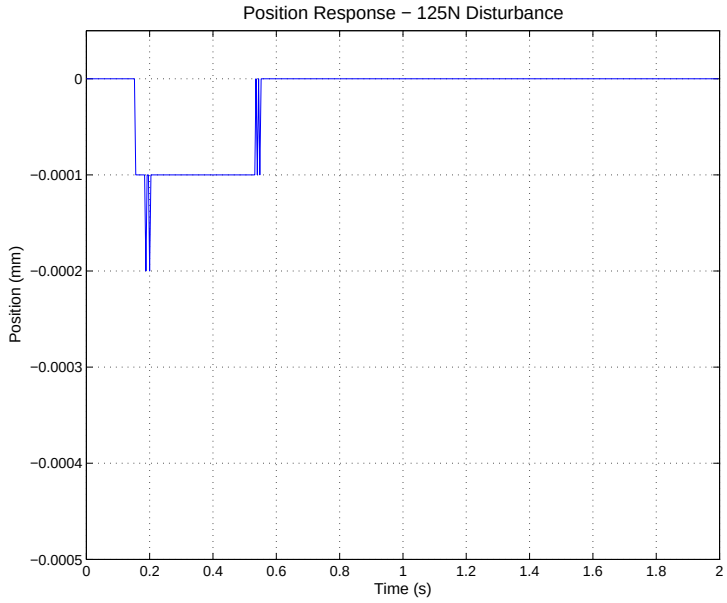


Figure 5.11: Belt Driven Ballscrew Position (125N Disturbance)

A maximum position error of $0.4\mu m$ can be seen in the direct driven ballscrew response of Figure 5.10. The position error of the direct driven ballscrew can be seen to be very close to the resolution of the CNC system's data logger, which is $0.1\mu m$. Further, the belt driven ballscrew response of Figure 5.11 exhibits an even lower maximum position error

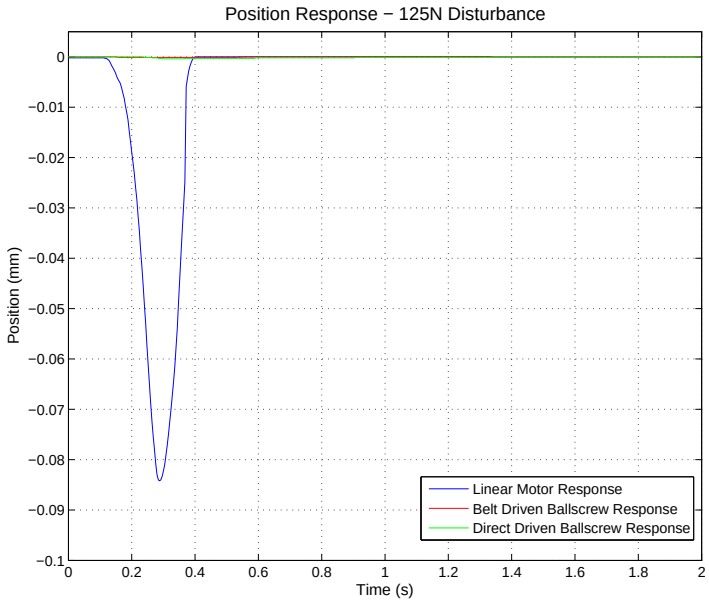


Figure 5.12: Linear Motor and Ballscrew Positions (125N Disturbance)

of $0.2\mu m$. For a direct comparison with the Linear Motor Test-Bed, the two ballscrew responses are shown on the same graph as the linear motor response in Figure 5.12.

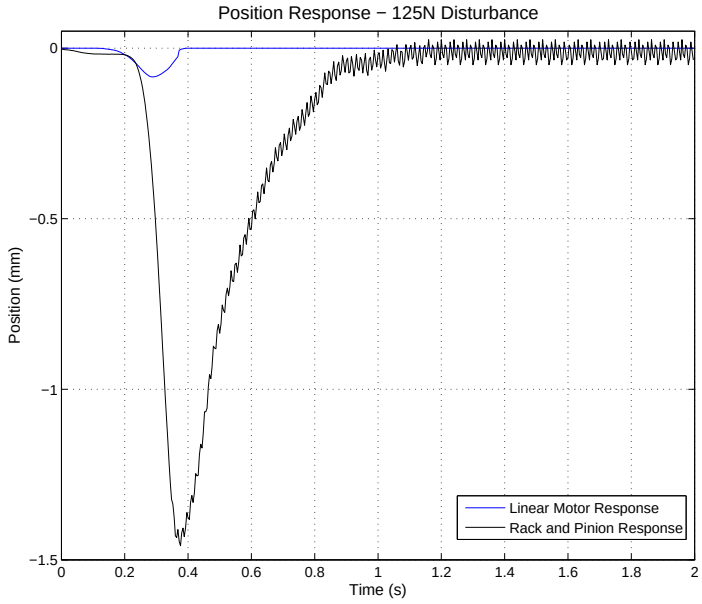


Figure 5.13: Linear Motor and Rack and Pinion Positions (125N Disturbance)

In Figure 5.13, the response of the linear motor is shown on the same graph as the response of the Drive Comparison Test-Bed in the rack and pinion configuration. Although the

inherent dynamic stiffness of the rack and pinion configuration was shown to be almost identical to that of the Linear Motor Test-Bed in Section 5.3, it can be seen in Figure 5.13 that the rack and pinion response exhibits a much higher maximum position error of almost 1.5*mm*. The reason for such a high position error is that the standard tuning of the control system is severely limited by the backlash in the rack and pinion configuration. Along with the poor disturbance response exhibited by this configuration, the oscillations introduced by the backlash are clearly visible in Figure 5.13.

The results presented throughout this section clearly show that while the ballscrew driven axes exhibited very high dynamic stiffness under the manufacturer's standard velocity and position control, the linear motor and rack and pinion driven axes exhibited poor dynamic stiffness. The poor performance of the rack and pinion configuration was primarily due to the backlash in this system. However, the poor performance of the linear motor was primarily due to insufficient integral action in the controller design. The reason for the low integral action was that the design approach concentrated on overall system bandwidth and not disturbance rejection. The integral action in this design approach was only iteratively added up to the point where the closed-loop gain reached the maximum specification of 5db. In Section 5.4.2, a QFT design approach that includes both system bandwidth and disturbance rejection as design specifications is presented.

### 5.4.2 A QFT Design Approach for High Dynamic Stiffness

From the literature reviewed in Section 2.2.2, it was found that robust techniques, such as $H_\infty$ and sliding mode control, had been successfully used to improve the dynamic stiffness of linear motor driven axes. However, the QFT technique was completely absent from the available literature. In this section, a QFT design approach for high dynamic stiffness is presented, along with an example design for the Linear Motor Test-Bed. The Linear Motor Test-Bed was chosen due to its low inherent dynamic stiffness (as shown in Section 5.3) and the fact that the reduced mechanical system of this test-bed allowed for

an analysis of dynamic stiffness that would not be affected by additional factors such as backlash. The presented approach can be extended to other axis configurations.

The QFT design objective is to design and implement robust controllers that satisfy a set of desired performance specifications for the system. This design process is usually undertaken on systems with structured parametric uncertainty; however, it can also be effective on plants with constant parameters. A block diagram representing the standard QFT design problem is shown in Figure 5.14.

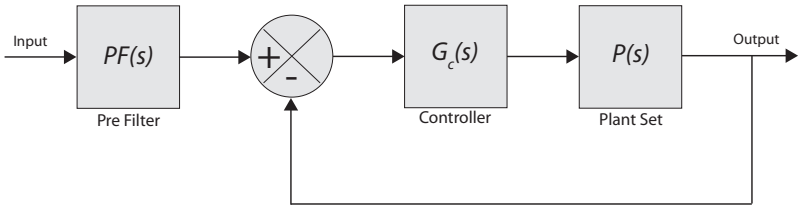


Figure 5.14: QFT Design Block Diagram

In Figure 5.14, $P(s)$ represents the complete set of plants that describe the range of parametric uncertainty of an actual plant. The loop controller $G_c(s)$ is designed, through loop shaping on the Nichols Chart, such that the closed loop stability and disturbance bounds are satisfied for the complete set of plants. The loop controller $G_c(s)$ is also used to ensure that the closed loop uncertainty is within the range specified by any robust tracking bounds. The Pre Filter $PF(s)$, if required, is used to shape the complete closed loop response to satisfy the upper and lower limits of the robust tracking bounds. A very thorough survey of QFT and its applications is provided by Horowitz (the original author of QFT) [15]. Another comprehensive treatment of QFT, including the detailed steps involved in a complete design, is given by Houpis and Rasmussen [102]. The design steps for all of the QFT designs developed in this thesis can be summarised by:

1. Determination of the desired set of closed loop performance specifications in the frequency domain (the performance specifications may consist of stability, tracking and disturbance specifications).
2. Determination of plant templates that can pictorially describe the region of open loop plant parameter uncertainty on the Nichols Chart.

3. Computation of bounds that can be plotted on the Nichols Chart to describe the performance specifications at specified frequencies of interest. These bounds are constraints that a nominal open loop plant transfer function must satisfy at each frequency of interest, so that the complete set of plant templates satisfy the closed loop performance specifications.
4. Design of the loop controllers (and Pre Filter if necessary) by manual loop shaping, such that the controlled nominal plant satisfies all performance bounds.
5. Detailed analysis of the design, through simulation, to verify that the performance specifications have been met.

Detailed procedures associated with each of these five steps are presented in this section.

**1. Determination of the closed loop performance specifications.**

The cascaded velocity and position loop structure of the experimental CNC system was maintained in the QFT design approach, since this structure is typical of that found in industrial servo controllers. The complete velocity and position control structure for the Linear Motor Test-Bed, subject to an external load disturbance, can be illustrated by the block diagram of Figure 5.15, where $P_{lm}(s)$ describes the complete set of plants (details of the plant set for the example design are provided at Step 2).

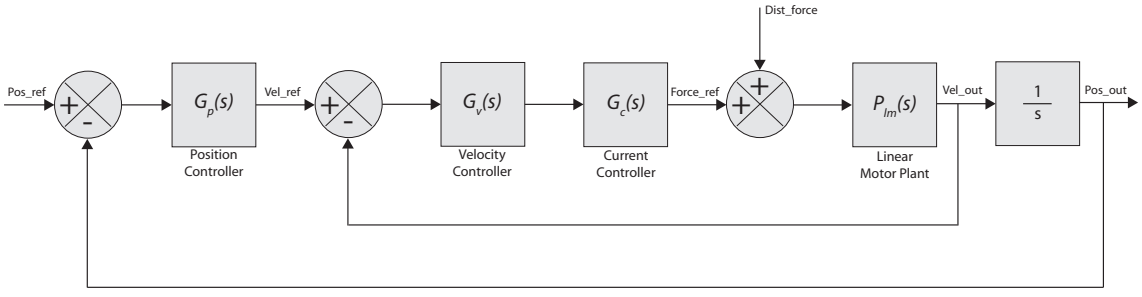


Figure 5.15: Block Diagram of Velocity and Position Loops

For the Linear Motor Test-Bed, the current controller ($G_c(s)$) is described by Equations (4.7) and (4.8). The velocity and position controllers shown in Figure 5.15 ($G_v(s)$ and $G_p(s)$) are determined throughout the design process. Complete details of the final controllers for the example design are given at each of the relevant steps in this section.

In Step 1 the QFT technique requires all closed-loop performance specifications to be described in the frequency domain. Hence, the frequency domain relationships between each input and output of interest must be determined. For the system shown in Figure 5.15, the output velocity (Vel_out) for a given velocity reference (Vel_ref) and a zero disturbance force (Dist_force = 0) is described by the transfer function given in Equation (5.11). Similarly, the output position (Pos_out) for a given position reference (Pos_ref) and a zero disturbance force (Dist_force = 0) is described by the transfer function given in Equation (5.12).

$$\frac{\text{Vel\_out}}{\text{Vel\_ref}} = \frac{G_v(s)G_c(s)P_{lm}(s)}{1+G_v(s)G_c(s)P_{lm}(s)} \tag{5.11}$$

$$\frac{\text{Pos\_out}}{\text{Pos\_ref}} = \frac{G_p(s)G_v(s)G_c(s)P_{lm}(s)}{s(1+G_v(s)G_c(s)P_{lm}(s))+G_p(s)G_v(s)G_c(s)P_{lm}(s)} \tag{5.12}$$

Again for the system shown in Figure 5.15, the output velocity (Vel_out) for a given disturbance force (Dist_force) and a zero velocity reference (Vel_ref = 0) is described by the transfer function given in Equation (5.13). Similarly, the output position (Pos_out) for a given disturbance force (Dist_force) and a zero position reference (Pos_ref = 0) is described by the transfer function given in Equation (5.14).

$$\frac{\text{Vel\_out}}{\text{Dist\_force}} = \frac{P_{lm}(s)}{1+G_v(s)G_c(s)P_{lm}(s)} \tag{5.13}$$

$$\frac{\text{Pos\_out}}{\text{Dist\_force}} = \frac{P_{lm}(s)}{s(1+G_v(s)G_c(s)P_{lm}(s))+G_p(s)G_v(s)G_c(s)P_{lm}(s)} \tag{5.14}$$

Since the velocity loop is faster than the outer position loop it is important that both tracking and dynamic stiffness are addressed at this level. Hence, velocity loop performance specifications are determined for stability, robust tracking and disturbance rejection:

- Stability – the velocity loop stability specification consists of an upper bound on the gain magnitude of the closed-loop velocity response (Equation (5.11)) for all frequencies. For the example design, this specification was set such that the closed-loop velocity response of the Linear Motor Test-Bed did not exceed the CNC manufacturer's recommendation of 5dB.

- Robust Tracking – the velocity loop tracking specification consists of upper and lower bounds on the closed-loop velocity response (Equation (5.11)), which the complete set of plants $P_{lm}(s)$ must satisfy. Generally these bounds are based on the desired closed-loop bandwidth, with the upper bound chosen to be a fast underdamped response and the lower bound chosen to be a slower overdamped response. For the example design, the desired closed-loop bandwidth of the Linear Motor Test-Bed was chosen to be 1000 rad/s (which is equivalent to the bandwidth achieved using the manufacturer's standard tuning technique). The upper and lower tracking bounds were then chosen to provide an allowable margin, for the entire set of closed-loop velocity responses, about this bandwidth. The upper tracking bound (Tru) and lower tracking bound (Trl) are given in Equations (5.15) and (5.16) respectively. Figure 5.16 shows the frequency responses of these bounds.

$$\text{Tru} = \frac{\frac{s}{3000}+1}{\frac{s^2}{1100^2}+\frac{0.7s}{1100}+1} \tag{5.15}$$

$$\text{Trl} = \frac{1}{\left(\frac{s}{1200}+1\right)\left(\frac{s^2}{900^2}+\frac{3s}{900}+1\right)} \tag{5.16}$$

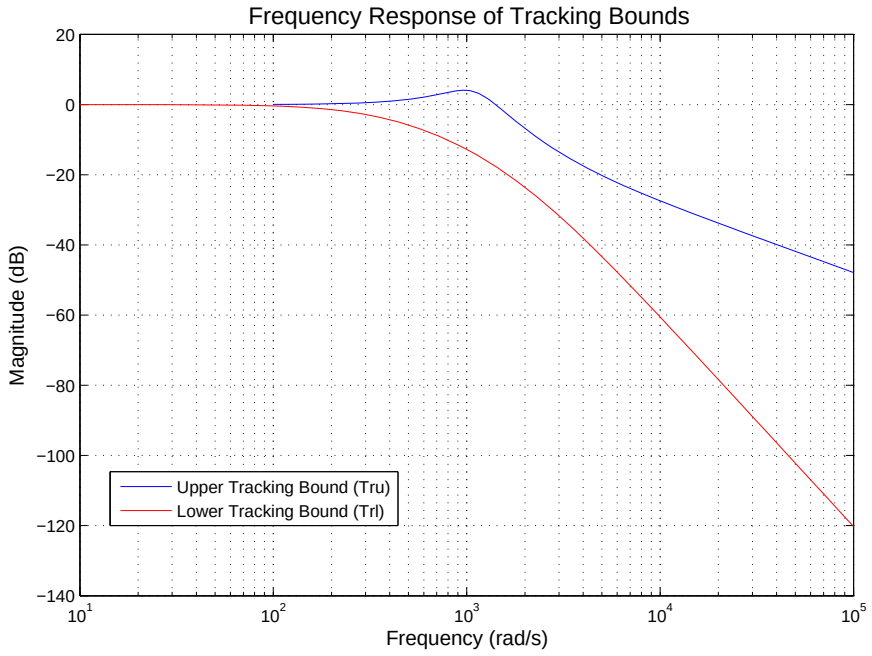


Figure 5.16: Upper and Lower Robust Tracking Bounds

- Disturbance Rejection – To ensure high dynamic stiffness, the closed-loop system must have low sensitivity to force disturbances at the load. Hence, the velocity loop disturbance specification consists of a bound on the velocity disturbance response (Equation (5.13)), such that load force disturbances are attenuated to an acceptable level at all frequencies. With reference to Equation (2.6), it can be seen that the required level of attenuation at each frequency is determined by specifying an allowable peak position error (E) for a particular disturbance force. If the velocity loop was solely responsible for meeting this position error specification, the allowable peak velocity at each frequency would then be $\omega$E (Equation (2.2)). It can be seen from Figure 5.15 and Equation (5.14) that the position loop also contributes to the overall dynamic stiffness. However, since the velocity loop is faster than the position loop, a limit of $\omega$E on the peak velocity will guarantee the required stiffness. Any additional contribution from the position loop will only improve the overall dynamic stiffness. For the example design, a maximum peak position error of 5$\mu$m was specified for a peak disturbance force of 125N at all frequencies. A disturbance bound of $D_{bv}(s) = 4 \times 10^{-8} s \ \left(\frac{5e^{-6}}{125} s\right)$ was hence set for the velocity disturbance response of the Linear Motor Test-Bed.

The only position loop specification that is required in this design is the stability specification, as the overall tracking and dynamic stiffness requirements have already been addressed at the velocity loop level. Since dynamic stiffness is specified via a limit on the peak position error, a position disturbance specification has however been included for completeness. Hence, the position loop specifications in this design approach are:

- Stability – the position loop stability specification consists of an upper bound on the gain magnitude of the closed-loop position response (Equation (5.12)) for all frequencies. For the example design, this specification was set such that the closed-loop position response of the Linear Motor Test-Bed did not exceed the CNC manufacturer's recommendation of 0dB.
- Disturbance Rejection – The position loop disturbance specification consists of a bound on the position disturbance response (Equation (5.14)), such that the allow-

able peak position error (for a specified peak disturbance force) is not exceeded at all frequencies. For the example design, the maximum peak position error of $5\mu$m (at 125N) results in a disturbance bound of $D_{bp}(s) = 4 \times 10^{-8}$ (-148dB) on the position disturbance response of the Linear Motor Test-Bed.

### 2. Determination of Plant Templates

Since $P_{lm}(s)$ in Figure 5.15 describes a set of plants with a range of parametric uncertainty, there is a corresponding region of uncertainty in the response of $P_{lm}(s)$ at any given frequency. Equation (3.57) was used to describe the Linear Motor Test-Bed for the example design, with the test-bed mass considered to be uncertain within the range 10kg to 100kg and all other system parameters considered to be constant (as detailed in Table 4.8).

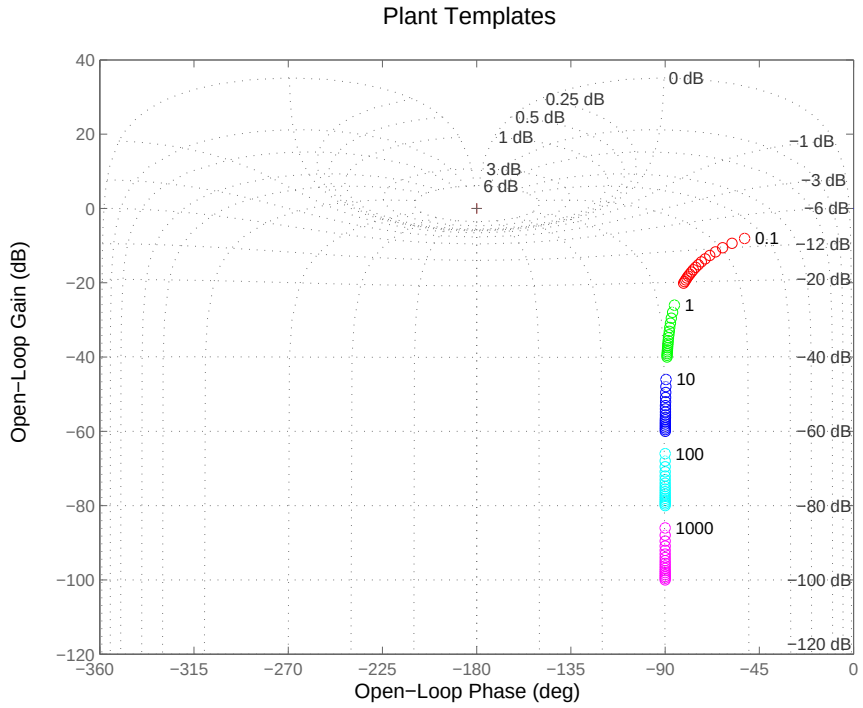


Figure 5.17: Plant Templates - Linear Motor Test-Bed

The region of parametric uncertainty in the response of $P_{lm}(s)$ is important in the QFT design process as the complete set of plants must satisfy each performance specification. Hence, plant templates are used to describe the region of uncertainty at each frequency of

interest. Plant templates can generally be represented by their boundaries on the Nichols Chart; however, a sufficient number of points on the boundary must be selected so that the contour of the template accurately reflects the region of uncertainty.

The plant templates (at 0.1, 1, 10, 100 and 1000 rad/s) for the example design are shown in Figure 5.17. Each circle shown in Figure 5.17 represents an individual point on a template boundary. It can be seen that the plant templates in this case are described by simple continuous curves, due to the single uncertain parameter.

**3. Computation of the Nichols Chart Performance Bounds**

Nichols Chart performance bounds are determined for each of the performance specifications detailed in Step 1 (with the exception of the position loop disturbance specification). The bounds are determined using the plant templates at particular frequencies of interest, such that if a nominal open-loop plant ($P_{nom}$) satisfies a bound on the Nichols Chart then the complete set of controlled plants will meet the related closed-loop performance specification. Although any plant belonging to the complete set of open-loop plants can be chosen as the nominal plant, it is common practice to use the plant represented by the bottom left corner of the template boundaries. Since the templates in the example design are described by simple continuous curves, the plant represented by the lowest point on the template boundaries was chosen as the nominal plant.

The final Nichols Chart bounds for the velocity loop are shown in Figure 5.18. These bounds represent the most stringent of the design requirements and are a combination of the individual stability, tracking and disturbance bounds. The bounds for the velocity stability specification were determined at frequencies of 1, 10, 20, 50, 100, 200, 500, 1000, 2000 and 5000 rad/s. This set of frequencies was chosen to cover the desired closed-loop bandwidth, since the stability specification consisted of an upper limit of 5dB for all frequencies. The stability bounds form an enclosed area at the centre of the Nichols Chart shown in Figure 5.18. At each frequency of interest, the nominal plant must be outside the area enclosed by the associated stability bound.

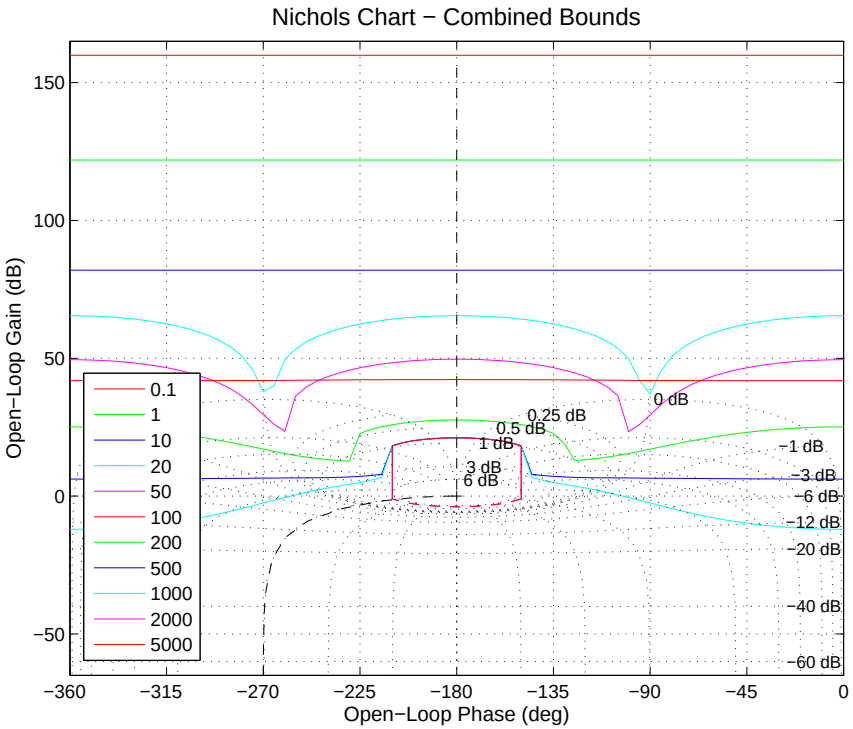


Figure 5.18: Velocity Loop Combined Bounds - Linear Motor Test-Bed

Since the velocity loop tracking specification is based on the desired closed-loop bandwidth, the Nichols Chart bounds for the tracking specification were determined at the same frequencies as the stability bounds. The bounds for the velocity loop disturbance specification were determined at frequencies of 0.1, 1, 10, 100 and 1000 rad/s. This set of frequencies was chosen after examining the inherent dynamic stiffness of the Linear Motor Test-Bed. From Figure 5.5, it can be seen that the lower frequencies are of most interest when designing a control system for high dynamic stiffness. As the frequency increases above 1000 rad/s, the physical system becomes capable of inherently supplying the required stiffness.

At each frequency of interest, the nominal plant must be above the associated tracking and disturbance bounds on the Nichols Chart. Hence, only the highest bounds at each frequency, or the intersection that results in the highest overall bound, is required for loop shaping. For example, the stability and tracking bounds at 1, 10 and 100 rad/s do not form part of the critical bounds shown in Figure 5.18, as the associated disturbance bounds at these frequencies placed a higher demand on the control system design. Further, the

bounds at 500 and 1000 rad/s in Figure 5.18 were constructed from the upper intersection of the individual performance bounds at those frequencies.

Position loop bounds are determined in the same manner as velocity loop bounds. However, the position loop bounds should not be determined until the velocity loop design has been completed, as these bounds are dependent on the final velocity loop design.

**4. Design of Loop Controllers and Pre Filter**

The design of loop controllers in QFT involves a manual shaping process, such that the nominal loop transmission function ($L_{nom}$) satisfies all of the Nichols Chart bounds. For the velocity loop shown in Figure 5.15, the nominal loop transmission function is:

$$L_{nom} = G_v(s)G_c(s)P_{nom} \tag{5.17}$$

For the example design, the final shape of the nominal velocity loop transmission function is shown in Figure 5.19. It can be seen that this transmission function satisfies all of the final performance bounds. The associated velocity controller is given in Equation (5.18).

$$G_v(s) = 3.75 \times 10^5 \left( \frac{\left(\frac{s}{315}+1\right)\left(\frac{s}{5000}+1\right)}{s} \right) \tag{5.18}$$

The closed-loop velocity frequency responses, for the complete set of plants, are shown in Figure 5.20 (dark blue curves). Although the complete set of controlled plant responses can be seen to satisfy the stability bound, the responses are outside the upper and lower tracking bounds. The reason for this is that the loop controller $G_c(s)$ only ensures that the closed loop uncertainty is within the range specified by the robust tracking bounds. In this case a simple Pre Filter is required to shape the complete set of controlled plants so that they satisfy the upper and lower limits of the robust tracking bounds. In terms of the overall control structure shown in Figure 5.15 the Pre Filter would be placed directly after the Position Controller.

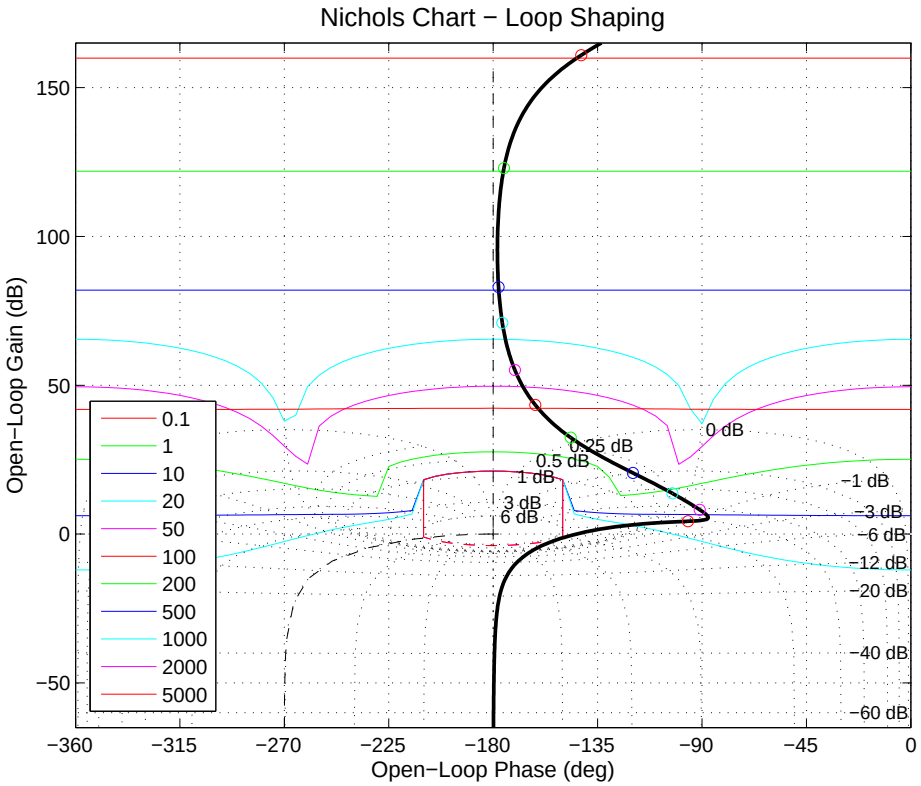


Figure 5.19: Loop Shaping – Dynamic Stiffness Controller

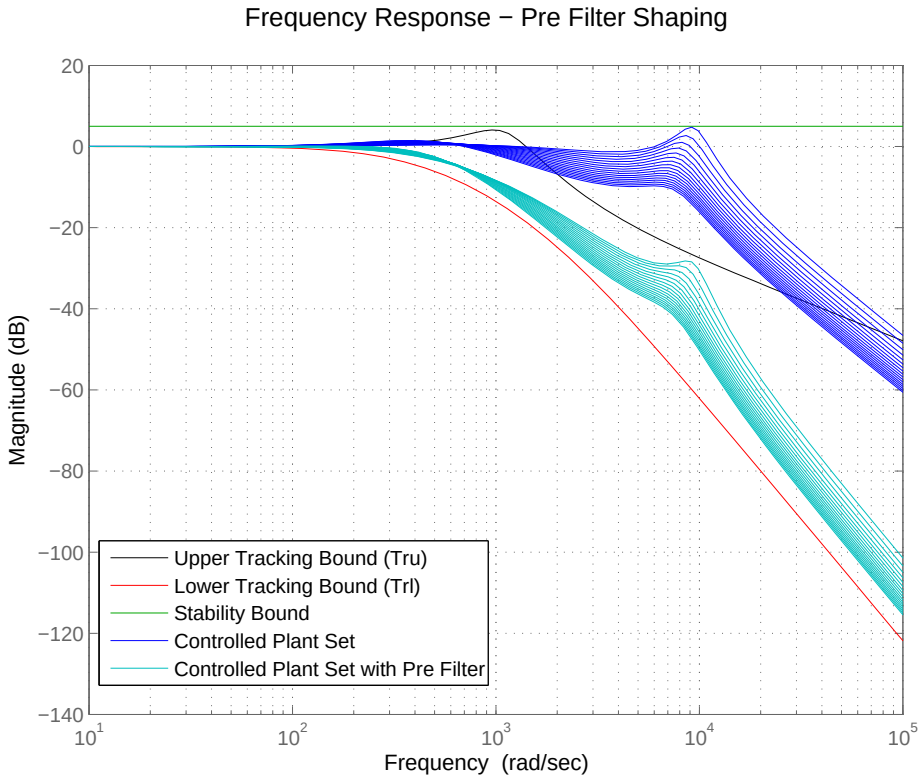


Figure 5.20: Velocity Loop Pre Filter Design - Dynamic Stiffness Controller

The Pre Filter design for this system is given in Equation (5.19). The velocity loop frequency responses with the Pre Filter are also shown in Figure 5.20 (cyan curves). It can be seen that with the addition of the Pre Filter, the complete set of controlled plant responses satisfy the upper and lower tracking bounds.

$$G_{vpf}(s) = \frac{\left(\frac{s}{5000}+1\right)}{\left(\frac{s}{450}+1\right)\left(\frac{s}{2000}+1\right)} \tag{5.19}$$

The position loop design is undertaken in the same manner as the velocity loop design. The nominal loop transmission function for the position loop is:

$$L_{nom} = G_p(s)\left(\frac{P_{v\_nom}(s)}{s}\right) \tag{5.20}$$

where:

$$P_{v\_nom}(s) = G_{vpf}(s)\left(\frac{G_v(s)G_c(s)P_{nom}(s)}{1+G_v(s)G_c(s)P_{nom}(s)}\right) \tag{5.21}$$

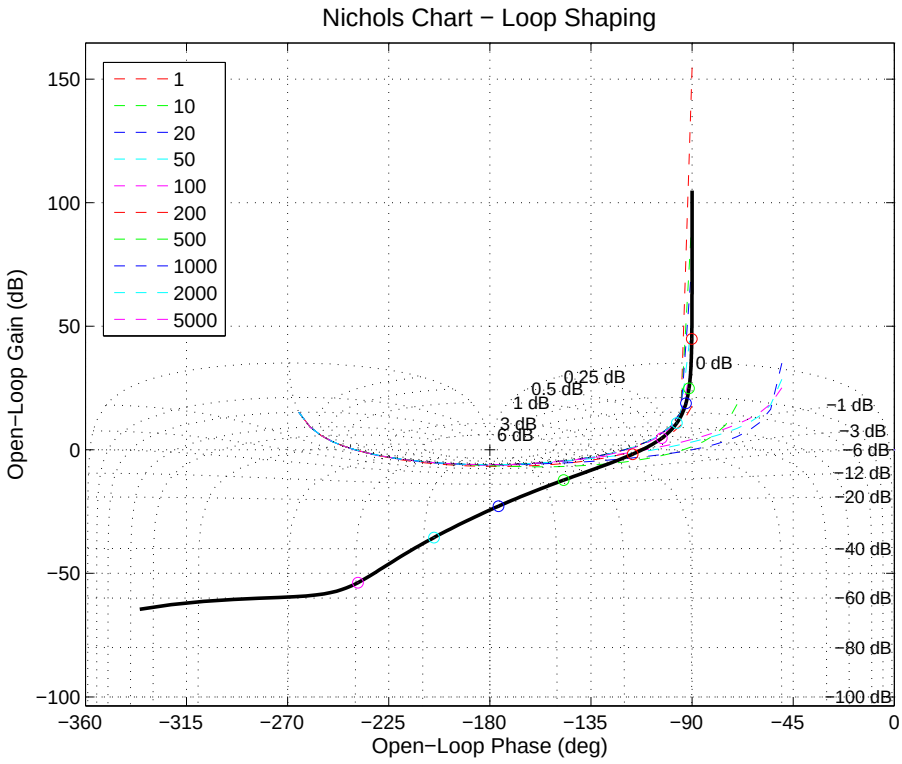


Figure 5.21: Position Loop Shaping - Dynamic Stiffness Controller

The final shape of the nominal position loop transmission function is shown in Figure 5.21. Although there are four stability bounds that cross the loop transmission function, these bounds are above the transmission function at the associated frequencies (500, 1000, 2000 and 5000 rad/s). Hence, the final transmission function satisfies all of the position loop performance bounds. The associated position controller consists of a simple proportional gain:

$$G_p(s) = 175 \tag{5.22}$$

**5. Analysis of the Design**

The final step in the QFT approach is to analyse the design and verify that all of the performance specifications have been met. For the velocity loop, the stability and robust tracking specifications have already been verified through the responses shown in Figure 5.20. The velocity loop disturbance responses (Equation (5.13)), for the complete set of controlled plants, are shown in Figure 5.22. It can be seen that all of the responses satisfy the disturbance bound of $D_{bv}(s) = 4 \times 10^{-8}s$.

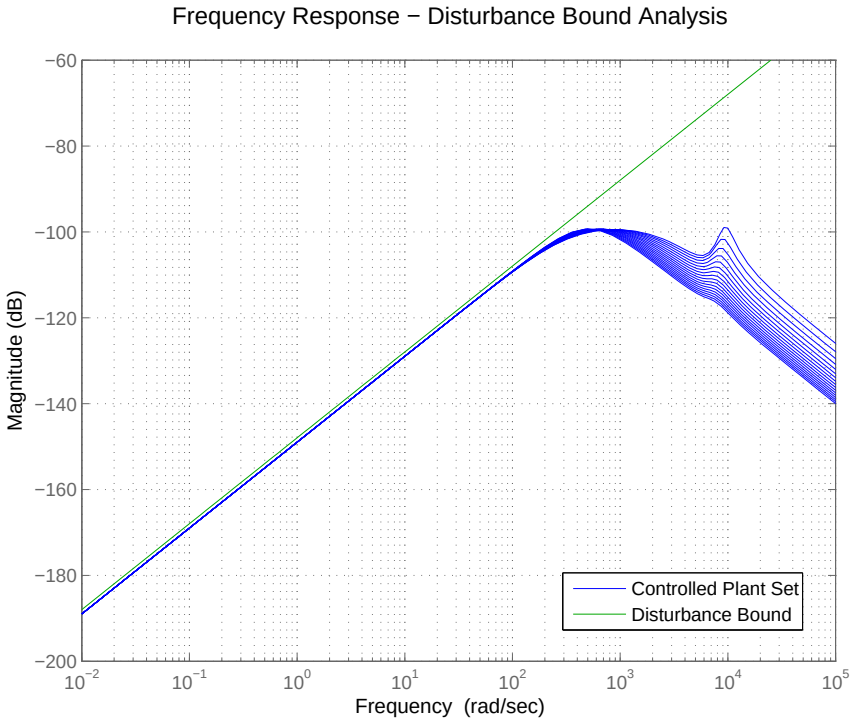


Figure 5.22: Velocity Loop Disturbance Analysis - Dynamic Stiffness Controller

The position loop frequency responses, for the complete set of controlled plants, are shown in Figure 5.23 (dark blue curves). It can be seen that all of the responses satisfy the stability performance specification (0dB upper limit). The position disturbance responses, for the complete set of controlled plants, are also shown in Figure 5.23 (cyan curves). Although the disturbance specification was addressed at the velocity loop design stage, it can be seen that all of the position disturbance responses still satisfy the original disturbance bound of $D_{bp}(s) = 4 \times 10^{-8}$.

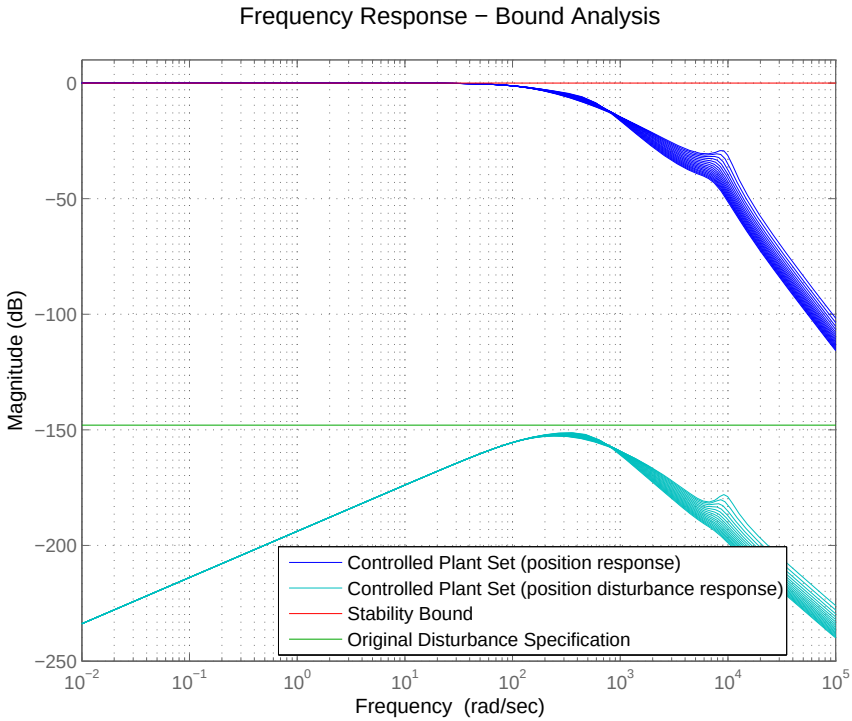


Figure 5.23: Position Loop Analysis - Dynamic Stiffness Controller

The responses shown in Figures 5.20, 5.22 and 5.23 verify that all of the performance specifications were met in the example QFT design. It is however interesting to note that the final structure of the velocity controller (Equation (5.18)) had no higher order than that of a standard PID regulator and the final structure of the position controller (Equation (5.22)) was the same as a standard P regulator. Although there is no limit on the number of poles and zeros in a QFT designed controller, it was found that all of the performance specifications could be met with these conventional control structures.

Higher order controllers were also examined during the velocity loop shaping step of the example QFT design. It was found that for the Linear Motor Test-Bed, with a fixed current controller, the higher order velocity controllers did not provide any further benefits. Although some higher order controllers did allow for further increases in dynamic stiffness, these increases could not be achieved without violating the other performance specifications.

### 5.4.3 Dynamic Stiffness of the QFT Controlled Linear Motor

The QFT controller developed in Section 5.4.2 was implemented on the Linear Motor Test-Bed. During the implementation of this controller, it was found that the Linear Motor Test-Bed had a minor system resonance at approximately 200 Hz. A notch filter was successfully added to the controller to reduce this resonance; however, the proportional gain of the velocity controller was also slightly reduced to ensure a stable system.

The 125N step disturbance force, used in Section 5.4.1, was again applied to the load side of the Linear Motor Test-Bed. The response of the Linear Motor Test-Bed, with the QFT designed control system, is shown in Figure 5.24. A maximum position error of $3.4\mu m$ can be seen in this response. In comparison, the maximum position error of the Linear Motor Test-Bed with the standard manufacturer recommended controller tuning was approximately $85\mu m$. While the QFT designed controller reduced the maximum position error by more than an order of magnitude, the closed-loop bandwidths of the two controllers were approximately equivalent. This result clearly demonstrates the importance of including dynamic stiffness in the design approach.

For a direct comparison, Figure 5.25 shows the response of the QFT designed control system on the same graph as the standard controller responses of the Linear Motor Test-Bed and the ballscrew configurations of the Drive Comparison Test-Bed. Although still an order of magnitude higher than the maximum position errors of the two ballscrew configurations, a maximum error of $3.4\mu m$ to a disturbance force of 125N would be considered

acceptable in many machining operations.

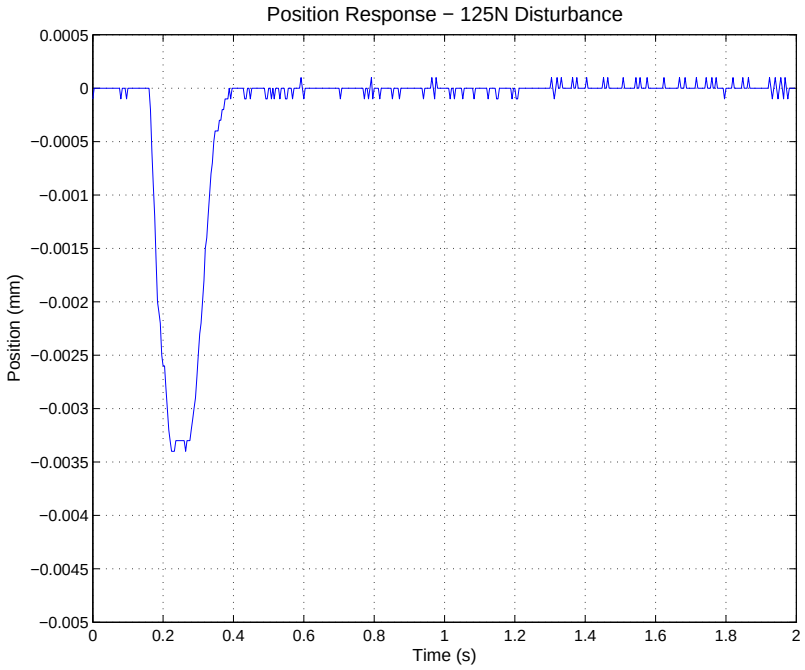


Figure 5.24: Linear Motor Position – QFT (125N Disturbance)

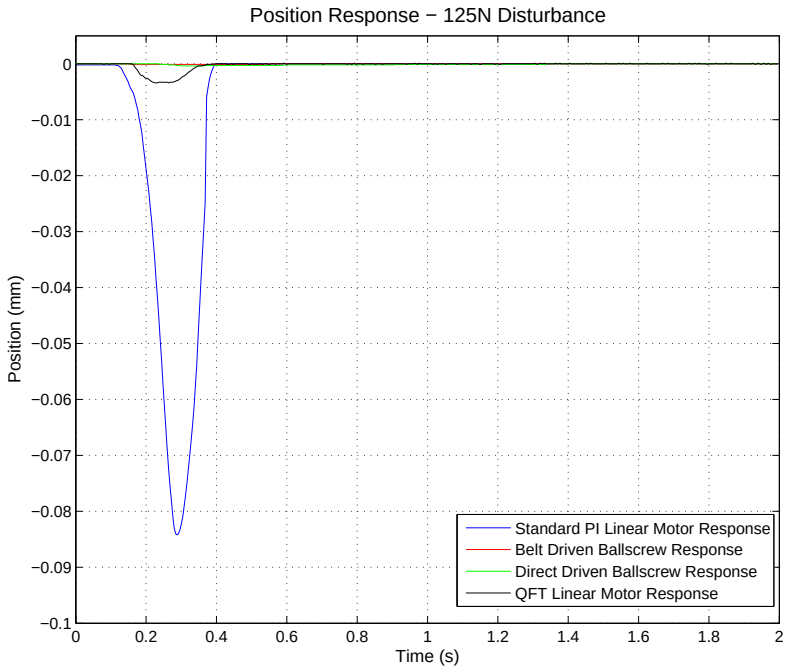


Figure 5.25: Linear Motor and Ballscrew Positions – QFT (125N Disturbance)

## 5.5 Conclusions

A study of dynamic stiffness in precision machine tool feed axes has been presented in this chapter. In particular, the study focused on the use of linear motors in precision feed axes. The advantages of linear motors in reducing periodic torque/force disturbances in feed axes were analysed, along with the disadvantages associated with the inherently low dynamic stiffness of linear motors. Control system design was also examined from the perspective of dynamic stiffness, with a QFT approach presented that includes dynamic stiffness in the design process.

The periodic torque/force disturbances of both linear and rotary motor driven feed axes were studied in Section 5.2. Through the use of position frequency spectra, the most significant cyclic disturbances were quantified for the Linear Motor Test-Bed and all three configurations of the Drive Comparison Test-Bed. Although the reduction of periodic torque/force variations is one of the recognised advantages of linear motor driven axes, the study presented in this section both quantified and compared actual disturbances in real linear and rotary driven axes.

The results presented in Section 5.2 clearly showed that the only significant disturbances in the Linear Motor Test-Bed were due to the motor's electrical cycle and associated cogging forces. In comparison, it was found that additional disturbances were significant on all three configurations of the Drive Comparison Test-Bed. These additional disturbances were due to the associated mechanical transmission mechanisms of each configuration. It was also found that the mechanical power required to overcome friction at 200mm/min was more than an order of magnitude higher for the ballscrew configurations, when compared with the linear motor and rack and pinion configurations.

The inherent dynamic stiffnesses of rack and pinion, ballscrew and linear motor driven axes were compared mathematically in Section 5.3. The resulting mathematical expressions clearly illustrated the relationship between dynamic stiffness, load mass and transmission gearing. The force disturbances required to exceed given position error tolerances

were also calculated for the Linear Motor Test-Bed and all three configurations of the Drive Comparison Test-Bed in Section 5.3. Through a comparison of the calculated force disturbances, it was found that the linear motor and rack and pinion configurations were only capable of providing significant stiffness at high frequencies. In contrast, the dynamic stiffness of the ballscrew driven configurations was shown to be inherently higher and less affected by changes in load mass. These results are primarily due to the inherent gearing in the ballscrew configurations.

The design of control systems for increased dynamic stiffness was also examined in this chapter. The standard control structure and tuning process of the CNC system (based primarily on overall system bandwidth) was examined first in Section 5.4.1, with a 125N step disturbance force applied to the Linear Motor Test-Bed and all three configurations of the Drive Comparison Test-Bed. When comparing the responses of the test-bed configurations, it was found that the maximum position error on the two ballscrew configurations was more than 2 orders of magnitude lower than that of the linear motor configuration and almost 4 orders of magnitude lower than that of the rack and pinion configuration. The much larger error of the rack and pinion configuration was shown to be due to high backlash in the system. Methods that can be used to improve the performance of systems with backlash are examined in Chapter 7.

A QFT approach to designing control systems that simultaneously address performance specifications based on stability, robustness, overall response speed and dynamic stiffness was presented in Section 5.4.2. A method for generating QFT performance bounds based on the dynamic stiffness requirements was also presented. An example design for the Linear Motor Test-Bed was shown to reduce the maximum position error of this system (when subjected to the 125N disturbance force) by more than an order of magnitude, while not affecting the closed-loop bandwidth of the system. In the example design it was found that the velocity loop control structure did not require any higher order than that of a standard PID regulator. Higher order control structures were also examined during the QFT design process; however, while it was possible to increase the dynamic stiffness of

this design using a higher order control structure, it was found that the other performance specifications were compromised. Hence, there was no advantage in using a higher order structure in this particular example.

Through the example design presented in this chapter, the QFT approach was shown to provide a structured and transparent design process. The effects of any changes in the control structure were able to be assessed simultaneously for each of the given performance specifications. In comparison, the standard approaches to designing PID regulators are very limited, with any trade-offs between robustness, transient performance and dynamic stiffness not always clear to the designer.

Chapter 6

# Drive-Train Flexing and Torsional Vibrations

## 6.1 Introduction

A theoretical analysis of the various factors that interact to cause torsional vibrations, and associated stability problems, in servo systems is presented in this chapter. In particular, the analysis focuses on flexing in the drive-trains commonly used for machine tool feed axes. Although drive-train flexing is directly responsible for the transmission of torque (or force) to the load, it is also directly associated with the resulting oscillations that can be observed in the motor and load responses. Industry has traditionally dealt with these stability problems through 'matching' the inertias of the motor and load in systems; however, the analysis presented in this chapter shows that in some cases excessive torsional vibrations can occur even in drive-trains with a 1:1 inertia ratio.

While load position is the most critical output of a machine tool feed axis, torsional vibrations have an impact on both velocity and position. Since the control structure in most feed axes is cascaded, the inner velocity loop is faster than the outer position loop. For this reason, most approaches to controlling torsional vibrations are implemented in the velocity loop. Similarly, the analysis presented in this chapter concentrates on the motor and load velocity responses, rather than position. Throughout the presented analysis

the effectiveness of velocity control solutions from all of the three fundamental groups (identified in Section 2.3.3) are also compared both theoretically and experimentally.

In Section 6.2 a theoretical analysis of flexing and system oscillations in a simple motor-transmission-load system is presented, along with a discussion on absolute stability. A mathematical analysis of the different control solutions that use specific flex related feedback quantities, to reduce torsional vibrations, is also presented in Section 6.2.

In Section 6.3 various proposed control solutions are compared through simulation and application to the Motor-Transmission-Load Test-Bed. As described in Section 4.3, this test-bed was designed to allow for a concentrated analysis of drive-train flexing and torsional vibrations (with other important performance limiting factors minimised). As a result of this comparison the most effective control solutions are identified.

In Section 6.4 the overall analysis of torsional vibrations (both theoretical and experimental) is extended to the common machine tool drive configurations. The Drive Comparison Test-Bed (described in Section 4.4) is used for the experimental analysis in this section.

The results presented throughout this chapter are discussed further in Section 6.5, with the development of a standard approach to the problem suggested. Other key points and conclusions that can be drawn from this chapter are also summarised in Section 6.5.

## 6.2 Theoretical Analyses of Transmission Flexing and Control Solutions for Torsional Vibrations

### 6.2.1 Overview

The analyses presented in this section examine the various factors that can interact to cause torsional vibrations and absolute stability problems in motor-transmission-load systems. The use of specific flex related feedback quantities to reduce torsional vibrations in a closed loop control system is also examined.

The inherent flexing of the transmission element in a motor-transmission-load system is analysed in Section 6.2.2. This analysis examines how each of the system inertias and the torsional stiffness of the transmission element can influence the natural frequency of oscillation of the system. To further understand the effects that torsional stiffness and each of the system inertias have on a closed loop control system, the open loop frequency responses of a motor-transmission-load system with both motor velocity and load velocity as outputs are examined in Section 6.2.3. It is shown in both Sections 6.2.2 and 6.2.3 that motor-load inertia ratio has a very limited effect on the natural frequency of oscillation of a system and on any resonant peaks that can result when closing the loop. Limitations associated with using feedback sensors placed at the motor are also identified in Section 6.2.3.

The issues associated with feedback sensor location are further examined in Sections 6.2.4 and 6.2.5. In Section 6.2.4 the influence of feedback sensor location on absolute stability is examined, with stability problems identified when the feedback is restricted to the load side. The influence of different flex related feedback quantities (based on combinations of motor and load feedback) on the closed loop flex response is examined in Section 6.2.5. Through the analysis presented in Section 6.2.5 many previously published control solutions, which use these flex related feedback quantities, are shown to be mathematically equivalent.

### 6.2.2 Transmission Flexing

For an initial analysis of flexing, the 'traditional' two-body model was considered. If all friction and damping sources are considered negligible, a transfer function with transmission flex as output can be obtained from Equations (3.3) and (3.4):

$$\frac{\theta_s}{\mathrm{T}_m} = \frac{\frac{1}{\mathrm{J}_m}}{s^2 + \frac{\mathrm{K}_s(\mathrm{J}_l+\mathrm{J}_m)}{\mathrm{J}_l\mathrm{J}_m}} \tag{6.1}$$

Applying a unit impulse and taking the inverse Laplace transform of Equation (6.1), results in a description of flex as a function of time. If $J_l$ is also substituted with $I_r J_m$ (ie $I_r = \frac{J_l}{J_m}$) this time function can be described in terms of motor-load inertia ratio:

$$\theta_s(t) = \frac{1}{J_m}\sqrt{\frac{J_m I_r}{K_s(1+I_r)}}\sin\left(\sqrt{\frac{K_s(1+I_r)}{J_m I_r}}t\right) \tag{6.2}$$

From Equation (6.2) it can be seen that increasing the torsional stiffness of the transmission also increases the natural frequency of oscillation of the motor-transmission-load system, while decreasing the amplitude of this oscillation. It is also worth noting that when $K_s = \infty$, flex reduces to zero (as expected). Examining the influence of inertia ratio shows that the effects are opposite to that of torsional stiffness – as the inertia ratio increases, the natural frequency of oscillation decreases and the amplitude increases. However, as the inertia ratio continues to increase above unity it tends to cancel, reducing the effects it has on both the frequency and amplitude of the oscillation.

One problem with using the 'traditional' two-body model to analyse flex is that, as shown in Section 3.2.3, the 'traditional' two-body model does not always provide an accurate description of the system's natural frequency, particularly when the inertia of the transmission element is significant. For this reason, a transfer function with transmission flex as output was also obtained using the 'adjusted' two-body model:

$$\frac{\theta_s}{T_m} = \frac{\frac{2}{2J_m+J_s}}{s^2 + \frac{8Ks(J_m+J_l+J_s)}{8J_mJ_l+3J_s(J_m+J_l)+J_s^2}} \tag{6.3}$$

Applying a unit impulse and taking the inverse Laplace transform of Equation (6.3) results in a more accurate description of flex as a function of time:

$$\theta_s(t) = \frac{2}{2J_m(1+I_s)}\sqrt{\frac{J_m\left(8I_r+3I_s(1+I_r)+I_s^2\right)}{8K_s(1+I_r+I_s)}}\sin\left(\sqrt{\frac{8K_s(1+I_r+I_s)}{J_m\left(8I_r+3I_s(1+I_r)+I_s^2\right)}}t\right) \tag{6.4}$$

In Equation (6.4) $J_l$ has once again been substituted with $I_r J_m$, so that the time function is described in terms of inertia ratio. To reduce the complexity of Equation (6.4), the inertia of the transmission element ($J_s$) has also been described in terms of an inertia ratio ($I_s$, where $I_s = \frac{J_s}{J_m}$). Note that when $I_s = 0$, Equation (6.4) reduces to Equation(6.2).

From Equation (6.4) it can be seen that varying torsional stiffness of the transmission has the same effect as in Equation (6.2). Also when $I_s$ (and subsequently, $J_s$) is very small, varying the motor-load inertia ratio has the same effect as in Equation (6.2). As $I_s$ increases though, the influence of motor-load inertia ratio on both the frequency and amplitude of the oscillation reduces. The importance of this result can be understood best when considering a long ballscrew with significant inertia but low torsional stiffness. In this case, the effects of varying the motor-load inertia ratio, on both the frequency and amplitude of any oscillations present, are significantly reduced. However, a ballscrew with a larger diameter and the same length would have increased stiffness and inertia – resulting in an increase in the natural frequency of oscillation and a decrease in the amplitude. What is particularly evident from both Equations (6.2) and (6.4) is that torsional stiffness of the transmission has a much greater influence on any flexing than the inertia ratio does.

### 6.2.3 Oscillations in the Closed Loop System

To analyse the effects of varying inertia ratio and torsional stiffness when closing the velocity loop, the open loop frequency responses of a motor-transmission-load system with both motor velocity and load velocity as outputs were examined. The frequency response with motor velocity as output is shown in Figure 6.1 (a), while the frequency response with load velocity as output is shown in Figure 6.1 (b).

A comparison of Figures 6.1 (a) and 6.1 (b) reveals that for all frequencies higher than the quadratic zeros (in Figure 6.1 (a)) the motor and load velocities quickly become 180 degrees out of phase. Of particular note is the frequency range between the quadratic

zeros and quadratic poles of the motor response. Since the quadratic poles represent a resonance in both the motor and load responses, it can be seen that the magnitude of the resonant peak in the motor response increases with the width of this frequency range. This characteristic, coupled with the fact that in this range the motor sensor provides feedback that leads the total torque rather than lagging it (as the load does), highlights one of the major problems faced by system designers who use feedback sensors at the motor. This result is also consistent with that found by Welch [43].

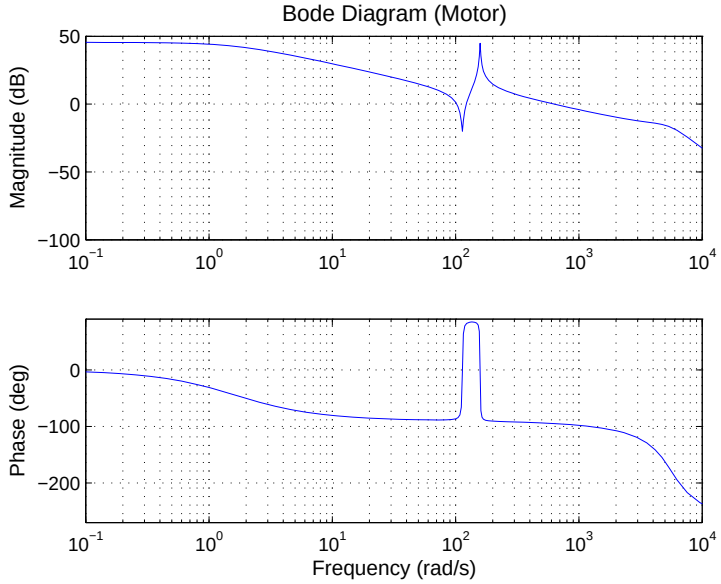


(a) Motor Velocity

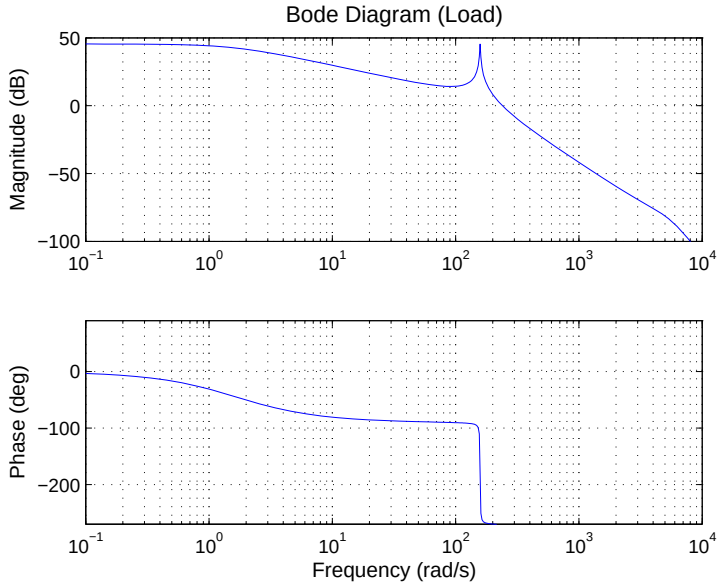


(b) Load Velocity

Figure 6.1: Frequency Responses – Oscillation Analysis

Equations (2.9) and (2.10) describe the corner frequencies of the quadratic zeros and quadratic poles in the motor response when the transmission inertia is assumed to be negligible. If the transmission inertia is taken into account the quadratic zeros of the motor response are described by Equation (6.5) and the quadratic poles are described by Equation (6.6). Note also that Equation (6.6) is equivalent to the frequency in the flex expression of Equation (6.4).

$$\omega_z = \sqrt{\frac{8K_sJ_m + 4K_sJ_s}{8J_mJ_l + 3J_s(J_m + J_l) + J_s^2}} = \sqrt{\frac{4K_s(2 + I_s)}{J_m(8I_r + 3I_s(1 + I_r) + I_s^2)}} \tag{6.5}$$

$$\omega_p = \sqrt{\frac{8K_s(J_m + J_l + J_s)}{8J_mJ_l + 3J_s(J_m + J_l) + J_s^2}} = \sqrt{\frac{8K_s(1 + I_r + I_s)}{J_m(8I_r + 3I_s(1 + I_r) + I_s^2}} \tag{6.6}$$

When examining Equations (6.5) and (6.6) it can be seen that the corner frequencies of both the quadratic zeros and quadratic poles are proportional to the torsional stiffness of the transmission element. Hence, a transmission element with a higher torsional stiffness would result in the zeros and poles moving further to the right in the frequency response of Figure 6.1 (a). As the zeros and poles move further to the right and away from the cross-over frequency, relative stability is increased when closing the loop.

Analysing the influence of motor-load inertia ratio in Equations (6.5) and (6.6) shows that $\omega_z$ reduces with an increase in inertia ratio, while $\omega_p$ is relatively unaffected (as discussed in Section 6.2.2). This means that the band between the two corner frequencies is increased, resulting in an increase in magnitude of the resonance. Unless the torsional stiffness of the coupling is relatively high, this band of frequencies will occur near the cross over frequency, resulting in poor relative stability when closing the loop.

The most interesting factor in this analysis is the influence of motor inertia. Increasing the motor inertia to overcome a large motor-load inertia mismatch (which is a common solution used in industry) does reduce the width of this band of frequencies. However, this is primarily achieved by reducing $\omega_p$, while $\omega_z$ remains relatively unaffected (if the transmission inertia is negligible, $\omega_z$ does not change at all). Although this does reduce

the range between the two corner frequencies (and hence will reduce the magnitude of the resonance to an extent), it does not move this band of frequencies away from the cross-over frequency. Hence, high amplitude oscillations can still exist when closing the loop. The only reliable method of moving this band of frequencies away from the cross-over frequency is to increase the torsional stiffness of the transmission element.

### 6.2.4 Absolute Stability

Consider the block diagram shown in Figure 6.2, where both motor and load feedback are proportionally applied to a motor-transmission-load system (through gains $K_m$ and $K_l$ respectively). The influence of feedback sensor location on absolute stability was examined for this system using Routh's Stability Criterion [61].

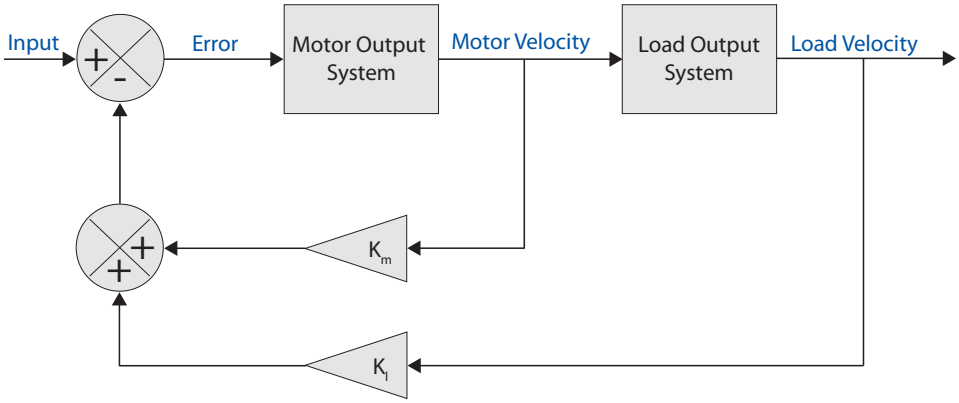


Figure 6.2: Absolute Stability Analysis – Closed Loop System

The motor and load output systems shown in Figure 6.2 were modelled using the 'adjusted' two-body model. Equation (6.7) represents the transfer function of the 'Motor Output System', while Equation (6.8) represents the transfer function of the 'Load Output System'. These two transfer functions can be obtained from Equations (3.19) and (3.20).

$$\frac{\dot{\theta_m}}{\text{Error}} = \frac{2\left(\left(8J_mJ_l + 3J_s\left(J_m + J_l\right) + J_s^2\right)s^2 + 4K_s\left(2J_m + J_s\right)\right)}{s\left(2J_m + J_s\right)\left(\left(8J_mJ_l + 3J_s\left(J_m + J_l\right) + J_s^2\right)s^2 + 8K_s\left(J_m + J_l + J_s\right)\right)} \tag{6.7}$$

$$\frac{\dot{\theta}_l}{\dot{\theta_m}} = \frac{4K_s\left(2J_m + J_s\right)}{\left(8J_mJ_l + 3J_s\left(J_m + J_l\right) + J_s^2\right)s^2 + 4K_s\left(2J_m + J_s\right)} \tag{6.8}$$

From Equations (6.7) and (6.8) the characteristic equation of the feedback system shown in Figure 6.2 was determined to be:

$$(2J_m + J_s)\left(8J_mJ_l + 3J_s(J_m + J_l) + J_s^2\right)s^3 + 2K_m\left(8J_mJ_l + 3J_s(J_m + J_l) + J_s^2\right)s^2$$
$$+8K_s(2J_m + J_s)(J_m + J_l + J_s)s + 8K_s(K_m + K_l)(2J_m + J_s) \qquad (6.9)$$

From the characteristic equation, Routh's array of coefficients can be constructed. Table 6.1 represents Routh's array of coefficients resulting from Equation (6.9).

Table 6.1: Array of Coefficients for Routh's Stability Analysis

| | | |
|---|---|---|
| $s^3$ | $(2J_m + J_s)\left(8J_mJ_l + 3J_s(J_m + J_l) + J_s^2\right)$ | $8K_s(2J_m + J_s)(J_m + J_l + J_s)$ |
| $s^2$ | $2K_m\left(8J_mJ_l + 3J_s(J_m + J_l) + J_s^2\right)$ | $8K_s(K_m + K_l)(2J_m + J_s)$ |
| $s^1$ | $\frac{4K_s(2J_m+J_s)(K_m(2J_l+J_s)-K_l(2J_m+J_s))}{K_m}$ | |
| $s^0$ | $8K_s(K_m + K_l)(2J_m + J_s)$ | |

For absolute stability, all of the coefficients in the first data column of Table 6.1 must be positive. Since each of the individual parameters in the characteristic equation are positive, this condition will hold true as long as the first entry in the $s^1$ row is positive, ie:

$$K_m > K_l\frac{2J_m + J_s}{2J_l + J_s}$$

Hence, through careful choice of $K_m$ and $K_l$, the system shown in Figure 6.2 is absolutely stable regardless of the inertia ratio or transmission element stiffness. If the feedback is restricted to motor velocity (ie $K_l = 0$), the condition for absolute stability holds true regardless of the value of $K_m$. Conversely, if the feedback is restricted to load velocity (ie $K_m = 0$), the system is unstable regardless of the value of $K_l$.

In a practical system, where friction and damping of the transmission element are present, it is possible to design an absolutely stable system with only load velocity feedback. However, absolute stability problems are still likely to be a serious issue when designing a practical motor-transmission-load control system with only load velocity as feedback.

### 6.2.5 An Analysis of Feedback Approaches

It is clear, from the analysis presented in Section 6.2.3, that a feedback device attached to the load can provide valuable information on flex in a servo system (as long as it is not the only feedback available). In this section the use of load feedback in higher order controllers is theoretically analysed. In particular, the control approaches that use specific flex-related feedback quantities (which can consist of motor and load feedback, as discussed in Section 2.3.3) are analysed and compared.

Consider the block diagram shown in Figure 6.3. The solid section at the centre of this diagram represents the system described by the 'traditional' two-body model. The dashed sections in the diagram show how the different feedback quantities, which were discussed in Section 2.3.3, can be used to form inner feedback loops of a higher order velocity controller.

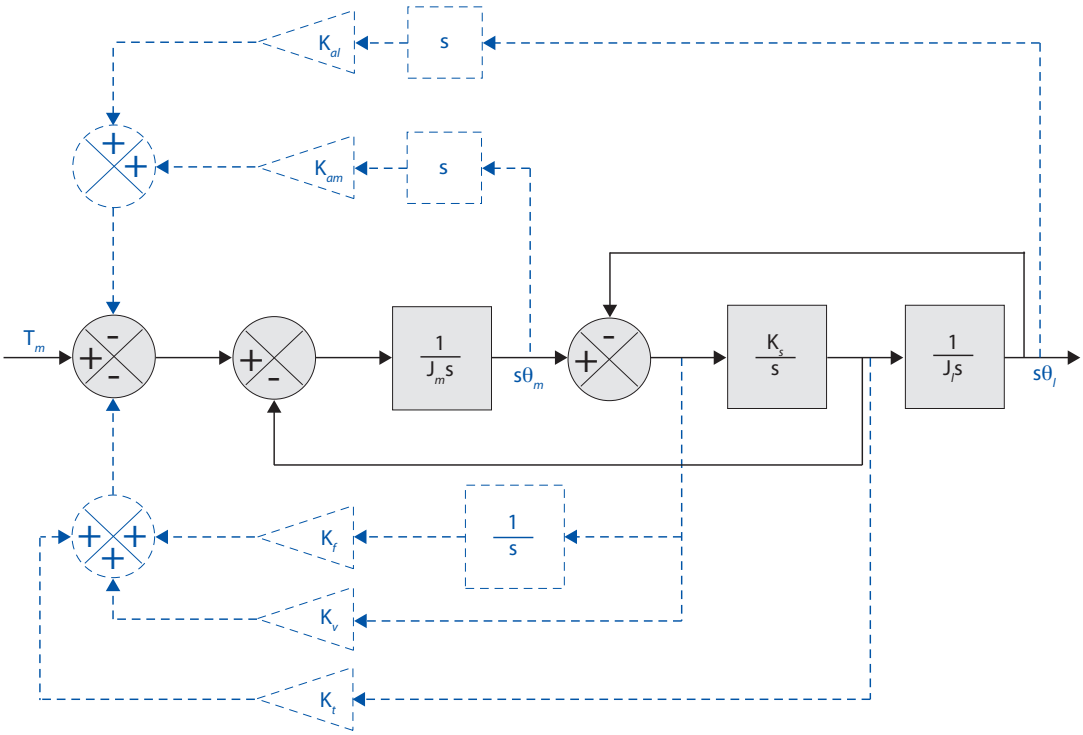


Figure 6.3: Feedback System Block Diagram

Recall that Equation (6.2) describes the flex of the 'traditional' two-body model as a function of time. Through the same method of applying unit impulses to the relevant

transfer functions and taking inverse Laplace transforms, transmission flex as a function of time can also be determined for each of the feedback approaches shown in Figure 6.3. The 'traditional' two-body model is used in this analysis to limit the size of the resulting equations. However, each of the time functions derived in this section can be described in terms of the 'adjusted' two-body model by applying the following substitutions:

$$J_m = J_{m(adj)} = J_m + \frac{J_s}{2}$$

$$J_l = J_{l(adj)} = J_l + \frac{J_s}{2}$$

$$K_s = K_{s(adj)} = \frac{2K_s\,(2J_m + J_s)\,(2J_l + J_s)}{8J_mJ_l + 3J_s\,(J_m + J_l) + J_s^2}$$

**Shaft Flex Feedback**

Consider first the use of shaft-flex feedback, which was successfully used by the author of this thesis in [52] to reduce system oscillations on the Motor-Transmission-Load Test-Bed. This can be achieved by setting each of $K_{am}$, $K_{al}$, $K_v$ and $K_t$ (in Figure 6.3) to zero, while $K_f$ is the non-zero shaft-flex gain. Equation (6.10) represents the transfer function for this system, with transmission flex as output. Equation (6.11) represents the system flex response as a function of time.

$$\frac{\theta_s}{T_m} = \frac{\frac{1}{J_m}}{s^2 + \frac{K_s(J_l+J_m)+K_fJ_l}{J_lJ_m}} \tag{6.10}$$

$$\begin{aligned} \theta_s(t) &= \frac{1}{J_m\omega}\sin(\omega t) \\ \text{where, } \omega &= \sqrt{\frac{K_s(1+I_r)+K_fI_r}{J_mI_r}} \end{aligned} \tag{6.11}$$

A comparison between Equations (6.11) and (6.2), reveals that Equation (6.11) contains an additional element ($K_fI_r$) in the numerator of the natural frequency of oscillation.

Since this element cannot be grouped with every instance of inertia ($J_m$ and $J_l$) or with the torsional stiffness of the transmission ($K_s$), it is not strictly correct to claim an effective change in the total inertia or the torsional stiffness of the system. However, it is clear that increasing the feedback gain $K_f$ has a similar effect to the preferred approach of increasing $K_s$, in that the frequency of oscillation increases while the amplitude of this oscillation decreases.

**Shaft Torque Feedback**

Equation (6.12) represents the transfer function of the system when shaft-torque feedback is used, as suggested by Brandenburg et al [45]. This can be achieved by setting each of $K_{am}$, $K_{al}$, $K_f$ and $K_v$ (in Figure 6.3) to zero, while $K_t$ is the non-zero shaft-torque gain. Equation (6.13) represents the flex response of this system, as a function of time.

$$\frac{\theta_s}{T_m} = \frac{\frac{1}{J_m}}{s^2 + \frac{K_s(J_l+J_m+K_tJ_l)}{J_lJ_m}} \tag{6.12}$$

$$\begin{aligned} \theta_s(t) &= \frac{1}{J_m\omega}\sin(\omega t) \\ \text{where, } \omega &= \sqrt{\frac{K_s(1+I_r+K_tI_r)}{J_mI_r}} \end{aligned} \tag{6.13}$$

Comparing Equation (6.13) with Equation (6.11) shows that they are almost identical. The only difference between these two approaches is that the additional element in the numerator of the natural frequency is now also dependent on $K_s$. This is expected since $K_s$ is a constant of proportionality between shaft-flex and shaft-torque. Although this proportionality may not be exact in a practical system (where friction and sensor inaccuracies are significant), from a theoretical perspective the shaft-flex feedback and shaft-torque feedback approaches are fundamentally equivalent. It is also worth noting that when friction is considered negligible, load-torque feedback (as suggested by Ji and Sul [46]) is identical

to shaft-torque feedback and hence also results in a fundamentally equivalent approach.

**Acceleration Feedback**

Equation (6.14) represents the transfer function of the system when motor and load acceleration feedback are used. In this case, $K_f$, $K_v$ and $K_t$ (in Figure 6.3) are set to zero, while $K_{am}$ is the motor acceleration gain and $K_{al}$ is the load acceleration gain.

$$\frac{\theta_s}{T_m} = \frac{\frac{1}{J_m+K_{am}}}{s^2 + \frac{K_s(J_l+(J_m+K_{am})+K_{al})}{J_l(J_m+K_{am})}} \tag{6.14}$$

Equation (6.15) represents the flex response, as a function of time, when $K_{am}$ is set to zero. This configuration provides acceleration feedback from the load only, as suggested by Hori et al [49].

$$\begin{aligned} \theta_s(t) &= \frac{1}{J_m\omega}\sin(\omega t) \\ \text{where, } \omega &= \sqrt{\frac{K_s\left(1+I_r+\frac{K_{al}}{J_m}\right)}{J_m I_r}} \end{aligned} \tag{6.15}$$

Equation (6.16) represents the flex response, as a function of time, when $K_{al}$ is set to zero. This configuration provides acceleration feedback from the motor only, as suggested by Welch [43].

$$\begin{aligned} \theta_s(t) &= \frac{1}{(J_m+K_{am})\,\omega}\sin(\omega t) \\ \text{where, } \omega &= \sqrt{\frac{K_s\left((J_m+K_{am})+J_l\right)}{(J_m+K_{am})\,J_l}} \end{aligned} \tag{6.16}$$

A comparison between Equation (6.15) and Equations (6.11) and (6.13) shows that the load acceleration feedback approach is almost identical to both shaft-flex and shaft-torque feedback. This result is due to the fact that transmission torque is equivalent to the product

of load inertia and load acceleration in an undamped system. A comparison between the additional elements in Equations (6.13) and (6.15) shows that they satisfy this relationship. In contrast, the motor acceleration feedback approach differs in that it has the same effect as altering the motor-load inertia ratio of the system. Note that Equation (6.16) has been written in terms of the inertias $J_m$ and $J_l$ to show that $K_{am}$ can be grouped with every instance of $J_m$. Hence, Equation (6.16) is equivalent to Equation (6.2) if the inertia ratio is re-defined as $I_r = \frac{J_l}{J_m + K_{am}}$.

**Velocity Difference Feedback**

Equation (6.17) represents the transfer function of the system when the difference between motor and load velocity ($\dot{\theta}_s$) is used for feedback. This can be achieved by setting each of $K_{am}$, $K_{al}$, $K_f$ and $K_t$ to zero, while $K_v$ is used as a velocity difference gain. Equation (6.18) represents the flex response of this system as a function of time.

$$\frac{\theta_s}{T_m} = \frac{\frac{1}{J_m}}{s^2 + \frac{K_v}{J_m}s + \frac{K_s(J_m+J_l)}{J_m J_l}} \tag{6.17}$$

$$\theta_s(t) = \frac{1}{J_m \omega}\sqrt{\frac{4J_m^2\omega^2}{4J_m^2\omega^2 - K_v^2}}e^{-\frac{K_v}{2J_m}t}\sin\left(\omega\sqrt{\frac{4J_m^2 w^2 - K_v^2}{4J_m^2\omega^2}}t\right) \tag{6.18}$$

$$\text{where, } \omega = \sqrt{\frac{K_s(1+I_r)}{J_m I_r}}$$

An examination of both Equations (6.17) and (6.18) reveals that, unlike the other forms of feedback examined in this section, velocity difference feedback does not effectively alter either the natural frequency or the inertia ratio of the system. Instead, increasing $K_v$ increases the damping of the system oscillations, which is also a desirable result.

When comparing the different feedback approaches, it can be seen that the feedback gains used in shaft-flex feedback, shaft-torque feedback, load-torque feedback and load acceleration feedback are all related by system constants. Hence, each of these approaches are

fundamentally equivalent and have a similar effect to varying the torsional stiffness of the system. Only motor acceleration feedback and velocity difference feedback produce different results, with motor acceleration feedback effectively altering the motor-load inertia ratio of the system and velocity difference feedback affecting the system damping. All of these approaches can theoretically reduce the amplitude of the flex response. However, the effects of varying the inertia ratio of the system (as is effectively achieved through motor acceleration feedback) were shown in Sections 6.2.2 and 6.2.3 to be very limited.

## 6.3 A Comparison of Control Solutions

### 6.3.1 Overview

Recall from Section 2.3.3, that the different approaches for controlling torsional vibrations can generally be classified as belonging to one of three fundamental groups:

1. Conventional control, with vibration suppression filtering and a single feedback device (usually attached to the motor),
2. Higher order control, with multiple feedback devices (attached to both the motor and load) and
3. Higher order control, with a single feedback device (usually attached to the motor).

In order to evaluate the performance of control solutions from each of these three groups, representative control approaches were applied to the Motor-Transmission-Load Test-Bed. Through both simulation and actual data acquisition from the test-bed, the transient responses of the controllers (to a velocity step input of 100 rad/s) were compared. A total of 9 different control approaches were included in this comparison, with PI control chosen as a performance benchmark:

1. Group 1 (conventional control with/without filtering)
    - PI control with no filtering
    - PI control with simple notch filtering
2. Group 2 (higher order control – motor and load feedback)
    - PI with shaft flex feedback
    - PI with velocity difference feedback
    - PI with load acceleration feedback
    - State feedback
3. Group 3 (higher order control – motor feedback)
    - PI with motor acceleration feedback
    - State feedback with observer
    - Unrestricted QFT design (motor velocity loop)

The general design criteria for all of the controllers consisted of achieving a fast response, while limiting overshoot and oscillation in both the motor and load responses. This resulted in a single design specification that the closed loop gain magnitudes had to be 0dB or less at all frequencies, in both the motor and load velocity responses. The poles of the state feedback controllers were chosen to ensure that the 0dB design specification was satisfied, with the well known Ackermann's formula [61] used to determine each state feedback gain matrix. For the case where an observer was used, the observer gains were also determined using Ackermann's formula with the observer poles chosen to be 5 times faster than the slowest poles of the state feedback controller. For all other cases a QFT design approach was used, with the design restricted to the relative feedback and compensator structure of each case.

Since the design specification related to both the motor and load velocity responses, nominal plant transfer functions for both the motor and load were included in each step of the QFT designs presented in this chapter. This is an important addition to standard QFT, as the Nichols Chart used in a single loop design is usually restricted to a single nominal transfer function. This approach provided a distinct advantage over traditional tuning methods in that both the motor and load specifications could be addressed simultaneously,

even for the benchmark PI controllers. The method developed to include both the motor and load transfer functions in a single QFT design is presented in Section 6.3.2.

The simulated and experimental transient responses of the benchmark PI controllers are presented in Section 6.3.3. To effectively simulate the Motor-Transmission-Load Test-Bed, the Matlab package was used. With the addition of the Simulink toolbox, a block diagram approach to modelling and simulation was employed. This approach allowed for the current loop characteristics, system nonlinearities and various disturbances to be easily included in all of the simulations performed. The main interface of the simulator is shown in Figure 6.4. This interface allowed for easy adjustment of transmission stiffness, transmission inertia, motor inertia, inertia ratio and control method. The block diagram of the overall simulation model is shown in Figure 6.5.

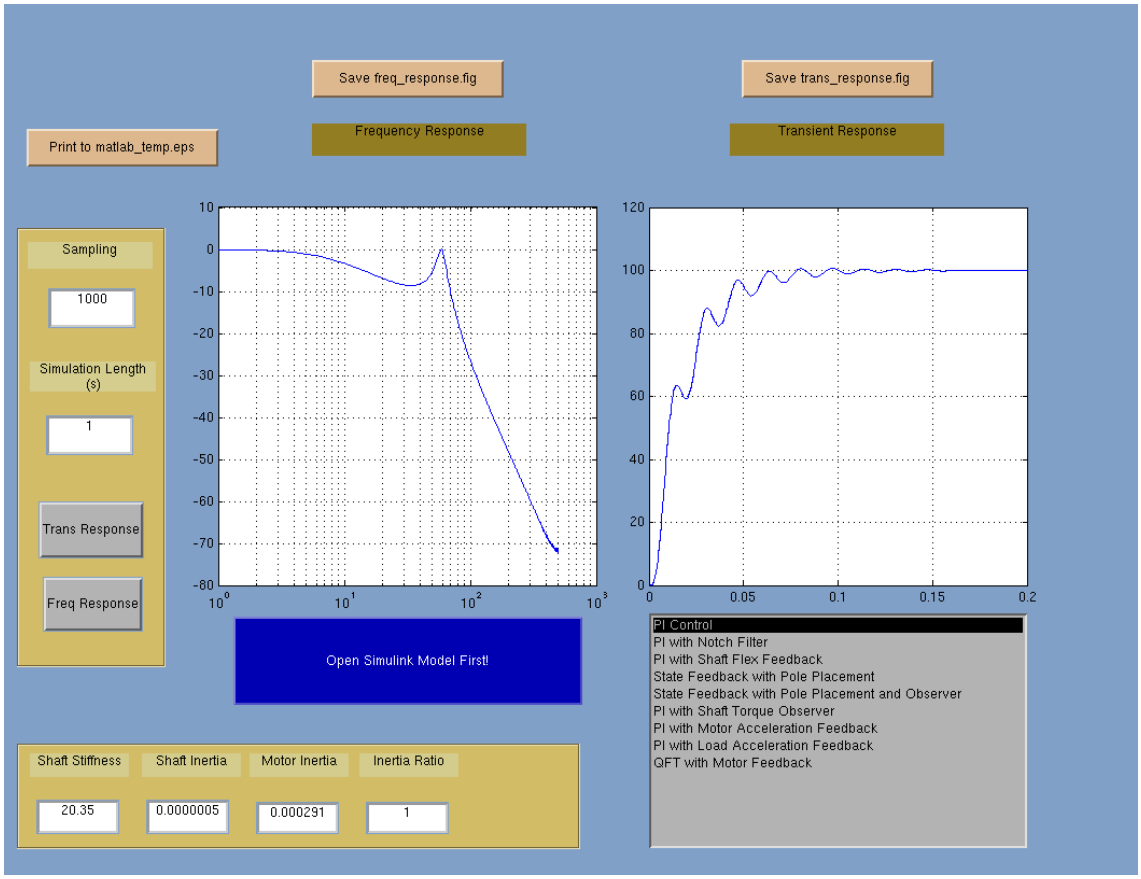


Figure 6.4: Simulation System – Main Interface

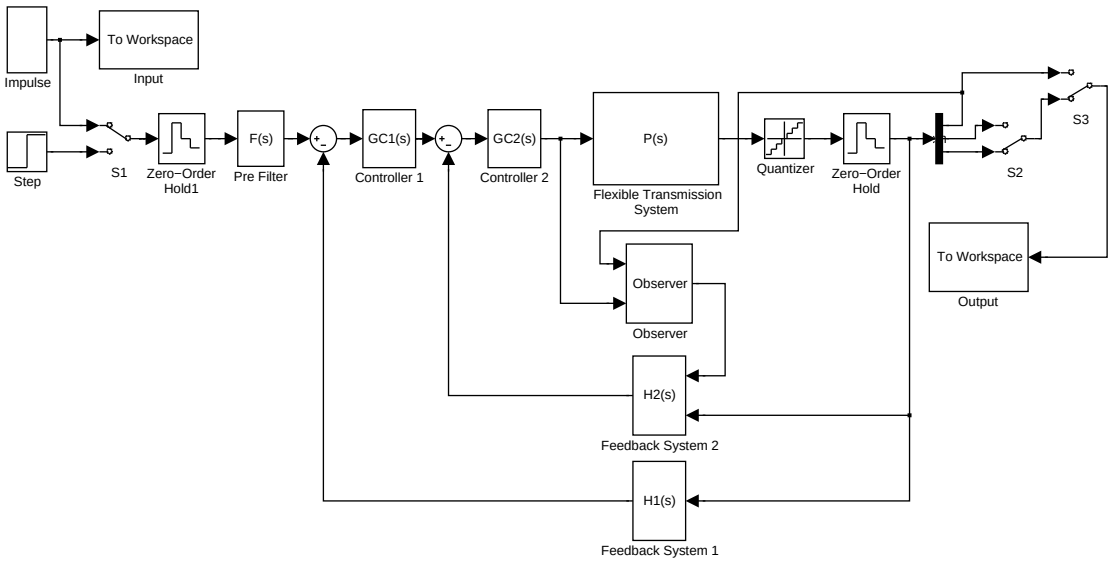


Figure 6.5: Simulation System – Simulink Block Diagram

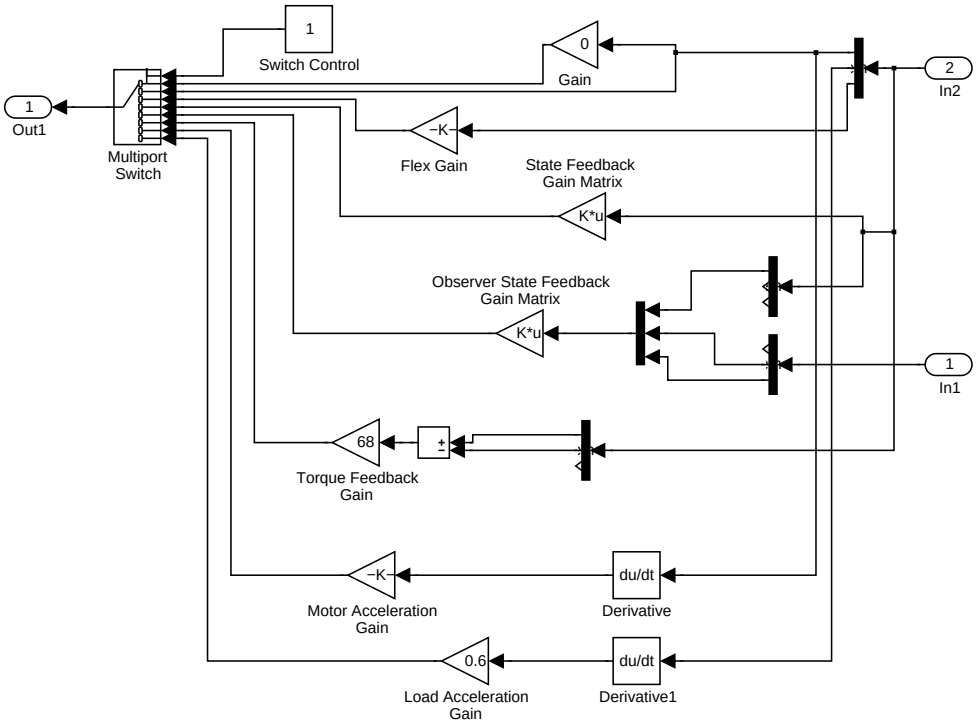


Figure 6.6: Simulation System – Feedback System 2

A change in control method on the main interface results in changes to the control and feedback subsystems of Figure 6.5. An example of one of these subsystems ('Feedback System 2') is shown in Figure 6.6. It can be seen from Figure 6.6 that the actual feedback path is controlled via a multiport switch. The state of the multiport switch is updated every time a new control method is chosen on the main interface. Each of the 'Pre Filter',

‘Controller 1’, ‘Controller 2’ and ‘Feedback System 1’ subsystems (in Figure 6.5) contain similar multiport switches, so that the control algorithm and feedback gains implemented in each subsystem are dependent on the control method chosen via the main interface.

The block labelled ‘Flexible Transmission System’ (in Figure 6.5) contains the complete dynamics of the Motor-Transmission-Load Test-Bed including the current control loop. This block can easily be altered to represent the other test-beds.

The simulated and experimental transient responses of the alternative control solutions are presented in Section 6.3.4. All simulations for the alternative control solutions were performed using the described Matlab based system. The results for all of the control approaches are also compared in Section 6.3.4.

### 6.3.2 Dual Response QFT Method

As described in Section 6.3.1, nominal plant transfer functions for both the motor and load were included in the QFT designs presented in this chapter. Figure 6.7 shows an example Nichols Chart with both the motor and load nominal plants plotted (the solid black line represents the open loop motor velocity, while the solid blue line represents the open loop load velocity).

There is some difficulty in including a second plot in a single loop QFT design, as the design process assumes the designer is closing the loop with unity feedback from the output of the plotted transfer function. This can only be true for one of the plots when there are two outputs plotted. Consider the example plots shown in Figure 6.7. If the motor velocity is used in a unity feedback arrangement, the closed loop magnitudes represented by the standard Nichols Grid would provide an accurate indication of the closed loop magnitudes at each frequency for the motor velocity (black line). However, they would not provide any indication of the closed loop magnitudes for the load velocity (blue line). For the standard Nichols Grid to provide an accurate indication of the closed loop magnitudes for load velocity, load velocity feedback must be used. Hence, two sets of bounds for

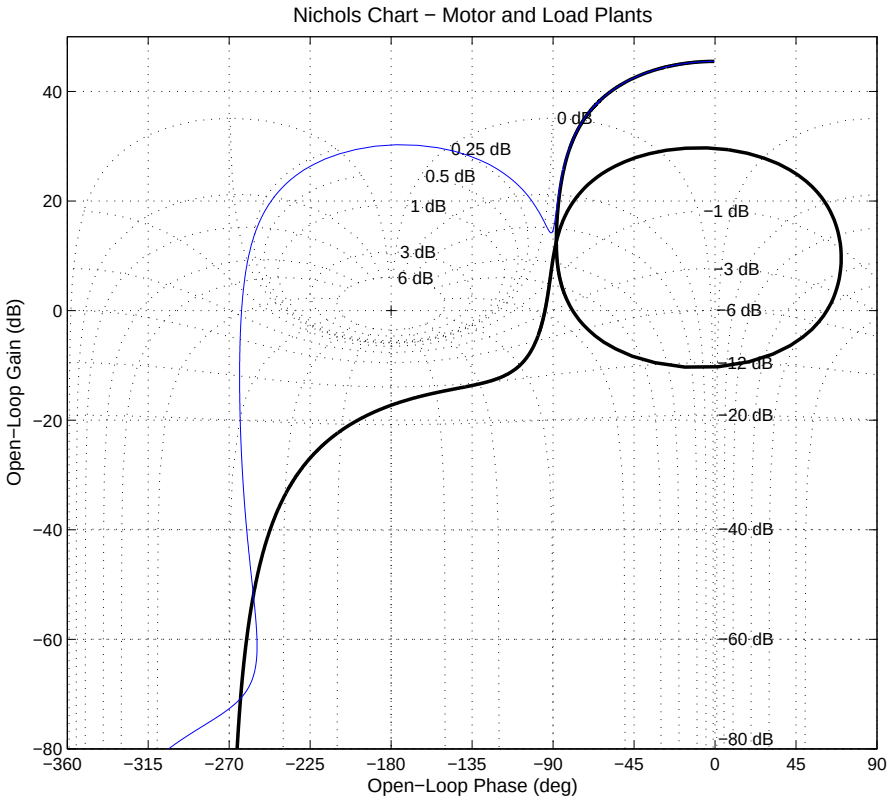


Figure 6.7: Nichols Chart with Nominal Transfer Functions for both Motor and Load

each performance specification are required when both motor and load transfer functions are included in the design process.

Figure 6.8 shows an example of two separate bounds for the motor and load responses, based on a single performance specification. In this case a simple stability specification was set, limiting the closed loop magnitude of both motor and load responses to 0dB at 158 rad/s. In Figure 6.8 the bound for the motor response is represented by the red dashed line and can be seen to match the 0dB closed loop magnitude of the standard Nichols Grid. The bound for the load response is represented by the green dashed line and is completely different. If G(s) represents the controller to be designed (which is the same for both nominal plants), $P_m(s)$ represents the motor transfer function and $P_l(s)$ represents the load transfer function, the two sets of bounds are calculated such that:

$$\left| \frac{G(s)P_m(s)}{1+G(s)P_m(s)} \right| \quad < \quad \text{0dB for the motor}$$

$$\text{and} \left| \frac{G(s)P_l(s)}{1+G(s)P_m(s)} \right| \quad < \quad 0\text{dB for the load}$$

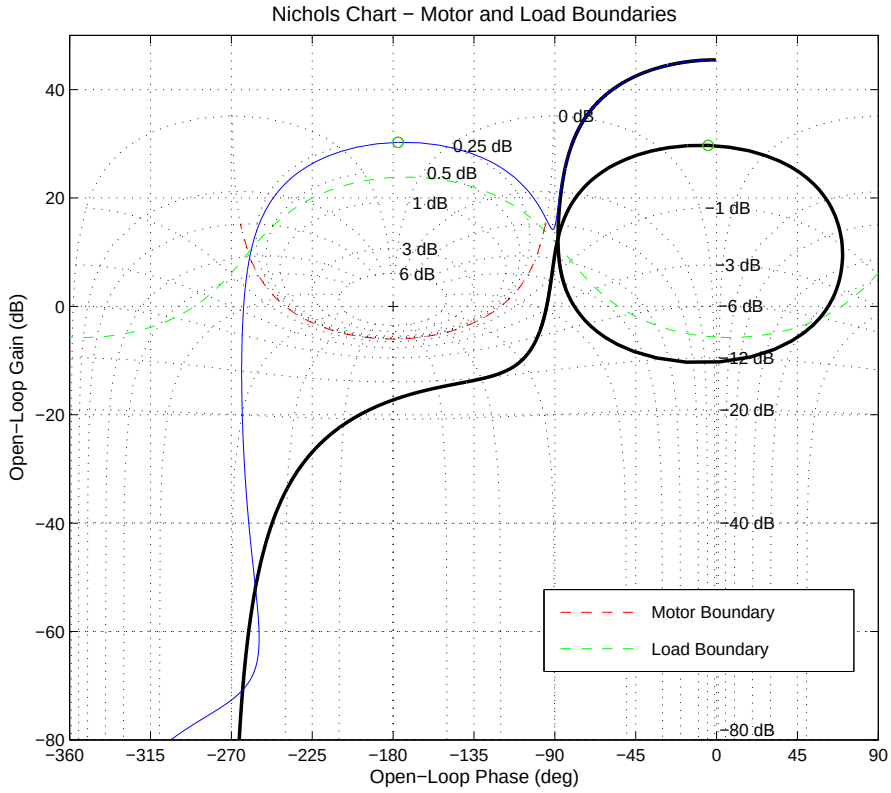


Figure 6.8: An Example of QFT Stability Bounds for both Motor and Load

The importance of including the load response in the design process is evident from Figure 6.8, as it can be seen that the nominal motor plant already satisfies the performance bound (even with G(s) = 1) while the nominal load plant does not. This is shown by the fact that the entire motor plant is outside the red bound, but the load plant is above the green bound at 158 rad/s (158 rad/s is shown by a circle on each of the plots). In order to satisfy a closed loop specification of both motor and load magnitudes being less than 0dB at 158 rad/s, the controller G(s) must be modified so that both plants satisfy their respective bounds.

### 6.3.3 Performance of PI Velocity Controllers

The benchmark PI controllers were tested using all of the available inertia discs and shafts of the Motor-Transmission-Load Test-Bed (refer to Section 4.3.2 for details). In particular, four different motor-load inertia configurations were tested on each of the 3 shafts:

1. No discs attached to either the motor or load (inertia ratio 1:1),
2. Disc 1 attached to the motor and Disc 3 attached to the load (inertia ratio 1.07:1),
3. Discs 1 and 2 attached to the motor, with no discs attached to the load (inertia ratio 16.9:1),
4. No discs attached to the motor, with Discs 1 and 2 attached to the load (inertia ratio 1:16.9).

An example design is shown in Figure 6.9, where the system uses Shaft 3 and motor-load inertia configuration 2 (inertia ratio 1.07:1).

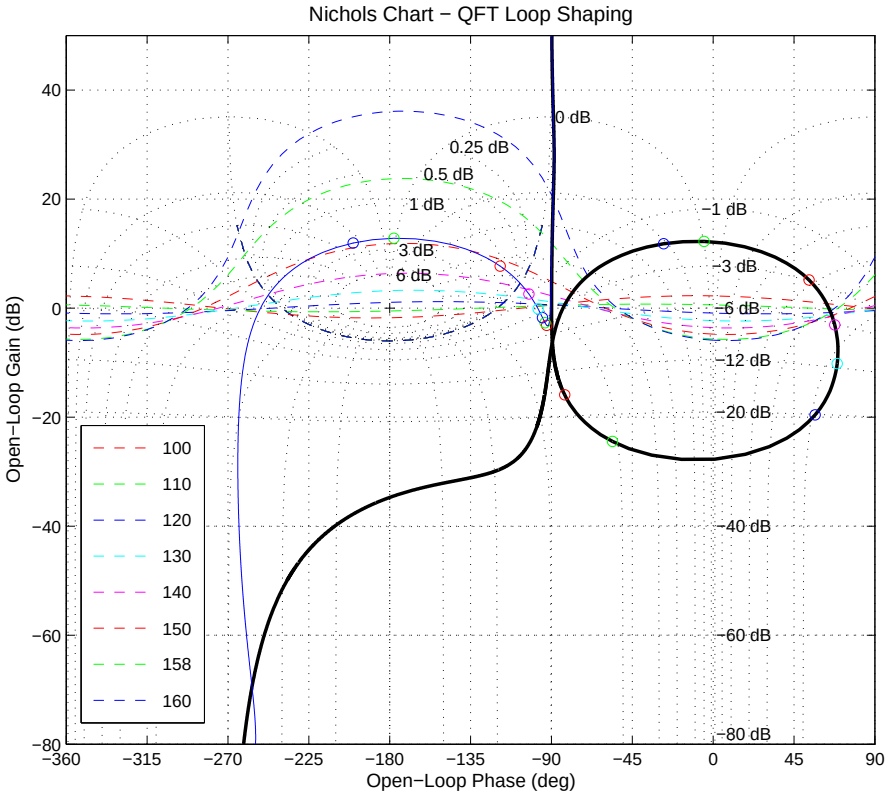


Figure 6.9: Loop Shaping - PI Control

In Figure 6.9 all of the motor bounds lie on the 0dB closed loop magnitude of the standard Nichols Grid, while the load bounds can be seen to vary with frequency (the Legend in Figure 6.9 refers to the bound frequencies). The general design goal, to ensure the fastest response, is to get as close as possible to the bounds without violating them. The controller design shown in Figure 6.9 can be seen to satisfy all of the bounds, with the dominant bounds being the load bounds at 140 and 150 rad/s. Figure 6.10 shows the actual closed loop frequency responses for the design example of Figure 6.9. As can be seen the design specifications have been met and 140-150 rad/s in the load response is confirmed as the critical frequency range.

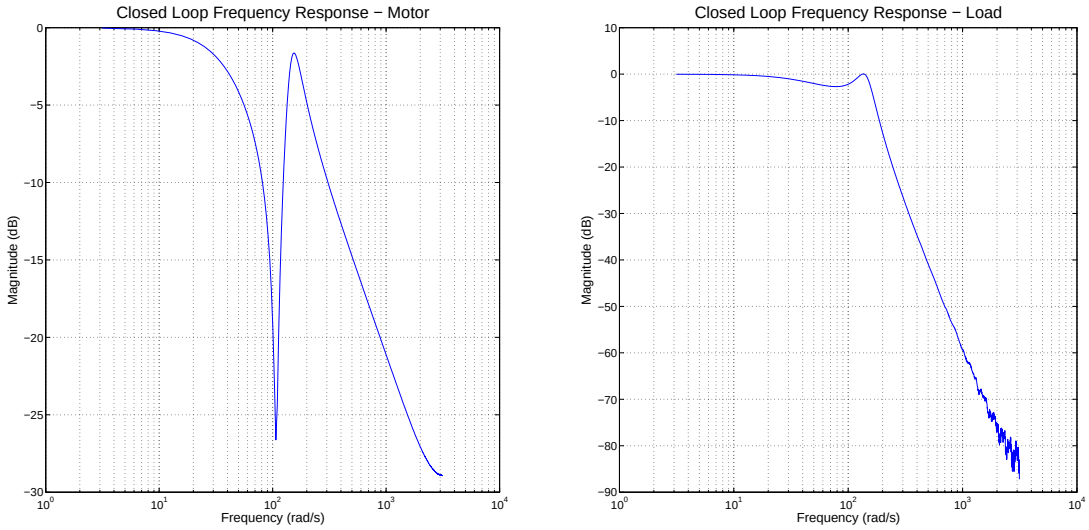


Figure 6.10: Closed Loop Frequency Response - PI Control

The simulated motor and load transient responses for PI control of the system with Shaft 3 as the transmission element are shown in Figure 6.11. Similarly, the motor and load transient responses for PI control of the experimental system, under the same conditions, are shown in Figure 6.12. In each of Figures 6.11 and 6.12, the motor responses are shown in the upper graph, while the load responses are shown in the lower graph.

The first thing to note about all of the transients shown in Figures 6.11 and 6.12 is that standard PI control does not effectively limit oscillations in this system. Recall from Table 4.2 that Shaft 3 has the lowest torsional stiffness of the 3 experimental shafts; consequently, excessive oscillations are observed in this system even when the motor-load

inertia ratio is approximately 1:1 (as in Cases 1 and 2). The only way to reduce these oscillations is to reduce the proportional and/or integral gains, which would result in slower overall responses.

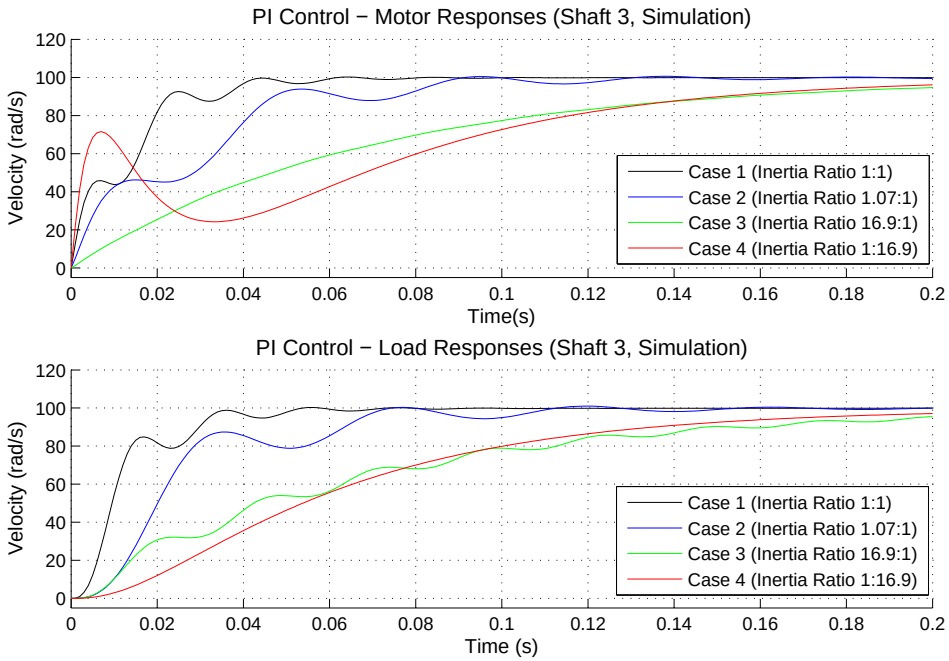


Figure 6.11: Simulated Motor and Load Velocity Responses - PI Control, Shaft 3

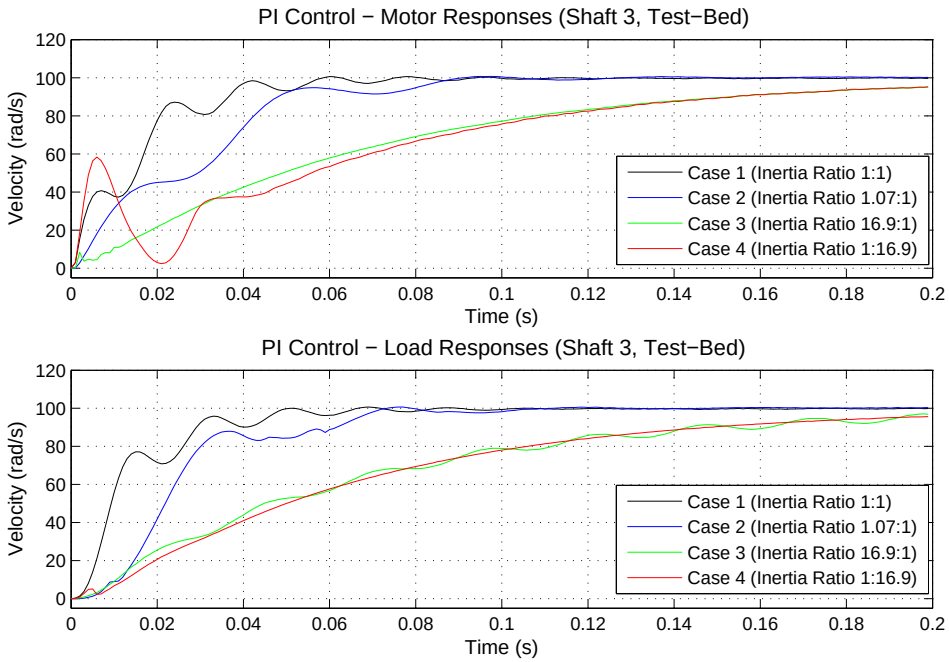


Figure 6.12: Experimental Motor and Load Velocity Responses - PI Control, Shaft 3

It is also evident from both Figures 6.11 and 6.12 that when the motor inertia is much larger than the load inertia the motor response is relatively smooth while the load response exhibits significant oscillation, and vice versa (Cases 3 and 4). However, inertia ratios closer to unity can become even more difficult for designers, as significant oscillations are present in both the motor and load responses (especially when both motor and load inertias are relatively large – Case 2).

When comparing Figures 6.11 and 6.12, it can be seen that the simulated system responses provide a very accurate representation of the actual experimental responses. Some backlash dynamics are noticeable in the experimental responses (due to the use of interchangeable inertia discs), although these dynamics have not had a significant affect on the major response attributes. Another minor difference is that the simulated motor response of Case 4 appears to be more damped than the actual experimental response.

The simulated motor and load transient responses for PI control of the system with Shaft 2 as the transmission element are shown in Figure 6.13. The corresponding experimental responses are shown in Figure 6.14. Similarly, the simulated responses for the system with Shaft 1 as the transmission element are shown in Figure 6.15, while the corresponding experimental responses are shown in Figure 6.16.

An important observation that can be made from Figures 6.13 to 6.16 is that as the torsional stiffness of the transmission element increases (shown successively with Shaft 2 and Shaft 1) the frequencies of all system oscillations increase, while the amplitudes decrease. This was predicted in the analysis presented in Section 6.2. These results clearly demonstrate that the significance of system oscillations is reduced as torsional stiffness of the transmission element is increased. In comparison, the standard industry practice of ensuring a unity inertia ratio can actually result in very significant amplitudes of oscillation in both motor and load responses.

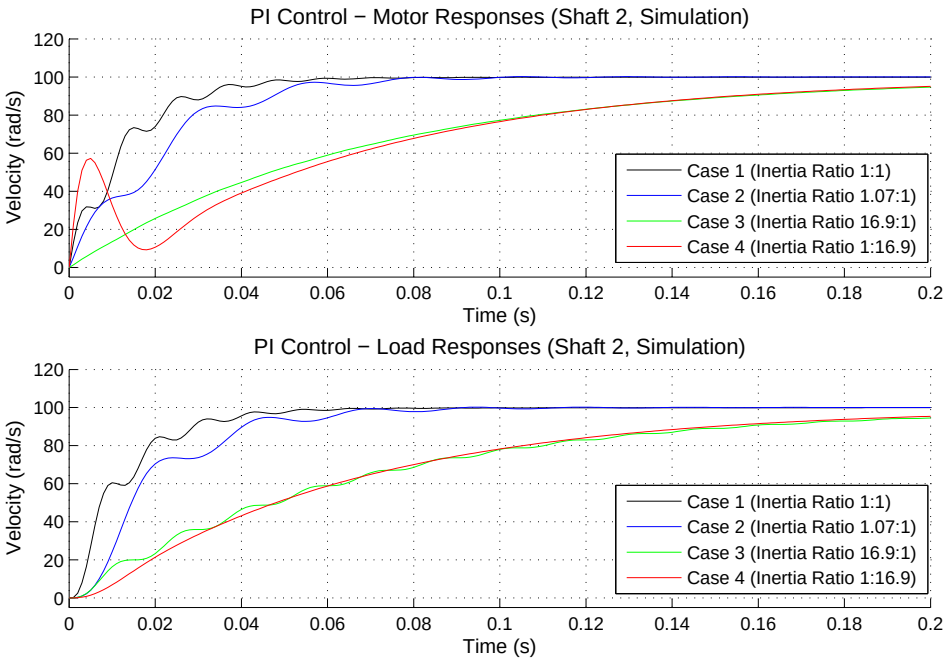


Figure 6.13: Simulated Motor and Load Velocity Responses - PI Control, Shaft 2

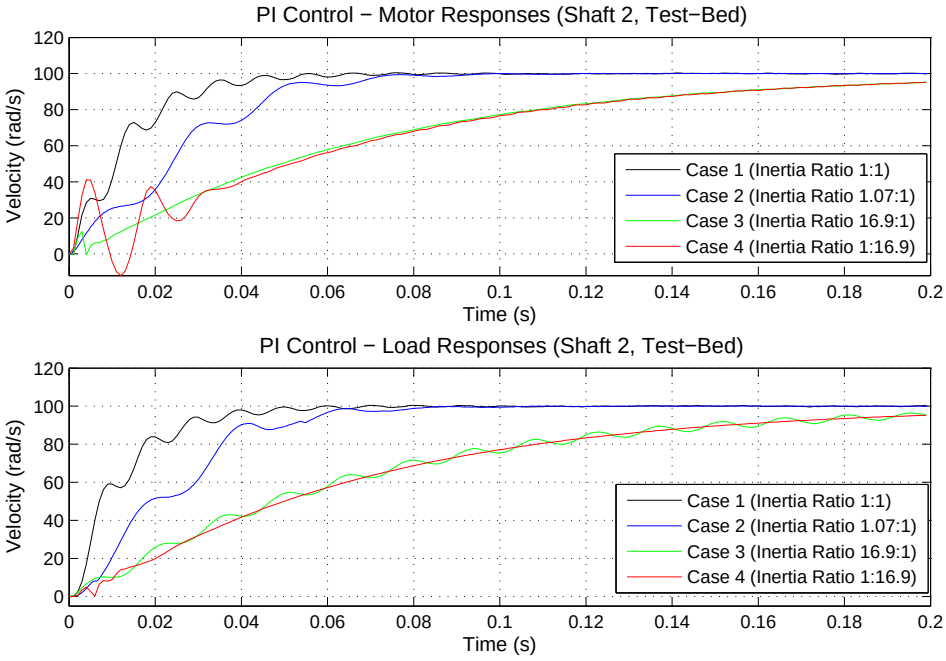


Figure 6.14: Experimental Motor and Load Velocity Responses - PI Control, Shaft 2

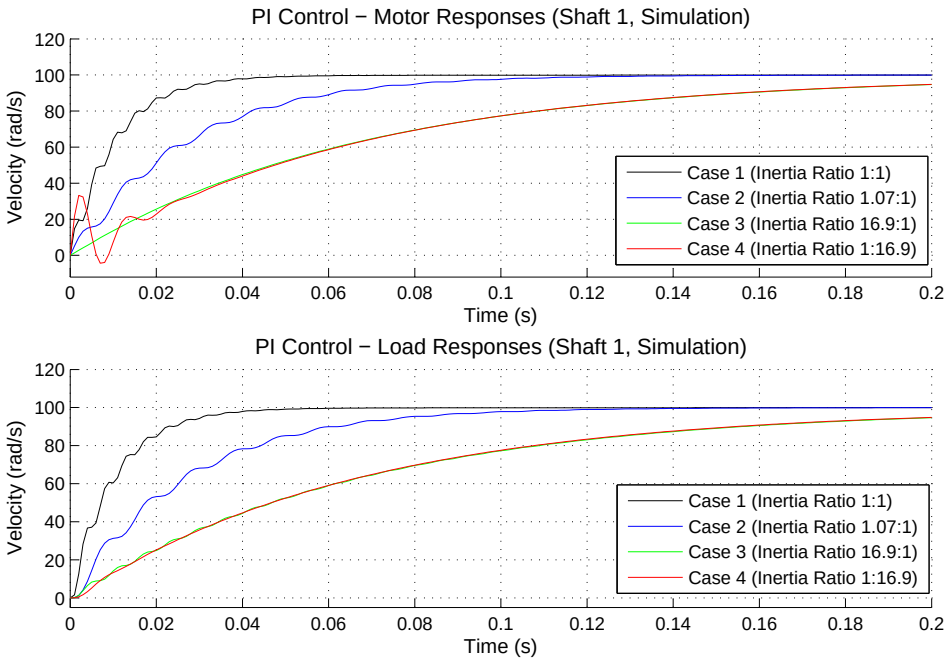


Figure 6.15: Simulated Motor and Load Velocity Responses - PI Control, Shaft 1

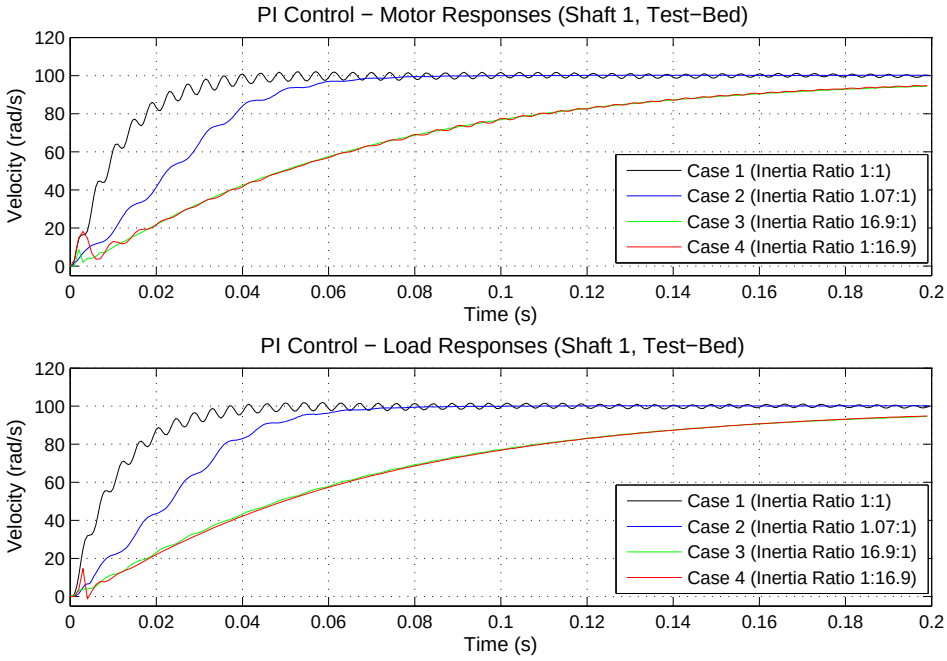


Figure 6.16: Experimental Motor and Load Velocity Responses - PI Control, Shaft 1

A summary of the characteristics for all of the responses presented in Figures 6.11 to 6.16 is given in Table 6.2.

Table 6.2: Transient Response Characteristics - PI Control

| | | Rise Time (ms) | | Oscillation Frequency (rad/s) | | Max Oscillation Amplitude (% of step) | |
|---|---|---|---|---|---|---|---|
| | | Motor | Load | Motor | Load | Motor | Load |
| Shaft 1 Simulated | Case 1 | 23 | 21 | 1470 | 1470 | 0.45 | 0.27 |
| | Case 2 | 41 | 40 | 658 | 658 | 0.48 | 0.47 |
| | Case 3 | 149 | 148 | N/A | 977 | 0 | 0.33 |
| | Case 4 | 155 | 147 | 571$^{@}$ | N/A | 6.59 | 0 |
| Shaft 1 Experimental | Case 1 | 21 | 22 | 1480 | 1480 | 1.66$^{*}$ | 1.89$^{*}$ |
| | Case 2 | 43 | 39 | 668 | 668 | 0.49 | 0.39 |
| | Case 3 | 147 | 147 | 3141$^{+}$ | 937 | 1.87$^{+}$ | 0.41 |
| | Case 4 | 153 | 153 | 785 | 3141$^{+}$ | 5.07 | 4.59$^{+}$ |
| Shaft 2 Simulated | Case 1 | 32 | 25 | 591 | 591 | 1.16 | 1.27 |
| | Case 2 | 46 | 34 | 277 | 277 | 1.6 | 1.8 |
| | Case 3 | 149 | 149 | N/A | 428 | 0 | 0.88 |
| | Case 4 | 153 | 137 | 241$^{@}$ | N/A | 23.18 | 0 |
| Shaft 2 Experimental | Case 1 | 30 | 23 | 608 | 608 | 2.03 | 1.93 |
| | Case 2 | 44 | 32 | 289 | 289 | 1.6 | 2.11 |
| | Case 3 | 151 | 142 | 3141$^{+}$ | 438 | 3.6$^{+}$ | 1.87 |
| | Case 4 | 152 | 142 | 418 | 3141$^{+}$ | 22.7 | 1.49$^{+}$ |
| Shaft 3 Simulated | Case 1 | 38 | 27 | 331 | 331 | 2.17 | 2.01 |
| | Case 2 | 46 | 54 | 155 | 155 | 4.16 | 5.82 |
| | Case 3 | 149 | 138 | N/A | 261 | 0 | 1.76 |
| | Case 4 | 150 | 117 | 125$^{@}$ | N/A | 24.94 | 0 |
| Shaft 3 Experimental | Case 1 | 35 | 25 | 339 | 339 | 3.4 | 3.39 |
| | Case 2 | 45 | 50 | 157 | 157 | 2.66 | 3.47 |
| | Case 3 | 143 | 133 | 785$^{+}$ | 261 | 1.82$^{+}$ | 1.6 |
| | Case 4 | 152 | 135 | 224 | 3141$^{+}$ | 27.2 | 0.86$^{+}$ |

$^{@}$ Frequencies affected by higher damping in simulations
$^{*}$ Amplitudes affected by excitation of structural natural frequency
$^{+}$ Short sharp oscillations observed due to backlash dynamics of inertia discs

The summary in Table 6.2 again illustrates the close agreement between the simulation and experimental responses. The simulated motor responses for Case 4 (high load inertia) do commonly appear to be more damped than the actual experimental responses. However, the testing was performed over a wide range of motor-transmission-load conditions and the complete set of results confirm that the approximate simulation model provides a very accurate representation of the real system. One other minor difference between simulated and experimental results can be seen in the Case 1 responses of Figure 6.16, where the experimental motor and load responses have a larger than predicted amplitude

of oscillation. This is due to the excitation of a structural resonance on the test-bed. The relatively high frequency of this resonance would however allow for simple filtering without a costly reduction in response speed. The effects of each of these minor differences are clearly identified in Table 6.2.

### 6.3.4 Performance of Alternative Velocity Control Solutions

In order to test the performance of the alternative control solutions, each controller was applied to the Motor-Transmission-Load Test-Bed using Shaft 3 and motor-load inertia configuration 2. This particular configuration was shown in Section 6.3.3 to exhibit significant oscillations in both the motor and load responses, and at a lower frequency than any of the other configurations tested. For these reasons, the combination of Shaft 3 and motor-load inertia configuration 2 provides a demanding set-up for comparing controller performance.

Figures 6.17 to 6.24 show the simulated and experimental velocity responses for the tested controllers. In each figure the upper graph shows the simulated motor and load responses, while the lower graph shows the experimental motor and load responses. The responses of the PI controller with notch filtering are shown in Figure 6.17. The design of the notch filter was undertaken in the *s*-domain and has the form given in Equation (6.19), where the width and depth of the notch are adjusted via the damping ratio ($\zeta$). To implement the notch filter on the digital drives (of the CNC system) a Tustin transformation of Equation (6.19) was performed to translate the notch into the *z*-domain. The general *z*-domain form of a 2nd order filter (after a Tustin transformation) is given in Equation (6.20), where $h$ is the sampling period. For the case of the notch filter: $\omega_1 = \omega_2 = \omega$, $\zeta_1 = 0$ and $\zeta_2 = \zeta$.

$$\frac{\frac{s^2}{\omega^2} + 1}{\frac{s^2}{\omega^2} + \frac{2\zeta s}{\omega} + 1} \tag{6.19}$$

$$\frac{\frac{\omega_2^2\left(4+4\omega_1 h\zeta_1+\omega_1^2h^2\right)}{\omega_1^2\left(4+4\omega_2 h\zeta_2+\omega_2^2h^2\right)}z^2+\frac{\omega_2^2\left(2\omega_1^2h^2-8\right)}{\omega_1^2\left(4+4\omega_2 h\zeta_2+\omega_2^2h^2\right)}z+\frac{\omega_2^2\left(4-4\omega_1 h\zeta_1+\omega_1^2h^2\right)}{\omega_1^2\left(4+4\omega_2 h\zeta_2+\omega_2^2h^2\right)}}{z^2+\frac{2\omega_2^2h^2-8}{4+4\omega_2 h\zeta_2+\omega_2^2h^2}z+\frac{4-4\omega_2 h\zeta_2+\omega_2^2h^2}{4+4\omega_2 h\zeta_2+\omega_2^2h^2}} \tag{6.20}$$

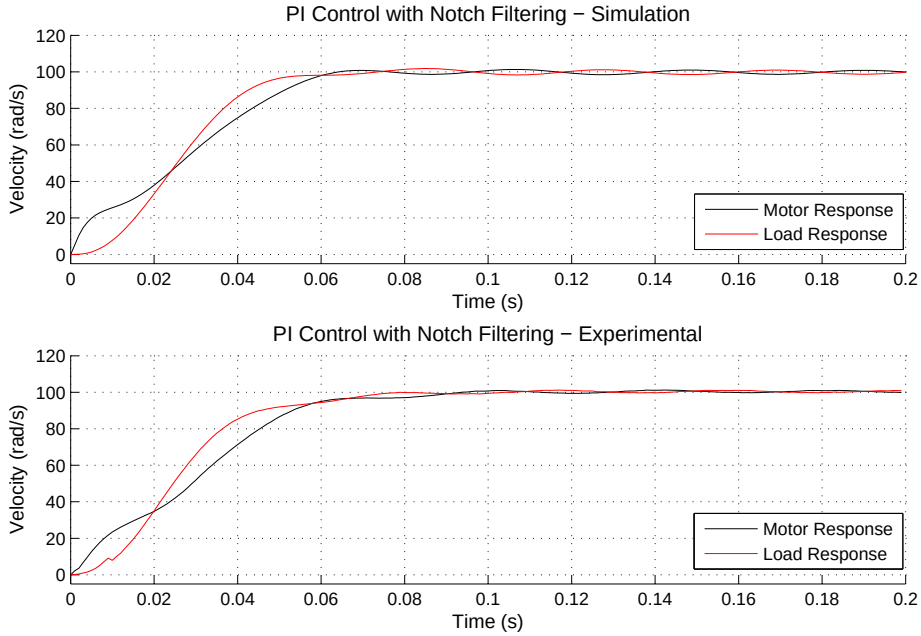


Figure 6.17: Motor and Load Velocity Responses - Notch Filtering

For the experimental implementation of shaft flex feedback, the shaft flex was calculated using direct motor and load position encoder measurements. Similarly, the experimental implementation of velocity difference feedback was achieved via differentiation of the same motor and load position encoder measurements. The responses for the PI controller with shaft flex feedback are shown in Figure 6.18. The responses for the PI controller with velocity difference feedback are shown in Figure 6.19.

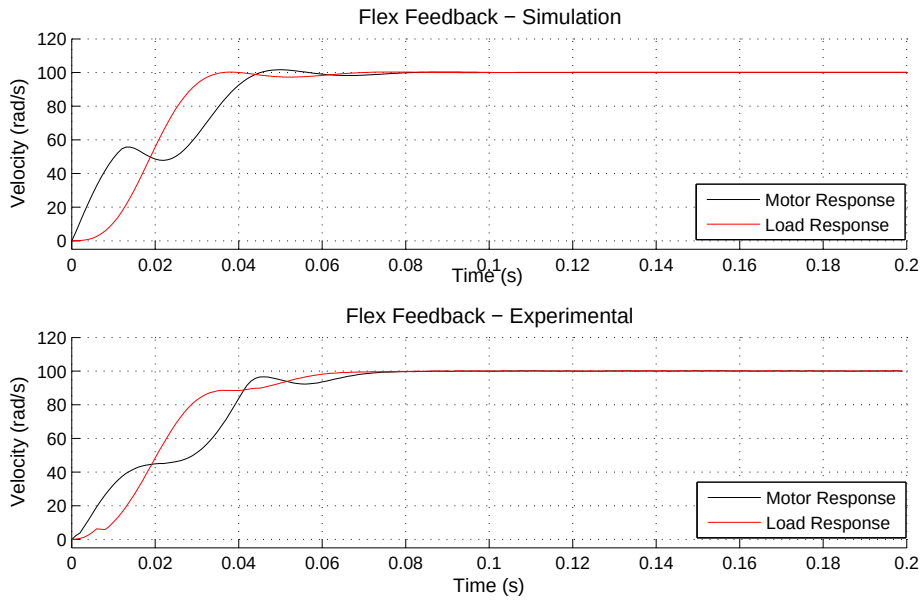


Figure 6.18: Motor and Load Velocity Responses - Shaft Flex Feedback

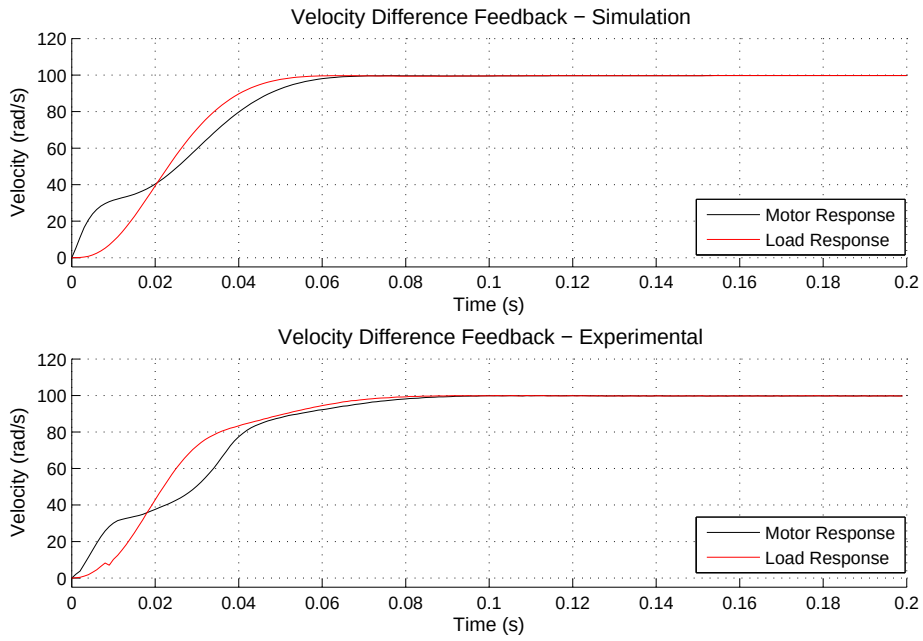


Figure 6.19: Motor and Load Velocity Responses - Velocity Difference Feedback

A Hübner rotary accelerometer was used to obtain the feedback signals for the experimental implementation of load and motor acceleration feedback. Double-differentiated position encoder measurements were initially tested for use as acceleration feedback. The resulting signals were found to contain large amounts of noise and were not suitable for

closed loop feedback. In comparison, the Hübner accelerometer provided smooth acceleration feedback signals. The responses for the PI controller with load acceleration feedback are shown in Figure 6.20. The responses for the PI controller with motor acceleration feedback are shown in Figure 6.21.

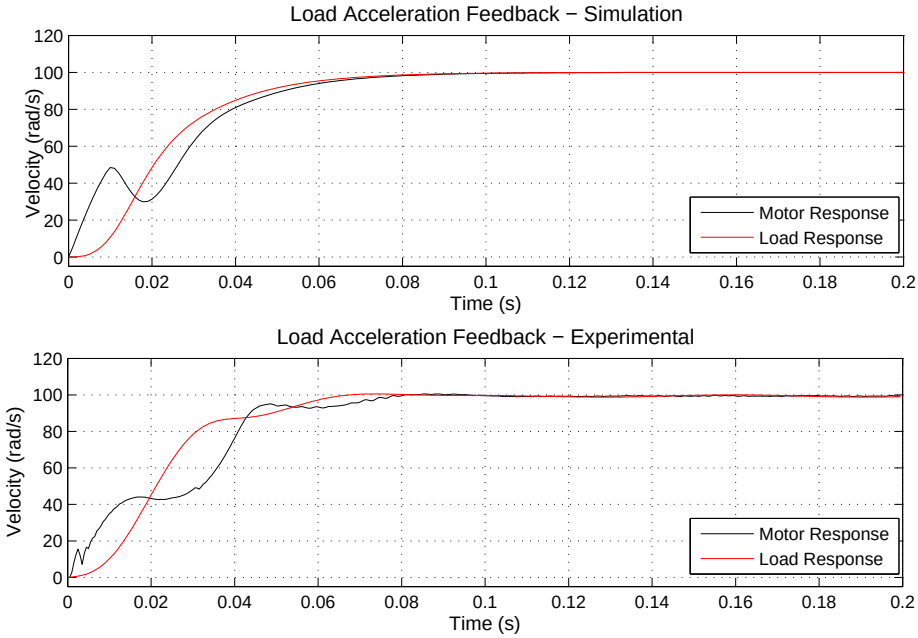


Figure 6.20: Motor and Load Velocity Responses - Load Acceleration Feedback

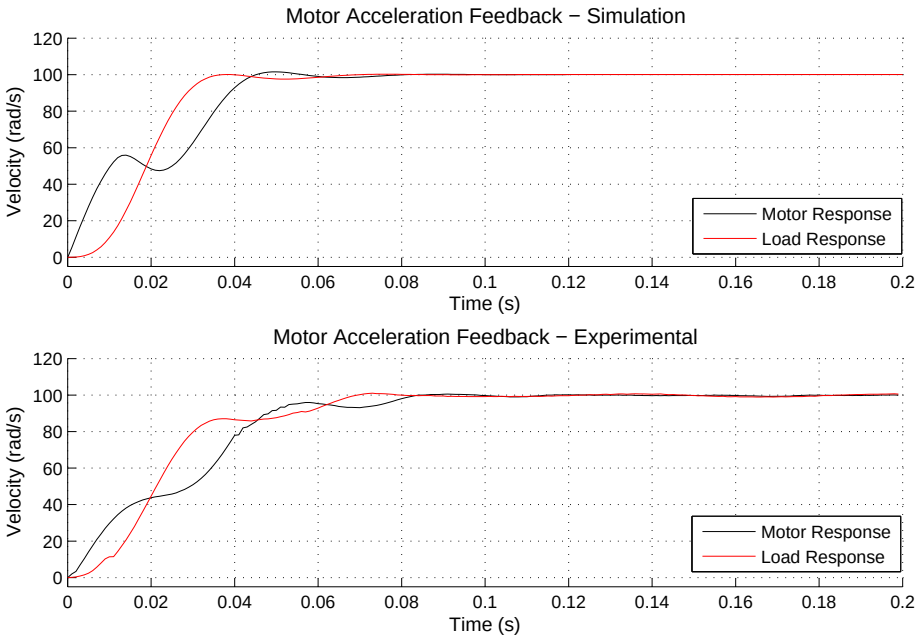


Figure 6.21: Motor and Load Velocity Responses - Motor Acceleration Feedback

The responses for the state feedback controller are shown in Figure 6.22. Three states were defined for the controller; namely, motor velocity, load velocity and shaft flex. Figure 6.23 shows the responses for the same state feedback controller with an observer added to estimate the load velocity and shaft flex states.

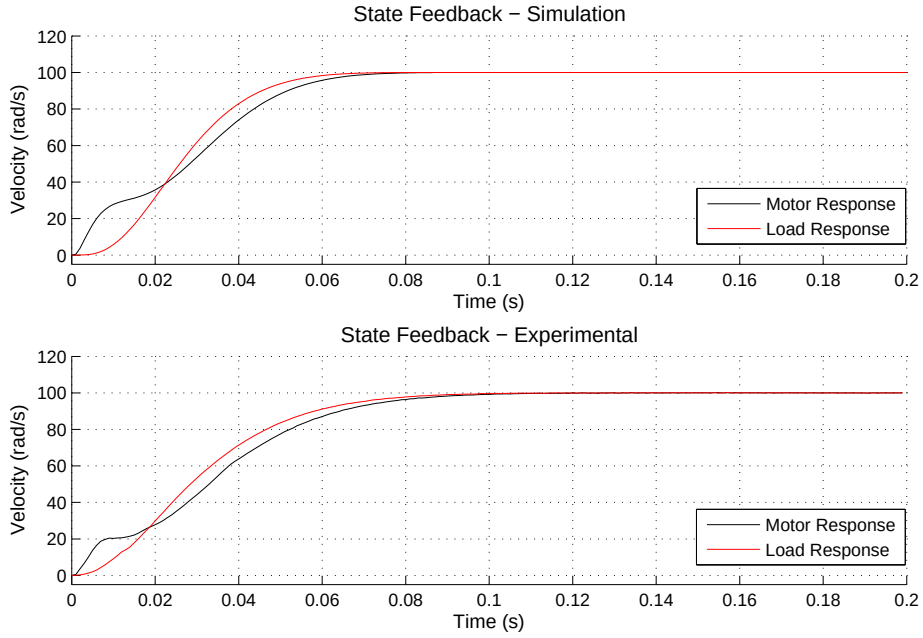


Figure 6.22: Motor and Load Velocity Responses - State Feedback

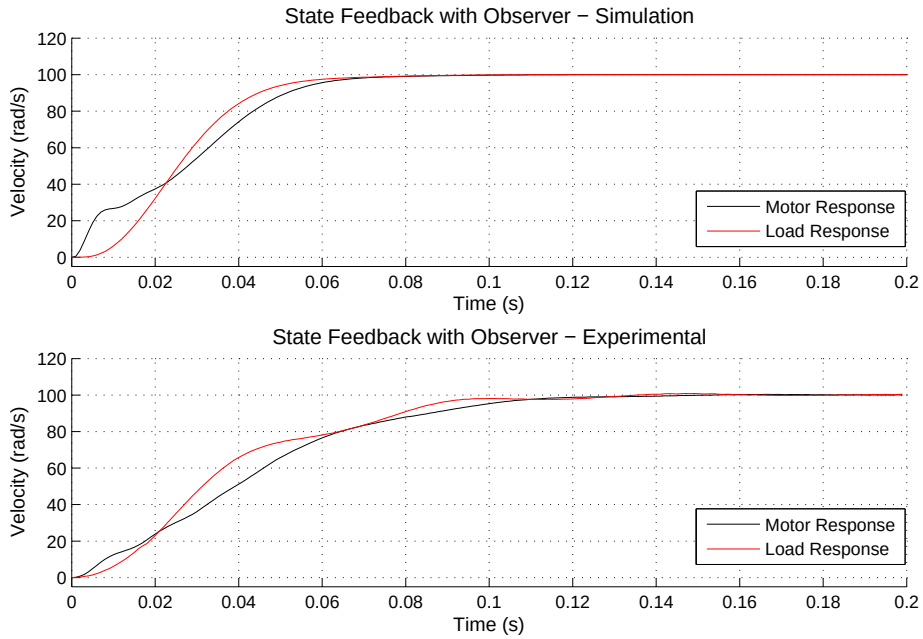


Figure 6.23: Motor and Load Velocity Responses - State Feedback with Observer

The responses for the unrestricted QFT designed motor velocity loop are shown in Figure 6.24. The final controller design consisted of a PI stage with two 2nd order loop filters. The 1st of the filters had the form of a notch filter, while the 2nd filter provided a band of phase lag to help compensate for the inherent band of phase lead between the quadratic zeros and quadratic poles of the system. The actual loop design is given in Equation (6.21). As with the simple notch filter, a Tustin transformation was used to translate the *s*-domain design to the *z*-domain (see Equation (6.20)).

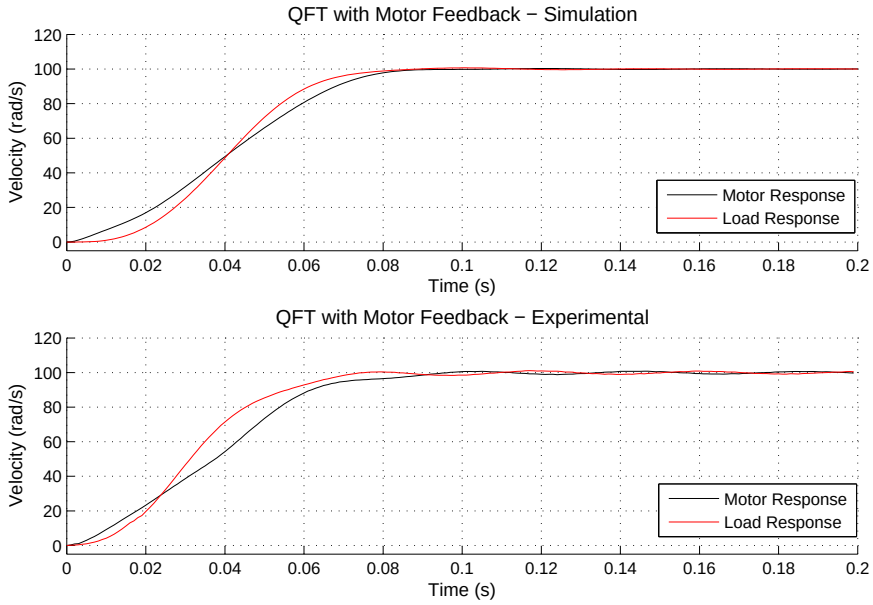


Figure 6.24: Motor and Load Velocity Responses - QFT with Motor Feedback Only

$$G(s) = 0.3\left(\frac{0.625s+1}{s}\right)\left(\frac{\frac{s^2}{\omega_1^2}+\frac{2\zeta_1 s}{\omega_1}+1}{\frac{s^2}{\omega_2^2}+\frac{2\zeta_2 s}{\omega_2}+1}\right)\left(\frac{\frac{s^2}{\omega_3^2}+\frac{2\zeta_3 s}{\omega_3}+1}{\frac{s^2}{\omega_4^2}+\frac{2\zeta_4 s}{\omega_4}+1}\right) \qquad (6.21)$$

$$\text{where: } \omega_1 = 158 \quad \zeta_1 = 0.025$$

$$\omega_2 = 158 \quad \zeta_2 = 0.5$$

$$\omega_3 = 158 \quad \zeta_3 = 0.1$$

$$\omega_4 = 140 \quad \zeta_4 = 0.2$$

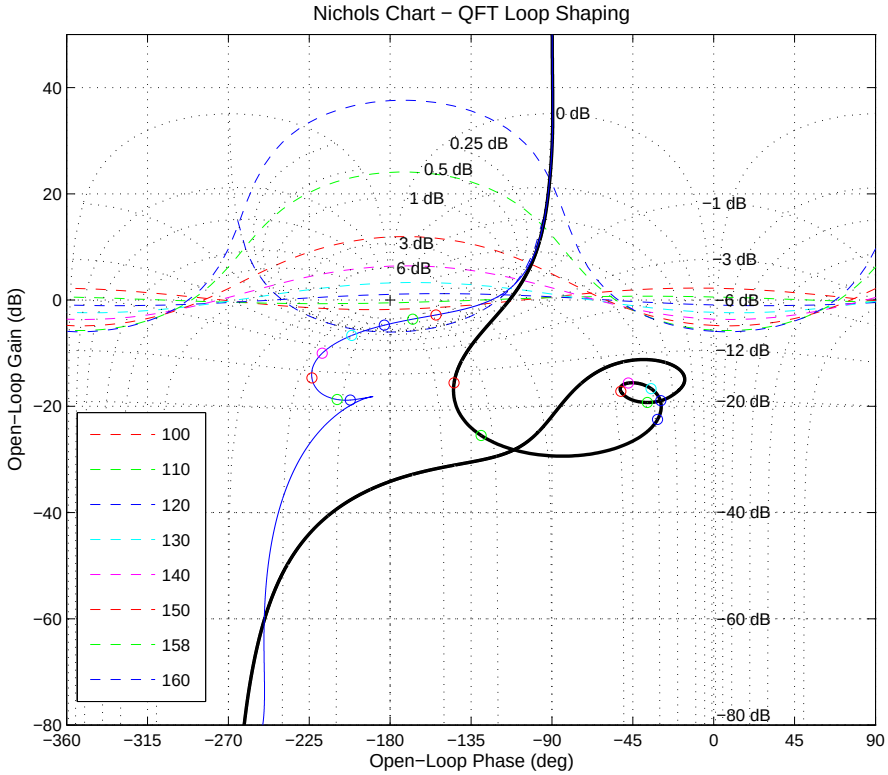


Figure 6.25: Loop Shaping - Shaft Flex Feedback

The Nichols chart for the loop design of Equation (6.21) is shown in Figure 6.25. The effects of the two filters can easily be seen when comparing Figure 6.25 with Figure 6.9 (the standard PI controller). The notch filter has the effect of reducing the closed loop magnitude at the natural frequency of oscillation, which is evident by the flatter circle in the motor velocity plot of Figure 6.25 (mathematically, this is equivalent to increasing the damping of the system). The phase lag introduced by the 2nd filter is also evident by the open loop phase not exceeding 0 degrees in Figure 6.25, whereas the open loop phase exceeds 45 degrees around the natural frequency of oscillation in Figure 6.9.

A summary of the characteristics for all of the responses presented in Figures 6.17 to 6.24 is given in Table 6.3. For comparison purposes, the characteristics of the benchmark PI controller for Shaft 3 and motor-load inertia configuration 2 are also repeated in Table 6.3.

Table 6.3: Transient Response Characteristics - Alternative Controllers

| | Rise Time (ms) | | Oscillation Frequency (rad/s) | | Max Oscillation Amplitude (% of step) | |
|---|---|---|---|---|---|---|
| | Motor | Load | Motor | Load | Motor | Load |
| PI Controller – Sim. | 46 | 54 | 155 | 155 | 4.16 | 5.82 |
| PI Controller – Exp. | 45 | 50 | 157 | 157 | 2.66 | 3.47 |
| Notch Filtering – Sim. | 50 | 31 | 159 | 159 | 1.18 | 1.55 |
| Notch Filtering – Exp. | 49 | 35 | 157 | 157 | 0.74 | 0.67 |
| Shaft Flex FB – Sim. | 37 | 19 | 169 | 169 | 3.56 | 1.42 |
| Shaft Flex FB – Exp. | 38 | 36 | 212 | 212 | 2.55 | 0.68 |
| Velocity Difference FB – Sim. | 46 | 30 | 261 | N/A | 1.2 | $\approx 0$ |
| Velocity Difference FB – Exp. | 51 | 42 | 224 | N/A | 1.6 | $\approx 0$ |
| Load Acceleration FB – Sim. | 50 | 38 | 349 | N/A | 5.88 | 0 |
| Load Acceleration FB – Exp. | 42 | 39 | 174 | 174 | 1.83 | 0.56 |
| Motor Acceleration FB – Sim. | 37 | 19 | 173 | 173 | 3.38 | 1.24 |
| Motor Acceleration FB – Exp. | 45 | 45 | 176 | 176 | 2.14 | 1.8 |
| State FB – Sim. | 48 | 33 | 390 | N/A | 0.99 | 0 |
| State FB – Exp. | 61 | 48 | 392 | N/A | 1.28 | 0 |
| State FB with Observer – Sim. | 48 | 33 | 628 | N/A | 0.42 | 0 |
| State FB with Observer – Exp. | 78 | 66 | 571 | 128 | 0.31 | 0.67 |
| QFT Controller – Sim. | 55 | 40 | 133 | 133 | 0.23 | 0.4 |
| QFT Controller – Exp. | 51 | 41 | 157 | 157 | 0.88 | 1.14 |
| FB - Feedback<br>Sim. - Simulated Responses<br>Exp. - Experimental Responses | | | | | | |

It can be seen, from Table 6.3 and Figures 6.17 to 6.24, that all of the studied control approaches were successful in reducing the maximum amplitudes of oscillation in the load responses. The improvement in oscillation amplitude did come at the cost of reduced response speed in some cases; however, this slight reduction in response speed is minimal in comparison to the effects of reducing the PI gains. Table 6.3 and Figures 6.17 to 6.24 again show close agreement between the experimental and simulated results. The fragile nature of the very thin transmission shaft, used on the test-bed to provide low torsional stiffness, did however make it difficult to use the optimal theoretical controller gains.

When comparing the relative performance of the control solutions, it can be seen that the best results were achieved by the state feedback controller and the PI controller with velocity difference feedback. Both of these controllers resulted in smooth responses for both

the motor and load, with minor impact on the system rise times. In both cases load velocity was used as an additional feedback signal. In comparison, the two PI controllers using load acceleration feedback and shaft flex feedback resulted in smooth load responses, but significant oscillations remained in the motor responses. In fact, the simulated motor response for load acceleration feedback actually predicted a slight increase in maximum amplitude of oscillation. In practice, the controller performance for both load acceleration feedback and shaft flex feedback appeared similar to decreasing the motor inertia of the system (refer to Case 4 for each of the shafts in Section 6.3.3). As a result, these approaches were found to be very similar to using motor acceleration feedback, which also effectively reduced the system motor inertia (as predicted in the mathematical analysis if Section 6.2.5). The advantage of motor acceleration feedback over load acceleration feedback and shaft flex feedback is that no feedback is required from the load end.

The other controllers, that used feedback from the motor only, produced mixed results. The simple notch filter and the unrestricted QFT design provided good overall performance in both the motor and load responses. However, the state feedback controller with observer was unstable on the experimental system when the original state feedback gains were used. Stable experimental results were obtained for this controller, but only after considerably reducing the system response speed. It was also found that the observer required more computational power than any of the other approaches. In Figure 6.26, 100 samples of the time taken to execute a complete control cycle, for each of the tested controllers, are plotted. In any system the total execution time for the control cycle must be less than the sample period of the control system (125$\mu$s on the digital servo drives of this system). The additional computational requirements of the observer are clearly illustrated in Figure 6.26, where the average control cycle execution is right on the limit and at times even exceeds the allowed 125$\mu$s (a drop to around zero in the recorded execution time is a result of the control cycle not completing within the allowed sample period). In comparison, all of the other control approaches take around 100$\mu$s to execute.

In general, out of all the approaches, the simple notch filter and the unrestricted QFT de-

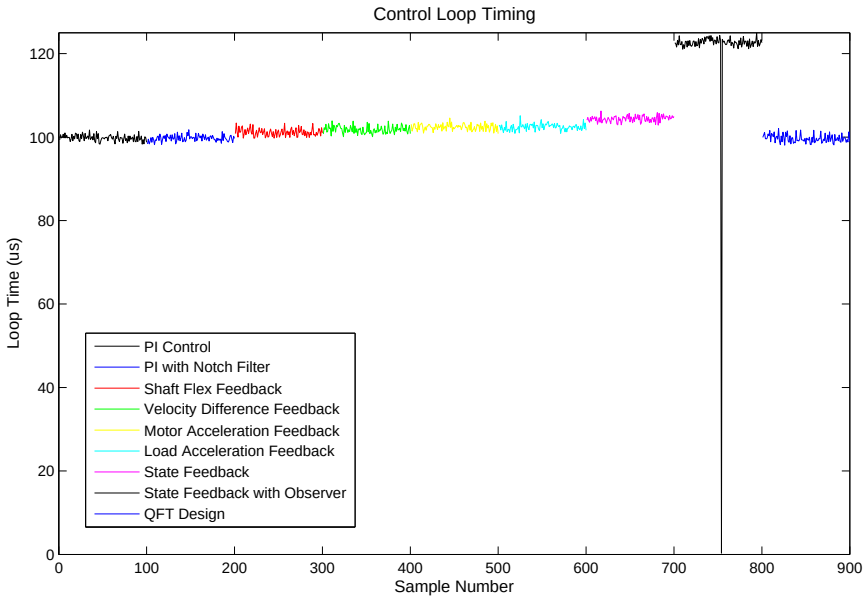


Figure 6.26: Control Cycle Timing for the Digital Servo Drives

sign were the easiest to implement and tune. Of these two approaches, the unrestricted QFT design produced a smoother motor response during the transient period, at the expense of a small increase in rise time. Although the state feedback controller (without an observer) produced the best overall results, this controller is more difficult to tune than the others (especially if fine tuning is required on the practical system) and requires additional feedback from the load. If the unrestricted QFT design approach was extended to include separate load velocity feedback, this approach would also allow for a controller design with the same structure as the state space controller.

## 6.4 Influence of Drive-Train Configuration

The influence of drive-train configuration on torsional vibrations was studied using the Drive Comparison Test-Bed (refer to Section 4.4 for details). Figure 6.27 shows the motor velocity frequency response (closed loop PI control) for the test-bed with the rotary motor directly coupled to the ballscrew transmission. A chirp signal was used in addition to a constant velocity command for logging the frequency data. For the response shown in Figure 6.27 the chirp signal was applied when the load was positioned as far away from

the motor as possible. This represents the worst case scenario, since the torsional stiffness of a ballscrew reduces as the load moves away from the motor (as described in Section 3.5.1).

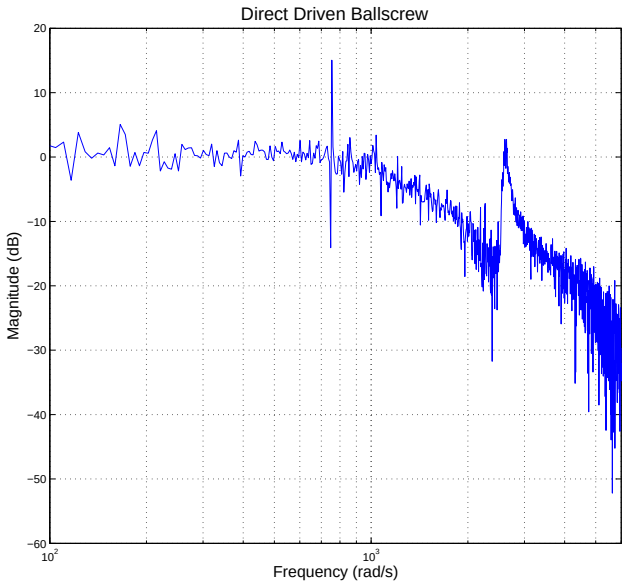


Figure 6.27: Frequency Response – Direct Driven Ballscrew Configuration

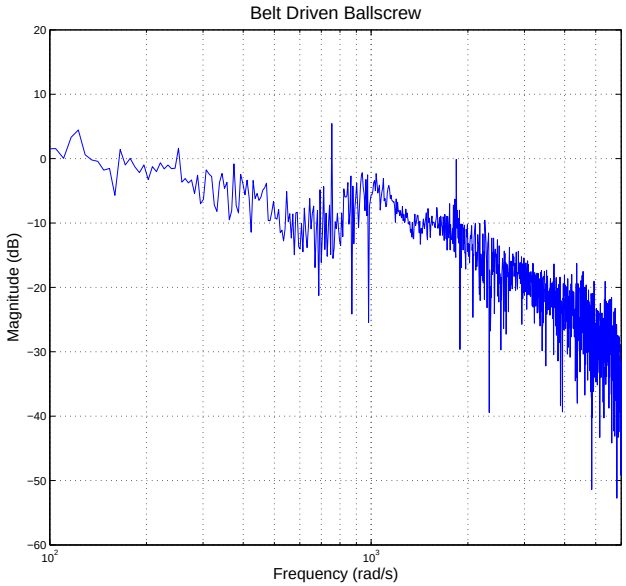


Figure 6.28: Frequency Response – Belt Driven Ballscrew Configuration

From Figure 6.27, it can be seen that the direct driven ballscrew configuration has a bandwidth of approximately 1000 rad/s. A resonant peak can also be observed between 2000

and 3000 rad/s. Figure 6.28 shows the motor velocity frequency response for the test-bed with the synchronous timing belt used to couple the rotary motor to the ballscrew transmission. The chirp signal was again applied with the load positioned as far away from the motor as possible.

When comparing Figure 6.28 with Figure 6.27 it can be seen that the synchronous timing belt has significantly damped the resonant peak observed in Figure 6.27 (the direct driven case). However, the reduced stiffness of the belt driven system has lowered the resonant frequency to approximately 1000 rad/s, resulting in a lower overall controller bandwidth.

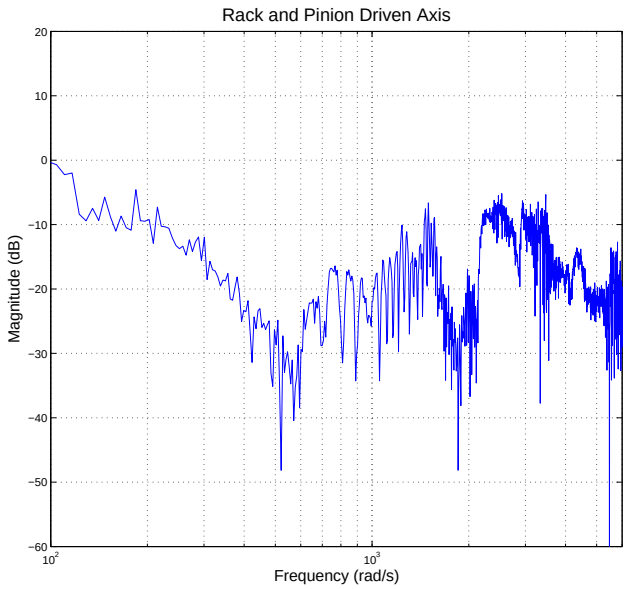


Figure 6.29: Frequency Response – Rack and Pinion Configuration

Figure 6.29 shows the motor velocity frequency response for the test-bed when configured to use the rack and pinion transmission. As can be seen, the overall controller bandwidth is much lower for the rack and pinion transmission than either of the ballscrew cases. The limited controller bandwidth is not however a result of any lower resonant frequencies (as can be seen from Figure 6.29), but rather the large amount of backlash inherent in the rack and pinion system. As a comparison, Figure 6.30 shows the motor velocity frequency response for the Linear Motor Test-Bed. Since linear motors provide a direct drive mechanism with zero backlash, the controller bandwidth of the Linear Motor Test-

Bed is higher than each of the other configurations and is not affected by any resonant frequencies.

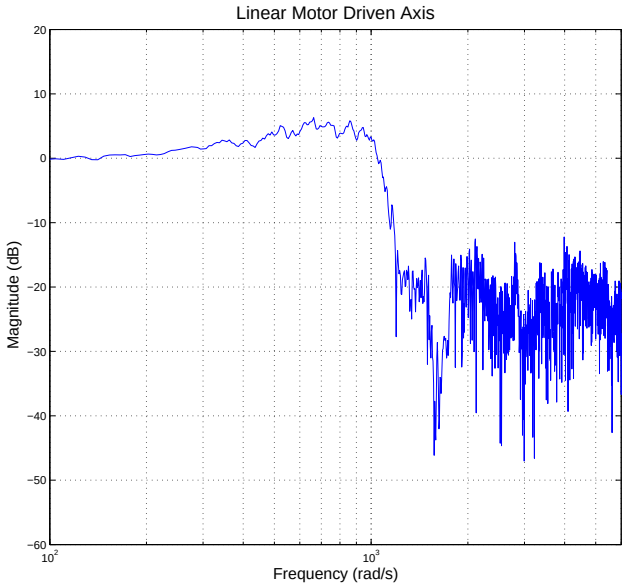


Figure 6.30: Frequency Response – Linear Motor Test-Bed

As can be seen from Figures 6.27 to 6.30, drive train configuration has a large influence on any resonant frequencies and subsequent torsional vibrations in a system. With reference to the configurations examined in this section, the direct driven ballscrew case had the largest resonant peak. The addition of a synchronous timing belt to this system resulted in significant damping of the resonance, but also resulted in a lower overall system bandwidth. The rack and pinion configuration and the linear motor system showed no significant resonant frequencies; however, the rack and pinion configuration had a low system bandwidth due to the presence of backlash. Since no anti-backlash mechanisms or advanced control techniques were used in this test, the system quickly became unstable whenever the PI controller gains were increased. Methods that can be used to improve the performance of systems with backlash are examined in Chapter 7.

Each of the methods examined in Section 6.3.4 can be applied to systems with a large resonant peak and subsequent torsional vibrations. As an example, the unrestricted QFT approach was used to design a new controller for the direct driven ballscrew configuration. The QFT approach is particularly suited to this problem, as the variation in torsional

stiffness (inherent in a ballscrew) can be included in the design process. Figure 6.31 shows the motor velocity response for the QFT controller. When comparing Figure 6.31 with Figure 6.27, it can be seen that the QFT designed controller successfully reduced the resonant peak, while maintaining the overall system bandwidth.

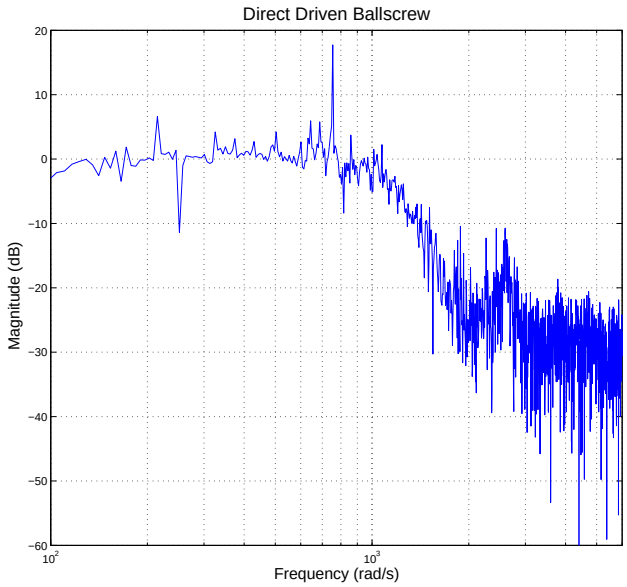


Figure 6.31: Frequency Response – QFT Controlled Direct Driven Ballscrew

## 6.5 Conclusions

A theoretical analysis of drive-train flexing and torsional vibrations has been presented in this chapter. Different control solutions to the problem were studied, with their effectiveness compared both theoretically and experimentally. The influence of the overall drive-train configuration was also analysed experimentally.

Open loop flexing of the transmission element in a system was studied in Section 6.2.2. The impact this flexing has on the closed loop system was further studied in Section 6.2.3. It was found that torsional stiffness of the transmission element has a much greater affect on both the frequency and amplitude of any resulting system oscillations than motor/load inertia ratio does. Also, as the inertia of the transmission element increased, it was found

that motor/load inertia ratio had less affect on system oscillations. This latter result is important as many practical transmissions (such as long ballscrews) have quite significant inertia.

In Section 6.2.3 it was found that the position and width of the band of frequencies between the quadratic zeros and quadratic poles of the motor response have a considerable impact on the resonant peak of a closed loop system. The common practice of varying motor inertia to maintain a unity motor/load inertia ratio was shown to vary the width of this band of frequencies, but not the position. Although narrowing the width of the frequency band can reduce the resonant peak of the closed loop system, varying torsional stiffness of the transmission element was shown to produce the improved result of varying both the width and position of the frequency band. As the actual frequencies in this band become higher, the impact of any resulting oscillations on the closed loop system is reduced.

The location of feedback sensors, in motor-transmission-load systems, was discussed in Sections 6.2.3 and 6.2.4. It was found that for some frequencies motor feedback leads the total torque rather than lagging it, as the load does. Hence, motor feedback does not always provide an accurate representation of the load. It was also shown that absolute stability problems can exist when load feedback is solely used. For these reasons, a combination of motor and load feedback (where practical) is the most appropriate approach for systems with low torsional stiffness.

In Section 6.2.5, control solutions using feedback from the motor were compared with solutions using a combination of motor and load feedback. When compared theoretically, it was found that shaft (transmission) torque feedback, load torque feedback, load acceleration feedback and shaft flex feedback are all fundamentally equivalent approaches, with the feedback gains of each approach related by system constants. Although all of these approaches are theoretically effective in reducing system oscillations, their fundamental equivalence was not discussed in any of the literature reviewed in Chapter 2.

Two of the feedback approaches, compared in Section 6.2.5, were developed as a part of

this thesis. The first approach, shaft flex feedback, was found to increase the frequency and reduce the amplitude of system oscillations, but was also found to be fundamentally equivalent to other published solutions (as already noted). However, the second approach, velocity difference feedback, was found to reduce system oscillations through effectively increasing the system damping. The fact that many of the published feedback approaches are fundamentally equivalent highlights the advantages of developing a standard approach to the problem of controlling torsional vibrations.

A method to include both motor and load specifications in a single QFT design procedure was presented in Section 6.3, along with an experimental comparison of control approaches. The test-bed used for the experimental comparison allowed for drive-train flexing and torsional vibrations to be directly analysed. Simulated and experimental transient responses were presented for a wide range of motor-transmission-load conditions. The limitations of using standard PI control on systems with low torsional stiffness were demonstrated, with both the motor and load responses exhibiting significant oscillations. Although the practice of re-sizing motors in order to maintain unity motor-load inertia ratios can improve system performance, the experimental results in Section 6.3 clearly show that excessive system oscillations can still be present in systems with a unity inertia ratio.

All of the alternative control approaches examined in Section 6.3 showed improvement over standard PI control, with state feedback and velocity difference feedback demonstrating the best results. However, both of these approaches require feedback from the load, which is not always practical in many machine tool designs. Of the controllers that require feedback from the motor only, the simple notch filter and further filtering through an unrestricted QFT design were shown to be very effective and easy to implement and tune. In comparison, state feedback was found to be difficult to fine-tune practically and with the addition of an observer required more computational power than all of the other approaches.

The results presented throughout Section 6.3 also demonstrated strong agreement between

the simulated and experimental responses, across the wide range of conditions. This strong agreement validates the accuracy of the system models, which were based on the 'adjusted' two-body model developed in Chapter 3.

The influence of drive-train configuration on torsional vibrations was studied experimentally in Section 6.4. It was found that the ballscrew configurations exhibited higher resonant peaks than the rack and pinion and linear motor configurations. In particular, the direct driven ballscrew case had the largest resonant peak. The addition of a synchronous timing belt to this system was shown to increase the damping of the resonance, but reduce the overall bandwidth of the system. The problems associated with ballscrew configurations also become more significant as the travel of the axis is increased, since longer ballscrews often suffer from low torsional stiffness and increased inertia. From the control perspective, the QFT approach was shown to successfully reduce the resonant peak of a ballscrew driven axis, without reducing the overall system bandwidth. The QFT approach allows for the inherent variation in ballscrew torsional stiffness to be taken into account during the design process.

Chapter 7

# Backlash

## 7.1 Introduction

A new approach to the non-linear control of machine tool servo systems with backlash is presented in this chapter. Backlash has historically been considered as one of the most serious problems associated with precision control in machine tools and has maintained the attention of engineers for over 60 years. As can be seen in both Chapter 5 and Chapter 6, the existence of backlash can limit the effectiveness of controllers designed to address other performance related factors such as torsional vibrations and dynamic stiffness. In fact, the changes in inertia experienced in a system with backlash can be a source of excitation for torsional vibrations. Further, some of the approaches that were shown to be effective in reducing torsional vibrations in Chapter 6 can actually increase the adverse effects of backlash if not applied carefully. For this reason, the control of backlash should always be treated in parallel with the problem of reducing torsional vibrations in any system where backlash is present.

The control approach presented in this chapter takes both backlash and torsional vibrations into account, using the accurate system models derived in Chapter 3. The approach also combines the concepts of ‘weak’ and ‘strong’ action during the backlash phase, which has the advantage of addressing both the dynamic stability and tracking performance of a system with backlash. Position and acceleration feedback from the motor

are used in this approach and, for the case of velocity tracking, the width of the backlash gap does not need to be known. However, if accurate position tracking is required, a measure of the backlash gap is essential when position feedback from the load is not available. The backlash gap of the experimental system used to evaluate the control approach was manually measured and is given in Chapter 4. Although a number of methods have been suggested for automatically measuring the width of a backlash gap (for examples the reader is referred to [103, 104, 105]), the work presented in this chapter was focused solely on the effective control of systems with backlash.

An analysis of describing functions for backlash models is presented in Section 7.2. The describing functions of the standard dead-zone model and the new backlash model, introduced in Section 3.4, are presented. The outputs of these describing functions are then compared in terms of phase and magnitude.

The hybrid weak/strong approach to controlling systems with backlash is presented in Section 7.3. The QFT technique is used to effectively design controllers for both the contact phase and backlash phase of systems with backlash. A method to accurately construct Nichols Chart stability bounds using the describing function of the new backlash model is shown and then used in the QFT design process. Advantages and disadvantages of the weak action control approach are demonstrated through simulation. The clear advantages of combining this weak action with an additive strong action are then demonstrated. Implications of the additive strong action are also discussed, especially with reference to the method used to identify when the system enters the backlash phase.

In Section 7.4 the hybrid weak/strong control approach is demonstrated on the Motor-Transmission-Load Test-Bed (described in Section 4.3). The combined effects of the weak and strong actions of this controller, along with the method used to identify when the system enters the backlash phase, are practically demonstrated. The computational requirements of this controller are also briefly discussed.

A summary of the key points and conclusions that can be drawn from this chapter are presented in Section 7.5.

## 7.2 Describing Functions and Backlash

As discussed in Section 2.4.3, the describing function technique has traditionally been the most common technique used to find linear approximations of general nonlinearities. In particular, the sinusoidal-input describing function has been successfully used to describe backlash since the 1950s. In this section, the sinusoidal-input describing function for the backlash model developed in Section 3.4 is presented and compared with the sinusoidal-input describing function of a standard dead-zone model. Although dual-input describing functions have also been successfully used to describe backlash [40, 82], the sinusoidal-input method is particularly suited to the QFT design technique where stability bounds are computed at particular frequencies of interest.

The sinusoidal-input describing function ($N$) for a non-linear element is defined by Equations (7.1) to (7.3) and can be described as the complex ratio between the fundamental harmonic component of the output and the input (of the non-linearity) [61]. The method relies on the assumption that higher order harmonics will have a lower amplitude than the fundamental and are also usually attenuated by the control system.

$$N = \frac{Y_1}{X}\angle\phi_1 = \frac{\sqrt{A_1^2 + B_1^2}}{X}\angle\tan^{-1}\left(\frac{A_1}{B_1}\right) \tag{7.1}$$

where: $X$ is the amplitude of the sinusoidal input $x(t)$

$Y_1$ is the fundamental harmonic of the output $y(t)$

$\phi_1$ is the phase shift between $y(t)$ and $x(t)$

and:
$$A_1 = \frac{1}{\pi}\int_0^{2\pi} y(t)\cos(\omega t)\,d(\omega t) \tag{7.2}$$

$$B_1 = \frac{1}{\pi}\int_0^{2\pi} y(t)\sin(\omega t)\,d(\omega t) \tag{7.3}$$

### 7.2.1 Describing Function for the Standard Dead Zone Model

The standard dead zone approach to modelling backlash is presented in Section 2.4.2 and is described by Equations (2.12) and (2.13). Figure 7.1 shows the input-output relationship of the dead zone model, where $\alpha = 0.05$ and $K_s = 25$. The input in Figure 7.1 is: $\theta_d = 0.15\sin(0.4\pi t)$.

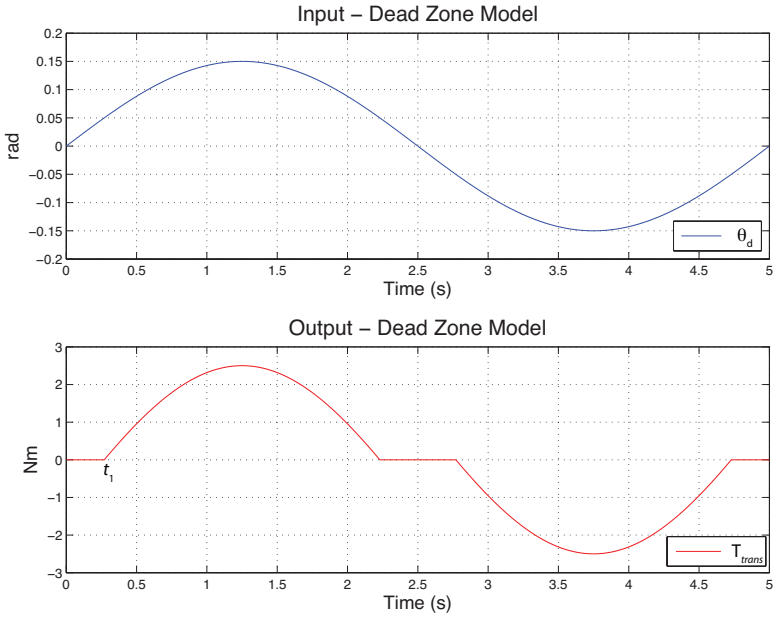


Figure 7.1: Input-Output Relationship – Standard Dead Zone Model

If $\theta_d = X\sin(\omega t)$ in the general case, then from Figure 7.1 and Equations (7.2), (7.3), (2.12) and (2.13) :

$$\begin{aligned} A_1 &= \frac{K_s}{\pi}\int_{\omega t_1}^{\pi-\omega t_1}(X\sin(\omega t)-\alpha)\cos(\omega t)\,d(\omega t) \\ &\quad +\frac{K_s}{\pi}\int_{\pi+\omega t_1}^{2\pi-\omega t_1}(X\sin(\omega t)+\alpha)\cos(\omega t)\,d(\omega t) \qquad (7.4) \\ B_1 &= \frac{K_s}{\pi}\int_{\omega t_1}^{\pi-\omega t_1}(X\sin(\omega t)-\alpha)\sin(\omega t)\,d(\omega t) \\ &\quad +\frac{K_s}{\pi}\int_{\pi+\omega t_1}^{2\pi-\omega t_1}(X\sin(\omega t)+\alpha)\sin(\omega t)\,d(\omega t) \qquad (7.5) \end{aligned}$$

From Equation (7.1) it can be seen that the describing function for the standard dead zone model is based on the solutions to Equations (7.4) and (7.5), which have previously been

shown to be [61]:

$$A_1 = 0 \tag{7.6}$$

$$B_1 = \frac{2K_sX}{\pi}\left[\frac{\pi}{2} - \sin^{-1}\left(\frac{\alpha}{X}\right) - \left(\frac{\alpha}{X}\right)\sqrt{1-\left(\frac{\alpha}{X}\right)^2}\right] \tag{7.7}$$

Hence, for the standard dead zone model the describing function reduces to:

$$N = \frac{B_1}{X}\angle 0 \tag{7.8}$$

### 7.2.2 Describing Function for the New Backlash Model

The new backlash model developed in Section 3.4 is described by Equations (3.31) to (3.34). With $\alpha = 0.05$, $K_s = 25$ and $C_s = 15$, the input-output relationship of the new backlash model is shown in Figure 7.2 (note also that $\theta_d = 0.15\sin(0.4\pi t)$ – as was the case in Figure 7.1).

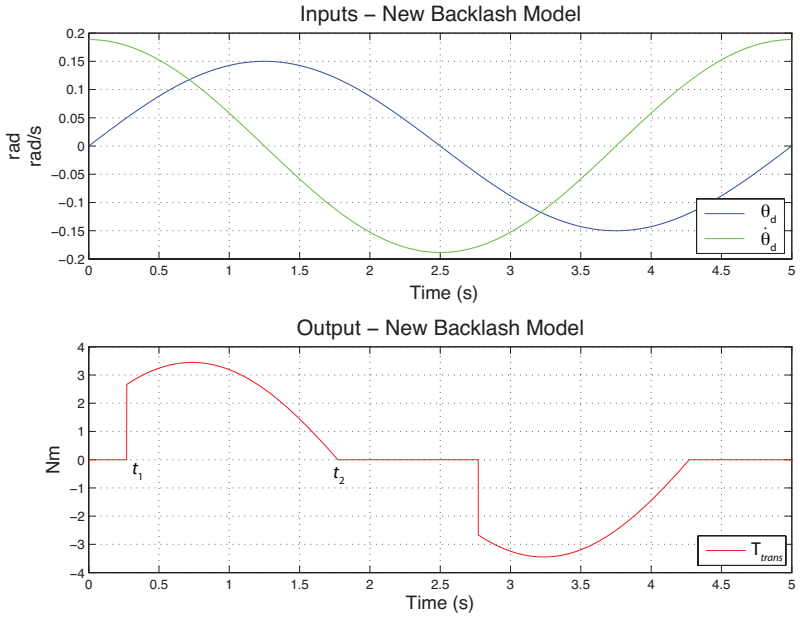


Figure 7.2: Input-Output Relationship – New Backlash Model

In order to highlight the differences between the dead zone model and the new backlash model a very large value of $C_s$ was used in the sample input-output relationship shown in

Figure 7.2. It is important to note that in the case where $C_s = 0$, the output of the new backlash model would be identical to that shown in Figure 7.1 for the dead zone model.

If $\theta_d = X\sin(\omega t)$ in the general case, then from Figure 7.2 and Equations (7.2), (7.3) and (3.31) to (3.34):

$$\begin{aligned}
A_1 &= \frac{K_s}{\pi}\int_{\omega t_1}^{\omega t_2}(X\sin(\omega t)-\alpha)\cos(\omega t)\,d(\omega t) \\
&\quad +\frac{C_s X\omega}{\pi}\int_{\omega t_1}^{\omega t_2}\cos^2(\omega t)\,d(\omega t) \\
&\quad +\frac{K_s}{\pi}\int_{\pi+\omega t_1}^{\pi+\omega t_2}(X\sin(\omega t)+\alpha)\cos(\omega t)\,d(\omega t) \\
&\quad +\frac{C_s X\omega}{\pi}\int_{\pi+\omega t_1}^{\pi+\omega t_2}\cos^2(\omega t)\,d(\omega t) \qquad (7.9) \\
B_1 &= \frac{K_s}{\pi}\int_{\omega t_1}^{\omega t_2}(X\sin(\omega t)-\alpha)\sin(\omega t)\,d(\omega t) \\
&\quad +\frac{C_s X\omega}{\pi}\int_{\omega t_1}^{\omega t_2}\cos(\omega t)\sin(\omega t)\,d(\omega t) \\
&\quad +\frac{K_s}{\pi}\int_{\pi+\omega t_1}^{\pi+\omega t_2}(X\sin(\omega t)+\alpha)\sin(\omega t)\,d(\omega t) \\
&\quad +\frac{C_s X\omega}{\pi}\int_{\pi+\omega t_1}^{\pi+\omega t_2}\cos(\omega t)\sin(\omega t)\,d(\omega t) \qquad (7.10)
\end{aligned}$$

From Equation (7.1) it can be seen that the describing function for the new backlash model is based on the solutions to Equations (7.9) and (7.10), which are:

$$\begin{aligned}
A_1 &= \frac{K_s X}{\pi}\left(\left(\frac{2T}{1+T^2}\right)^2-\left(\frac{\alpha}{X}\right)^2\right)-\frac{2K_s\alpha}{\pi}\left(\frac{2T}{1+T^2}-\frac{\alpha}{X}\right) \\
&\quad +\frac{C_s X\omega}{\pi}\left(\frac{2T\left(1-T^2\right)}{\left(1+T^2\right)^2}+2\tan^{-1}(T)-\frac{\alpha}{X}\sqrt{1-\left(\frac{\alpha}{X}\right)^2}-\sin^{-1}\left(\frac{\alpha}{X}\right)\right) \qquad (7.11) \\
B_1 &= \frac{K_s X}{\pi}\left(2\tan^{-1}(T)-\frac{2T\left(1-T^2\right)}{\left(1+T^2\right)^2}-\sin^{-1}\left(\frac{\alpha}{X}\right)+\frac{\alpha}{X}\sqrt{1-\left(\frac{\alpha}{X}\right)^2}\right) \\
&\quad +\frac{2K_s\alpha}{\pi}\left(\left(\frac{1-T^2}{1+T^2}\right)-\sqrt{1-\left(\frac{\alpha}{X}\right)^2}\right)+\frac{C_s X\omega}{\pi}\left(\left(\frac{2T}{1+T^2}\right)^2-\left(\frac{\alpha}{X}\right)^2\right) \qquad (7.12) \\
\text{where: } T &= \frac{1+\sqrt{1-\frac{\alpha^2}{X^2}+\frac{C_s^2\omega^2}{K_s^2}}}{\frac{\alpha}{X}+\frac{C_s\omega}{K_s}} \qquad (7.13)
\end{aligned}$$

The complete derivation of Equations (7.11), (7.12) and (7.13) is given in Appendix B. It is also shown in Appendix B that when $C_s = 0$, Equations (7.11) and (7.12) reduce to Equations (7.6) and (7.7) respectively (as expected).

Figure 7.3 shows plots of magnitude and phase versus X/$\alpha$ (the ratio of the sinusoidal input magnitude to the backlash gap) for the describing function of the new backlash model. These plots are shown for 5 different levels of system damping ($C_s = 0$, 0.01, 0.1, 1 and 10), where $K_s = 25$ and $\omega = 50\pi$. Note that when $C_s = 0$, the magnitude and phase plots are equivalent to those for the describing function of the standard dead zone model.

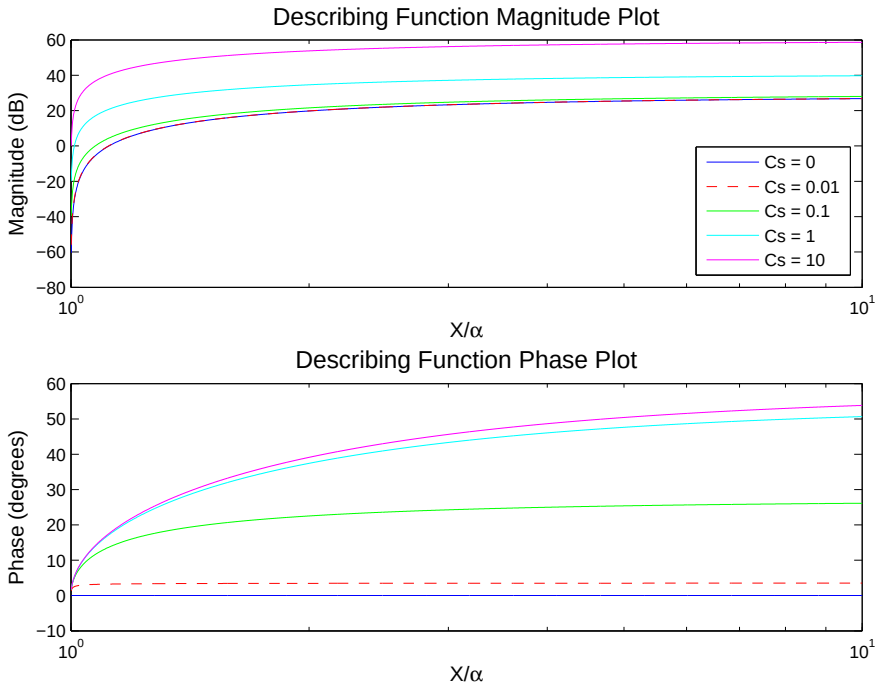


Figure 7.3: Magnitude and Phase Plots of the Backlash Describing Function

When the damping is low (ie $C_s = 0.01$ and $C_s = 0.1$) the magnitude plots shown in Figure 7.3 are almost identical to that of the dead zone model (represented by the zero damping case); however, the phase plots show significant shift that is not predicted by the dead zone model. As the damping increases, both the magnitude and phase plots can be seen to vary significantly from those of the dead zone model. Since the inherent damping in a practical system is usually much lower than the system stiffness ($K_s$), the low damping cases in Figure 7.3 are more representative of real system models. Hence, the major disadvantage of using a describing function based on the standard dead zone model is that it does not include any of the phase shift associated with backlash. For this reason, the describing function of the new backlash model is used in the design approach presented throughout the remainder of this chapter.

## 7.3 A Hybrid Weak/Strong Backlash Controller

### 7.3.1 Design Overview

The control approach presented in this section addresses both the dynamic stability and tracking performance of systems with backlash, through a combination of 'weak' and 'strong' action during the backlash phase. As detailed in Section 2.4.3, the weak approach to backlash control is based upon the concept of reducing the speed at which the system traverses the backlash gap in order to limit the severity of any collisions that may result when the backlash gap closes. Alternatively, the strong approach to backlash control is based upon the concept of increasing the speed at which the system traverses the backlash gap, so that regular contact between the motor and load is resumed as quickly as possible.

From the literature reviewed in Section 2.4.3, it was found that researchers have had much greater success implementing the weak action approaches to backlash control on practical systems. The main reason for this is that most of the proposed strong action approaches are either based on unrealistic system modelling or require excessive computational power. The hybrid weak/strong approach presented in this section is based on a switched non-linear controller [40, 70, 82], which switches between a linear controller tuned specifically for the contact phase and a second weak action linear controller that is used during the backlash phase. The weak approach ensures dynamic stability of the system, but suffers from poor tracking performance at low velocities. To improve the tracking performance, the hybrid weak/strong controller incorporates an impulse that is added to the velocity command when the system first enters a backlash phase. This impulse adds a degree of strong action during the backlash phase and is simple to implement, with comparatively low computational requirements.

Since the sources of backlash in practical dynamic systems are usually located between the motor and load (in the transmission system), the equations developed in Section 3.4 for a two-body system with transmission backlash (Equations (3.31) to (3.41)) were used

in the development of the proposed control approach. The Matlab and Simulink packages were once again used to simulate the effectiveness of the proposed controller, with real parameters from the Motor-Transmission-Load Test-Bed used as a representative plant. The block diagram of the overall simulation model is shown in Figure 7.4.

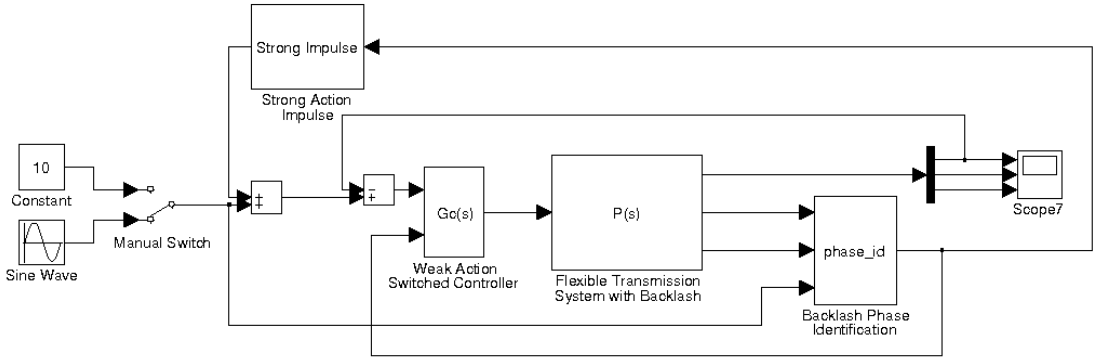


Figure 7.4: Backlash Simulation System – Simulink Block Diagram

The 'Backlash Phase Identification' block, in Figure 7.4, represents the method used by the hybrid weak/strong controller to identify when a system is in the backlash phase and is described in Section 7.3.2. The 'Weak Action Switched Controller' block represents the system for switching between the two linear controllers of the hybrid weak/strong controller and is described in Section 7.3.3. The 'Strong Action Impulse' block represents the method for applying a degree of strong action during the backlash phase and is described in Section 7.3.4.

### 7.3.2 Identification of the Backlash Phase

The accurate identification of whether a system is in the backlash phase or contact phase is one of the most important aspects of any non-linear backlash controller. Researchers often assume that both motor and load position feedback are available and the width of the backlash gap is known [69, 70], which makes identifying the backlash phase relatively uncomplicated. However, many practical systems are restricted to feedback from the motor and the task of identifying what phase the system is in can be quite difficult.

Of the literature reviewed in Section 2.4.3, only Nordin [40, 82] was found to have successfully identified the backlash phase on a system where the feedback was restricted to the motor. Nordin's method uses the motor torque reference signal (the output of the velocity controller) as an approximation for the torque transmitted to the load. With this approach the system is assumed to be in the contact phase whenever the motor torque reference is high. Alternatively, if the motor torque reference is very low, or zero, the system can be assumed to be in the backlash phase.

The backlash phase identification technique developed for the hybrid weak/strong controller also uses the motor torque reference signal. However, in addition to the motor torque reference signal, this new phase identification technique also takes the motor acceleration and velocity reference signals into account. The complete block diagram of the backlash phase identification method developed for the hybrid weak/strong controller is shown in Figure 7.5.

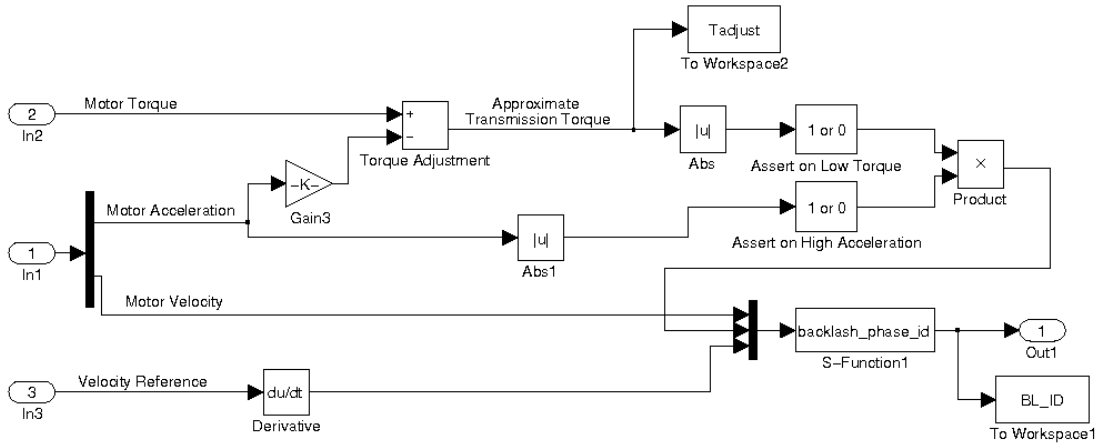


Figure 7.5: Phase Identification System - Simulink Block Diagram

From the upper section of the block diagram shown in Figure 7.5 it can be seen that the transmission torque is approximated by subtracting a value proportional to the motor acceleration from the motor torque reference signal. One problem with the identification method used by Nordin is that the motor torque reference signal includes the torque component that accelerates the motor inertia. Hence, the motor torque reference only provides a good approximation of the transmission torque when the load inertia is much higher than the motor inertia. However, if the motor acceleration signal is multiplied by a constant

equivalent to the motor inertia and then subtracted from the motor torque reference, the torque component that accelerates the motor can theoretically be removed. Figure 7.6 shows a simulation (on a system with a unity motor:load inertia ratio) comparing the transmission torque with the motor torque reference signal and the transmission torque approximation used in this thesis.

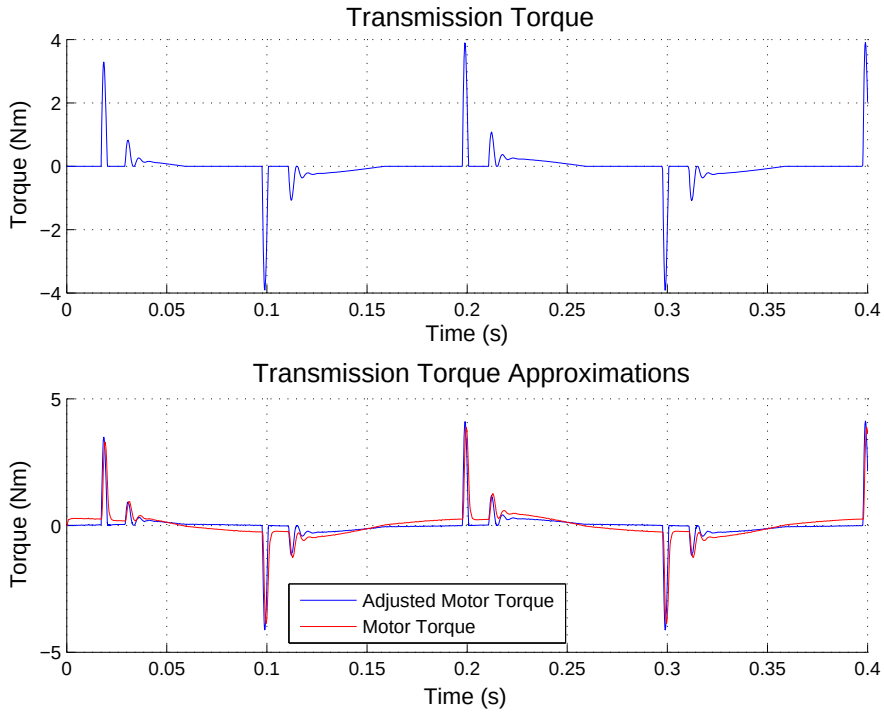


Figure 7.6: Transmission Torque and Approximations – Sinusoidal Input

From the lower graph of Figure 7.6, it can be seen that the motor acceleration feedback adjustment results in a much more accurate approximation of the torque transmitted to the load (solid blue line) , when compared with the unmodified motor torque reference signal (solid red line). The improvement achieved through the use of motor acceleration feedback is highlighted further when the controller includes a degree of strong action during the backlash phase. Figure 7.7 shows another simulated comparison (on the same system with unity motor:load inertia ratio) when strong action is applied during the backlash phase.

As can be seen in Figure 7.7, the motor torque reference signal (solid red line in the lower

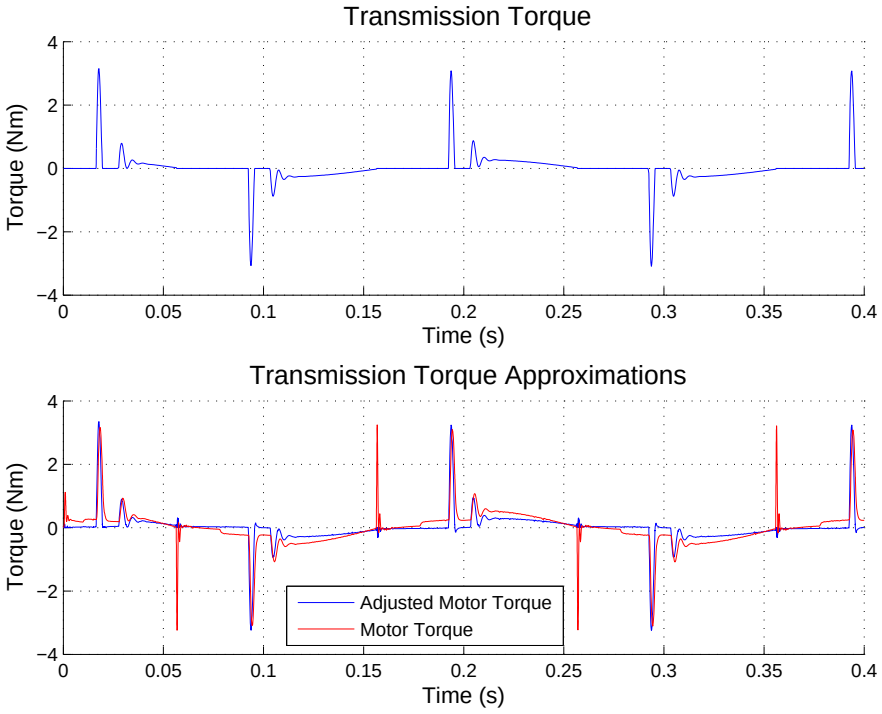


Figure 7.7: Transmission Torque and Approximations – Strong Action

graph of Figure 7.7) has additional torque peaks that are not present in the transmission torque. These additional peaks are due to the motor torque reference increasing with the applied strong action, and result in the motor inertia accelerating rapidly during the backlash phase. Hence, a switching algorithm that switches to the contact phase controller, as a result of the high motor torque reference, could result in high velocity collisions and limit cycles. In comparison, the signal that is adjusted using motor acceleration feedback (solid blue line in the lower graph of Figure 7.7) provides a much more accurate approximation of the transmission torque.

From the block diagram shown in Figure 7.5, it can be seen that the absolute value of the approximated transmission torque is passed through a function that returns a ‘1’ for low torque values and a ‘0’ for high torque values. Hence, a value of ‘1’ indicates that the system could be in the backlash phase. However, when the system is running at a constant velocity (ie the acceleration is zero), the transmission torque is often very low and a value of ‘1’ can result even though the system is in the contact phase. For this reason a second function that returns a ‘1’ when the motor acceleration is high and a ‘0’ when the motor

acceleration is low, is used to ensure the backlash phase is not falsely identified during a constant velocity state.

One other important issue to consider when identifying the backlash phase is what type of control action will be applied during this phase. Although weak action reduces the severity of any collisions when the backlash gap closes, collisions and a re-opening of the backlash gap can still occur. Hence, when weak control action is being applied, the initial opening and any subsequent re-openings of the backlash gap need to be identified. In contrast, when strong control action is being applied, only the initial opening of the backlash gap should be identified. Applying additional strong action during any subsequent re-openings of the backlash gap is undesirable and can result in further collisions and even instability. For these reasons, the backlash phase identification technique developed for the hybrid weak/strong controller has two different outputs, one to switch the weak action controller and another to trigger the strong action impulse.

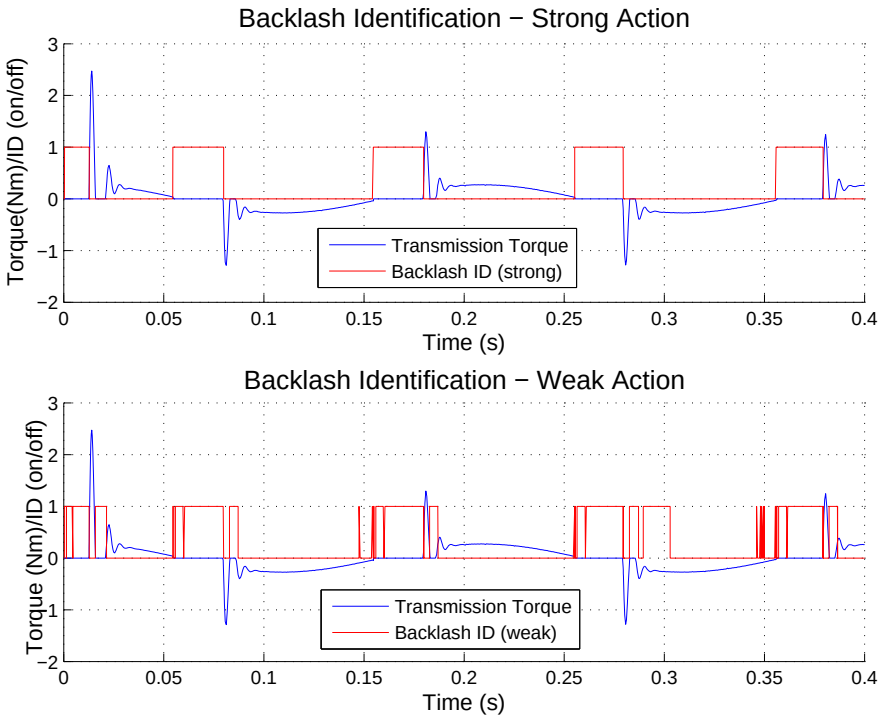


Figure 7.8: Backlash Phase Identification - Sinusoidal Input

In Figure 7.8, the two outputs of the backlash phase identification stage are compared with the transmission torque for a sinusoidal velocity reference. As can be seen, the output used

to trigger the strong action impulse (upper graph) only asserts on each initial opening of the backlash gap and not on the subsequent re-openings. In contrast, the output used to switch the weak action controller (lower graph) asserts on every opening of the backlash gap. Although both of these outputs are based on the same identification technique, the strong action output is only asserted after a zero crossing is detected in the differential of the velocity reference. The reason for this is that a complete traversing of the backlash gap would normally only occur when the actual reference signal initiates a change in polarity of the system acceleration.

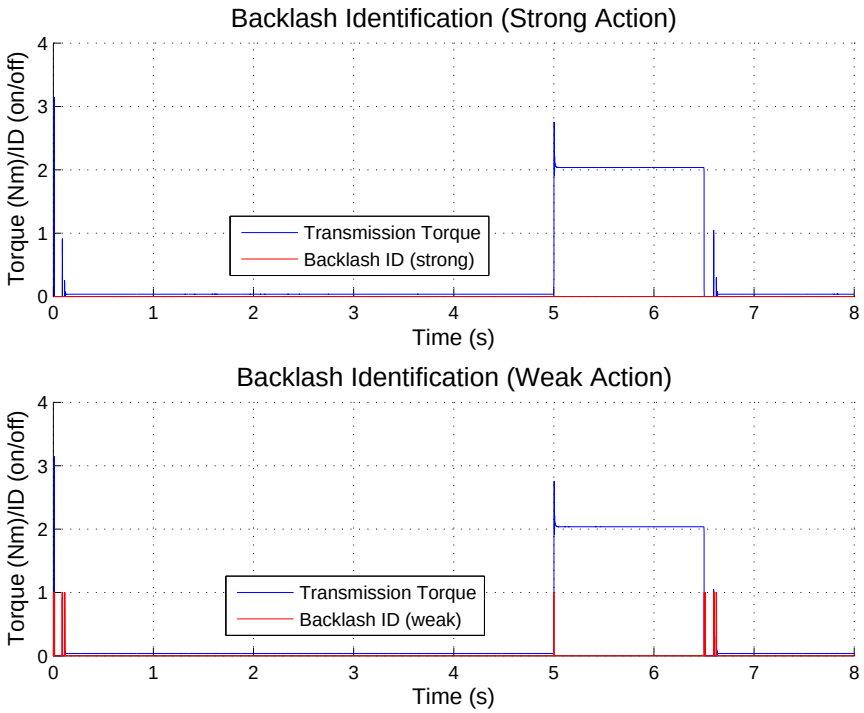


Figure 7.9: Backlash Phase Identification - Disturbance Input

In Figure 7.9, the two outputs of the backlash phase identification stage are compared with the transmission torque for a constant velocity reference. There is also a load disturbance torque applied at the 5 second mark in Figure 7.9, which is then removed at the 6.5 second mark. As can be seen, there are no false identifications of the backlash gap in either of the outputs during the constant velocity state, further confirming the accuracy of this identification technique. However, it is important to note that any openings of the backlash gap due to the disturbance torque are only identified in the output used to switch

the weak action controller (lower graph) and not in the output used to trigger the strong action impulse (upper graph). This highlights the one disadvantage of only asserting the strong action output after a zero crossing in the differential of the velocity reference. This disadvantage is only minor though, as the primary role of the strong action is to improve the tracking performance of the system and the most important system requirement during an applied disturbance is dynamic stability.

### 7.3.3 Weak Action during the Backlash Phase

As discussed in Section 7.3.1, the weak action of the hybrid weak/strong controller is implemented via switching between a linear controller tuned for the contact phase and a second linear controller tuned for the backlash phase. The block diagram of the switched weak action controller is shown in Figure 7.10.

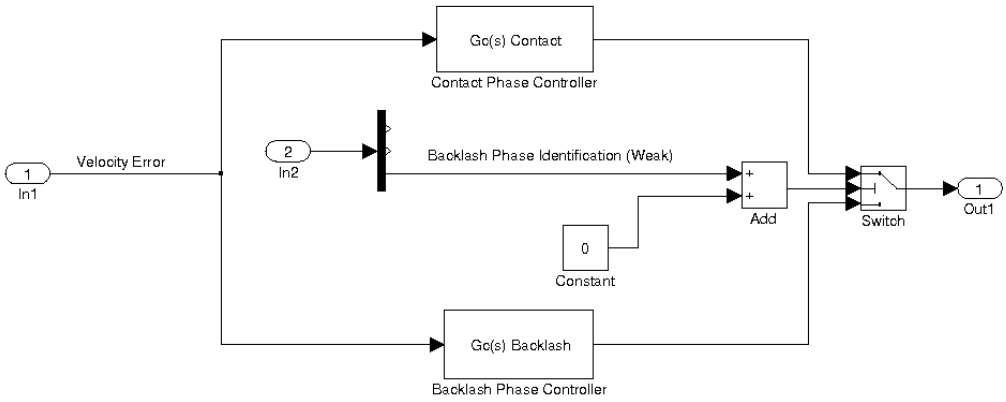


Figure 7.10: Weak Action Controller – Simulink Block Diagram

Switching between controllers of different gains is often referred to as ‘gain scheduling’ and is a technique that is commonly used in the field of non-linear control. The switching of the weak action controller shown in Figure 7.10 is based on the output of the phase identification stage described in Section 7.3.2; when the output of the phase identification stage is a ‘1’ the backlash phase controller is selected, while an output of ‘0’ results in selection of the contact phase controller. The actual linear controllers can include additional feedback and filter elements as appropriate for the particular system (such as

those studied in Section 6.3.4 to reduce torsional vibrations). The most important design aspect is to ensure that instability or excessive limit cycles are not introduced as a result of traversing the backlash gap. In this thesis the individual linear controllers were designed using the QFT technique, with describing functions used to ensure that the design of the backlash phase controller avoided limit cycles.

The traditional describing function stability analysis is based on the system shown in Figure 7.11, where the non-linear element (represented by the describing function $N$) can be separated from a linear representation of the plant $(G_p(s))$.

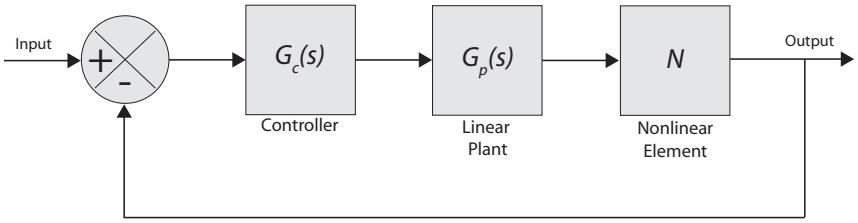


Figure 7.11: Non-Linear System Block Diagram

The closed loop transfer function for the system shown in Figure 7.11 is:

$$\frac{G_c(s)G_p(s)N}{1+G_c(s)G_p(s)N}$$

Hence, the characteristic equation of the system is: $1+G_c(s)G_p(S)N=0$, or:

$$G_c(s)G_p(s) \quad = \quad -\frac{1}{N} \tag{7.14}$$

The stability of this system is examined through a comparison of the $G_c(s)G_p(s)$ and $-\frac{1}{N}$ loci. If the $-\frac{1}{N}$ locus is not enclosed by the $G_c(s)G_p(s)$ locus, the system is stable and there is no limit cycle at steady state. If the $-\frac{1}{N}$ locus is enclosed by the $G_c(s)G_p(s)$ locus, the system is unstable. If the two loci intersect, a limit cycle is exhibited. The magnitude of this limit cycle is characterised by the value of X on the $-\frac{1}{N}$ locus at the point of intersection, while the frequency of the limit cycle is characterised by the value of $\omega$ on the $G_c(s)G_p(s)$ locus at the point of intersection [61].

As mentioned in Section 2.4.3, the sources of backlash in practical dynamic systems are usually located between the motor and load and rarely at the system input or output. Hence, the model of the plant in such systems is a function of both frequency and $N$, and it is not possible to completely separate $N$ from the plant (as per Figure 7.11). For this type of system, a comparison of the $G_c(s)G_p(s)$ and $-\frac{1}{N}$ loci would not result in a reliable stability analysis. Instead, the characteristic equation becomes:

$$1 + G_c(s)\,G_p(N,s) = 0$$

and:

$$G_c(s) \;=\; -\frac{1}{G_p(N,s)} \tag{7.15}$$

If both sides of Equation (7.15) are multiplied by the linear representation of the plant (with $N$ set to unity), then:

$$G_c(s)\,G_p(s) = -\frac{G_p(s)}{G_p(N,s)} \tag{7.16}$$

It can be seen from Equation (7.16) that the stability of this system can be examined through a comparison of the $G_c(s)G_p(s)$ and $-\frac{G_p(s)}{G_p(N,s)}$ loci, with the conditions for stability identical to those of the standard describing function analysis (where $G_c(s)\,G_p(s)$ is compared with $-\frac{1}{N}$). Since the $G_c(s)\,G_p(s)$ locus is equivalent to the loop transmission function in the QFT design process, a set of backlash stability bounds for a QFT design can be calculated directly from $-\frac{G_p(s)}{G_p(N,s)}$.

Figure 7.12 shows an example set of backlash stability bounds for the Motor-Transmission-Load Test-Bed, calculated using the describing function of the new backlash model (Equations (7.11) to (7.13)). The test-bed configuration for the bounds shown in Figure 7.12 consisted of Shaft 1 and backlash Coupling 2, with inertia Disc 2 attached to the load side (complete parameter details for this test-bed are given in Section 4.3.2). If the loop transmission function in a QFT design were to intersect any of these stability bounds at

the related frequency, a limit cycle would result. Note that the lower frequency bounds in Figure 7.12 (10 through to 200) are on the left hand side of the Nichols Chart. In general these low frequency bounds do not result in any new restrictions on the controller design, as the left hand side of the Nichols Chart is always avoided at low frequencies. Hence, it is the bounds on the right hand side of the Nichols Chart (in this case, 500 through to 1000) that are important during the design of the loop controller for the backlash phase.

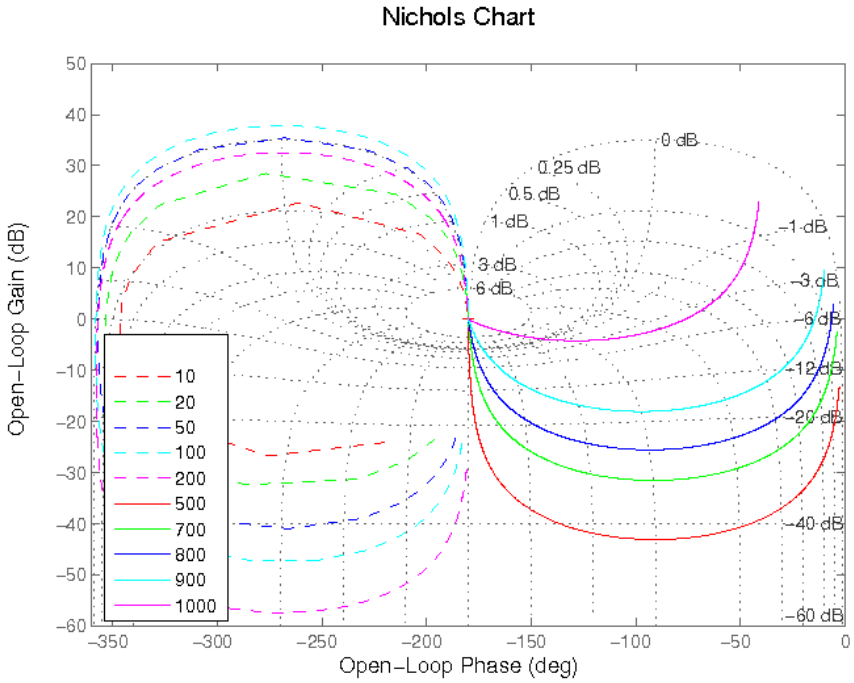


Figure 7.12: Backlash Stability Bounds using Describing Functions

As an example of the design technique and the effectiveness of the switched controller, a design for the Motor-Transmission-Load Test-Bed configuration described in the preceding paragraph is presented throughout the remainder of this section. Designs for both the contact phase and backlash phase are discussed and the final switched controller is simulated for a constant velocity reference with an applied load torque disturbance.

The design of the contact phase controller should always be based on the given controller design specifications, with the backlash gap assumed to be zero. Design specifications can vary widely depending on the system and the intended application. For the example design, the specifications were very general in that a fast response was required and

torsional vibrations should be suppressed. The only detailed design specification was a stability requirement that the closed loop gain magnitudes should be less than 3.5dB at all frequencies. An example loop design for the contact phase is shown on the Nichols Chart in Figure 7.13, along with the backlash stability bounds and the overall stability bound at 3.5dB. The solid black line in Figure 7.13 represents the loop transmission function of motor velocity loop, while the solid blue line represents the load velocity. The critical backlash stability bounds are calculated for the motor velocity only.

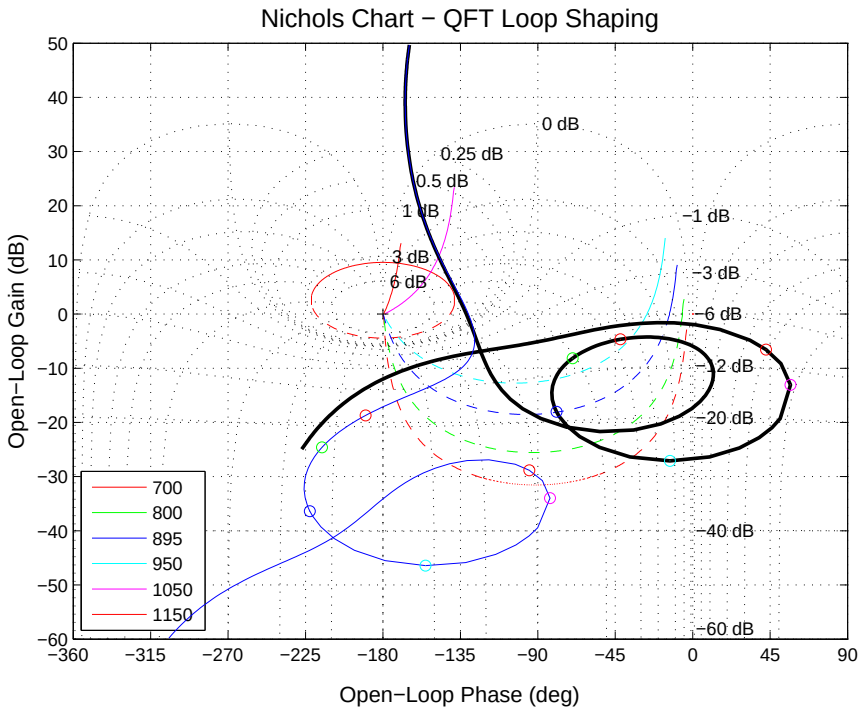


Figure 7.13: Higher Order QFT Design with Backlash Describing Function Bounds

The loop design shown in Figure 7.13 can be seen to intersect the 895 rad/s backlash stability bound at that frequency. Hence, it would be expected that the system would exhibit limit cycles as a result of this design. The actual design consists of a PI stage with two 2nd order loop filters, which are included to limit torsional vibrations. The 1st loop filter has the form of a notch filter, while the 2nd filter provides a band of phase lag to help compensate for the inherent band of phase lead in a two body system. This control approach was described in Section 6.3.4, and was shown to be effective in reducing torsional vibrations on the Motor-Transmission-Load Test-Bed. The complete filter design is given

in Equation (7.17).

$$G_c(s) = 55\left(\frac{0.1s+1}{s}\right)\left(\frac{\frac{s^2}{\omega_1^2}+\frac{2\zeta_1 s}{\omega_1}+1}{\frac{s^2}{\omega_2^2}+\frac{2\zeta_2 s}{\omega_2}+1}\right)\left(\frac{\frac{s^2}{\omega_3^2}+\frac{2\zeta_3 s}{\omega_3}+1}{\frac{s^2}{\omega_4^2}+\frac{2\zeta_4 s}{\omega_4}+1}\right) \qquad (7.17)$$

$$\begin{aligned} \text{where: } \omega_1 &= 950 \quad & \zeta_1 &= 0.025 \\ \omega_2 &= 950 \quad & \zeta_2 &= 0.5 \\ \omega_3 &= 950 \quad & \zeta_3 &= 0.1 \\ \omega_4 &= 920 \quad & \zeta_4 &= 0.2 \end{aligned}$$

The simulated response of this controller, with the test-bed configuration subjected to a 10 Nm disturbance torque, is shown in Figure 7.14. With the system in steady state velocity control (at 10 rad/s) the disturbance torque was applied at a time of 5.5 seconds, and then removed one second later.

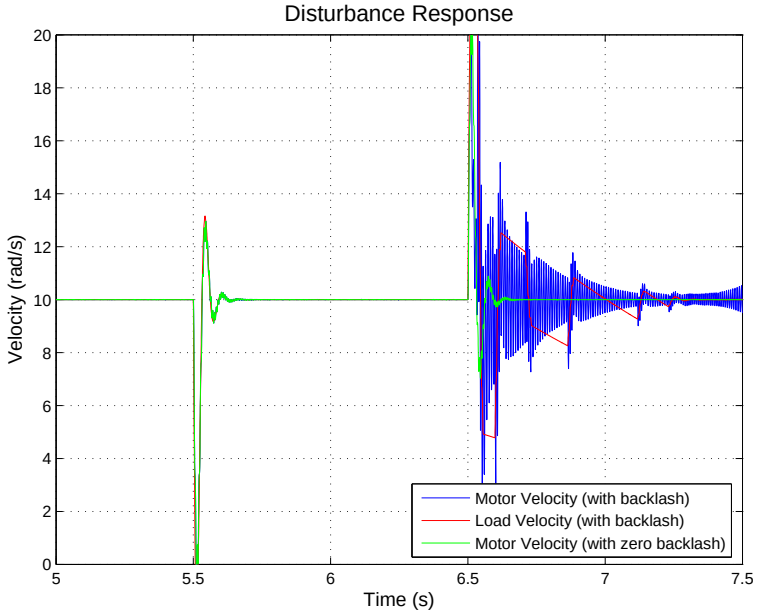


Figure 7.14: Disturbance Response for Contact Phase Controller

In Figure 7.14 the solid green line represents the motor response when the backlash gap

is set to zero, while the solid blue and red lines represent the motor and load responses (respectively) when the backlash is present. It can be seen that when the backlash gap is zero (which is assumed during the design of the contact phase controller), the system is stable. However, with the backlash present the system exhibits a limit cycle in the motor response (at approximately the predicted frequency of 895 rad/s) when the disturbance torque is removed.

The design of the backlash phase controller is also based on the given controller design specifications; however, the effects of backlash are taken into account. When shaping the loop for the backlash phase controller the transmission function must not intersect any of the backlash stability bounds at the related frequencies. An example loop design for the backlash phase is shown on the Nichols Chart in Figure 7.15, along with the backlash stability bounds and the overall stability bound at 3.5dB.

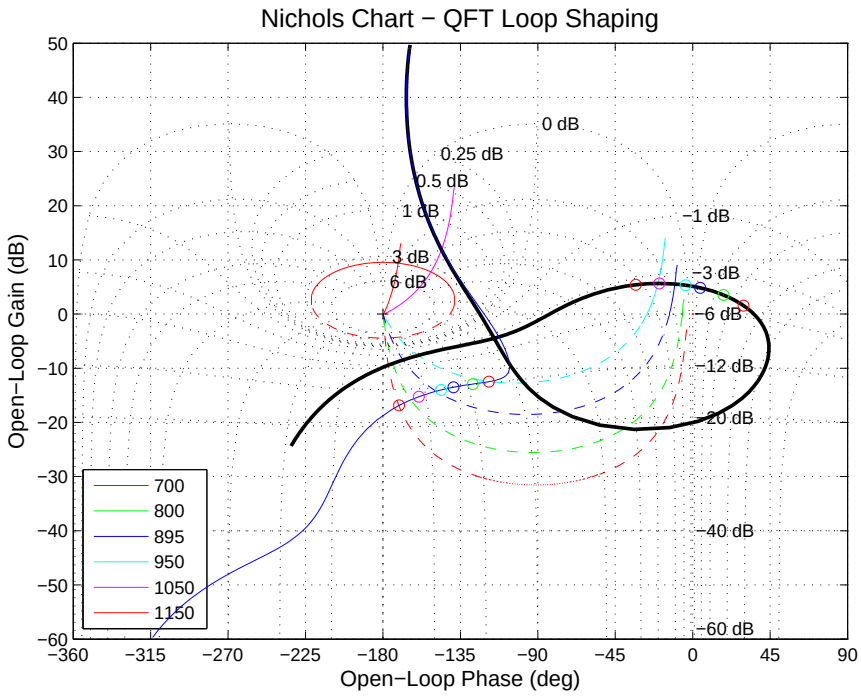


Figure 7.15: PI QFT Design with Backlash Describing Function Bounds

The loop design shown in Figure 7.15 consists of the same PI stage as the contact phase controller; however, the two additional 2nd order filters have been removed. It can be seen from Figure 7.15 that the loop transmission function of the basic PI controller does

not intersect any of the backlash stability bounds at the relative frequencies. Hence, no limit cycles would be expected as a result of this design. The simulated response of this controller, with the test-bed configuration subjected to the same 10 Nm disturbance torque, is shown in Figure 7.16. As can be seen, this system exhibits no limit cycles during steady state, or at either the application or removal of the disturbance torque.

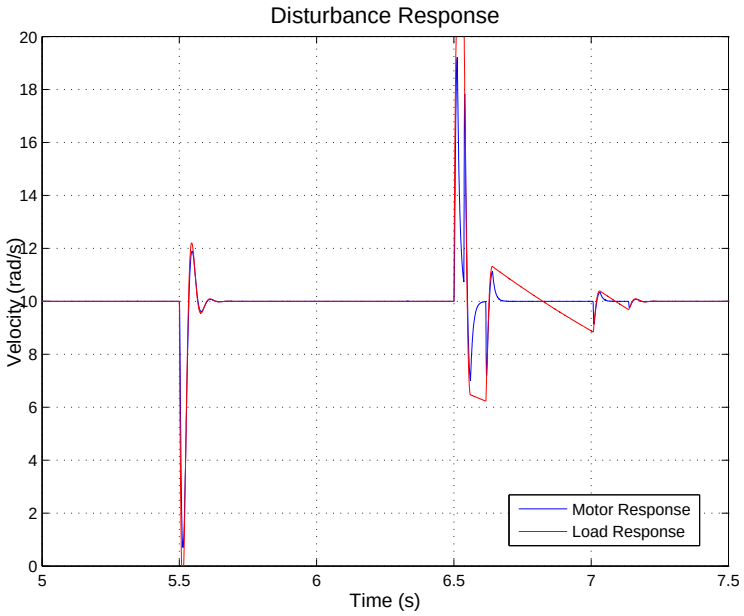


Figure 7.16: Disturbance Response for the Backlash Phase Controller

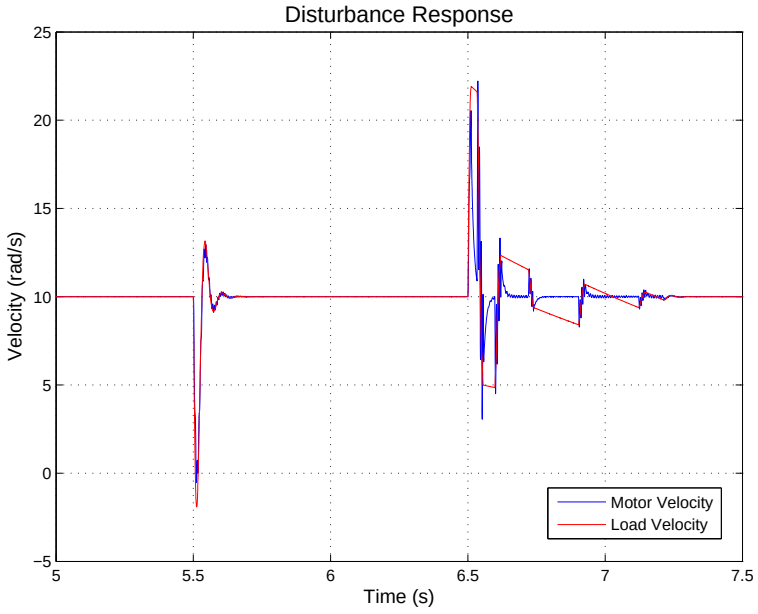


Figure 7.17: Disturbance Response for the Switched Controller

The simulated response of the complete switched controller is shown in Figure 7.17. As can be seen, the switched contact/backlash phase controller exhibits some small oscillations when the disturbance torque is removed; however, it is effective in avoiding the dangerous limit cycles exhibited by the contact phase controller. Although the backlash phase controller could have included some additional compensation for torsional vibrations, the simple PI stage was used in the example design to demonstrate the importance of treating backlash and torsional vibrations in parallel. The approach used to design the contact phase controller of Equation (7.17) was previously shown to be effective in reducing torsional vibrations in a system without backlash (refer to Section 6.3.4). However, with backlash present, it was the additional filters designed to reduce torsional vibrations that directly introduced limit cycles into this system.

### 7.3.4 Combined Weak/Strong Action during the Backlash Phase

Although weak control action is effective at addressing the dynamic stability problems associated with backlash, systems using only weak action during the backlash phase often exhibit poor tracking performance. For this reason, the hybrid weak/strong controller applies a degree of strong action, in the form of an impulse that is added to the velocity reference command, when the system first enters a backlash phase. The block diagram of the strong action controller is shown in Figure 7.18.

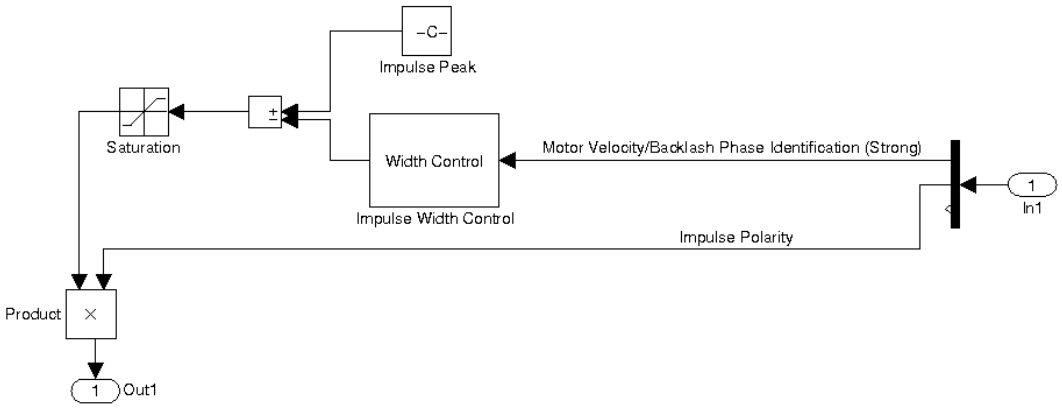


Figure 7.18: Strong Action Controller – Simulink Block Diagram

The additional strong action provided by the controller shown in Figure 7.18 is not actually an impulse in the pure sense of the term, but rather an initial step command that decays rapidly as the backlash gap is traversed. This form of signal allows for the additional strong action to be applied over an effective period of the backlash gap traversal, while also providing a smooth transition back to the original velocity reference command. The actual output of the strong action controller is compared with a pulse of the same width and a pure impulse in Figure 7.19.

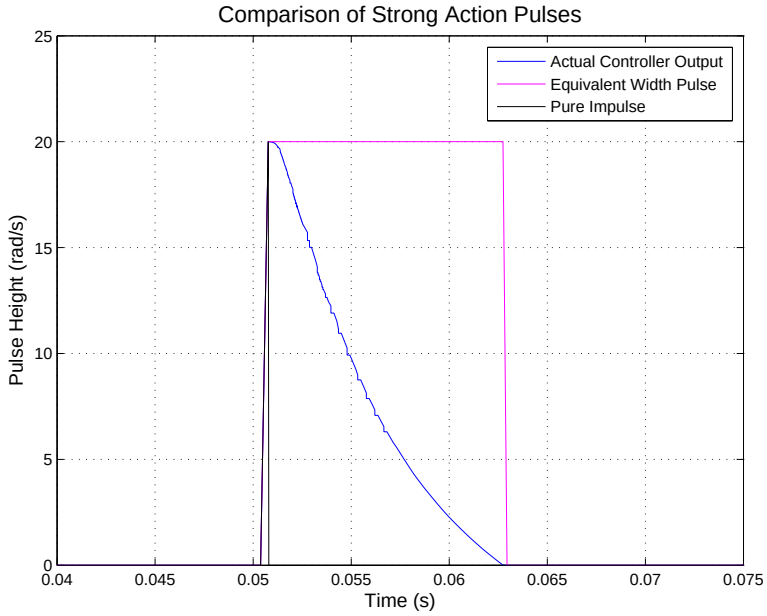


Figure 7.19: Output of Strong Action Controller Compared with Alternative Pulses

From Figure 7.19 it can be seen that a pure impulse (the black response) would not apply strong action over an effective period of the backlash gap traversal. Another alternative is a wider pulse with fixed amplitude (as shown in the purple response), which would apply strong action over an effective period; however, this action does not provide a smooth transition back to the original reference. A smooth transition back to the original velocity reference considerably reduces the risk of any high impact collisions when the backlash gap closes. In comparison, the output of the strong action controller (the blue response in Figure 7.19) decays as a function of the motor's position within the backlash gap.

Determining the position of the motor within the backlash gap is uncomplicated if the size of the backlash gap is known and both the motor and load positions are measurable. How-

ever, an approximation method is required for this task when feedback is only available from the motor. The approximation method used in the hybrid weak/strong controller is represented by the 'Impulse Width Control' block shown in Figure 7.18. This method is based on the motor velocity and the output of the phase identification stage described in Section 7.3.2. Whenever a transition from the contact phase to the backlash phase is identified, the position of the motor within the backlash gap is set to zero. At this instant in time it is assumed that the load velocity is equal to the motor velocity and that it will remain constant throughout the gap traversal. The difference between the motor velocity and this constant load velocity is then integrated to determine the position of the motor as it traverses the backlash gap. When the approximate motor position is equivalent to the total width of the backlash gap it is then held constant until the next transition from contact phase to backlash phase is identified.

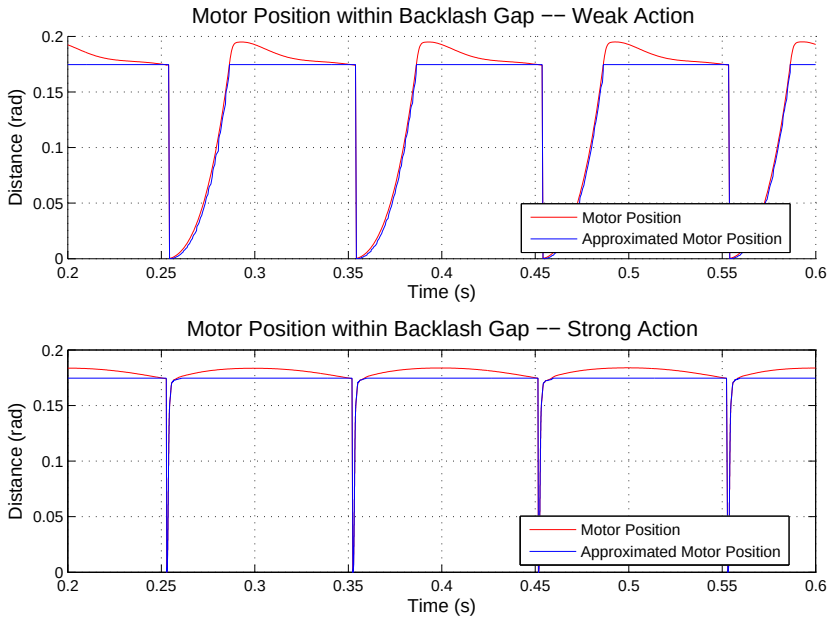


Figure 7.20: Approximate Backlash Gap Traversal

The simulated output of the described approximation method is compared with the simulated motor position in Figure 7.20. The top graph in Figure 7.20 shows the approximation and the motor position for the weak action controller, while the bottom graph shows the approximation and motor position when the strong action is added to the velocity command. As can be seen, the approximate method is very accurate in representing

the motor position during the backlash gap traversal. Of course, due to compliance in the motor-load transmission, the motor position will continue to vary once the backlash gap is closed. The only major assumption used in the approximation method is that the load velocity is constant during the gap traversal. Although this is not strictly true, it is a reasonable assumption as the time taken to traverse the backlash gap, especially when strong action is applied, is very small and the load is uncontrolled during this period.

The final output of the 'Impulse Width Control' block, shown in Figure 7.18, is a scaled version of the approximated motor position. Specifically, the approximate motor position is multiplied by the desired initial step value and then divided by the desired width of the strong action. If the backlash gap is known, the desired width can be chosen as a fraction of the overall backlash gap. However, both the desired width and the initial step value can be tuned manually through a simple trial and error process. The output of the 'Impulse Width Control' block is then subtracted from the initial step value to form the strong action output. Hence, when the backlash gap first opens, the output of the width control block is zero and the full value of the initial step is applied. As the motor traverses the gap the output of the width control block increases, which reduces the strong action output. The reducing strong action output is saturated at zero, which is reached once the motor position becomes greater than the chosen pulse width. The polarity of the strong action output is set to the same polarity as the differential of the velocity reference command.

The effects of the additional strong action are demonstrated in Figure 7.21, where the tracking performance of the weak action controller is compared with that of the hybrid weak/strong controller. The velocity reference command in Figure 7.21 is a 10 Hz sinusoidal signal with an amplitude of 20 rad/s. The simulated motor responses for both controllers are shown in the upper graph, while the simulated load responses are shown in the lower graph. When examining the load response of the weak action controller, it can be seen that the backlash severely affects the sinusoidal tracking performance. In comparison, the load response of the hybrid weak/strong controller is much more sinusoidal. The application of the strong action is clearly visible in the motor response of the hybrid

weak/strong controller, with sharp spikes observed each time the backlash gap opens. An initial step value of 200 rad/s and a strong action width of 0.12 rad (approximately 68% of the total backlash gap) were used in the strong action controller for the weak/strong responses shown in Figure 7.21.

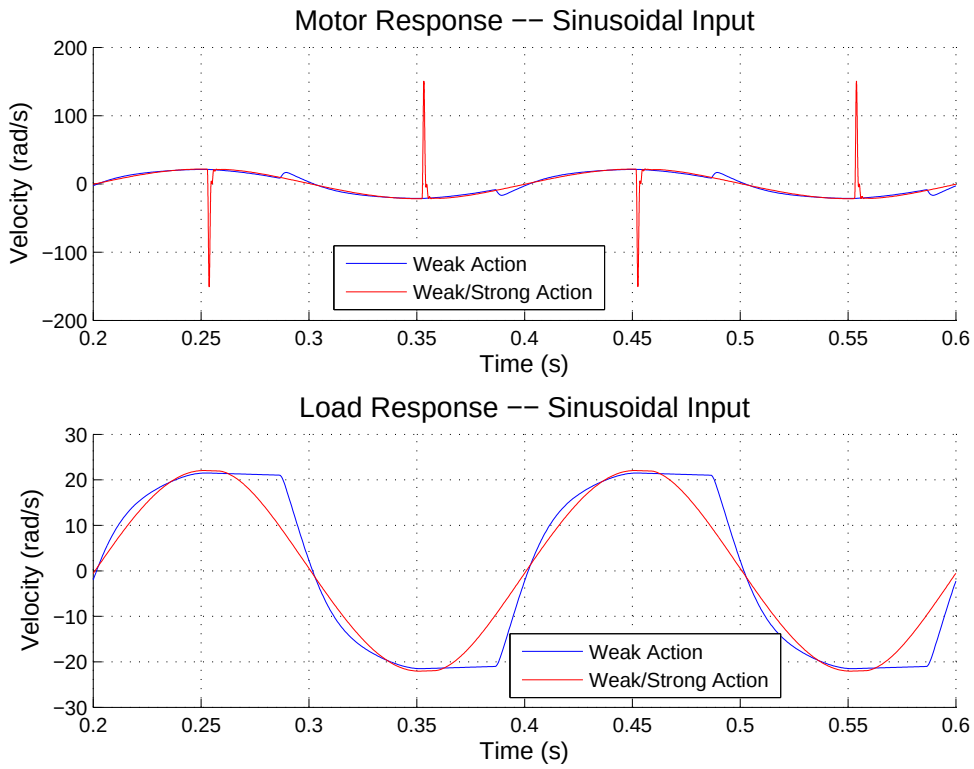


Figure 7.21: Low Amplitude Sinusoidal Responses – Weak Action Controller

Poor tracking performance in systems with backlash is predominately a problem at low velocities. When the velocity reference command is high, the system tends to inherently traverse the backlash gap quickly. Under these conditions added strong action could result in high impact collisions and a subsequent degradation of tracking performance. This problem is addressed in the hybrid weak/strong controller as the width of the strong action output reduces with respect to time at higher velocities. Hence, this controller is suitable for both high and low speed tracking.

The high speed tracking performance of the hybrid weak/strong controller is demonstrated in Figure 7.22, where the simulated motor and load responses are shown for a sinusoidal

input with the amplitude increased to 200 rad/s. The system used to simulate the responses shown in Figure 7.22 was identical to the system used to simulate the low velocity tracking in Figure 7.21, with the initial step and width of the strong action remaining unchanged at 200 rad/s and 0.12 rad respectively.

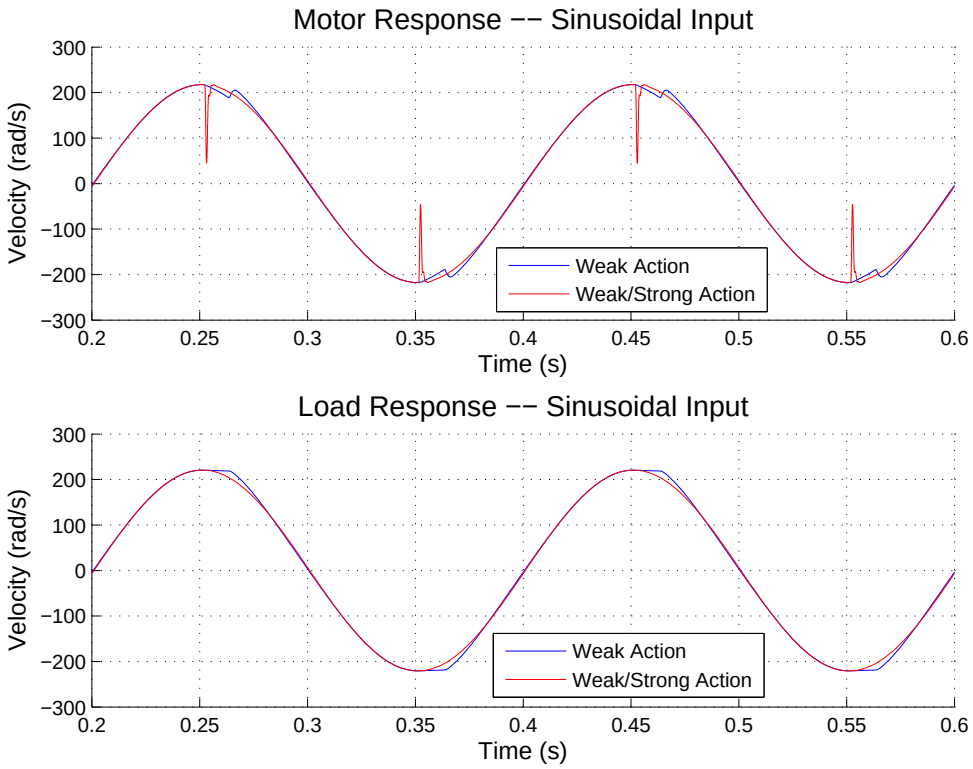


Figure 7.22: High Amplitude Sinusoidal Responses – Weak Action Controller

As can be seen in Figure 7.22, the load response for the weak action controller is much more sinusoidal than it was for the low amplitude input signal (Figure 7.21). However, the added strong action of the hybrid weak/strong controller still results in an improved load response, with no high speed collisions.

## 7.4 Experimental Analysis of the Hybrid Controller

The hybrid weak/strong controller presented in Section 7.3 was implemented on the Motor-Transmission-Load Test-Bed. This test-bed allowed for testing to be carried out

using different backlash gaps and load inertias. The complete parameter details for the Motor-Transmission-Load Test-Bed are given in Section 4.3.2.

Figure 7.23 shows the strong action output of the backlash phase identification technique when a sinusoidal input is applied to the experimental system (configured with Shaft 1, backlash Coupling 2 and inertia Disc 2 attached to the load). Through the use of motor acceleration feedback a very accurate approximation of the transmission torque can be obtained. The motor acceleration feedback on the experimental system was provided by the Hübner rotary accelerometer. The resulting transmission torque approximation is shown alongside the phase identification output in Figure 7.23.

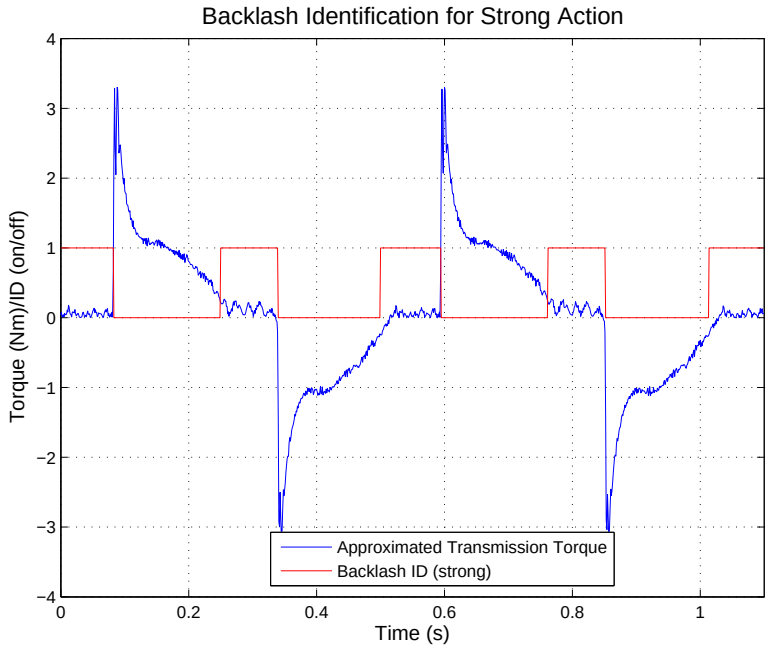


Figure 7.23: Experimental Backlash Phase Identification

As can be seen in Figure 7.23, both the transmission torque approximation and the phase identification output of the experimental system are consistent with the expected outputs described in Section 7.3.2. The response to a 10Nm disturbance torque, of the same experimental set-up, is shown in Figure 7.24.

It can be seen from Figure 7.24, that the switched weak action of the backlash controller produces a stable response to the disturbance (red response) torque, while the (non-switched) response of the controller designed for the contact phase (blue response) begins

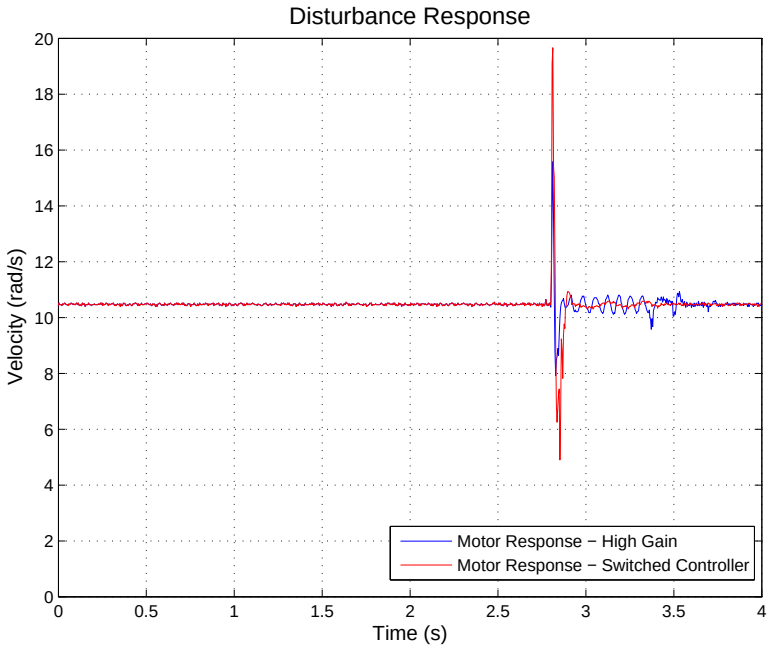


Figure 7.24: Experimental Disturbance Response

to exhibit limit cycles. The tuning of both the contact and backlash phase controllers for the experimental system were as described in Section 7.3.3; however, the gains of the contact phase controller were slightly reduced to ensure no damage would result on the experimental system when obtaining the non-switched response.

The tracking performance of the experimental system with and without the added strong action is compared in Figures 7.25 to 7.28. For each of the responses shown in these figures the test-bed was configured using Shaft 1, with the backlash coupling and load inertia varied. Inertia Disc 2 was attached to the load for the responses shown in Figures 7.25 and 7.26, with Coupling 1 used in Figure 7.25 and Coupling 2 used in Figure 7.26. Inertia Discs 1 and 2 were attached to the load for the responses shown in Figures 7.27 and 7.28, with Coupling 1 used in Figure 7.27 and Coupling 2 used in Figure 7.28.

The velocity reference command used for the responses shown in Figures 7.25 to 7.28 was a sinusoidal signal of 1.95 Hz, with an amplitude of 10.46 rad/s. This low amplitude sinusoidal input was chosen due to the fact that poor tracking performance in systems with backlash is predominately a problem at low velocities. The motor responses with and without the added strong action are shown in the upper graphs of Figures 7.25 to

7.28, while the load responses are shown in the lower graphs.

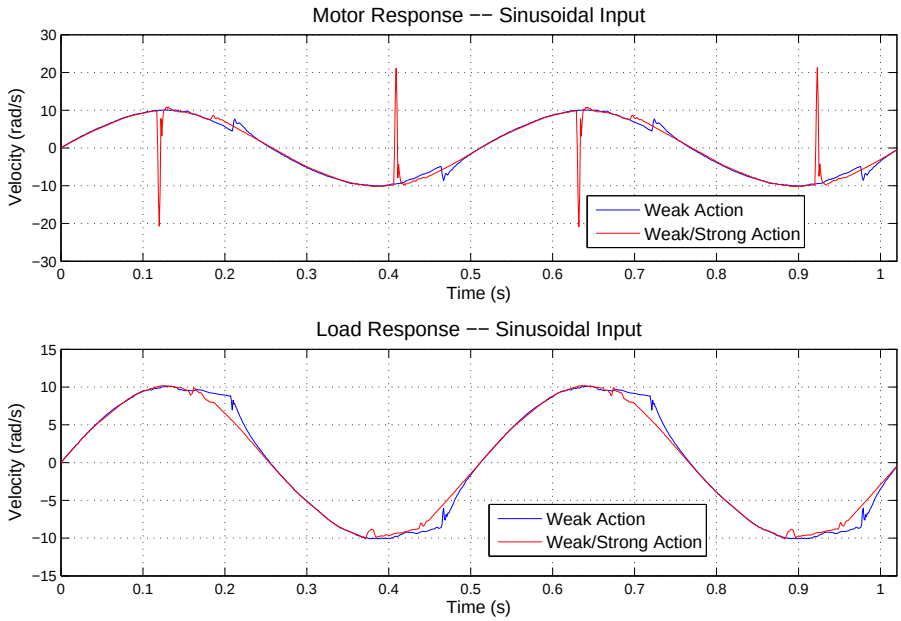


Figure 7.25: Sinusoidal Tracking – Coupling 1, Inertia Disc 2

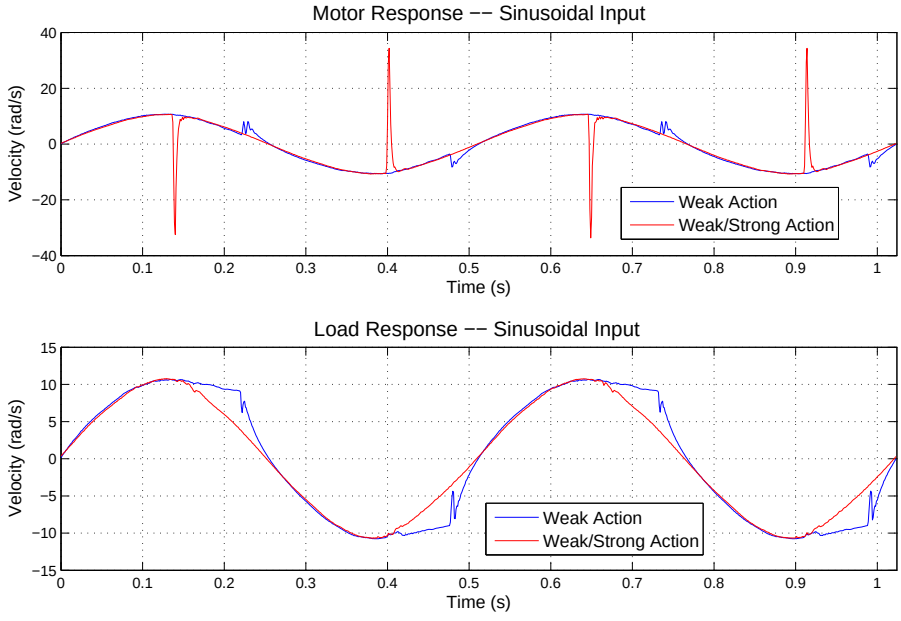


Figure 7.26: Sinusoidal Tracking – Coupling 2, Inertia Disc 2

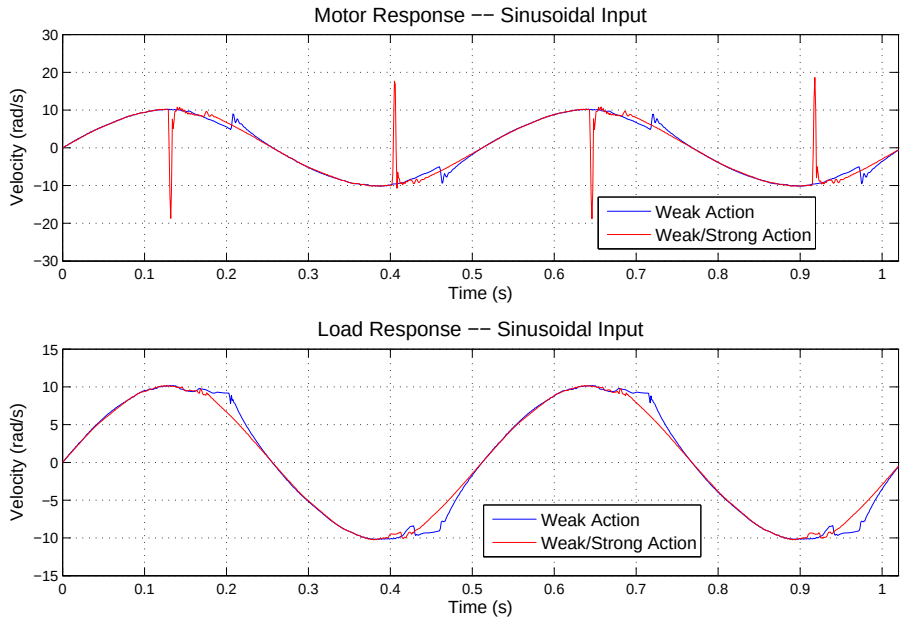


Figure 7.27: Sinusoidal Tracking – Coupling 1, Inertia Discs 1 & 2

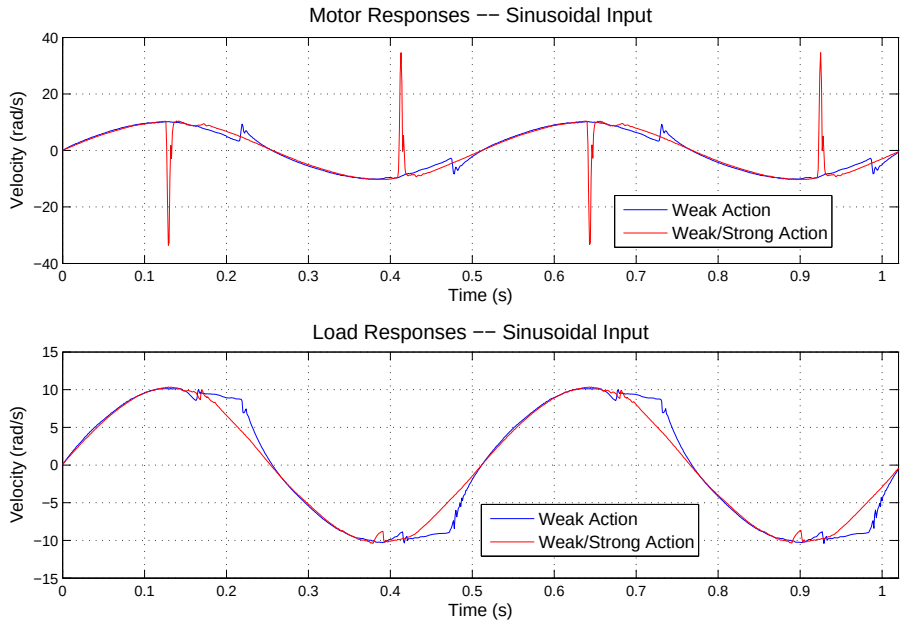


Figure 7.28: Sinusoidal Tracking – Coupling 2, Inertia Discs 1 & 2

The effects of the strong action in the hybrid weak/strong controller are clearly demonstrated in Figures 7.25 to 7.28. The added strong action greatly improves the tracking per-

formance of the system, resulting in much more sinusoidal load responses. The tracking performance of the system, with and without the added strong action, was also quantified by integrating the square of the tracking error over one period of the sinusoidal input. The tracking error in this case was defined as the difference between the sinusoidal input signal and the associated load response. A summary of the tracking error performances, of the responses shown in Figures 7.25 to 7.28, is given in Table 7.1.

Table 7.1: Tracking Error Performance

| Load Inertia ($kgm^2$) | Backlash Gap (rad) | Control Action | Integrated Error |
|---|---|---|---|
| $5.43\times10^{-3}$ | 0.0436 | weak | 0.3574 |
| | | weak/strong | 0.0753 |
| | 0.0873 | weak | 1.419 |
| | | weak/strong | 0.0327 |
| $6.94\times10^{-3}$ | 0.0436 | weak | 0.3706 |
| | | weak/strong | 0.0454 |
| | 0.0873 | weak | 0.8005 |
| | | weak/strong | 0.0446 |

It can be seen from Table 7.1 that the additional strong action improved the tracking error for all four configurations. In each case the strong action component of the controller was tuned manually, without using the known backlash gap values. The results in Table 7.1 also show that the final tracking errors are very similar for the different size backlash gaps. Hence, the overall improvement was greater (more than an order of magnitude) for the cases where the backlash gap was larger (0.0873 rad). These tracking performance results, coupled with the stable disturbance torque response shown in Figure 7.24, demonstrate practically the advantages of combining weak and strong action during the backlash phase. The results presented throughout this section also confirm that the methods used to identify the backlash phase and control the pulse width in the hybrid weak/strong controller can be successfully implemented practically.

One other important practical issue, associated with implementing backlash controllers on industrial control systems, is the required computational power. It was found that the time taken to execute a complete control cycle of the hybrid weak/strong controller, on the industry CNC system used throughout this thesis, was up to $120\mu$s. Since the

sample period of this system is 125$\mu$s, the control cycle execution is right on the limit of the system. In comparison, the complete control cycle for a traditional PI regulator takes around 100$\mu$s on this system. It has already been shown in Section 6.3.4 that state feedback control with an observer can exceed the 125$\mu$s sample period of this system. While the hybrid weak/strong controller was successfully implemented on this industry CNC, it would not be possible to implement many of the more complicated backlash controllers detailed in Section 2.4.3 due to the additional computational requirements.

## 7.5 Conclusions

A new approach to the non-linear control of servo systems with backlash has been presented in this chapter. This approach combined the concepts of 'weak' and 'strong' action during the backlash phase, resulting in a controller that demonstrated both dynamic stability and good tracking performance. New methods to construct backlash stability bounds on the Nichols Chart, identify when the system enters the backlash phase and approximate the position of the motor within the backlash gap were also presented in this chapter.

The sinusoidal-input describing function for the new backlash model (developed in Section 3.4) was presented in Section 7.2. When compared with the sinusoidal-input describing function of the standard dead-zone model it was shown that the new backlash model includes the phase shift associated with backlash, which is not addressed by the standard dead-zone model.

The complete hybrid weak/strong approach to controlling backlash was presented in Section 7.3. A new method to identify whether a system is in the backlash phase or contact phase, when the available feedback is restricted to the motor side, was presented in Section 7.3.2. The switched weak action controller was presented in Section 7.3.3 and the method for applying a degree of strong action during the backlash phase was presented in Section 7.3.4.

The backlash phase identification method presented in Section 7.3.2 is based on the motor torque reference signal, but also takes the motor acceleration and velocity reference signals into account. It was shown that motor acceleration feedback could be used to theoretically remove the torque component that accelerates the motor from the motor torque reference signal. The resulting signal provides a very good approximation of the torque transmitted to the load. When this approximated transmission torque is zero (or low) the system can be considered to be in the backlash phase. Alternatively, when the approximated transmission torque is high the system can be considered to be in the contact phase. It was also shown that the backlash identification requirements are different for weak and strong control actions. While weak control action requires every opening of the backlash gap to be identified, re-openings of the gap that result from collisions should not be identified when strong control action is being applied. It was shown that the differential of the velocity reference signal could be used to distinguish an initial opening of the backlash gap from any subsequent re-openings that occur due to collisions.

Although the switched weak action control approach is not unique to this thesis, a new method to construct backlash stability bounds for use in the QFT design was presented in Section 7.3.3. Since backlash is rarely located at the input or output of a system, this method takes the position of the backlash element into account. An example QFT design, using these backlash stability bounds, was also presented and showed that the stability bounds could predict limit cycle occurrence in the system. The importance of treating backlash and torsional vibrations in parallel was also demonstrated through this example design, with the additional filters included to reduce torsional vibrations shown to directly introduce limit cycles into the system. The switched weak action of the controller was however shown to be effective in removing these limit cycles from the system (these results were also confirmed experimentally in Section 7.4).

The design of the strong action component of the hybrid weak/strong controller was described in Section 7.3.4. This strong action component is based on an initial step that decays as the backlash gap is traversed, which provides a smooth transition back to the

actual velocity reference command and results in a controller that is suitable for both high and low speed tracking. A method that approximates the position of the motor during the backlash gap traversal was also presented. The motor position approximation method was used to control the width of the strong action pulse. The effectiveness of the additional strong control action was demonstrated through simulations, where it was shown that the tracking performance of the hybrid weak/strong controller was much better than that of a controller based on weak action only. It was also found that the additional strong control action did not degrade the stability performance of the controller.

The hybrid weak/strong controller was implemented on the Motor-Transmission-Load Test-Bed in Section 7.4, and shown to provide both dynamic stability and good tracking performance as designed. Since each component of this controller was essential for the overall method to work, the good practical performance of the controller confirmed the effectiveness of the hybrid approach along with that of the backlash phase identification technique and the method used to approximate the motor position within the backlash gap. It was also shown that this control approach was easy to implement and did not require excessive computational power.

Chapter 8

# Conclusions and Recommendations

## 8.1 Summary of Conclusions

The precision control of linear feed axes in machine tools has been studied in this thesis. Throughout this study, two specific aspects of controller design for improved precision were considered: i) the use of appropriate mathematical models and ii) the significance of various performance limiting factors. Three particular performance limiting factors were considered: i) dynamic stiffness, ii) torsional vibrations and iii) backlash. Also, four different linear feed axis drive configurations were included in the study: i) a rotary motor driving a rack and pinion transmission, ii) a rotary motor directly driving a ballscrew transmission, iii) a rotary motor driving a ballscrew transmission via a synchronous timing belt and iv) a direct drive linear motor.

Engineers have been examining the performance limitations of linear feed axes for many years; however, the most common solutions are still based on complex mechanical designs. Although considerable research has been undertaken on alternative control solutions, standard approaches to the control of dynamic stiffness, torsional vibrations and backlash have yet to be adopted. The key contributions of this thesis and the specific conclusions that can be drawn from the results presented in each chapter are summarised in this section.

A brief history of machine tools and precision in machining was presented in Chapter 1, along with a description of recent research undertaken in all areas of machine tool design. The motivation and significance of the research presented in this thesis was hence described, with an outline of the thesis also given.

A review of research undertaken by other scientists and engineers, in respect to each of the three performance limiting factors considered in this thesis, was presented in Chapter 2. This literature review highlighted limitations in the modelling and control solutions that have been previously published in these areas, and described the ways that such limitations are addressed through the research presented in this thesis.

Mathematical models for different linear feed axis configurations were developed in Chapter 3. Initially, a new 'adjusted' two-body model for simple motor-transmission-load systems was presented in Section 3.2. The lowest natural frequency of this 'adjusted' two-body model, along with the lowest natural frequency of 10 other approximate models, was compared with that of the continuous model. This comparison was performed over a wide range of motor-transmission-load conditions, with the 'adjusted' two-body model found to provide higher accuracy, under all of the conditions considered, than the standard two-body model that is traditionally used by researchers and system designers. The only approximate models that showed higher overall accuracy, than the 'adjusted' two-body model, were models with more than two degrees of freedom. However, with reduced complexity, the 'adjusted' two-body model was identified as the most appropriate model from a control perspective.

In Section 3.3 the 'adjusted' two-body model was extended to include simple expressions for damping, coulomb friction, viscous friction and general torque disturbances. A new model for accurately representing backlash in a two-body system was then presented in Section 3.4. The new backlash model was shown to address the shortcomings of previous backlash models. When combined with the 'adjusted' two-body model, the new backlash model provides dual advantages over previous descriptions of backlash with an improved representation of the backlash element itself and a more accurate prediction of the reso-

nant frequencies of a system. In Section 3.5 the complete two-body model was used to develop new models for the direct driven ballscrew, belt driven ballscrew, rack and pinion, and linear motor drive configurations.

The experimental equipment used throughout this research project was described in Chapter 4. The drive-level control scheme of the CNC system (used on each of the test-beds) was discussed, with simple second order filters shown to provide a good representation of the CNC system's closed loop current response. The mechanical system parameters, for each of the test-beds used during the project, were also identified. These mechanical system parameters were used in the system equations developed in Chapter 3, to provide accurate models of each test-bed configuration. All of the control approaches examined throughout this thesis were implemented practically, through extensive re-programming of the CNC system.

Contributions to the body of knowledge associated with dynamic stiffness were presented in Chapter 5. The periodic torque/force disturbances of both linear and rotary driven feed axes were quantified and compared in Section 5.2. It was shown that the only significant disturbances in the Linear Motor Test-Bed were due to the motor's electrical cycle and associated cogging forces. In comparison, the rotary driven configurations had additional significant disturbances due to the mechanical transmission mechanisms of each configuration. It was also shown that the mechanical power required to overcome friction at 200mm/min was more than an order of magnitude higher for the ballscrew configurations, when compared with the linear motor and rack and pinion configurations. The inherent dynamic stiffness of the same configurations were compared mathematically in Section 5.3. Through the mathematical comparison it was found that the linear motor and rack and pinion configurations were only capable of providing significant stiffness at high frequencies. In contrast, the dynamic stiffness of the ballscrew driven configurations was shown to be higher due to the inherent friction and gearing of the ballscrew transmission.

The dynamic stiffnesses of each test-bed configuration were compared experimentally in Section 5.4. When a 125N step disturbance force was applied, the maximum position

error on the ballscrew configurations was found to be more than 2 orders of magnitude lower than that of the linear motor and rack and pinion configurations. A QFT approach to designing control systems that simultaneously address performance specifications based on stability, robustness, overall response speed and dynamic stiffness was also presented in Section 5.4. Although the general QFT approach is not new to this thesis, a new method for specifying the dynamic stiffness requirements of a system and generating associated QFT performance bounds was presented. An example design for the Linear Motor Test-Bed was implemented, with the maximum position error found to be reduced by more than an order of magnitude when compared with the results using the original controller (which was tuned using the CNC manufacturer's recommended process).

Several key contributions to the body of knowledge associated with torsional vibrations, and the control of systems that exhibit torsional vibrations, were presented in Chapter 6. The open and closed loop effects of transmission flexing were analysed in Sections 6.2.2 and 6.2.3 respectively. It was found that maintaining unity motor/load inertia ratios can be beneficial to system performance; however, the effects of varying the motor/load inertia ratio are very limited and also reduce as the inertia of the transmission element is increased. In comparison, the effects of varying the torsional stiffness of the transmission element are much greater,.

The location of feedback sensors, for systems with a flexible transmission, was discussed in Sections 6.2.3 and 6.2.4. It was shown that motor feedback does not always provide an accurate representation of the load, with motor feedback leading the total torque at certain frequencies rather than lagging it (as the load does). It was also shown that absolute stability problems can exist when feedback is restricted to the load-side. Various control solutions that use combinations of motor and load feedback were theoretically compared in Section 6.2.5. It was found that many of the control solutions were fundamentally equivalent, with the feedback gains of each approach related by system constants. This equivalence was not discussed in any of the literature reviewed in Chapter 2.

A method to include both motor and load specifications in a single QFT design proce-

dure was presented in Section 6.3, along with an experimental comparison of control approaches for systems that exhibit torsional vibrations. Two of the control approaches included in the comparison, shaft flex feedback and velocity difference feedback, were developed as a part of this thesis. It was found that all of the examined control approaches were effective at reducing torsional vibrations, when compared with standard PI control. The controllers using state feedback and velocity difference feedback demonstrated the best results. Of the controllers that required feedback from the motor-side only, which is often the only practical approach in many machine tool designs, a simple notch filter and further filtering through an unrestricted QFT design were shown to be effective and easy to implement and tune. In comparison, the state feedback controller was found to be difficult to fine-tune practically and with the addition of an observer, required more computational power than all of the other approaches.

The general computational limitations of the CNC system used throughout this project were illustrated in Section 6.3, where the time taken to execute a complete control cycle of each of the controllers was compared with the sample period of the system. Although the computational power of servo drives will continue to increase, the timing issues illustrated in Section 6.3 remain a problem on many industry servo systems. Hence, theoretical control solutions with excessive computational requirements suffer from significant practical limitations.

Strong agreement between the simulated and experimental results in Section 6.3 validated the accuracy of the 'adjusted' two-body model developed in Chapter 3. The results presented in Section 6.3 also clearly showed that excessive system oscillations can still be present in systems with a unity motor/load inertia ratio. The influence of drive-train configuration on torsional vibrations was experimentally examined in Section 6.4. It was found that the ballscrew configurations exhibited higher resonant peaks than the rack and pinion and linear motor configurations considered. When the ballscrew was driven via a synchronous timing belt (rather than directly by the motor) the damping of the resonance was increased; however, the overall bandwidth of the system was reduced.

A new hybrid weak/strong approach to the non-linear control of systems with backlash was developed in Chapter 7. The sinusoidal-input describing function for the new backlash model (developed in Section 3.4) was presented in Section 7.2. This describing function was shown to include the phase shift associated with backlash, which is not addressed by the standard dead-zone model. A new backlash phase identification method, which uses the motor torque reference signal and motor acceleration feedback, was presented in Section 7.3.2. This phase identification technique was shown to provide a very accurate indication of when a system enters the backlash phase. It was also shown that the differential of the velocity reference signal could be used to distinguish an initial opening of the backlash gap from any subsequent re-openings that occur due to collisions.

A new method for constructing frequency dependent backlash stability bounds was presented in Section 7.3.3. This method is based on the describing function of the new backlash model and takes the location of the backlash element into account, rather than assuming the backlash is at the input or output of a system. An example QFT design, using these backlash stability bounds, was also presented in Section 7.3.3. It was hence shown that the stability bounds could accurately predict limit cycle occurrence in the example system. The importance of treating backlash and torsional vibrations simultaneously was demonstrated through this example design, with limit cycles occurring due to the additional filters that were included to reduce torsional vibrations. The switched weak action approach incorporated in the hybrid weak/strong controller was shown to be effective in avoiding these limit cycles.

The design of the strong action component of the hybrid weak/strong controller was detailed in Section 7.3.4. This strong action component is based on an initial step that decays as the backlash gap is traversed. A method that approximates the position of the motor during the backlash gap traversal is used to control the decay of the initial step. Through both simulation and experimental analysis, the hybrid weak/strong controller was shown to provide both dynamic stability and good tracking performance in the presence of backlash. In particular, the tracking performance achieved through the additional strong action

was shown to be much better than that of a controller based on weak action only. This additional strong action was also shown to be suitable for both high and low speed tracking, without degrading the stability performance of the weak action controller or requiring excessive computational power. Through the development of the hybrid weak/strong control approach and the new backlash model (Section 3.4), contributions to many aspects of the overall problem of controlling systems with backlash have been made in this thesis.

The original hypothesis, stated in Chapter 1, was that 'improved precision in linear feed axes can be achieved through the use of fast computer control algorithms, alternative actuator technologies and non-ideal mechanical components'. The results presented throughout this thesis show that fast computer control algorithms can be used to reduce the effects of performance limiting factors, such as dynamic stiffness, torsional vibrations and backlash. However, if the precision of the system is limited by multiple factors, the overall control solution is often compromised when taking all of the limiting factors into account. For example, Section 7.3.3 showed that a control solution designed to reduce torsional vibrations also directly introduced limit cycles when significant backlash was present in the system. Similarly, alternative actuator technologies can reduce the effects of some performance limiting factors, but reduce the system performance in other areas. As an example the linear motor option was shown, in Sections 5.2 and 5.3, to eliminate many common torque disturbances in a linear feed axis, but reduce the dynamic stiffness of the axis.

The overall choice of actuator, controller and mechanical components of a linear feed axis remains both an economic and application dependent decision. The precision of a system that uses non-ideal mechanical components can be increased through improved control; however, a more costly solution using the ideal mechanical components could still increase precision further. From the overall control perspective, the QFT approach to control design was successfully used to address each of the performance limiting factors studied in this thesis. This particular control approach was shown to provide a transparent design process, where the effects of any change in the control order and structure could be assessed simultaneously for each performance limiting factor.

## 8.2 Recommendations for Future Work

Although engineers have been examining the performance limitations in precision machine tools for many years, there remains areas for future research and further improvement on the methods presented in this thesis. In particular, there are immediate areas where the methods presented to address dynamic stiffness and backlash can be extended.

The QFT design approach was shown to be effective in designing velocity and position loop controllers for high dynamic stiffness in Chapter 5. Although the velocity and position loops are often the most practical for implementing improved control schemes in machine tool feed axes, there are clear advantages in addressing dynamic stiffness at the lower current or flux levels. It is hence recommended that the QFT approach be extended to the design of these lower level control loops. The structured and transparent design approach of QFT allows for changes in control structure to be assessed simultaneously for each performance specification. This approach would be very advantageous in the design of low level controllers, where faster sampling places a very significant restriction on the complexity of any final controller design.

The hybrid weak/strong controller presented in Chapter 7 was shown to provide both dynamic stability and good tracking performance. However, the strong action component of this controller required manual tuning for each system it was tested on. Although the tuning of the strong action component is relatively straight forward, it is recommended that methods be investigated to improve the robustness of this approach. This is an important area of study, as one of the major advantages of this controller is the low computational power required. The obvious methods to extend this controller, such as adaptive and artificial intelligence techniques, could significantly affect its computational requirements.

# References


[1] H. W. Dickinson, *James Watt - Craftsman & Engineer*, Messrs Babcock & Wilcox Ltd, Cambridge, 1935.

[2] J. L. Feirer and E. E. Tatro, *Machine Tool Metalworking - Principles and Practice*, McGraw-Hill Book Company, Inc., New York, 1961.

[3] L. T. C. Rolt, *Tools for the Job - A Short History of Machine Tools*, B. T. Batsford Ltd, London, 1965.

[4] W. H. Armstrong, *Machine Tools - for Metal Cutting*, McGraw-Hill Book Company Inc., New York, 1957.

[5] W. J. McC and R. A. McG, *The Encyclopedia of Britannica*, vol. 28, pp. 728–736, Fifteenth edition.

[6] Frederick W. Taylor, "On the art of cutting metals," *Transactions of the American Society of Mechanical Engineers*, vol. 28, pp. 31–350, 1906.

[7] J.J. D'Azzo, C.H. Houpis, and S.N. Sheldon, *Linear Control System Analysis and Design with Matlab*, Marcel Dekker Inc., New York, fifth edition, 2003.

[8] Bill Drury, *The Control Techniques Drives and Controls Handbook*, The Institution of Electrical Engineers, London, UK, 2001.

[9] E.J. Wightman, "Computer control systems for machine tools," *CME*, pp. 49–55, 1974.

[10] N.C. Ferguson, "A history of numerically controlled machine tools," *CME*, pp. 89–92, 1978.

[11] Eric Laithwaite, "Linear electric machines - a personal view," in *Proceedings of the IEEE*, 1975, vol. 63, pp. 250–290.

[12] David Alter and Tsu-Chin Tsao, "Control of linear motors for machine tool feed drives: Experimental investigation of optimal feedforward tracking control," *Journal of Dynamic Systems, Measurement and Control*, vol. 120, pp. 137–142, 1998.

[13] D. Howe, R.E. Clark, and Z.Q. Zhu, "Status of linear drive technologies in europe," in *The Third International Symposium on Linear Drives for Industry Applications*, Nagano, Japan, 2001, pp. 468–473.

[14] G Henneberger, "Linear motor direct drives for industrial applications - state of the art and research at the department of electrical machines (iem), aachen institute of technology (rwth), germany," in *The Third International Symposium on Linear Drives for Industry Applications*, Nagano, Japan, 2001, pp. 1–8.

[15] Isaac Horowitz, "Survey of quantitative feedback theory (qft)," *International Journal of Control*, vol. 53, pp. 255–291, 1991.

[16] D. M. Alter and T. Tsao, "Stability of turning processes with actively controlled linear motor feed drives," *Journal of Engineering for Industry*, vol. 116, pp. 298–307, 1994.

[17] Woodward C. Carter, "Mechanical factors affecting electrical drive performance," *IEEE Transactions on Industry and General Applications*, vol. IGA-5, no. 3, pp. 282–290, 1969.

[18] Y. Kakino, "Tools for high speed and high acceleration feed drive system of nc machine tools — present and future —," in *The Second International Symposium on Linear Drives for Industry Applications*, Tokyo, Japan, 1998, pp. 15–21.

[19] M. Karita, "Present status of linear drives for industry applications in japan," in *The Third International Symposium on Linear Drives for Industry Applications*, Nagano, Japan, 2001, pp. 462–467.

[20] Parker Hannifin Corporation, "Linear motors complement today's linear motion technologies," Parker Motion White Papers - URL: http://www.parkermotion.com/whitepages/linearmotorarticle.pdf.

[21] G. Pritschow, "A comparison of linear and conventional electromechanical drives," *Annals of CIRP*, vol. 47, pp. 541–548, 1998.

[22] T. R. Aston, "25 years of linear motoring," in *Sixth International Conference on Electrical Machines and Drives*, 1993, pp. 353–358.

[23] J. Floresta, "Driving linear motors," *PT Design Magazine*, pp. 31–34, October 1998.

[24] G. Pritschow and W. Phillip, "Research on the efficiency of feedforward controllers in direct drives," *Annals of CIRP*, vol. 41, pp. 411–415, 1992.

[25] J. Weigel and P. Mutschler, "Modelling and control of permanent magnet linear synchronous motor featuring unbalance and saturation including cross-saturation," in *35th Annual IEEE Power Electronics Specialists Conference*, 2004, pp. 2204–2210.

[26] J. Weigel and P. Mutschler, "Enhanced disturbance rejection due to highly dynamic parameter-adaptive control of saturated pm linear motor," in *2005 Industry Applications Conference*, 2005, pp. 723–730.

[27] J. Cui, C. Wang, J. Yang, and D. Yu, "Research on force and direct thrust control for a permanent magnet synchronous linear motor," in *30th Annual Conference of the IEEE Industrial Electronics Society*, 2004, pp. 2269–2272.

[28] L. Zhao, J. Cui, J. Wan, H. Wang, and L. Jiang, "Research on the parameters identification of direct thrust control system using wavelet transform," in *Sixth*

*Internatinoal Conference on Intelligent Systems Design and Applications*, 2006, pp. 132–136.

[29] D. Alter and T. Tsao, "Dynamic stiffness enhancement of direct linear motor feed drives for machining," in *Proceedings of the American Control Conference*, Baltimore, USA, 1994, pp. 3303–3307.

[30] B.-H. Shen and M.-C. Tsai, "Robust dynamic stiffness design of linear servomotor drives," *Control Engineering Practice*, vol. 14, pp. 1325–1336, 2006.

[31] H. Van Brussel and P. Van den Braembussche, "Robust control of feed drives with linear motors," in *CIRP Annals*, Switzerland, 1998, pp. 325–328.

[32] B. Yao and L. Xu, "Adaptive robust control of linear motors for precision manufacturing," in *14th IFAC World Congress*, Beijing, 1999, vol. A, pp. 25–30.

[33] L. Xu and B. Yao, "Adaptive robust precision motion control of linear motors with negligible electrical dynamics: Theory and experiments," *IEEE/ASME Transactions on Mechatronics*, vol. 6, pp. 444–452, 2001.

[34] L. Xu and B. Yao, "Output feedback adaptive robust precision motion control of linear motors," *Automatica*, vol. 37, pp. 1029–1039, 2001.

[35] Y. Hong and B. Yao, "A globally stable high-performance adaptive robust control algorithm with input saturation for precision motion control of linear motor drive systems," *IEEE/ASME Transactions on Mechatronics*, vol. 12, pp. 198–207, 2007.

[36] J. Yang, N. C. Cheung, and J. Wu, "The auto-disturbance rejection controller for speed regulation in permanent-magnet linear motors," in *The 30th Annual Conference of the IEEE Industrial Electronics Society*, Busan, Korea, 2004, pp. 1123–1127.

[37] D. Dolinar and G. Stumberger, "High performance tracking of linear synchronous reluctance servodrive," in *7th International Workshop on Advanced Motion Control*, 2002, pp. 182–187.

[38] D. Renton and M. A. Elbestawi, "Motion control for linear motor feed drives in advanced machine tools," *International Journal of Machine Tools and Manufacture*, vol. 41, pp. 479–507, 2001.

[39] D. Yu, Q. Guo, and Q. Hu, "Position control of linear servo system using intelligent feedback controller," in *Proceedings of the Sixth International Conference on Intelligent Systems Design and Applications*, 2006, pp. 128–131.

[40] Mattias Nordin, *Nonlinear Backlash Compensation for Speed Controlled Elastic Systems*, Ph.D. thesis, Royal Institute of Technology Stockholm, Sweden, 2000.

[41] Australia Baldor, "Servo products and positioning systems," Stock Products Catalogue, 1996.

[42] R. W. JR Armstrong, "Load to motor inertia mismatch: Unveiling the truth," in *Drives and Controls Conference*, Telford, England, 1998.

[43] R. H. JR Welch, "Mechanical resonance in a closed loop servo system; problems and solutions," (a tutorial), Welch Enterprises, 1995.

[44] S. N. Vukosavic, "Suppression of torsional oscillations in a high-performance speed servo drive," *IEEE Transactions on Industrial Electronics*, vol. 45, pp. 108–117, 1998.

[45] G. Brandenburg and U. Schafer, "Influence and adaptive compensation of simultaneously acting backlash and coulomb friction in elastic two-mass systems of robots and machine tools," in *ICCON '89*, 1989, pp. WA–4–5 1–3.

[46] J-K. Ji and S-K. Sul, "Kalman filter and lq based speed controller for torsional vibration suppression in a 2-mass motor drive system," *IEEE Transactions on Industrial Electronics*, vol. 42, pp. 564–571, 1995.

[47] G. Ferretti, G. Magnani, and P. Rocco, "Alternatives in precise load motion control of two-mass servomechanisms," in *IEEE/ASME International Conference on Advanced Intelligent Mechatronics*, Como, Italy, 2001, pp. 893–898.

[48] G. Suh, D. S. Hyun, J. I. Park, K. D. Lee, and S. G. Lee, "Design of a pole placement controller for reducing oscillation and settling time in a two-inertia motor system," in *IECON'01: The 27th Annual Conference of the IEEE Industrial Electronics Society*, Colorado, USA, 2001, pp. 615–620.

[49] Y. Hori, H. Iseki, and K. Sugiura, "Basic consideration of vibration suppression and disturbance rejection control of multi-inertia system using sflac (state feedback and load acceleration control)," *IEEE Transactions on Industry Applications*, vol. 30, pp. 889–896, 1994.

[50] D. Economou, C. Mavroidis, and I. Antoniadis, "Experiments on robust vibration suppression in mechatronic systems using iir digital filters," in *IEEE/ASME International Conference on Advanced Mechatonics*, Como, Italy, 2001, pp. 731–737.

[51] J. Moscrop, C. Cook, and F. Naghdy, "An analysis of motor/load inertia mismatch in machine tool servo systems," in *1st IFAC Conference on Mechatronic Systems*, Germany, 2000.

[52] J. Moscrop, C. Cook, and P. Moll, "Control of servo systems in the presence of motor-load inertia mismatch," in *IECON'01: The 27th Annual Conference of the IEEE Industrial Electronics Society*, Colorado, USA, 2001, pp. 351–356.

[53] C. Baril and J. Galic, "Speed control of an elastic two-mass system," *Technical Report TRITA/MA-94-29T, Optimization and Systems Theory, Royal Institute of Technology, Stockholm Sweden*, 1994.

[54] U. Schafer and G. Brandenburg, "State position control for elastic pointing and tracking systems with gear play and coulomb friction - a summary of results," in *European Conference on Power Electronics and Applications*, 1991, pp. 596 – 602.

[55] Oxford University, *Oxford English Dictionary*, Clarendon Press, Oxford, second edition, 1989.

[56] Merriam-Webster Inc., "Merriam-webster online dictionary," http://www.merriam-webster.com/dictionary/backlash.

[57] B. A. Chubb, *Modern Analytical Design of Instrument Servomechanisms*, Addison-Wesley Publishing Company Inc., USA, 1967.

[58] J. G. Truxal, *Control Engineers' Handbook*, McGraw-Hill Inc., USA, 1958.

[59] R. A. Bruns and R. M. Saunders, *Analysis of Feedback Control Systems: Servomechanisms and Automatic Regulators*, McGraw-Hill Inc., USA, 1955.

[60] Thomas P. Goodman, "Dynamic effects of backlash," *Machine Design*, pp. 150–157, 1963.

[61] Katsuhiko Ogata, *Modern Control Engineering*, Prentice Hall, Ind., Englewood Cliffs, New Jersey, 1990.

[62] G. Tao and P. V. Kokotovic, *Adaptive Control of Systems*, John Wiley and Sons Inc., New York, USA, 1996.

[63] B. C. Kuo, *Automatic Control Systems*, Prentice-Hall International, London England, 1991.

[64] Cun Wu Han and Yi Xin Zhong, "Robust adaptive control of time-varying systems with unknown backlash nonlinearity," in *Proceedings of the American Control Conference*, Albuquerque, New Mexico, 1997, pp. 763 – 767.

[65] Dong H. Chyung, "Output feedback controller for systems containing a backlash," in *Proceedings of the 31st Conference on Decision and Control*, Tuscan, Arizona, 1992, pp. 3429–3430.

[66] Rastko R. Selmic and Frank L. Lewis, "Neural net backlash compensation with hebbian tuning using dynamic inversion," *Automatica*, vol. 37, pp. 1269 – 1277, 2001.

[67] Gang Tao and Petar V. Kokotovic, "Adaptive control of systems with unknown output backlash," *IEEE Transactions on Automatic Control*, vol. 40, no. 2, pp. 326 – 330, 1995.

[68] H. Maeda, M. Ikeda, and S. Kodama, "Stability criterion for a feedback system with backlash – an extension of frequency-domain condition by the multiplier method," *IEEE Transactions on Automatic Control*, pp. 703–705, 1970.

[69] K. Ezal, P. V. Kokotovic, and G. Tao, "Optimal control of tracking systems with backlash and flexibility," in *36th Conference on Decision and Control*, San Diego, USA, 1997, pp. 1749–1754.

[70] R. Boneh and O. Yaniv, "Reduction of limit cycle amplitude in the presence of backlash," *Journal of Dynamic Systems, Measurement and Control - ASME*, vol. 121, pp. 278–284, 1999.

[71] C.-F. Lin, T.-J. Yu, and X. Feng, "Fuzzy control of a nonlinear pointing testbed with backlash and friction," in *35th Convference on Decision and Control*, Kobe, Japan, 1996, pp. 4363–4368.

[72] You Wu, K. Fujikawa, and H. Kobayashi, "A control method of speed control drive system with backlash," in *Proceedings of the 3rd AMC Workshop, IEEE*, 1996, pp. 631 – 636.

[73] M. Odai and Y. Hori, "Speed control of 2-inertia system with gear backlash using gear torque compensator," in *Proceedings of the 4th AMC Workshop, IEEE*, 1998, pp. 234 – 239.

[74] Y. Nakayama, K. Fujikawa, and H. Kobayashi, "A torque control method of three-inertia torsional system with backlash," in *Proceedings of the 5th AMC Workshop, IEEE*, 2000, pp. 193 – 198.

[75] Alistair G. J. MacFarlane, "The development of frequency-response methods in

automatic control," *IEEE Transactions on Automatic Control*, vol. AC-24, no. 2, pp. 250–265, 1979.

[76] A. Tustin, "The effects of backlash and of speed-dependent friction on the stability of closed-cycle control systems," *Journal of the Institute of Electrical Engineers*, vol. 94, Part IIA, pp. 143–151, 1947.

[77] H. Chestnut and N. Y. Schenectady, "Approximate frequency-response methods for representing saturation and dead band," *Transactions of the ASME*, pp. 1345–1363, 1954.

[78] C. H. Thomas and N. Y. Schenectady, "Stability characteristics of closed-loop systems with dead band," *Transactions of the ASME*, pp. 1365–1382, 1954.

[79] J. E. Tierno, K. Y. Kim, S. L. Lacy, and D. S. Bernstein, "Describing function analysis of an anti-backlash controller," in *Proceedings of the American Control Conference*, Chicago, Illinois, 2000, pp. 4164–4168.

[80] Antonio Barreiro and Alfonso Banos, "Input-output stability of systems with backlash," *Automatica*, vol. 42, pp. 1017–1024, 2006.

[81] G. Brandenburg, H. Unger, and A. Wagenpfeil, "Stability problems of a speed-controlled drive in an elastic system with backlash and corrective measures by a load observer," in *Proceedings of the International Conference on Electrical Machines, IEEE*, Munich, 1986, pp. 523–527.

[82] Mattias Nordin and Per-Olof Gutman, "Non-linear speed control of elastic systems with backlash," in *Proceedings of the 39th IEEE Conference on Decision and Control*, Sydney, Australia, 2000, pp. 4060 – 4065.

[83] Gang Tao and Petar V. Kokotovic, "Continuous-time adaptive control of systems with unknown backlash," *IEEE Transactions on Automatic Control*, vol. 40, no. 6, pp. 1083 – 1087, 1995.

[84] Gang Tao and Petar V. Kokotovic, "Adaptive control of systems with unknown output backlash," in *Proceedings of the 32nd Conference on Decision and Control*, San Antonio, Texas, 1993, pp. 2635 – 2640.

[85] Gang Tao and Xiaoli Ma, "Backlash compensation for multivariable nonlinear systems with actuator dynamics," in *Proceedings of the 38th Conference on Decision and Control*, Phoenix, Arizona, 1999, pp. 3382 – 3387.

[86] Yi Ling and Gang Tao, "Numerical design and analysis of backlash compensation for a multivariable nonlinear tracking system," in *Proceedings of the American Control Conference*, San Diego, California, 1999, pp. 3539 – 3543.

[87] Gang Tao, Xiaoli Ma, and Yi Ling, "Optimal and nonlinear decoupling control of systems with sandwiched backlash," *Automatica*, vol. 37, pp. 165 – 176, 2001.

[88] Stephen R. H. Dean, Brian W. Surgenor, and Harry N. Iordanou, "Experimenal evaluation of a backlash inverter as applied to a servo-motor with gear train," in *Proceedings of the 4th IEEE Conference on Control Applications*, 1995, pp. 580 – 585.

[89] Jung-Hua Yang and Li-Chen Fu, "Nonlinear adaptive control for manipulator system with gear backlash," in *Proceedings of the 35th Conference on Decision and Control*, Kobe, Japan, 1996, pp. 4369 – 4374.

[90] M. T. Mata-Jiménez, B. Brogliato, and A. Goswami, "On the control of mechanical systems with dynamic backlash," in *Proceedings of the 36th IEEE Conference on Decision and Control*, 1997, pp. 1990 – 1995.

[91] I. Schöling and B. Orlik, "Control of a nonlinear two-mass system with uncertain parameters and unknown states," in *Conference Record of the 2000 IEEE Industry Applications Conference*, 2000, pp. 1096 – 1103.

[92] C. W. Tao, "Fuzzy control for linear plants with uncertain output backlashes," *IEEE Transactions on Systems, Man and Cybernetics*, vol. 32, pp. 373 – 380, 2002.

[93] Chun-Yi Su, Masahiro Oya, and Henry Hong, "Stable adaptive fuzzy control of nonlinear systems preceded by unknown backlash-like hysteresis," *IEEE Transactions on Fuzzy Systems*, vol. 11, pp. 1 – 8, 2003.

[94] David r. Seidl, Sui-Lun Lam, Jerry A. Putman, and Robert D. Lorenz, "Neural network compensation of gear backlash hysteresis in position-controlled mechanisms," *IEEE Transactions on Industry Applications*, vol. 31, pp. 1475–1483, 1995.

[95] K. Menon and K. Krishnamurthy, "Control of low velocity friction and gear backlash in a machine tool feed drive system," *Mechatronics*, vol. 9, pp. 33 – 52, 1999.

[96] Leonard Meirovitch, *Principles and Techniques of Vibrations*, Prentice-Hall Inc., New Jersey, USA, 1997.

[97] J.J. D'Azzo and C.H. Houpis, *Linear Control System Analysis and Design*, McGraw-Hill, USA, 1988.

[98] Dare A. Wells, *Theory and Problems of Lagrangian Dynamics*, Schaum Publishing Company, New York, 1967.

[99] Den Hartog, *Mechanical Vibrations*, McGraw-Hill Book Company, 1947.

[100] B. Armstrong-Hélouvry, *Control of Machines with Friction*, Kluwer Academic Publishers, Massachusetts, USA, 1991.

[101] J.W.L. Simpson, *Force and Low Speed Control in Mechatronic Systems with Friction*, Ph.D. thesis, The University of Wollongong, Wollongong, Australia, 2003.

[102] C.H. Houpis and S.J. Rasmussen, *Quantitative Feedback Theory - Fundamentals and Applications*, Marcel Dekker Inc., New York, 1999.

[103] Jeffrey L. Stein and Churn-Hway Wang, "Estimation of gear backlash: Theory and simulation," *Journal of Dynamic Systems, Measurement and Control*, vol. 120, pp. 74 – 82.

[104] Bernhard T. Angerer, Christian Hintz, and Dierk Schröder, "Online identification of a nonlinear mechatronic system," *Control Engineering Practice*, vol. 12, pp. 1465 – 1478, 2004.

[105] John G. O'Donovan, Richard C. Kavanagh, Murphy John M. D., and Michael G. Egan, "Modular approach to parameter estimation in geared and linear resonant systems," *Control Engineering Practice*, vol. 12, pp. 75 – 86, 2004.

Appendix A

# Glossary

This appendix contains a list of symbols that were used throughout the text.

| | |
|---|---|
| $A^+, A^-, A^0$ | areas on a phase plane plot |
| $A_+, A_-, A_r$ | areas on a phase plane plot |
| $B_l$ | viscous friction at the load |
| $B_m$ | viscous friction at the motor |
| $C_s$ | coefficient of internal damping of a transmission element |
| $C_{sblt}$ | internal damping coefficient of a belt |
| D | continuous system Domain |
| $D(\theta_d)$ | dead zone backlash model output |
| DS | dynamic stiffness |
| $e_x$ | compliance between inertial bodies |
| E | maximum allowable position displacement |
| $E_f$ | maximum position displacement at frequency $f$ |
| $f$ | frequency |
| F | force |
| $F_{blt}$ | linear force transmitted through a synchronous belt |
| $F_{fc}$ | coulomb frictional force |
| G | shear modulus |
| G(s) | transfer function |
| $i_d$ | direct axis current |

| | |
|---|---|
| $i_q$ | quadrature axis current |
| $I_r$ | motor/load inertia ratio |
| $I_s$ | motor/transmission inertia ratio |
| $I(x)$ | mass moment of inertia density |
| $J_l$ | load inertia |
| $J_m$ | motor inertia |
| $J_p$ | inertia of a ballscrew driving pulley |
| $J_{PIN}$ | inertia of a pinion |
| $J_s$ | transmission element inertia |
| $J(x)$ | area polar moment of inertia |
| $K_l$ | load feedback gain |
| $K_m$ | motor feedback gain |
| $K_p$ | proportional gain |
| $K_s$ | torsional stiffness of a transmission element |
| $K_{sadj}$ | adjusted torsional stiffness of a transmission element |
| $K_{sblt}$ | belt stiffness coefficient |
| $K_t$ | motor torque constant |
| L | Lagrangian |
| $\hat{L}$ | Lagrangian Density |
| $L_{BS}$ | overall ballscrew length |
| $L_{nom}$ | nominal loop transmission function |
| M | mass |
| $N$ | sinusoidal-input describing function |
| $P_{BS}$ | ballscrew pitch |
| $P_{nom}$ | nominal plant |
| $P(s)$ | plant set |
| $q$ | generalised system coordinate |
| $R_m$ | radius of a motor pulley |
| $R_p$ | radius of a ballscrew driving pulley |
| S | continuous system boundary |
| T | total kinetic energy |
| $T_{bs}$ | torque transmitted through a ballscrew |
| $T_{fcl}$ | coulomb frictional torque at the load |

| | |
|---|---|
| $T_{fcm}$ | coulomb frictional torque at the motor |
| $T_i$ | integral action |
| $T_m$ | torque produced by driving motor |
| $T_{trans}$ | transmission element torque |
| V | total potential energy |
| $x$ | linear position displacement |
| $Z$ | total number of stator conductors |
| $\alpha$ | half of the total backlash gap |
| $\beta$ | angle between stator and rotor MMFs |
| $\eta$ | material loss factor |
| $\theta_b$ | angular input position of a backlash element |
| $\theta_{BL}$ | the backlash angle (the difference between the input and output positions at a backlash element) |
| $\theta_d$ | overall angular position displacement between the motor and load |
| $\theta_l$ | angular position at the load |
| $\theta_m$ | angular position at the motor |
| $\theta_p$ | angular position of a ballscrew driving pulley |
| $\theta_s$ | transmission shaft flex |
| $\phi$ | magnetic flux |
| $\omega_l$ | angular velocity of the load |
| $\omega_m$ | angular velocity of the motor |
| $\omega_p$ | natural frequency due to poles in a system |
| $\omega_z$ | natural frequency due to zeros in a system |
| $\Omega_0$ | fundamental angular position frequency |

Appendix B

# Mathematical Derivations

This appendix contains the mathematical derivations that were referred to throughout the main body of this thesis. The equations of motion for the simple motor-transmission-load system with the transmission shaft split into 4 equal sections are derived in Section B.1. The boundary value problem of the continuous model for the simple motor-transmission-load system is derived in Section B.2. The solution to this boundary value problem is also presented in Section B.2. The equation used in Chapter 4 to determine internal damping coefficients for the various test-beds (Equation (4.11)) is derived in Section B.3. Finally, the sinusoidal-input describing function of the new backlash model is derived in Section B.4.

## B.1 Equations of Motion of a 4-Sectioned Transmission Shaft

The system with the transmission shaft split into 4 equal sections is shown in Figure 3.1. This system is described by six generalised coordinates, $\theta_m$, $\theta_{s1}$, $\theta_{s2}$, $\theta_{s3}$, $\theta_{s4}$ and $\theta_l$. The Lagrangian for this system is formulated as follows:

- Kinetic Energy

$$\begin{aligned}
\mathrm{T}_m &= \frac{1}{2}\mathrm{J}_m\dot{\theta}_m^2 \text{ (motor)} \\
\mathrm{T}_{s1} &= \frac{1}{2}\frac{\mathrm{J}_s}{4}\dot{\theta}_{s1}^2 \text{ (shaft section 1)} \\
\mathrm{T}_{s2} &= \frac{1}{2}\frac{\mathrm{J}_s}{4}\dot{\theta}_{s2}^2 \text{ (shaft section 2)} \\
\mathrm{T}_{s3} &= \frac{1}{2}\frac{\mathrm{J}_s}{4}\dot{\theta}_{s3}^2 \text{ (shaft section 3)} \\
\mathrm{T}_{s4} &= \frac{1}{2}\frac{\mathrm{J}_s}{4}\dot{\theta}_{s4}^2 \text{ (shaft section 4)} \\
\mathrm{T}_l &= \frac{1}{2}\mathrm{J}_l\dot{\theta}_l^2 \text{ (load)} \\
\mathrm{T} &= \mathrm{T}_m + \mathrm{T}_{s1} + \mathrm{T}_{s2} + \mathrm{T}_{s3} + \mathrm{T}_{s4} + \mathrm{T}_l \\
&= \frac{1}{2}\mathrm{J}_m\dot{\theta}_m^2 + \frac{1}{8}\mathrm{J}_s\dot{\theta}_{s1}^2 + \frac{1}{8}\mathrm{J}_s\dot{\theta}_{s2}^2 + \frac{1}{8}\mathrm{J}_s\dot{\theta}_{s3}^2 + \frac{1}{8}\mathrm{J}_s\dot{\theta}_{s4}^2 + \frac{1}{2}\mathrm{J}_l\dot{\theta}_l^2 \text{ (total)}
\end{aligned}$$

- Potential Energy (noting that the potential energy of a spring is $\frac{1}{2}kx^2$)

$$\begin{aligned}
\mathrm{V} &= 4\mathrm{K}_s(\theta_m - \theta_{s1})^2 + 2\mathrm{K}_s(\theta_{s1} - \theta_{s2})^2 + 2\mathrm{K}_s(\theta_{s2} - \theta_{s3})^2 + 2\mathrm{K}_s(\theta_{s3} - \theta_{s4})^2 \\
&\quad + 4\mathrm{K}_s(\theta_{s4} - \theta_l)^2
\end{aligned}$$

- Lagrangian

$$\begin{aligned}
\mathrm{L} &= \mathrm{T} - \mathrm{V} \\
&= \frac{1}{2}\mathrm{J}_m\dot{\theta}_m^2 + \frac{1}{8}\mathrm{J}_s\dot{\theta}_{s1}^2 + \frac{1}{8}\mathrm{J}_s\dot{\theta}_{s2}^2 + \frac{1}{8}\mathrm{J}_s\dot{\theta}_{s3}^2 + \frac{1}{8}\mathrm{J}_s\dot{\theta}_{s4}^2 + \frac{1}{2}\mathrm{J}_l\dot{\theta}_l^2 \\
&\quad - 4\mathrm{K}_s(\theta_m - \theta_{s1})^2 - 2\mathrm{K}_s(\theta_{s1} - \theta_{s2})^2 - 2\mathrm{K}_s(\theta_{s2} - \theta_{s3})^2 \\
&\quad - 2\mathrm{K}_s(\theta_{s3} - \theta_{s4})^2 - 4\mathrm{K}_s(\theta_{s4} - \theta_l)^2
\end{aligned}$$

Applying Lagrange's Equation (Equation (3.1)), with $q_r = \theta_m$:

$$\begin{aligned}
\frac{\partial \mathrm{L}}{\partial \dot{\theta}_m} &= \mathrm{J}_m\dot{\theta}_m \\
\frac{d}{dt}\left[\frac{\partial \mathrm{L}}{\partial \dot{\theta}_m}\right] &= \mathrm{J}_m\ddot{\theta}_m
\end{aligned}$$

$$\begin{aligned} \frac{\partial \mathrm{L}}{\partial \theta_m} &= -8\mathrm{K}_s(\theta_m - \theta_{s1}) \\ \mathrm{F}_{\theta_m} &= \mathrm{T}_m \end{aligned}$$

thus:

$$\begin{aligned} \mathrm{J}_m\ddot{\theta}_m + 8\mathrm{K}_s(\theta_m - \theta_{s1}) &= \mathrm{T}_m \\ \Rightarrow \mathrm{J}_m\ddot{\theta}_m &= \mathrm{T}_m - 8\mathrm{K}_s(\theta_m - \theta_{s1}) \end{aligned}$$

Applying Lagrange's Equation (Equation (3.1)), with $q_r = \theta_{s1}$:

$$\begin{aligned} \frac{\partial \mathrm{L}}{\partial \dot{\theta}_{s1}} &= \frac{\mathrm{J}_s}{4}\dot{\theta}_{s1} \\ \frac{d}{dt}\left[\frac{\partial \mathrm{L}}{\partial \dot{\theta}_{s1}}\right] &= \frac{\mathrm{J}_s}{4}\ddot{\theta}_{s1} \\ \frac{\partial \mathrm{L}}{\partial \theta_{s1}} &= 8\mathrm{K}_s(\theta_m - \theta_{s1}) - 4\mathrm{K}_s(\theta_{s1} - \theta_{s2}) \\ \mathrm{F}_{\theta_{s1}} &= 0 \end{aligned}$$

thus:

$$\begin{aligned} \frac{\mathrm{J}_s}{4}\ddot{\theta}_{s1} - 8\mathrm{K}_s(\theta_m - \theta_{s1}) + 4\mathrm{K}_s(\theta_{s1} - \theta_{s2}) &= 0 \\ \Rightarrow \frac{\mathrm{J}_s}{4}\ddot{\theta}_{s1} &= 8\mathrm{K}_s(\theta_m - \theta_{s1}) - 4\mathrm{K}_s(\theta_{s1} - \theta_{s2}) \end{aligned}$$

Through a similar application of Lagrange's Equation to the other 4 generalised coordinates, the equations of motion for this 'multi-body' system can be determined as:

$$\mathrm{J}_m\ddot{\theta}_m = \mathrm{T}_m - 8\mathrm{K}_s(\theta_m - \theta_{s1}) \quad \text{(B.1)}$$

$$\mathrm{J}_s\ddot{\theta}_{s1} = 32\mathrm{K}_s(\theta_m - \theta_{s1}) - 16\mathrm{K}_s(\theta_{s1} - \theta_{s2}) \quad \text{(B.2)}$$

$$\mathrm{J}_s\ddot{\theta}_{s2} = 16\mathrm{K}_s(\theta_{s1} - \theta_{s2}) - 16\mathrm{K}_s(\theta_{s2} - \theta_{s3}) \quad \text{(B.3)}$$

$$\mathrm{J}_s\ddot{\theta}_{s3} = 16\mathrm{K}_s(\theta_{s2} - \theta_{s3}) - 16\mathrm{K}_s(\theta_{s3} - \theta_{s4}) \quad \text{(B.4)}$$

$$\mathrm{J}_s\ddot{\theta}_{s4} = 16\mathrm{K}_s(\theta_{s3}-\theta_{s4}) - 32\mathrm{K}_s(\theta_{s4}-\theta_l) \quad \text{(B.5)}$$

$$\mathrm{J}_l\ddot{\theta}_l = 8\mathrm{K}_s(\theta_{s4}-\theta_l) \quad \text{(B.6)}$$

## B.2 Characteristic Equation of the Continuous Model

In order to derive a continuous model of the simple motor-transmission-load system, the transmission shaft must be treated with distributed inertia (as shown in Figure 3.2). In Figure 3.2, the shaft flex ($\theta$) is a function of both the position ($x$) along the length of the shaft and time ($t$). The inertia and torsional stiffness of the shaft are also functions of $x$, with I($x$) being the mass moment of inertia density and GJ($x$) the product of the shear modulus (G) and the area polar moment of inertia of the cross section J($x$). It should also be noted that L in Figure 3.2 is the overall length of the transmission shaft.

The distributed-parameter Lagrangian for this system can be formulated as follows:

- Kinetic Energy

$$\begin{aligned}
\mathrm{T}_m = \mathrm{T}_0 &= \frac{1}{2}\mathrm{J}_m\dot{\theta}^2(0,t) \text{ [motor]} \\
\mathrm{T}_l = \mathrm{T}_\mathrm{L} &= \frac{1}{2}\mathrm{J}_l\dot{\theta}^2(\mathrm{L},t) \text{ [load]} \\
\mathrm{T}_{sh} = \hat{\mathrm{T}} &= \frac{1}{2}\mathrm{I}(x)\dot{\theta}^2(x,t) \text{ [shaft]} \\
\mathrm{T} &= \mathrm{T}_0 + \mathrm{T}_\mathrm{L} + \int_0^\mathrm{L}\hat{\mathrm{T}}dx \\
&= \frac{1}{2}\mathrm{J}_m\dot{\theta}^2(0,t) + \frac{1}{2}\mathrm{J}_l\dot{\theta}^2(\mathrm{L},t) + \frac{1}{2}\int_0^\mathrm{L}\mathrm{I}(x)\dot{\theta}^2(x,t)dx \text{ [total]}
\end{aligned}$$

- Potential Energy

$$\begin{aligned}
\mathrm{V}_m = \mathrm{V}_0 &= 0 \text{ [motor]} \\
\mathrm{V}_l = \mathrm{V}_\mathrm{L} &= 0 \text{ [load]} \\
\mathrm{V}_{sh} = \hat{\mathrm{V}} &= \frac{1}{2}\mathrm{GJ}(x)\theta'^2(x,t) \text{ [shaft]}
\end{aligned}$$

$$\begin{aligned} \mathrm{V} &= \mathrm{V}_0 + \mathrm{V}_\mathrm{L} + \int_0^\mathrm{L} \hat{\mathrm{V}} dx \\ &= \frac{1}{2}\int_0^\mathrm{L} \mathrm{GJ}(x)\theta'^2(x,t)dx \text{ [total]} \end{aligned}$$

- Lagrangian

$$\begin{aligned} \mathrm{L}_0 &= \mathrm{T}_0 - \mathrm{V}_0 \\ &= \frac{1}{2}\mathrm{J}_m\dot{\theta}^2(0,t) \\ \mathrm{L}_\mathrm{L} &= \mathrm{T}_\mathrm{L} - \mathrm{V}_\mathrm{L} \\ &= \frac{1}{2}\mathrm{J}_l\dot{\theta}^2(\mathrm{L},t) \\ \hat{\mathrm{L}} &= \hat{\mathrm{T}} - \hat{\mathrm{V}} \\ &= \frac{1}{2}\mathrm{I}(x)\dot{\theta}^2(x,t) - \frac{1}{2}\mathrm{GJ}(x)\theta'^2(x,t) \\ \mathrm{L} &= \mathrm{L}_0 + \mathrm{L}_\mathrm{L} + \int_0^\mathrm{L} \hat{\mathrm{L}} dx \\ &= \frac{1}{2}\mathrm{J}_m\dot{\theta}^2(0,t) + \frac{1}{2}\mathrm{J}_l\dot{\theta}^2(\mathrm{L},t) + \frac{1}{2}\int_0^\mathrm{L} \left(\mathrm{I}(x)\dot{\theta}^2(x,t) - \mathrm{GJ}(x)\theta'^2(x,t)\right) dx \end{aligned}$$

Applying Lagrange's equation for distributed systems (Equation (3.2)), with $q = \theta$:

$$\begin{aligned} \frac{\partial \hat{\mathrm{L}}}{\partial \theta} &= 0 \\ \frac{\partial \hat{\mathrm{L}}}{\partial \theta'} &= -\mathrm{GJ}(x)\theta'(x,t) \\ \frac{\partial}{\partial x}\left(\frac{\partial \hat{\mathrm{L}}}{\partial \theta'}\right) &= -\frac{\partial}{\partial x}\left(\mathrm{GJ}(x)\theta'(x,t)\right) \\ \frac{\partial \hat{\mathrm{L}}}{\partial \theta''} &= 0 \\ \frac{\partial^2}{\partial x^2}\left(\frac{\partial \hat{\mathrm{L}}}{\partial \theta''}\right) &= 0 \\ \frac{\partial \hat{\mathrm{L}}}{\partial \dot{\theta}} &= \mathrm{I}(x)\dot{\theta}(x,t) \\ \frac{\partial}{\partial t}\left(\frac{\partial \hat{\mathrm{L}}}{\partial \dot{\theta}}\right) &= \mathrm{I}(x)\ddot{\theta}(x,t) \\ \frac{\partial \hat{\mathrm{L}}}{\partial \dot{\theta}'} &= 0 \\ \frac{\partial^2}{\partial x \partial t}\left(\frac{\partial \hat{\mathrm{L}}}{\partial \dot{\theta}'}\right) &= 0 \end{aligned}$$

thus:

$$\frac{\partial}{\partial x}\left(\mathrm{GJ}(x)\theta'(x,t)\right) - \mathrm{I}(x)\ddot{\theta}(x,t) + \mathrm{F}_\theta = 0 \tag{B.7}$$

$$(\text{where } \mathrm{F}_\theta \text{ is a distributed Torque})$$

With $q = \theta$, the Boundary Condition at x=0 can be determined via:

$$\frac{\partial \mathrm{L}_0}{\partial q(0,t)} - \frac{\partial}{\partial t}\left(\frac{\partial \mathrm{L}_0}{\partial \dot{q}(0,t)}\right) - \left[\frac{\partial \hat{\mathrm{L}}}{\partial q'} - \frac{\partial}{\partial x}\left(\frac{\partial \hat{\mathrm{L}}}{\partial q''}\right) - \frac{\partial}{\partial t}\left(\frac{\partial \hat{\mathrm{L}}}{\partial \dot{q}'}\right)\right]\Bigg|_{x=0} = 0$$

where:

$$\begin{aligned}
\frac{\partial \mathrm{L}_0}{\partial \theta(0,t)} &= 0 \\
\frac{\partial \mathrm{L}_0}{\partial \dot{\theta}(0,t)} &= \mathrm{J}_m\dot{\theta}(0,t) \\
\frac{\partial}{\partial t}\left(\frac{\partial \mathrm{L}_0}{\partial \dot{\theta}(0,t)}\right) &= \mathrm{J}_m\ddot{\theta}(0,t) \\
\frac{\partial \hat{\mathrm{L}}}{\partial \theta'} &= -\mathrm{GJ}(x)\theta'(x,t) \\
\frac{\partial \hat{\mathrm{L}}}{\partial \theta''} &= 0 \\
\frac{\partial}{\partial x}\left(\frac{\partial \hat{\mathrm{L}}}{\partial \theta''}\right) &= 0 \\
\frac{\partial \hat{\mathrm{L}}}{\partial \dot{\theta}'} &= 0 \\
\frac{\partial}{\partial t}\left(\frac{\partial \hat{\mathrm{L}}}{\partial \dot{\theta}'}\right) &= 0
\end{aligned}$$

thus:

$$\mathrm{GJ}(x)\theta'(0,t) = \mathrm{J}_m\ddot{\theta}(0,t) \tag{B.8}$$

Similarly, the Boundary Condition at x=L can be determined via:

$$\frac{\partial \mathrm{L}_\mathrm{L}}{\partial q(\mathrm{L},t)} - \frac{\partial}{\partial t}\left(\frac{\partial \mathrm{L}_\mathrm{L}}{\partial \dot{q}(\mathrm{L},t)}\right) + \left[\frac{\partial \hat{\mathrm{L}}}{\partial q'} - \frac{\partial}{\partial x}\left(\frac{\partial \hat{\mathrm{L}}}{\partial q''}\right) - \frac{\partial}{\partial t}\left(\frac{\partial \hat{\mathrm{L}}}{\partial \dot{q}'}\right)\right]\Bigg|_{x=\mathrm{L}} = 0$$

where:

$$\begin{aligned}
\frac{\partial \mathrm{L_L}}{\partial \theta(\mathrm{L},t)} &= 0 \\
\frac{\partial \mathrm{L_L}}{\partial \dot{\theta}(\mathrm{L},t)} &= \mathrm{J}_l \dot{\theta}(\mathrm{L},t) \\
\frac{\partial}{\partial t}\left(\frac{\partial \mathrm{L_L}}{\partial \dot{\theta}(\mathrm{L},t)}\right) &= \mathrm{J}_l \ddot{\theta}(\mathrm{L},t) \\
\frac{\partial \hat{\mathrm{L}}}{\partial \theta'} &= -\mathrm{GJ}(x)\theta'(x,t) \\
\frac{\partial \hat{\mathrm{L}}}{\partial \theta''} &= 0 \\
\frac{\partial}{\partial x}\left(\frac{\partial \hat{\mathrm{L}}}{\partial \theta''}\right) &= 0 \\
\frac{\partial \hat{\mathrm{L}}}{\partial \dot{\theta}'} &= 0 \\
\frac{\partial}{\partial t}\left(\frac{\partial \hat{\mathrm{L}}}{\partial \dot{\theta}'}\right) &= 0
\end{aligned}$$

thus:

$$\mathrm{GJ}(x)\theta'(\mathrm{L},t) = -\mathrm{J}_l \ddot{\theta}(\mathrm{L},t) \tag{B.9}$$

Equation (B.7) is the partial differential equation of motion for the continuous model of the system shown in Figure 2.1. Equations (B.8) and (B.9) are the boundary conditions at x=0 and x=L respectively. Equations (B.7), (B.8) and (B.9) together represent the boundary value problem for the continuous model of the system shown in Figure 2.1.

In order to determine the natural frequencies of the continuous model, the boundary-value problem represented by Equations (B.7), (B.8) and (B.9) must be solved. The solution of such a boundary-value problem requires the solution of an associated differential eigenvalue problem consisting of an infinite set of eigenvalues and eigenfunctions. However, the eigenvalue problem of the continuous model must first be derived before it can be solved. To derive the eigenvalue problem, first let the distributed torque $\mathrm{F}_\theta$ in Equation

(B.7) equal 0 – so that the transmission shaft is in free vibration:

$$\frac{\partial}{\partial x}\left(\mathrm{GJ}(x)\theta'(x,t)\right) = \mathrm{I}(x)\ddot{\theta}(x,t),\ 0 < x < \mathrm{L} \tag{B.10}$$

Hence, the free vibration of the transmission shaft is described by Equation (B.10) and the boundary conditions of Equations (B.8) and (B.9). Now assume a solution in the form:

$$\begin{aligned} \theta(x,t) &= \Theta(x)\mathrm{F}(t) \qquad \text{(B.11)} \end{aligned}$$

where $\mathrm{F}(t)$ is harmonic and satisfies :

$$\begin{aligned} \ddot{\mathrm{F}}(t) &= -\lambda \mathrm{F}(t) \qquad \text{(B.12)} \\ \lambda &= \omega^2 \ (\omega \text{ is the frequency of oscillation}) \end{aligned}$$

Substituting Equations (B.11) and (B.12) into (B.10):

$$\begin{aligned} \frac{\partial}{\partial x}\left(\mathrm{GJ}(x)\frac{\partial}{\partial x}(\Theta(x)\mathrm{F}(t))\right) &= \mathrm{I}(x)\frac{\partial^2}{\partial t^2}(\Theta(x)\mathrm{F}(t)),\ 0 < x < \mathrm{L} \\ \Rightarrow \mathrm{F}(t)\frac{d}{dx}\left(\mathrm{GJ}(x)\Theta'(x)\right) &= \mathrm{I}(x)\Theta(x)\ddot{\mathrm{F}}(t),\ 0 < x < \mathrm{L} \\ \Rightarrow \mathrm{F}(t)\frac{d}{dx}\left(\mathrm{GJ}(x)\Theta'(x)\right) &= -\mathrm{I}(x)\Theta(x)\lambda\mathrm{F}(t),\ 0 < x < \mathrm{L} \\ \Rightarrow \frac{d}{dx}\left(\mathrm{GJ}(x)\Theta'(x)\right) &= -\lambda\mathrm{I}(x)\Theta(x),\ 0 < x < \mathrm{L} \qquad \text{(B.13)} \end{aligned}$$

Substituting Equations (B.11) and (B.12) into (B.8):

$$\begin{aligned} \mathrm{GJ}(x)\frac{\partial}{\partial x}(\Theta(0)\mathrm{F}(t)) &= \mathrm{J}_m\frac{\partial^2}{\partial t^2}(\Theta(0),\mathrm{F}(t)) \\ \Rightarrow \mathrm{F}(t)\mathrm{GJ}(x)\Theta'(0) &= \mathrm{J}_m\Theta(0)\ddot{\mathrm{F}}(t) \\ \Rightarrow \mathrm{F}(t)\mathrm{GJ}(x)\Theta'(0) &= -\mathrm{J}_m\Theta(0)\lambda\mathrm{F}(t) \\ \Rightarrow \mathrm{GJ}(x)\Theta'(0) &= -\lambda\mathrm{J}_m\Theta(0) \qquad \text{(B.14)} \end{aligned}$$

And Substituting Equations (B.11) and (B.12) into (B.9):

$$\begin{aligned} \mathrm{GJ}(x)\frac{\partial}{\partial x}(\Theta(\mathrm{L})\mathrm{F}(t)) &= -\mathrm{J}_l\frac{\partial^2}{\partial t^2}(\Theta(\mathrm{L}),\mathrm{F}(t)) \\ \Rightarrow \mathrm{F}(t)\mathrm{GJ}(x)\Theta'(\mathrm{L}) &= -\mathrm{J}_l\Theta(\mathrm{L})\ddot{\mathrm{F}}(t) \\ \Rightarrow \mathrm{F}(t)\mathrm{GJ}(x)\Theta'(\mathrm{L}) &= \mathrm{J}_l\Theta(\mathrm{L})\lambda\mathrm{F}(t) \\ \Rightarrow \mathrm{GJ}(x)\Theta'(\mathrm{L}) &= \lambda\mathrm{J}_l\Theta(\mathrm{L}) \end{aligned} \tag{B.15}$$

Now, assuming that the transmission shaft is uniform (ie GJ($x$) and I($x$) are constants), Equation (B.13) becomes:

$$\begin{aligned} \mathrm{GJ}\Theta''(x) &= -\lambda\mathrm{I}\Theta(x),\ 0<x<\mathrm{L} \\ \Rightarrow \Theta''(x)+\frac{\lambda\mathrm{I}}{\mathrm{GJ}}\Theta(x) &= 0 \\ \Rightarrow \Theta''(x)+\beta^2\Theta(x) &= 0 \end{aligned} \tag{B.16}$$

$$\text{where } \beta^2 = \frac{\lambda\mathrm{I}}{\mathrm{GJ}} = \frac{\omega^2\mathrm{I}}{\mathrm{GJ}} \tag{B.17}$$

Similarly, Equation (B.14) becomes:

$$\begin{aligned} \Theta'(0)+\frac{\lambda\mathrm{J}_m}{\mathrm{GJ}}\Theta(0) &= 0 \\ \Rightarrow \Theta'(0)+\frac{\beta^2\mathrm{J}_m}{\mathrm{I}}\Theta(0) &= 0 \end{aligned} \tag{B.18}$$

And, Equation (B.15) becomes:

$$\begin{aligned} \Theta'(\mathrm{L})-\frac{\lambda\mathrm{J}_l}{\mathrm{GJ}}\Theta(\mathrm{L}) &= 0 \\ \Rightarrow \Theta'(\mathrm{L})-\frac{\beta^2\mathrm{J}_l}{\mathrm{I}}\Theta(\mathrm{L}) &= 0 \end{aligned} \tag{B.19}$$

Now, Equation (B.16) has the solution:

$$\Theta(x) = \mathrm{C}_1\sin\beta x+\mathrm{C}_2\cos\beta x \tag{B.20}$$

Hence, the boundary condition given by Equation (B.18) leads to:

$$\begin{aligned} C_1\beta\cos 0 - C_2\beta\sin 0 + \frac{\beta^2 J_m}{I}(C_1\sin 0 + C_2\cos 0) &= 0 \\ \Rightarrow C_1\beta + \frac{C_2\beta^2 J_m}{I} &= 0 \\ \Rightarrow C_1 &= -\frac{C_2\beta J_m}{I} \end{aligned} \tag{B.21}$$

And the boundary condition given by Equation (B.19) leads to:

$$\begin{aligned} C_1\beta\cos\beta L - C_2\beta\sin\beta L - \frac{\beta^2 J_l}{I}(C_1\sin\beta L + C_2\cos\beta L) &= 0 \\ \Rightarrow \cos\beta L\left(\frac{C_1\beta I - C_2\beta^2 J_l}{I}\right) &= \sin\beta L\left(\frac{C_2\beta I + C_1\beta^2 J_l}{I}\right) \\ \Rightarrow \tan\beta L &= \frac{C_1 I - C_2\beta J_l}{C_2 I + C_1\beta J_l} \end{aligned} \tag{B.22}$$

Substituting Equation (B.21) into Equation (B.22):

$$\begin{aligned} \tan\beta L &= \frac{\left(-\frac{C_2\beta J_m}{I}\right) I - C_2\beta J_l}{C_2 I + \left(-\frac{C_2\beta J_m}{I}\right)\beta J_l} \\ &= -\frac{\beta(J_m + J_l)}{I - \frac{\beta^2 J_m J_l}{I}} \end{aligned} \tag{B.23}$$

Equation (B.23) is the characteristic equation of the continuous model and must be solved numerically for $\beta$.

## B.3 Internal Damping in a Transmission Element

Equations (2.7) and (2.8) are the equations of motion for the two-body model of a simple motor-transmission-load system, where the only damping in the system is the inherent internal damping of the transmission element. Using the Laplace transform a transfer

function for this system with flex as output can be obtained:

$$\begin{aligned}
J_m s^2 \theta_m &= T_m - K_s(\theta_m - \theta_l) - C_s(s\theta_m - s\theta_l) \\
J_l s^2 \theta_l &= K_s(\theta_m - \theta_l) + C_s(s\theta_m - s\theta_l) \\
\text{Hence: } J_m J_l s^2(\theta_m - \theta_l) &= J_l T_m - C_s s(J_m + J_l)(\theta_m - \theta_l) - K_s(J_m + J_l)(\theta_m - \theta_l) \\
\text{And: } \frac{\theta_m - \theta_l}{T_m} &= \frac{J_l}{J_m J_l s^2 + C_s(J_m + J_l)s + K_s(J_m + J_l)} \\
&= \frac{\frac{1}{J_m}}{s^2 + \frac{C_s(J_m + J_l)}{J_m J_l}s + \frac{K_s(J_m + J_l)}{J_m J_l}}
\end{aligned} \tag{B.24}$$

If Equation (B.24) is equated with the standard form of a 2nd order system, expressions for damping ratio and natural frequency can be obtained:

$$\begin{aligned}
\omega_n &= \sqrt{\frac{K_s(J_m + J_l)}{J_m J_l}} \\
2\zeta\omega_n &= \frac{C_s(J_m + J_l)}{J_m J_l} \\
\text{and: } \zeta &= \frac{C_s}{2}\sqrt{\frac{(J_m + J_l)}{J_m J_l K_s}}
\end{aligned}$$

When levels of damping are low, the loss factor of a material is considered to be double the damping ratio:

$$\eta = 2\zeta$$

Hence, for low levels of damping the internal damping coefficient of a transmission shaft can be expressed as:

$$C_s = \eta\sqrt{\frac{J_m J_l K_s}{(J_m + J_l)}} \tag{B.25}$$

## B.4 Derivation of Describing Function for New Backlash Model

Consider first Equation (7.9). After performing the integration:

$$\begin{aligned}
A_1 &= \frac{K_s}{\pi}\left(\frac{X}{2}\sin^2(\omega t)-\alpha\sin(\omega t)\right)|_{\omega t_1}^{\omega t_2}+\frac{C_s X\omega}{\pi}\left(\frac{1}{2}\sin(\omega t)\cos(\omega t)+\frac{\omega t}{2}\right)|_{\omega t_1}^{\omega t_2}\\
&\quad+\frac{K_s}{\pi}\left(\frac{X}{2}\sin^2(\omega t)+\alpha\sin(\omega t)\right)|_{\pi+\omega t_1}^{\pi+\omega t_2}+\frac{C_s X\omega}{\pi}\left(\frac{1}{2}\sin(\omega t)\cos(\omega t)+\frac{\omega t}{2}\right)|_{\pi+\omega t_1}^{\pi+\omega t_2}\\
&= \frac{K_s X}{2\pi}\left(\sin^2(\omega t_2)-\sin^2(\omega t_1)\right)-\frac{K_s\alpha}{\pi}\left(\sin(\omega t_2)-\sin(\omega t_1)\right)\\
&\quad+\frac{C_s X\omega}{2\pi}\left(\sin(\omega t_2)\cos(\omega t_2)+\omega t_2-\sin(\omega t_1)\cos(\omega t_1)-\omega t_1\right)\\
&\quad+\frac{K_s X}{2\pi}\left(\left(\sin\pi\cos(\omega t_2)+\cos\pi\sin(\omega t_2)\right)^2-\left(\sin\pi\cos(\omega t_1)+\cos\pi\sin(\omega t_1)\right)^2\right)\\
&\quad+\frac{K_s\alpha}{\pi}\left(\left(\sin\pi\cos(\omega t_2)+\cos\pi\sin(\omega t_2)\right)-\left(\sin\pi\cos(\omega t_1)+\cos\pi\sin(\omega t_1)\right)\right)\\
&\quad+\frac{C_s X\omega}{2\pi}\left(\left(\sin\pi\cos(\omega t_2)+\cos\pi\sin(\omega t_2)\right)\left(\cos\pi\cos(\omega t_2)-\sin\pi\sin(\omega t_2)\right)+\omega t_2\right)\\
&\quad-\frac{C_s X\omega}{2\pi}\left(\left(\sin\pi\cos(\omega t_1)+\cos\pi\sin(\omega t_1)\right)\left(\cos\pi\cos(\omega t_1)-\sin\pi\sin(\omega t_1)\right)+\omega t_1\right)\\
&= \frac{K_s X}{2\pi}\left(\sin^2(\omega t_2)-\sin^2(\omega t_1)\right)-\frac{K_s\alpha}{\pi}\left(\sin(\omega t_2)-\sin(\omega t_1)\right)\\
&\quad+\frac{C_s X\omega}{2\pi}\left(\sin(\omega t_2)\cos(\omega t_2)+\omega t_2-\sin(\omega t_1)\cos(\omega t_1)-\omega t_1\right)\\
&\quad+\frac{K_s X}{2\pi}\left(\sin^2(\omega t_2)-\sin^2(\omega t_1)\right)+\frac{K_s\alpha}{\pi}\left(-\sin(\omega t_2)+\sin(\omega t_1)\right)\\
&\quad+\frac{C_s X\omega}{2\pi}\left(\sin(\omega t_2)\cos(\omega t_2)+\omega t_2-\sin(\omega t_1)\cos(\omega t_1)-\omega t_1\right)\\
&= \frac{K_s X}{\pi}\left(\sin^2(\omega t_2)-\sin^2(\omega t_1)\right)-\frac{2K_s\alpha}{\pi}\left(\sin(\omega t_2)-\sin(\omega t_1)\right)\\
&\quad+\frac{C_s X\omega}{\pi}\left(\sin(\omega t_2)\cos(\omega t_2)+\omega t_2-\sin(\omega t_1)\cos(\omega t_1)-\omega t_1\right) \qquad \text{(B.26)}
\end{aligned}$$

Consider also Equation (7.10). After performing the integration:

$$\begin{aligned}
B_1 &= \frac{K_s}{\pi}\left(\frac{X}{2}\left(\omega t-\sin(\omega t)\cos(\omega t)\right)+\alpha\cos(\omega t)\right)|_{\omega t_1}^{\omega t_2}+\frac{C_s X\omega}{\pi}\left(\frac{1}{2}\sin^2(\omega t)\right)|_{\omega t_1}^{\omega t_2}\\
&\quad+\frac{K_s}{\pi}\left(\frac{X}{2}\left(\omega t-\sin(\omega t)\cos(\omega t)\right)-\alpha\cos(\omega t)\right)|_{\pi+\omega t_1}^{\pi+\omega t_2}+\frac{C_s X\omega}{\pi}\left(\frac{1}{2}\sin^2(\omega t)\right)|_{\pi+\omega t_1}^{\pi+\omega t_2}\\
&= \frac{K_s X}{2\pi}\left(\omega t_2-\sin(\omega t_2)\cos(\omega t_2)-\omega t_1+\sin(\omega t_1)\cos(\omega t_1)\right)\\
&\quad+\frac{K_s\alpha}{\pi}\left(\cos(\omega t_2)-\cos(\omega t_1)\right)+\frac{C_s X\omega}{2\pi}\left(\sin^2(\omega t_2)-\sin^2(\omega t_1)\right)\\
&\quad+\frac{K_s X}{2\pi}\left(\omega t_2-\left(\sin\pi\cos(\omega t_2)+\cos\pi\sin(\omega t_2)\right)\left(\cos\pi\cos(\omega t_2)-\sin\pi\sin(\omega t_2)\right)\right)\\
&\quad-\frac{K_s X}{2\pi}\left(\omega t_1-\left(\sin\pi\cos(\omega t_1)+\cos\pi\sin(\omega t_1)\right)\left(\cos\pi\cos(\omega t_1)-\sin\pi\sin(\omega t_1)\right)\right)\\
&\quad-\frac{K_s\alpha}{\pi}\left(\left(\cos\pi\cos(\omega t_2)-\sin\pi\sin(\omega t_2)\right)-\left(\cos\pi\cos(\omega t_1)-\sin\pi\sin(\omega t_1)\right)\right)
\end{aligned}$$

$$
\begin{aligned}
& + \frac{C_s X \omega}{2\pi} \left( (\sin\pi\cos(\omega t_2) + \cos\pi\sin(\omega t_2))^2 - (\sin\pi\cos(\omega t_1) + \cos\pi\sin(\omega t_1))^2 \right) \\
= \quad & \frac{K_s X}{2\pi} (\omega t_2 - \sin(\omega t_2)\cos(\omega t_2) - \omega t_1 + \sin(\omega t_1)\cos(\omega t_1)) \\
& + \frac{K_s \alpha}{\pi} (\cos(\omega t_2) - \cos(\omega t_1)) + \frac{C_s X \omega}{2\pi} \left( \sin^2(\omega t_2) - \sin^2(\omega t_1) \right) \\
& + \frac{K_s X}{2\pi} (\omega t_2 - \sin(\omega t_2)\cos(\omega t_2) - \omega t_1 + \sin(\omega t_1)\cos(\omega t_1)) \\
& - \frac{K_s \alpha}{\pi} (-\cos(\omega t_2) + \cos(\omega t_1)) + \frac{C_s X \omega}{2\pi} \left( \sin^2(\omega t_2) - \sin^2(\omega t_1) \right) \\
= \quad & \frac{K_s X}{\pi} (\omega t_2 - \sin(\omega t_2)\cos(\omega t_2) - \omega t_1 + \sin(\omega t_1)\cos(\omega t_1)) \\
& + \frac{2K_s \alpha}{\pi} (\cos(\omega t_2) - \cos(\omega t_1)) + \frac{C_s X \omega}{\pi} \left( \sin^2(\omega t_2) - \sin^2(\omega t_1) \right) \qquad \text{(B.27)}
\end{aligned}
$$

Note that Equations (B.26) and (B.27) are both functions of $\omega t_1$ and $\omega t_2$. Hence, the values of $\omega t_1$ and $\omega t_2$ are required to find a solution to $A_1$ and $B_1$. From Figure 7.2 it can be seen that $\omega t_1$ represents the point where the system enters the *right contact* state. Since $\dot{\theta}_d > 0$ at $\omega t_1$, the transition into the *right contact* state occurs when $\theta_d = \alpha$ (see Equation (3.32)). Hence, at $\omega t_1$:

$$X \sin(\omega t_1) = \alpha$$

and:

$$\omega t_1 = \sin^{-1}\left(\frac{\alpha}{X}\right) \qquad \text{(B.28)}$$

Also, from Figure 7.2 it can be seen that $\omega t_2$ represents the point where the system leaves the *right contact* state and enters the backlash region. Since $\dot{\theta}_d < 0$ at $\omega t_2$, the transition into the backlash region occurs when $K_s(\theta_d - \alpha) + C_s\dot{\theta}_d = 0$ (see Equation (3.32)). Hence, at $\omega t_2$:

$$K_s(X\sin(\omega t_2) - \alpha) + C_s X \omega \cos(\omega t_2) = 0 \qquad \text{(B.29)}$$

Now, let $T = \tan\left(\frac{\omega t_2}{2}\right)$. Hence, from the Half Angle Tangent Formula:

$$\sin(\omega t_2) = \frac{2T}{1+T^2} \qquad \text{(B.30)}$$

$$\cos(\omega t_2) = \frac{1-T^2}{1+T^2} \qquad \text{(B.31)}$$

Substituting Equations (B.30) and (B.31) into Equation (B.29):

$$\begin{aligned} \mathrm{K}_s\left(\frac{2XT}{1+T^2}-\alpha\right)+\frac{\mathrm{C}_s X\omega\left(1-T^2\right)}{(1+T^2)} &= 0 \\ \therefore \mathrm{K}_s 2XT-\mathrm{K}_s\alpha-\mathrm{K}_s\alpha T^2+\mathrm{C}_s X\omega-\mathrm{C}_s X\omega T^2 &= 0 \\ \text{and } \left(\mathrm{K}_s\alpha+\mathrm{C}_s X\omega\right)T^2-2\mathrm{K}_s XT+\left(\mathrm{K}_s\alpha-\mathrm{C}_s X\omega\right) &= 0 \end{aligned}$$

Applying the Quadratic Formula:

$$\begin{aligned} T &= \frac{2\mathrm{K}_s X\pm\sqrt{4\mathrm{K}_s^2X^2-4\left(\mathrm{K}_s\alpha+\mathrm{C}_s X\omega\right)\left(\mathrm{K}_s\alpha-\mathrm{C}_x X\omega\right)}}{2\left(K_s\alpha+C_s X\omega\right)} \\ &= \frac{\mathrm{K}_s X\pm\sqrt{\mathrm{K}_s^2X^2-\mathrm{K}_s^2\alpha^2+\mathrm{C}_s^2X^2\omega^2}}{\mathrm{K}_s\alpha+\mathrm{C}_s X\omega} \\ &= \frac{1\pm\sqrt{1-\frac{\alpha^2}{X^2}+\frac{\mathrm{C}_s^2\omega^2}{\mathrm{K}_s^2}}}{\frac{\alpha}{X}+\frac{\mathrm{C}_s\omega}{\mathrm{K}_s}} \end{aligned}$$

Hence:

$$\omega t_2 = 2\tan^{-1}\left(\frac{1\pm\sqrt{1-\frac{\alpha^2}{X^2}+\frac{\mathrm{C}_s^2\omega^2}{\mathrm{K}_s^2}}}{\frac{\alpha}{X}+\frac{\mathrm{C}_s\omega}{\mathrm{K}_s}}\right)$$

Recall that at $\omega t_2$, $\theta_d > 0$ and $\dot{\theta}_d < 0$. Hence, $\sin(\omega t_2) > 0$ and $\cos(\omega t_2) < 0$. From Equations (B.30) and (B.31):

$$\begin{aligned} \frac{2T}{1+T^2} &> 0 \\ \therefore T &> 0 \\ \frac{1-T^2}{1+T^2} &< 0 \\ \therefore T^2 &> 1 \end{aligned}$$

Hence, $T$ must be greater than 1 at $\omega t_2$. Checking this for the first solution of $T$:

$$\begin{aligned}
\frac{1+\sqrt{1-\frac{\alpha^2}{X^2}+\frac{C_s^2\omega^2}{K_s^2}}}{\frac{\alpha}{X}+\frac{C_s\omega}{K_s}} &> 1 \\
\therefore 1+\sqrt{1-\frac{\alpha^2}{X^2}+\frac{C_s^2\omega^2}{K_s^2}} &> \frac{\alpha}{X}+\frac{C_s\omega}{K_s} \\
\text{and } \left(1-\frac{\alpha}{X}\right)+\left(\sqrt{1-\frac{\alpha^2}{X^2}+\frac{C_s^2\omega^2}{K_s^2}}-\frac{C_s\omega}{K_s^2}\right) &> 0
\end{aligned} \tag{B.32}$$

Since the describing function solution is only valid when $\alpha < X$, Equation (B.32) is always true. Note that when $\alpha > X$, the value of the describing function is zero. Checking also the second solution of $T$:

$$\begin{aligned}
\frac{1-\sqrt{1-\frac{\alpha^2}{X^2}+\frac{C_s^2\omega^2}{K_s^2}}}{\frac{\alpha}{X}+\frac{C_s\omega}{K_s}} &> 1 \\
\therefore 1-\sqrt{1-\frac{\alpha^2}{X^2}+\frac{C_s^2\omega^2}{K_s^2}} &> \frac{\alpha}{X}+\frac{C_s\omega}{K_s} \\
\text{and } 1-\frac{\alpha}{X}-\frac{C_s\omega}{K_s} &> \sqrt{1-\frac{\alpha^2}{X^2}+\frac{C_s^2\omega^2}{K_s^2}}
\end{aligned} \tag{B.33}$$

Now, since $\alpha < X$ the right hand side of Equation (B.33) is always real and positive. Hence, the left hand side of Equation (B.33) must also be positive and it is possible to square both sides:

$$\begin{aligned}
1-\frac{\alpha}{X}-\frac{C_s\omega}{K_s}-\frac{\alpha}{X}+\frac{\alpha^2}{X^2}+\frac{\alpha C_s\omega}{XK_s}-\frac{C_s\omega}{K_s}+\frac{\alpha C_s\omega}{XK_s}+\frac{C_s^2\omega^2}{K_s^2} &> 1-\frac{\alpha^2}{X^2}+\frac{C_s^2\omega^2}{K_s^2} \\
\therefore \frac{2\alpha^2}{X^2}-\frac{2\alpha}{X}-\frac{2C_s\omega}{K_s}+\frac{2\alpha C_s\omega}{XK_s} &> 0 \\
\frac{\alpha}{X}\left(\frac{\alpha}{X}+\frac{C_s\omega}{XK_s}\right) &> \frac{\alpha}{X}+\frac{C_s\omega}{K_s} \\
\text{and } \frac{\alpha}{X} &> 1
\end{aligned} \tag{B.34}$$

Note that Equation (B.34) is never true. Hence, there is only one true solution to $T$, and:

$$\omega t_2 = 2\tan^{-1}\left(\frac{1+\sqrt{1-\frac{\alpha^2}{X^2}+\frac{C_s^2\omega^2}{K_s^2}}}{\frac{\alpha}{X}+\frac{C_s\omega}{K_s}}\right) \tag{B.35}$$

Equations (B.26) and (B.27) can now be re-written using the values of $\omega t_1$ and $\omega t_2$:

$$\begin{aligned}
A_1 &= \frac{K_s X}{\pi}\left(\left(\frac{2T}{1+T^2}\right)^2-\sin^2\left(\sin^{-1}\left(\frac{\alpha}{X}\right)\right)\right)-\frac{2K_s\alpha}{\pi}\left(\frac{2T}{1+T^2}-\sin\left(\sin^{-1}\left(\frac{\alpha}{X}\right)\right)\right)\\
&\quad+\frac{C_s X\omega}{\pi}\left(\left(\frac{2T}{1+T^2}\right)\left(\frac{1-T^2}{1+T^2}\right)+2\tan^{-1}(T)\right)\\
&\quad-\frac{C_s X\omega}{\pi}\left(\sin\left(\sin^{-1}\left(\frac{\alpha}{X}\right)\right)\cos\left(\sin^{-1}\left(\frac{\alpha}{X}\right)\right)+\sin^{-1}\left(\frac{\alpha}{X}\right)\right)\\
&= \frac{K_s X}{\pi}\left(\left(\frac{2T}{1+T^2}\right)^2-\left(\frac{\alpha}{X}\right)^2\right)-\frac{2K_s\alpha}{\pi}\left(\frac{2T}{1+T^2}-\frac{\alpha}{X}\right)\\
&\quad+\frac{C_s X\omega}{\pi}\left(\frac{2T\left(1-T^2\right)}{\left(1+T^2\right)^2}+2\tan^{-1}(T)-\frac{\alpha}{X}\sqrt{1-\left(\frac{\alpha}{X}\right)^2}-\sin^{-1}\left(\frac{\alpha}{X}\right)\right)
\end{aligned} \tag{B.36}$$

$$\begin{aligned}
B_1 &= \frac{K_s X}{\pi}\left(2\tan^{-1}(T)-\left(\frac{2T}{1+T^2}\right)\left(\frac{1-T^2}{1+T^2}\right)\right)\\
&\quad-\frac{K_s X}{\pi}\left(\sin^{-1}\left(\frac{\alpha}{X}\right)-\sin\left(\sin^{-1}\left(\frac{\alpha}{X}\right)\right)\cos\left(\sin^{-1}\left(\frac{\alpha}{X}\right)\right)\right)\\
&\quad+\frac{2K_s\alpha}{\pi}\left(\left(\frac{1-T^2}{1+T^2}\right)-\cos\left(\sin^{-1}\left(\frac{\alpha}{X}\right)\right)\right)+\frac{C_s X\omega}{\pi}\left(\left(\frac{2T}{1+T^2}\right)^2-\sin^2\left(\sin^{-1}\left(\frac{\alpha}{X}\right)\right)\right)\\
&= \frac{K_s X}{\pi}\left(2\tan^{-1}(T)-\frac{2T\left(1-T^2\right)}{\left(1+T^2\right)^2}-\sin^{-1}\left(\frac{\alpha}{X}\right)+\frac{\alpha}{X}\sqrt{1-\left(\frac{\alpha}{X}\right)^2}\right)\\
&\quad+\frac{2K_s\alpha}{\pi}\left(\left(\frac{1-T^2}{1+T^2}\right)-\sqrt{1-\left(\frac{\alpha}{X}\right)^2}\right)+\frac{C_s X\omega}{\pi}\left(\left(\frac{2T}{1+T^2}\right)^2-\left(\frac{\alpha}{X}\right)^2\right)
\end{aligned} \tag{B.37}$$

Now, consider the case where $C_s = 0$:

$$\begin{aligned}
T &= \frac{1+\sqrt{1-\frac{\alpha^2}{X^2}}}{\frac{\alpha}{X}}\\
T^2 &= \frac{2+2\sqrt{1-\frac{\alpha^2}{X^2}}-\frac{\alpha^2}{X^2}}{\frac{\alpha^2}{X^2}}\\
1+T^2 &= \frac{2+2\sqrt{1-\frac{\alpha^2}{X^2}}}{\frac{\alpha^2}{X^2}}\\
1-T^2 &= \frac{2\frac{\alpha^2}{X^2}-\left(2+2\sqrt{1-\frac{\alpha^2}{X^2}}\right)}{\frac{\alpha^2}{X^2}}
\end{aligned}$$

$$\frac{2T}{1+T^2} = \frac{\alpha}{X} \tag{B.38}$$

$$\frac{1-T^2}{1+T^2} = -\sqrt{1-\frac{\alpha^2}{X^2}} \tag{B.39}$$

Hence, from Equations (B.30), (B.31), (B.38) and (B.39):

$$\begin{aligned} \sin(\omega t_2) &= \frac{\alpha}{X} \\ \cos(\omega t_2) &= -\sqrt{1-\frac{\alpha^2}{X^2}} \\ \therefore\ \omega t_2 &= \pi - \sin^{-1}\left(\frac{\alpha}{X}\right) \\ \text{and } 2\tan^{-2}(T) &= \pi - \sin^{-1}\left(\frac{\alpha}{X}\right) \end{aligned} \tag{B.40}$$

If Equations (B.38), (B.39) and (B.40) are then substituted into Equations (B.36) and (B.37) (with $C_s = 0$):

$$\begin{aligned} A_1 &= \frac{K_s X}{\pi}\left(\left(\frac{\alpha}{X}\right)^2 - \left(\frac{\alpha}{X}\right)^2\right) - \frac{2K_s\alpha}{\pi}\left(\frac{\alpha}{X} - \frac{\alpha}{X}\right) \\ &= 0 \\ B_1 &= \frac{K_s X}{\pi}\left(\pi - \sin^{-1}\left(\frac{\alpha}{X}\right) + \frac{\alpha}{X}\sqrt{1-\left(\frac{\alpha}{X}\right)^2} - \sin^{-1}\left(\frac{\alpha}{X}\right) + \frac{\alpha}{X}\sqrt{1-\left(\frac{\alpha}{X}\right)^2}\right) \\ &\quad + \frac{2K_s\alpha}{\pi}\left(-\sqrt{1-\left(\frac{\alpha}{X}\right)^2} - \sqrt{1-\left(\frac{\alpha}{X}\right)^2}\right) \\ &= \frac{2K_s X}{\pi}\left[\frac{\pi}{2} - \sin^{-1}\left(\frac{\alpha}{X}\right) - \left(\frac{\alpha}{X}\right)\sqrt{1-\left(\frac{\alpha}{X}\right)^2}\right] \end{aligned}$$

Hence, it can be seen that when $C_s = 0$ the describing function of the new backlash model reduces to that of the standard dead zone model (which is given by Equations (7.6) and (7.7)).

Appendix C

# Matlab Code

## C.1 Code for Natural Frequency Calculations

The mathematics package 'Matlab' was used to automate the numerical methods and calculate the various natural frequencies for the continuous model and the approximate models compared in Section 3.2.3. The code for each of the Matlab functions developed for this task is given in this appendix. The functions "distribute_inertia" and "distribute_inertia_chareq" were used to determine the natural frequencies of the continuous model. The functions "multi_body_freq" and "holzer" were used to determine the natural frequencies of the multiple body approximate models.

### Function: distribute_inertia

```
function [freq] = distribute_inertia(motor_inertia,load_inertia,shaft_diameter,shaft_length,freq_estimate)
% [freq] = distribute_inertia(motor_inertia,load_inertia,shaft_diameter,shaft_length,freq_estimate)
%
GJ = (80e9*pi*shaft_diameter^4)/32;
I = (pi*(shaft_diameter/2)^4*8000)/2;
Ks = GJ/shaft_length
orig_ks = Ks
ShI = I*shaft_length
```

```
Ir = motor_inertia/load_inertia;

mI = (motor_inertia/(motor_inertia+load_inertia))*ShI;

lI = (load_inertia/(motor_inertia+load_inertia))*ShI;

mshL = (motor_inertia/(motor_inertia+load_inertia))*shaft_length;

lshL = (load_inertia/(motor_inertia+load_inertia))*shaft_length;

beta(1) = 0;

chareq_left(1) = 0;

chareq_right(1) = 0;

chareq(1) = chareq_left(1) - chareq_right(1);

freq_plot(1) = 0;

for index=2:1000,

beta(index) = beta(index-1) + (pi/(250*shaft_length));

[chl,chr,chq,dchq] = distribute_inertia_chareq(motor_inertia,load_inertia,I,shaft_length,beta(index));

chareq_left(index) = chl;

if chareq_left(index) > 20

chareq_left(index) = 20;

elseif chareq_left(index) < -20

chareq_left(index) = -20;

end

chareq_right(index) = chr;

if chareq_right(index) > 20

chareq_right(index) = 20;

elseif chareq_right(index) < -20

chareq_right(index) = -20;

end

chareq(index) = chareq_left(index)-chareq_right(index);

freq_plot(index) = beta(index)*sqrt(GJ/I);

end

plot(freq_plot,chareq);

freq = freq_estimate*sqrt(I/GJ);

beta_estimate = freq + 10;

while abs((beta_estimate - freq)) > 0.0001

beta_estimate = freq;
```

```
[chl,chr,chq,dchq] = distribute_inertia_chareq(motor_inertia,load_inertia,I,shaft_length,beta_estimate);

freq = beta_estimate - chq/dchq;

end

disp('The natural frequency for two-body model with negligible shaft inertia is:');

wn1 = sqrt((Ks*(1+load_inertia/motor_inertia))/(load_inertia));

disp('The natural frequency for two-body model with shaft inertia equally lumped at motor and load is:');

motor_new = motor_inertia + ShI/2;

load_new = load_inertia+ ShI/2;

wn2 = sqrt((Ks*(1+load_new/motor_new))/(load_new));

disp('The natural frequency for two-body model with shaft inertia lumped at motor is:');

motor_new = motor_inertia + ShI;

load_new = load_inertia;

wn3 = sqrt((Ks*(1+load_new/motor_new))/(load_new));

disp('The natural frequency for two-body model with shaft inertia lumped at load is:');

motor_new = motor_inertia;

load_new = load_inertia + ShI;

wn4 = sqrt((Ks*(1+load_new/motor_new))/(load_new));

disp('The natural frequency for two-body model with shaft inertia split and lumped at motor and load while maintaining Inertia ratio is:');

motor_new = motor_inertia+mI;

load_new = load_inertia + lI;

wn5 = sqrt((Ks*(1+load_new/motor_new))/(load_new));

disp('The natural frequency for two-body model with shaft inertia split and lumped at motor and load while maintaining Inertia ratio, but adjusting shaft length is:');

motor_new = motor_inertia+mI;

m_new_length = ((motor_inertia*mshL)+(mI*mshL/2))/motor_new;

load_new = load_inertia+lI;

l_new_length = ((load_inertia*lshL)+(lI*lshL/2))/load_new;

Ks = GJ/(m_new_length+l_new_length);

wn6 = sqrt((Ks*(1+load_new/motor_new))/(load_new));

disp('The natural frequency for two-body model with shaft inertia equally split and Ks adjusted is:');

motor_new = motor_inertia + ShI/2;

load_new = load_inertia + ShI/2;

m_new_length = ((motor_inertia*shaft_length/2)+((ShI/2)*(shaft_length/4)))/motor_new;

l_new_length = ((load_inertia*shaft_length/2)+((ShI/2)*(shaft_length/4)))/load_new;
```

```
Ks = GJ/(m_new_length+l_new_length)

wn7 = sqrt((Ks*(1+load_new/motor_new))/(load_new))

disp('The natural frequency for two-body model with shaft inertia equally split and Ks adjusted directly is:');

motor_new = motor_inertia + ShI/2;

load_new = load_inertia + ShI/2;

cs = 1/orig_ks;

cs_left = ((motor_inertia*cs/2)+((ShI/2)*(cs/4)))/motor_new;

cs_right = ((load_inertia*cs/2)+((ShI/2)*(cs/4)))/load_new;

Ks = 1/(cs_left+cs_right)

wn8 = sqrt((Ks*(1+load_new/motor_new))/(load_new))

disp('The natural frequency for two-body model with 1 shaft inertia and moments taken about motor is:');

load_new = load_inertia + ShI;

cs = 1/orig_ks

cs = ((load_inertia*cs)+(ShI*cs/2))/load_new;

Ks = 1/cs

wn9 = sqrt((Ks*(1+load_new/motor_inertia))/(load_new))

disp('The natural frequency for two-body model with 8 shaft inertias and moments taken about motor is:');

load_new = load_inertia + ShI;

cs = 1/orig_ks;

Ks = load_new/((load_inertia*cs)+((cs/16)*(ShI/8))+((3*cs/16)*(ShI/8))+((5*cs/16)*(ShI/8))+((7*cs/16)*(ShI/8))

+((9*cs/16)*(ShI/8))+((11*cs/16)*(ShI/8))+((13*cs/16)*(ShI/8))+((15*cs/16)*(ShI/8)))

wn10 = sqrt((Ks*(1+load_new/motor_inertia))/(load_new))

disp('The natural frequency (for distributed inertia case) is:');

freq = freq*sqrt(GJ/I)

disp('The percentage differences are:');

two_body = abs(wn1-freq)/freq * 100

two_body_split = abs(wn2-freq)/freq * 100

two_body_motor = abs(wn3-freq)/freq * 100

two_body_load = abs(wn4-freq)/freq * 100

two_body_Ir = abs(wn5-freq)/freq * 100

two_body_Ir_Ks_adjust = abs(wn6-freq)/freq * 100

two_body_split_Ks_adjust = abs(wn7-freq)/freq * 100

distribute_inertia = abs(freq-freq)/freq * 100
```

# Function: distribute_inertia_chareq

```
function [chareq_left,chareq_right,chareq,dchareq] = distribute_inertia_chareq(motor_inertia,load_inertia,I,shaft_length,beta)

% [freq] = distribute_inertia_chareq(motor_inertia,load_inertia,I,shaft_length,beta)

%

chareq_left = tan(beta*shaft_length);

chareq_right = - (beta*(motor_inertia + load_inertia))/(I - ((motor_inertia*load_inertia)/I)*beta^2);

chareq = chareq_left - chareq_right;

dchareq = shaft_length*(1 + (tan(beta*shaft_length))^2) + (motor_inertia + load_inertia)*((I+(motor_inertia*load_inertia*beta^2)/I)/((I-(motor_inertia*load_inertia*beta^2)/I)^2));
```

# Function: multi_body_freq

```
function [freq] = multi_body_freq(motor_inertia,load_inertia,shaft_diameter,shaft_length,n,freq_estimate,cont_freq)

% [freq] = multi_body_freq(motor_inertia,load_inertia,shaft_diameter,shaft_length,n,freq_estimate,cont_freq)

%

Torque = holzer(motor_inertia,load_inertia,shaft_diameter,shaft_length,n,freq_estimate);

if Torque > 0

dir = 1;

else

dir = 0;

end

variation = freq_estimate/10;

while variation > 0.01

if dir == 1

freq_estimate = freq_estimate + variation;

else

freq_estimate = freq_estimate - variation;

end

Torque = holzer(motor_inertia,load_inertia,shaft_diameter,shaft_length,n,freq_estimate);

if Torque > 0

pos = 1;

else
```

```
pos = 0;
end
if pos ~= dir
if dir == 1
freq_estimate = freq_estimate - variation;
else
freq_estimate = freq_estimate + variation;
end
variation = variation/10;
end
end
freq = freq_estimate;
percent_error = abs(freq-cont_freq)*100/cont_freq
```

# Function: holzer

```
function [Torque] = holzer(motor_inertia,load_inertia,shaft_diameter,shaft_length,n,freq_estimate)
% [Torque] = holzer(motor_inertia,load_inertia,shaft_diameter,shaft_length,n,freq_estimate)
%
GJ = (80e9*pi*shaft_diameter^4)/32;
I = (pi*(shaft_diameter/2)^4*8000)/2;
Ks = GJ/shaft_length;
ShI = I*shaft_length;
I = load_inertia;
Iwsq = I*freq_estimate^2;
Beta = 1;
Torque = Iwsq*Beta;
K = 2*n*Ks;
angle = Torque/K;
for index = 2:n+2
if index < (n+2)
I = ShI/n;
K = n*Ks;
```

```
else
I = motor_inertia;
K = 2*n*Ks;
end
Iwsq = I*freq_estimate^2;
Beta = Beta - angle;
Torque = Torque + Iwsq*Beta;
angle = Torque/K;
end
```

## C.2 Code for Disturbance Force Calculations

Matlab was also used to calculate the disturbance forces required to exceed the given position error tolerances in the comparison of inherent dynamic stiffness presented in Section 5.3. The code for these calculations is also given in this appendix. The function "dyn_stiff_lin" was used to calculate the required forces on a linear motor system. The function "dyn_stiff_ddbs" was used to calculate the required forces for a direct driven ballscrew configuration. Similarly, the functions "dyn_stiff_bdbs" and "dyn_stiff_randp" were used to calculate the required forces for a belt driven ballscrew configuration and a rack and pinion configuration respectively.

### Function: dyn_stiff_lin

```
function [force_dist] = dyn_stiff_lin(Mass,w,allow_error,plot_col);
% [force_dist] = dyn_stiff_lin(Mass,w,allow_error);
%
Bm = 1.56;
sys1 = tf(1,[Mass,0]);
sys2 = feedback(sys1,Bm);
```

```
sys3 = tf(1,[1,0]);

final_sys = sys2*sys3;

[mag,phase] = bode(final_sys,w);

for index = 1:length(mag)

force_dist(index) = allow_error/mag(index);

end

plot(w,force_dist,plot_col);
```

# Function: dyn_stiff_ddbs

```
function [force_dist] = dyn_stiff_ddbs(Mass,w,allow_error,plot_col);

% [force_dist] = dyn_stiff_ddbs(Mass,w,allow_error,plot_col);

% The general parameters used here are from the Drive Comparison Test-Bed

% The load table is assumed to be at pos x = 0.5m

%

Pitch = 5e-3;

Bl = 1.75e-3;

Bm = 3.05e-3;

Jbs = 3.22e-5*0.5;

Jm = 3.716e-4;

Ks = 225/0.5;

Cs = 1.75e-3/((0.5)^(1/2));

Jl = (Mass*(Pitch/(2*pi))^2) + Jbs;

Ksadj = (2*Ks*(2*Jm+Jbs)*(2*Jl+Jbs))/(8*Jm*Jl+3*Jbs*(Jm+Jl)+Jbs^2);

Flex = tf([Cs,0],1);

Flex = Ksadj + Flex;
```

```
JL = (2*Jl + Jbs)/2;

JM = (2*Jm + Jbs)/2;

sys1 = tf(1,[JL,Bl,0]);

sys2 = tf(1,[JM,Bm,0]);

sys3 = ((Pitch/(2*pi))*sys1)/(1+Flex*(sys1+sys2));

final_sys = (Pitch/(2*pi))*sys1*(Flex*sys3 - (Pitch/(2*pi)));

[mag,phase] = bode(final_sys,w);

for index = 1:length(mag)

force_dist(index) = allow_error/mag(index);

end

plot(w,force_dist,plot_col);
```

# Function: dyn_stiff_bdbs

```
function [force_dist] = dyn_stiff_bdbs(Mass,w,allow_error,plot_col);

% [force_dist] = dyn_stiff_bdbs(Mass,w,allow_error,plot_col);

% The general parameters used here are from the Drive Comparison Test-Bed

% The load table is assumed to be at pos x = 0.5m

%

Pitch = 5e-3;

Rm = 34.5e-3;

Rp = 15*34.5e-3;

Bl = 1.75e-3;

Bm = 1.6e-3;

Bp = 1.45e-3;

Jbs = 3.22e-5*0.5;
```

```
Jm = 6.67e-4;

Jp = 3.53e-4;

Ks = 225000/0.5;

Cs = 2.137e-3/((0.5)^(1/2));

Kblt = 997000000;

Cblt = 0.048;

Jl = (Mass*(Pitch/(2*pi))^2) + Jbs;

Ksadj = (2*Ks*(2*Jp+Jbs)*(2*Jl+Jbs))/(8*Jp*Jl+3*Jbs*(Jp+Jl)+Jbs^2);

Flexbs = tf([Cs,0],1);

Flexbs = Ksadj + Flexbs;

Flexblt = tf([Cblt,0],1);

Flexblt = Kblt + Flexblt;

JL = (2*Jl + Jbs)/2;

JP = (2*Jp + Jbs)/2;

sys1 = tf(1,[JL,Bl,0]);

sys2 = tf(1,[JP,Bp,0]);

sys3 = tf(Rm,[Jm,Bm,0]);

sys4 = (Flexbs*Rp*sys2)/(1+Flexblt*(sys3*Rm + sys2*Rp*Rp));

sys5 = ((Pitch/(2*pi))*sys1)/(1-sys2*sys4*Rp*Flexblt + Flexbs*(sys1+sys2));

final_sys = (Pitch/(2*pi))*sys1*(Flexbs*sys5 - (Pitch/(2*pi)));

[mag,phase] = bode(final_sys,w);

for index = 1:length(mag)

force_dist(index) = allow_error/mag(index);

end

plot(w,force_dist,plot_col);
```

# Function: dyn_stiff_randp

```
function [force_dist] = dyn_stiff_randp(Mass,w,allow_error,plot_col);

% [force_dist] = dyn_stiff_randp(Mass,w,allow_error,plot_col);

% The general parameters used here are from the Drive Comparison Test-Bed

% The load table is assumed to be at pos x = 0.5m

%

Rpin = 20e-3;

Bl = 32.8e-3;

Bm = 1.6e-3;

Js = 4e-6;

Jm = 3.43e-4;

Jpin = 4.4e-5;

Ks = 25588;

Cs = 0.0499;

Jl = Jpin + Mass*Rpin^2;

Ksadj = (2*Ks*(2*Jm+Js)*(2*Jl+Js))/(8*Jm*Jl+3*Js*(Jm+Jl)+Js^2);

Flex = tf([Cs,0],1);

Flex = Ksadj + Flex;

JL = (2*Jl + Js)/2;

JM = (2*Jm + Js)/2;

sys1 = tf(1,[JL,Bl,0]);

sys2 = tf(1,[JM,Bm,0]);

sys3 = (Rpin*sys1)/(1+Flex*(sys1+sys2));

final_sys = Rpin*sys1*(Flex*sys3 - Rpin);

[mag,phase] = bode(final_sys,w);

for index = 1:length(mag)

force_dist(index) = allow_error/mag(index);

end

plot(w,force_dist,plot_col);
```

Appendix D

# Test-Bed Details

This appendix contains some of the details of the three test-beds used throughout this research. In particular, details of the feedback elements used in each of the test-beds is given. Detailed drawings of each test-bed are also provided. Figure D.1 details the main structure design of the Motor-Transmission-Load Test-Bed. The design of the motor mounting brackets for the Motor-Transmission-Load Test-Bed is detailed in Figure D.2. The special backlash couplings for the Motor-Transmission-Load Test-Bed are also detailed in Figure D.3. Two drawings of the Drive Comparison Test-Bed are provided. Figure D.4 details the main test-bed structure, while Figure D.5 shows an assembled view of the test-bed. Two drawings of the Linear Motor Test-Bed are also provided. Figure D.6 shows the structure and machining details of the main test-bed frame, while Figure D.7 shows the details of the load carrying table.

As described in Sections 4.3 and 4.4, position feedback for both the Motor-Transmission-Load Test-Bed and the Drive Comparison Test-Bed was achieved through rotary encoders embedded in the Siemens motors. The CNC system interpolates using instantaneous sine and cosine information, along with the basic period of the encoders, to improve the resolution of the position feedback. The specifications of the Siemens rotary encoders are:

| | |
|---|---|
| Power Supply | 5V |
| Output Signal | 2 Channels ($V_1$ and $V_2$) of differential sinusoids in quadrature |
| Output Amplitude ($V_{pp}$) | 1 |
| Output Period (mrad) | 3.068 |

The embedded encoders provide two further sine and cosine signals for commutation purposes. Along with the position and commutation signals, a once per revolution reference signal is also provided. Since the position encoder signals are incremental, the reference signal is used to initialise the absolute position of the motor.

For additional acceleration feedback, a Hübner accelerometer (ACC 93) was also used on the Motor-Transmission-Load Test-Bed. This accelerometer was coupled with a Hübner sensor amplifier (HEAG 164-15) and could be attached to either the motor or load end of the system. The specifications of the ACC 93 are:

| | |
|---|---|
| Output Amplitude | max. 2 Vpp |
| Sensitivity | down to 1 mV/0.001 m/s$^2$ |
| Bandwidth | $\approx$ 1 kHz |
| Weight | $\approx$ 120g |

The specifications of the HEAG 164-15 sensor amplifier are:

| | |
|---|---|
| Power Supply | 15V $\pm$20% max. $\pm$70mA |
| Differential Output | max. 22V max. $\pm$50mA |
| Gain (Jumper 1) | $\pm$3V = $\pm$1 rad/s$^2$ |
| Gain (Jumper 2) | $\pm$3V = $\pm$20 rad/s$^2$ |

For the Linear Motor Test-Bed, position feedback was achieved through an incremental linear encoder (Renishaw – RGS-S/RGH22B) mounted on one side of the frame structure. The CNC system interpolates using instantaneous sine and cosine information, along with

the basic period of the linear encoder, to improve the resolution of position feedback. The CNC system also uses this position feedback for commutation purposes. The specifications of the Renishaw linear encoder are:

| | |
|---|---|
| Power Supply | 5V $\pm$5% 120mA (typical) |
| Output Signal | 2 Channels ($V_1$ and $V_2$) of differential sinusoids in quadrature |
| Output Amplitude ($V_{pp}$) | 0.6-1.2 |
| Output Period ($\mu$m) | 20 |
| Amplitude at 1m/s | Approximately 100% |
| Amplitude at 2m/s | Approximately 90% |
| Amplitude at 4m/s | Approximately 65% |
| Max Acceleration | 30g |
| Weight | 45g (read-head) |
| Dimensions [Length/Width/Height (mm)] | 44/27/16 |

Two magnetic actuators (Renishaw RGM22S) were also used as reference marks for the linear encoder. These actuators were positioned adjacent to the tape scale and trigger a sensor in the read-head as it passes over. The trigger signal from these actuators enables a pulse to be outputed from the read-head, which is used during the axis homing process to initialise the absolute position.

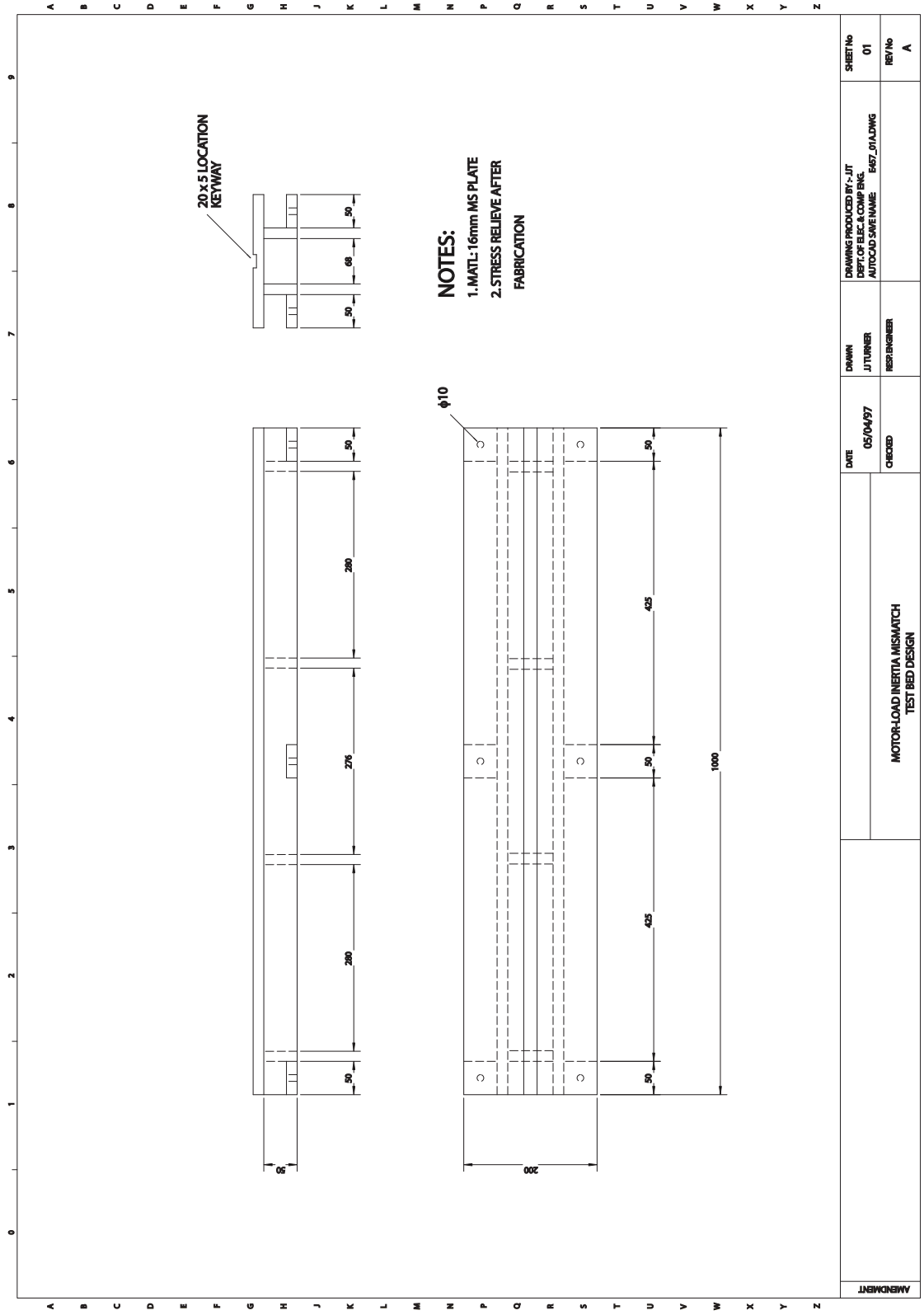


Figure D.1: Motor-Transmission-Load Test-Bed – Drawing 1

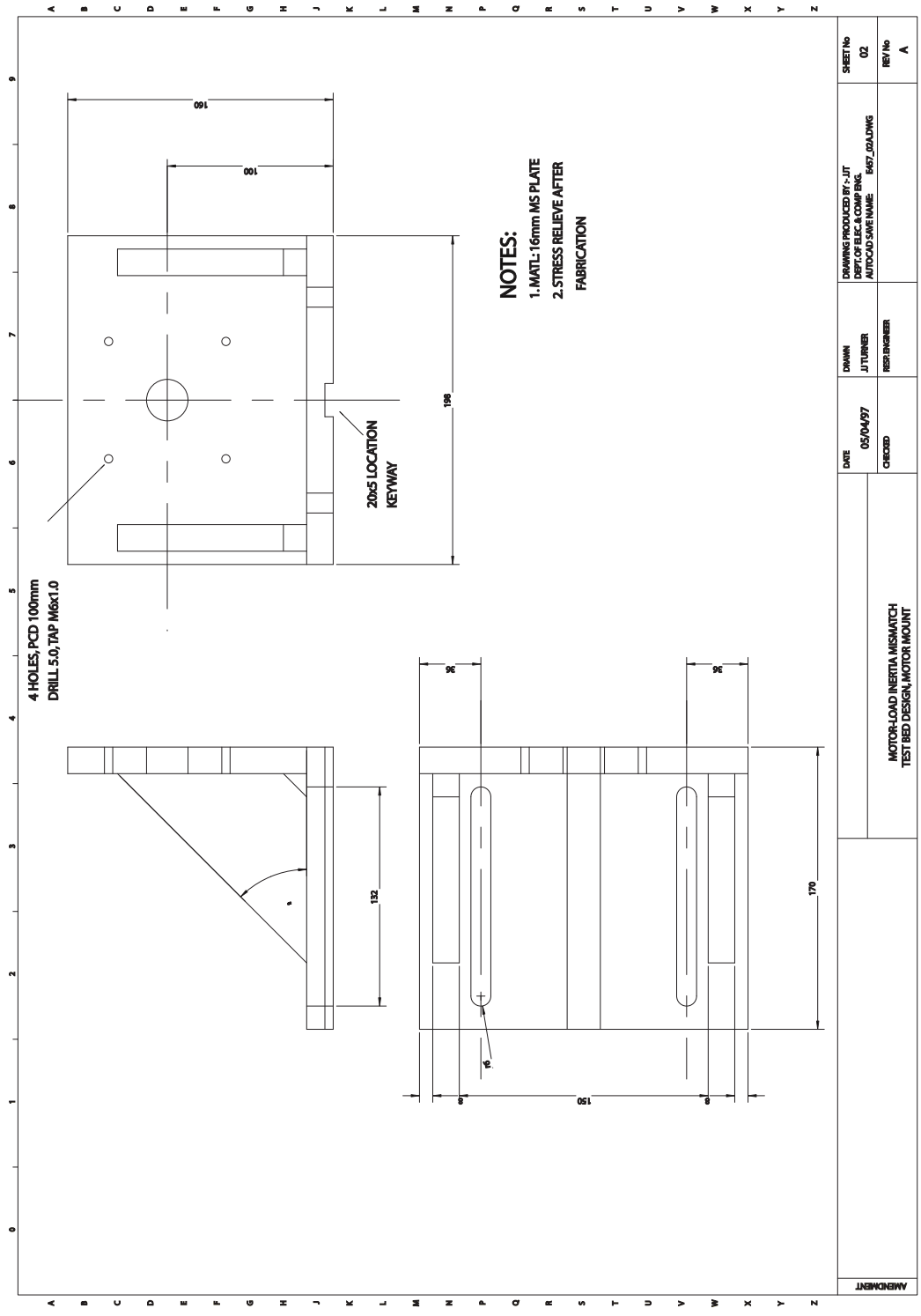


Figure D.2: Motor-Transmission-Load Test-Bed – Drawing 2

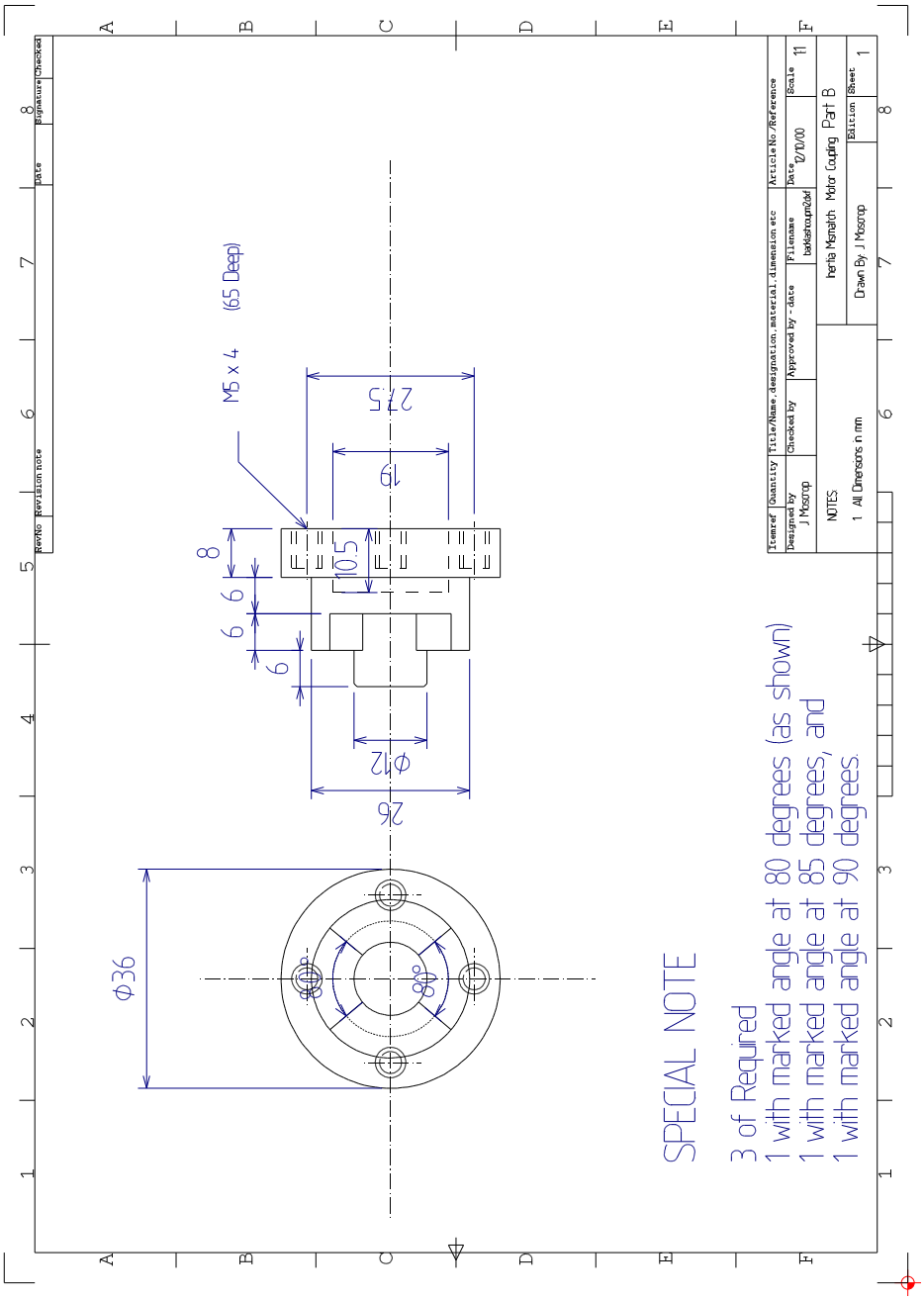


Figure D.3: Motor-Transmission-Load Test-Bed – Backlash Couplings

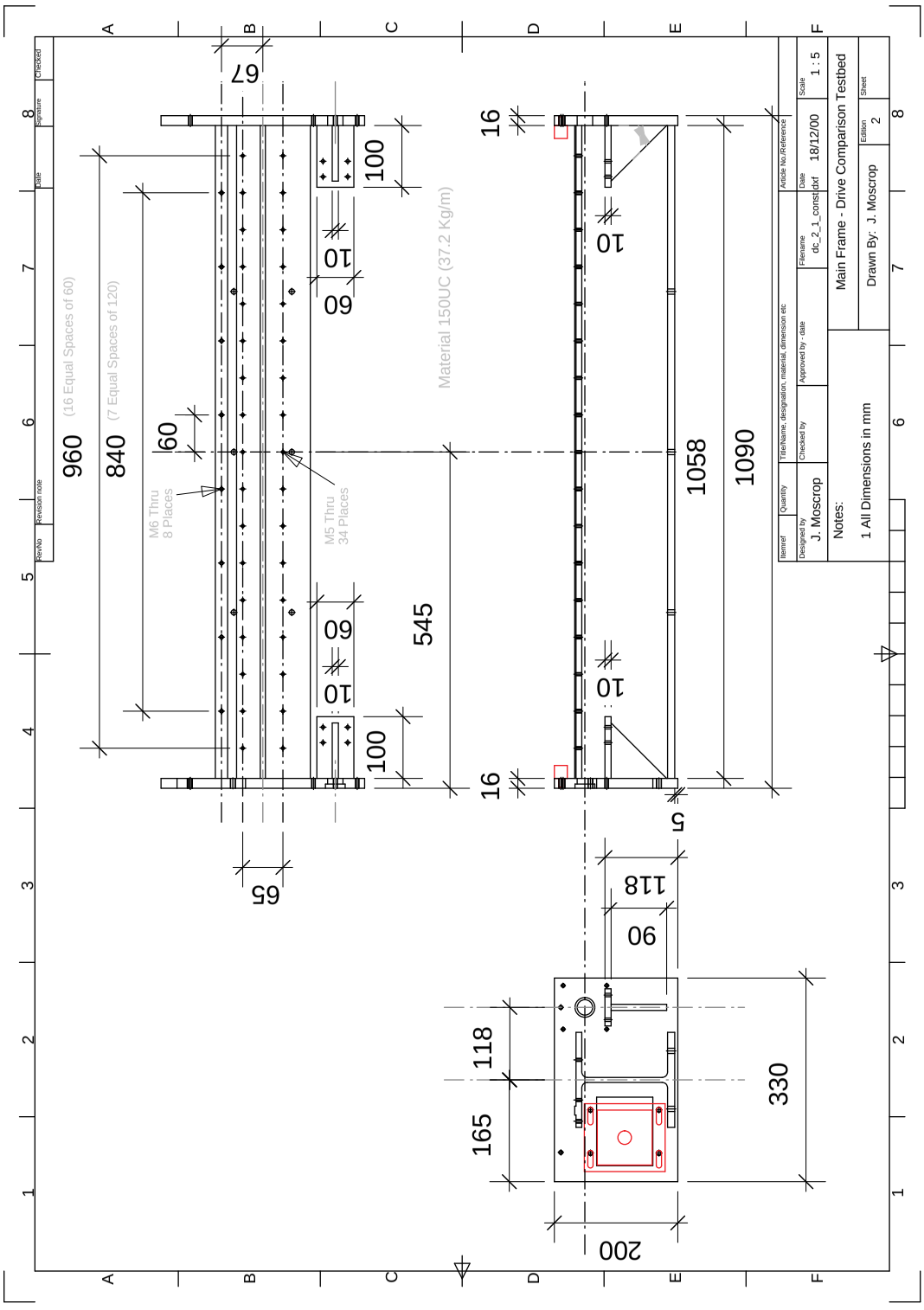


Figure D.4: Drive Comparison Test-Bed – Detailed Drawing

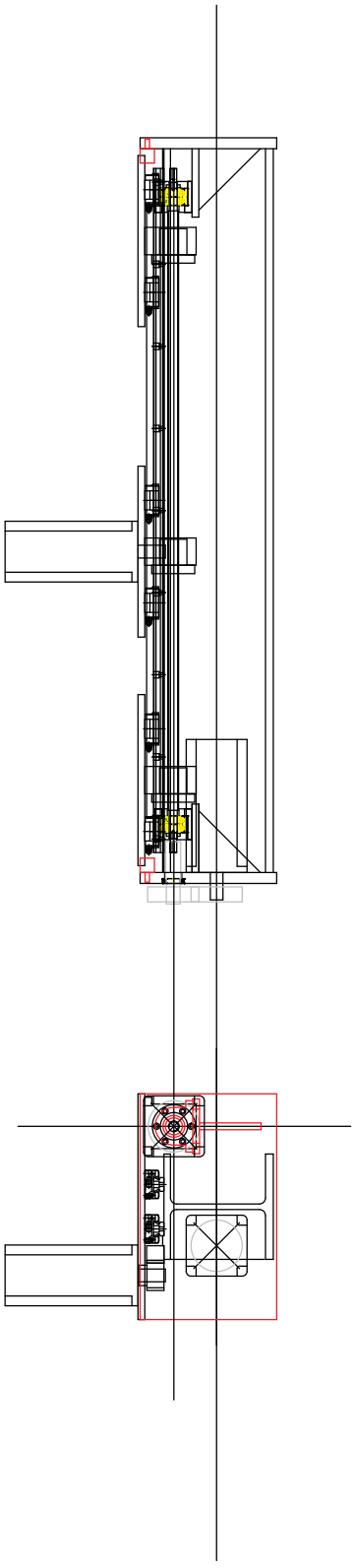

Figure D.5: Drive Comparison Test-Bed – Assembly

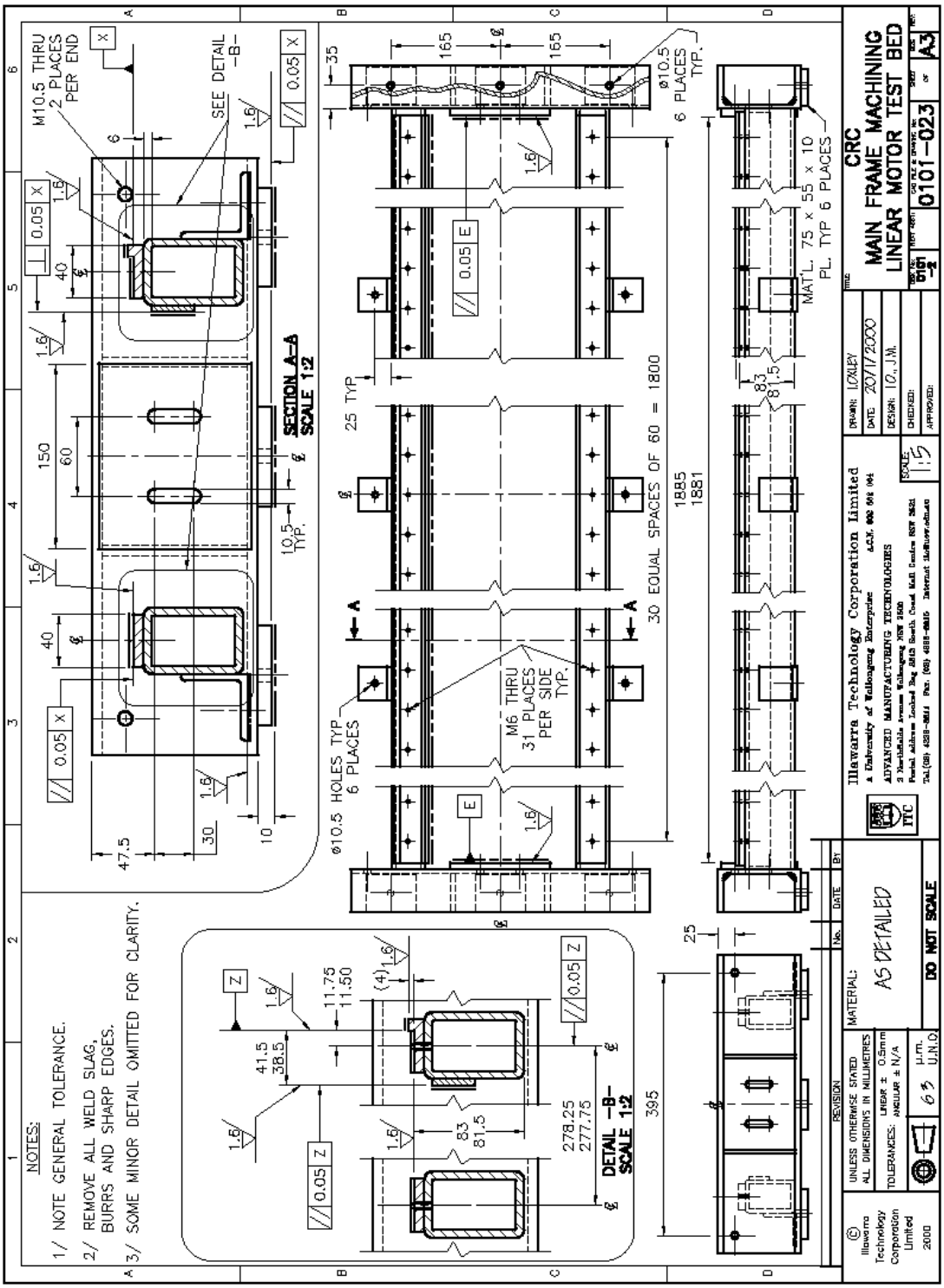


Figure D.6: Linear Motor Test-Bed – Frame Drawing

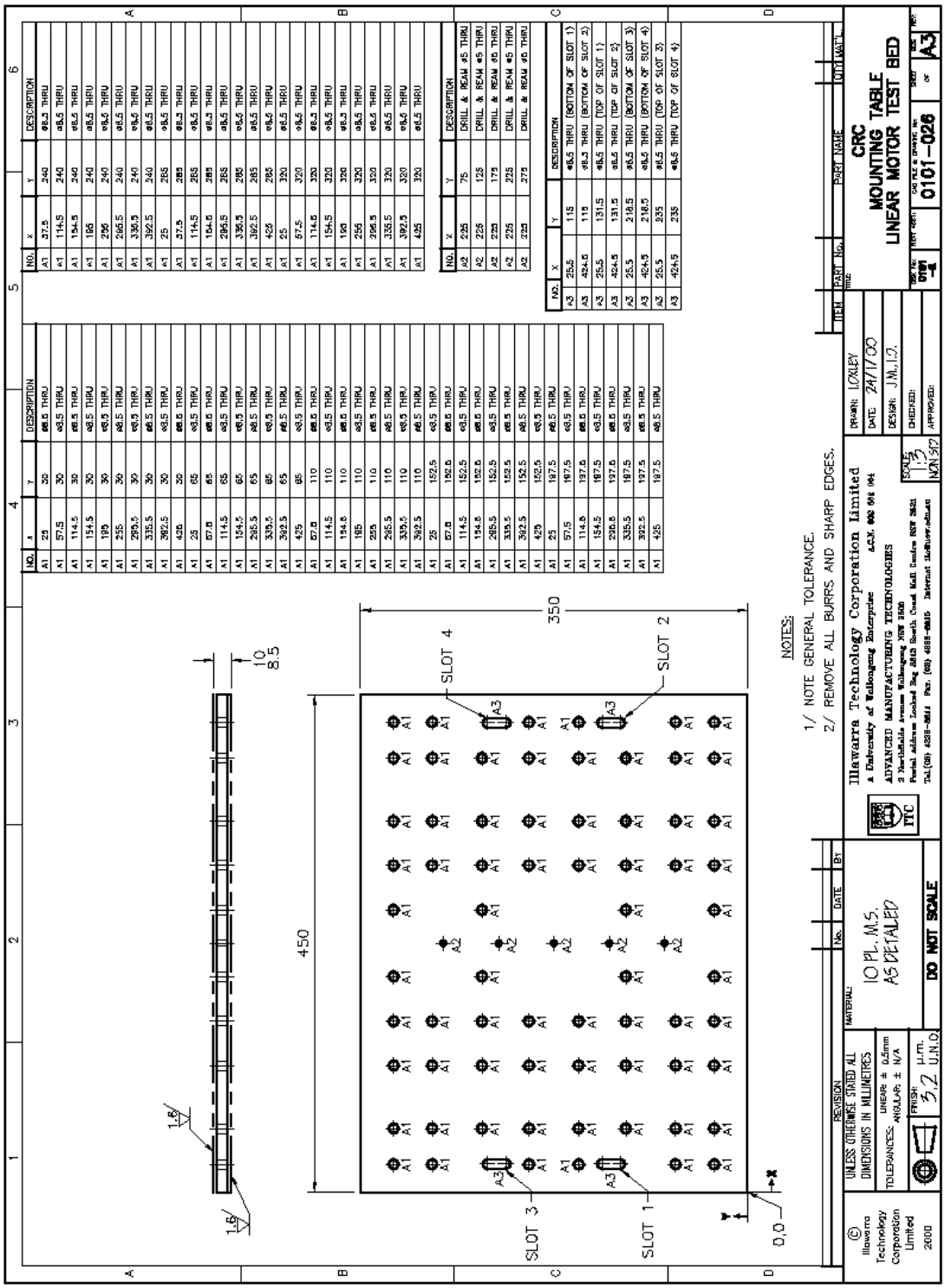


Figure D.7: Linear Motor Test-Bed – Load Table